TECHNICAL CHEMISTRY I
BARCIKOWSKI GROUP

UNIVERSITÄT
DUISBURG
ESSEN

Offen im Denken

Laser synthesis and functionality of heterogeneous catalysts

Dissertation

zur Erlangung des akademischen Grades eines
Doktors der Naturwissenschaften
– Dr. rer. nat. –

vorgelegt von

Galina Marzun
geboren in Angren

Lehrstuhl für Technische Chemie 1
der
Universität Duisburg-Essen

Duisburg, 2017

The current thesis has been conducted from December 2013 till April 2017 in the working group of Prof. Dr. Ing. Stephan Barcikowski at the Technical Chemistry I of the University of Duisburg-Essen.

Tag der Disputation: 22.06.2017

Referee:	Prof. Dr. Ing. Stephan Barcikowski
	Prof. Dr. Jennifer Strunk
Chairman:	Prof. Dr. Jochen S. Gutmann

Abstract

Catalysis is one of the most important key disciplines to achieve a sustainable future. Despite its significance in chemistry, environmental technology and mobility, there are still numerous open questions related to catalysis. In particular, a targeted catalyst synthesis is crucial in order to control chemical processes in a resource-conserving and sustainable manner. In this sense, the Pulsed Laser Ablation in Liquids (PLAL) technique and the subsequent colloidal particle adsorption to supports is a novel promising approach for the synthesis of ligand-free nanomaterials with high purity for catalytic applications. Yet, to establish this preparation method, deeper insights into the properties of particles as well as their defined settings are necessary.

In this thesis, an entire research process from fundamental analysis to application-related investigations is integrated. Since heterogeneous catalysis occurs at the interface of catalysts and reactants, the surface properties of laser-generated, catalytically relevant nanoparticles are investigated in the first part of this thesis. The characteristics of laser-generated platinum and copper nanoparticles were examined, and the results were related to their impact on the formation of alloy nanoparticles, which utilizes combinations of these transition metals. The development of active alloy catalysts is of great importance, since they implement superior properties such as higher catalytic activities as their mono-metals and enable the use of a decreased amount of noble expensive metals. The surface investigations allow a better understanding of underlying synthesis parameters and processes that enables the preparation of well-defined catalytically active materials. By *in situ* characterization of the surface structure, it was proven that laser-generated platinum nanoparticles are partially oxidized (in case of platinum positively charged) in liquids. While their surface properties are retained after particle deposition, an altered nanoparticle interaction with the solvent was analysed on the basis of the changed number of bonds. Apart from the investigations on noble nanoparticles, concepts to control the properties of ignoble metals (Cu, Ni, Mo) by the solvent will be given. Following these investigations, further conclusions on the preparation of alloy nanoparticles are presented. The question regarding how ignoble catalytically active alloy nanoparticles can be synthesized and modified in their properties by PLAL is addressed. It is shown that particle oxidation has a crucial effect on alloy formation and its stability, which is highly influenced by the solvent.

In order to be applied in heterogeneous catalysis, the metal nanoparticles must be adsorbed on support materials. Thus, in the last part of this work, the adsorption of ligand-free nanoparticles on oxide and carbon supports is addressed. Parameters that control the nanoparticle adsorption

on TiO_2 are identified. It is demonstrated that particle adsorption can be controlled by the pH and ionic strength, whereby also nanoparticles fully covered by various ligands could be adsorbed on the support by attractive electrostatic interactions. These experimental studies reveal the mechanism of colloidal particle deposition. Following these results, a transferable processing route to a manifold of supports is established. Subsequently, a good chemical stability of the so-prepared catalysts is displayed. This thesis suggests the significance and application potential of the catalyst synthesis route for future use.

The present studies are based on four selected publications (of, overall, nine peer-reviewed publications), which were created within the doctorate studies. The ‘state of the art’ section consists of an extract of a planned non-published review. The thesis is written in a half-cumulative manner, where the text is divided into different chapters with the respective introductions to the interrelated research topics. At the end, the results are summarized, and an outlook for future investigations is given.

Zusammenfassung

Die Katalyse ist eine der wichtigsten Schlüsseldisziplinen für eine nachhaltige Zukunft. Trotz ihrer Bedeutung in der Chemie, Umwelttechnik und Mobilität gibt es noch zahlreiche offene Fragen zur Katalyse. Insbesondere ist eine gezielte Katalysatorsynthese entscheidend, um chemische Prozesse ressourcenschonend und nachhaltig kontrollieren zu können. In diesem Zusammenhang ist die Methode der gepulsten Laserablation in Flüssigkeiten (PLAL) und die anschließende kolloidale Partikelabscheidung auf Trägermaterialien ein neuartiger und vielversprechender Ansatz zur Synthese ligandenfreier Nanomaterialien, welche eine hohe Reinheit besitzen und somit für katalytische Anwendungen von Interesse sind. Um diese Synthese zu etablieren, sind jedoch tiefere Einblicke in die Partikeleigenschaften sowie deren definierte Einstellungen erforderlich.

In dieser Arbeit wird ein gesamter Forschungsprozess von der Grundlagenforschung bis hin zu anwendungsorientierten Untersuchungen integriert. Da heterogene Katalysereaktionen an der Grenzfläche von Katalysatoren und Reaktanten stattfindet, werden im ersten Teil dieser Arbeit die Oberflächeneigenschaften von lasergenerierten, katalytisch relevanten Nanopartikeln untersucht. Die Eigenschaften von lasergenerierten Platin- und Kupfer-Nanopartikeln wurden untersucht und die Auswirkungen dieser Ergebnisse auf die Bildung von Legierungs-Nanopartikeln damit begründet. Die Entwicklung von aktiven Legierungskatalysatoren ist von großer Bedeutung, da sie maßgebende Eigenschaften wie höhere katalytische Aktivitäten als ihre Mono-Metalle implementieren und die Verwendung einer geringeren Menge an teuren Edelmetallen ermöglichen.

Die Oberflächenuntersuchungen ermöglichen ein besseres Verständnis der zugrunde liegenden Syntheseparameter und Prozesse, die die Herstellung von gut definierten katalytisch aktiven Materialien ermöglichen. Durch eine *In- situ*-Charakterisierung der Oberflächenstruktur mittels Röntgenabsorptionsspektroskopie wurde nachgewiesen, dass lasergenerierte Platin-Nanopartikel in Flüssigkeiten teils oxidiert (und damit positiv geladen) sind. Während die Partikeloberflächeneigenschaften nach der Adsorption auf einem Träger erhalten bleiben, wurde eine veränderte Nanopartikel-Wechselwirkung mit dem Lösungsmittel auf der Basis der geänderten Anzahl von Bindungen analysiert. Neben den Untersuchungen an edlen Nanopartikeln werden Konzepte zur Kontrolle der Eigenschaften von unedlen Metallen (wie Cu, Ni, Mo) durch das Lösungsmittel vorgestellt. Nach diesen Untersuchungen werden weitere Schlussfolgerungen zur Herstellung von Legierungsnanopartikeln gezogen und beschrieben. Hierbei wird auf die Frage eingegangen, wie unedle katalytisch aktive Legierungsnanopartikel,

welche mittels PLAL hergestellt werden, in ihren Eigenschaften modifiziert werden können. Es wird gezeigt, dass die Partikeloxidation, welche stark vom Lösungsmittel beeinflusst wird, einen entscheidenden Einfluss auf die Legierungsbildung und die Partikelstabilität hat.

Für eine Anwendung in der heterogenen Katalyse müssen die Metallnanopartikel auf Trägermaterialien adsorbiert werden. So wird im letzten Teil dieser Arbeit die Adsorption von ligandenfreien Nanopartikeln auf Oxid- und Kohlenstoffträger adressiert. Die einflussgebenden Parameter, die die Nanopartikeladsorption auf TiO_2 kontrollieren, werden bestimmt. Es wird gezeigt, dass die Partikeladsorption durch den pH-Wert und die Ionenstärke gesteuert werden kann, wobei auch Nanopartikel, die volständig mit verschiedenen Liganden bedeckt sind, auf dem Träger durch elektrostatische Wechselwirkung adsorbiert werden können. Somit ermöglichten diese experimentellen Untersuchungen den Mechanismus der kolloidalen Partikelablagerung zu ermitteln. Darauf basierend kann die Herstellungsprozesskette der laserbasierten heterogenen Katalysatoren auf verschiedene Trägermaterialien übertragen werden. Zum Schluss wird gezeigt, dass die so hergestellten Katalysatoren bei geringen pH-Werten chemisch beständig sind und somit ein Anwendungspotential der Katalysatorsynthese besteht.

Die vorliegenden Studien basieren auf vier ausgewählten Publikationen (von insgesamt neun Peer-Review-Publikationen), die im Promotionsstudium erstellt wurden. Der Abschnitt "State of the art" besteht aus einem Auszug aus einem geplanten, nicht veröffentlichten Review. Diese Dissertation ist halbkumulativ geschrieben, in der der Text in verschiedene Kapitel mit den jeweiligen Einführungen zu den zusammenhängenden Forschungsthemen aufgeteilt wird. Am Ende werden die Ergebnisse zusammengefasst und ein Ausblick für zukünftige Untersuchungen gegeben.

Content

1. State of the art

Sven Reichenberger, Stephan Barcikowski, Galina Marzun,

Laser-generated nanoparticles heterogeneous catalysts, manuscript to be submitted as a review

---

1.1 Introduction

The rising demand for clean nano-based products (i.e., in biomedicine, optics or catalysis) reflects the need for new innovative methods to straightforwardly synthesize pure nanomaterials. Recently, Pulsed Laser Ablation in Liquids (PLAL) has proved to be a valuable method for the production of promising functional materials for broad research and application fields. [1] In particular in the field of catalysis, the growing interest of laser-generated nanoparticles is among other reasons due to its process elegance, purity of the materials, transferability of the synthesis route and the possibility for an up-scaling.

Heterogeneous catalysis is one of the most trailblazing disciplines in environmental and chemical industry covering about 80% of the overall catalytically synthesized chemical products [2]. By lowering the activation energy of a chemical reaction, the catalyst is intended to increase the reaction rate and selectivity without being consumed itself. With this being an idealistic scenario, realistic catalysts and active sites often tend to degrade losing their initial selectivity and overall activity because of morphology changes due to structural rearrangements [3] [4] [5] [6] [7] [8] [9], partial loss of catalyst components [10] [11] or by-product poisoning [12] [11]. Typical mechanisms describing these degradation processes are among others:

- Ostwald-ripening [4] [5] [6] [7]
- dealloying [13]
- sintering [14] [15] [11]
- coking [12] [11]

These processes lead to a diminished active surface area and hence total number of active sites per mass unit (of catalyst) resulting in a significant decrease of the catalyst turn over frequency. Accordingly, one of the most important influencing factors regarding catalytic research is based on generating excellent catalysts with a high activity and selectivity while sustaining surface and structural properties of nanostructured materials even under reaction conditions. To that end research on structure-activity-, structure-stability-correlations as well as the development of novel nanomaterials and composites embodies one of the dominant topics in current and past literature on organic and inorganic reactions and applied surface science [16]. For laser-based

catalysts, the degradation issue of the materials has been less reported, but will be addressed here by introducing the previous studies and critically discussing the future prospects of laser-generated materials for catalysis.

Up to now alloys containing highly active precious metals such as platinum, rhodium and palladium are frequently utilized in research on heterogeneous catalysis. Thanks to the low required over-potential including favorable hydrogen adsorption and desorption properties (Sabatier principle), platinum has been used for decades as an active catalyst material for hydrogenation [17] [18], photocatalytic water splitting [19] [20], hydrogen evolution reaction [21] and fuel cells reactions like oxidation of hydrogen and reduction of oxygen [10] [22] [23]. Yet due to its high costs and limited resistance against Ostwald ripening [6] research endeavors are mainly focused on alloy formation either being free of expensive noble metals [24] or respectively containing only minute amounts of platinum [13] [25] [26]. Hereby the alloy formation introduces synergetic effects modifying the structural stability [26] and educt activation [27] in order to increase the overall catalyst activity and selectivity [28]. Thus the preparation of homogenous alloy nanoparticles in various compositions presents one of the main prerequisites in this field of research. Additionally the catalytic activity is governed by the morphology of nanostructures including nanoparticle size as well as dominating crystallographic facets. As a general deduction an enhanced catalytic activity is mainly provided by less densely packed planes with an open structure and higher surface energy [29] [30]. Other structure-activity-correlations aim of optimizing the adsorption enthalpy of educt molecules in order to minimize the impact of rate determining reaction steps as was shown by Norskov et al. in case of the oxygen activation during the oxygen reduction reaction (ORR) [27] [31]. Yet in order to develop and prove composition-activity- or structure-activity-correlations like given by Norskov et al., suitable catalyst preparation method needs to be employed [31].

There are three main synthesis routes for the synthesis of heterogeneous catalysts. A frequently reported classical preparation approach is the impregnation method as shown in Fig. 1 A. The wet impregnation method is mainly based on the loading of a support material with metal-salt precursors (i.e., metal chloride or acetate salt) and their subsequent chemical reduction [22]. Novel variations of this method are based on using supercritical fluids as dispersant which are favorable candidates for the impregnation of high surface mesoporous materials [32]. Yet due to the simultaneously occurring nanoparticle nucleation and growth processes during precursor reduction (see Fig. 1 A), independent investigations of nanoparticle composition and –size while excluding changes in the catalyst morphology, defect density and nanoparticle loading

are rather complex to realize [33] [22]. For example the particle loading on the support can be easily increased by adding more precursor salt, however the particle size increases simultaneously with the salt concentration [34] [35]. Obviously when choosing a sufficient precursor, its wettability and adsorption properties on the support surface need to be considered as well [32] rendering parametric studies under variation of the support material even more complex. Furthermore another established chemical synthesis method for heterogeneous catalysts is the deposition-precipitation method. The approach is based on the co-precipitation of a metal and support material precursor by adding a precipitating agent or changing the pH followed by a successive ageing step of the generated slurry at defined temperature conditions [36]. Hereby the nanoparticle nucleation and growth are again concurrent processes. Hence, for increasing the nanoparticle mass-loading a higher amount of metal precursor as well as additional adjustments of the nucleation parameters (e.g. temperature or stirring speed) are being required. Accordingly on adjusting nanoparticle properties (e.g. composition, size or loading) e.g. for screening purposes, additional changes of the precipitation conditions are to be individually developed. These changes yet again are likely to alter the resulting support material properties (e.g. defect density) introducing further cross-correlations which have to be regarded in parametric studies [37] [33].

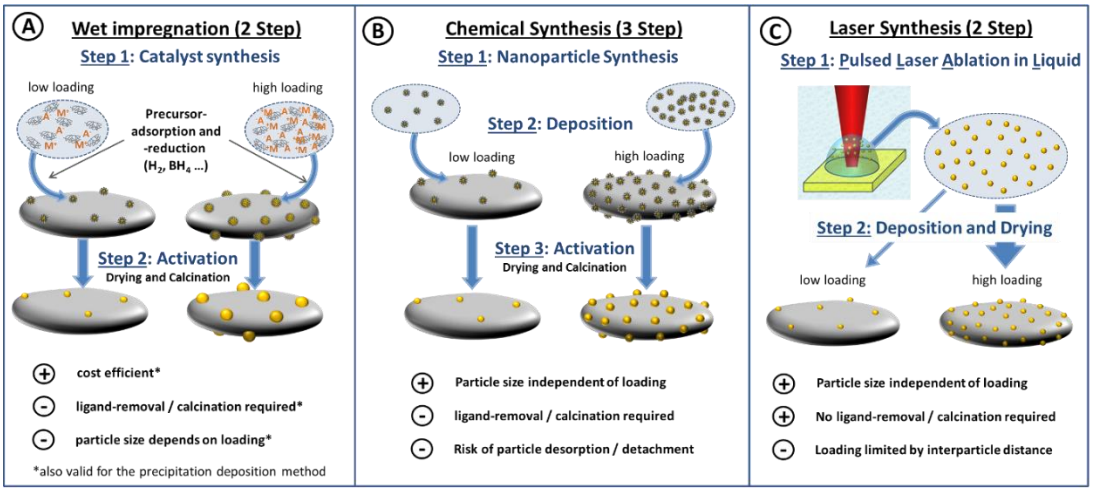

Fig. 1 Comparison of different preparation principles of heterogenous catalysts as well as their advantages and disadvantages.

In order to circumvent the previously described dependencies a more defined synthesis route (initially designed for preparing electro-catalysts) is given by the *Bönnemann* method allowing an independent control of particle and surface properties (see Fig. 1 B) [38]. Herein colloidal nanoparticles are prepared by a traditional precursor reduction method, often in the presence of size-quenching surfactant additives (ligands) [38] [39]. These size-controlled nanoparticles are

subsequently adsorbed onto a supporting material in a separate step by simply mixing the surfactant-stabilized particles with a surface-modified support with ligands [40] [39]. However, due to the protecting ligand layer around the nanoparticles a direct contact between nanoparticle and support is only achieved after subsequent calcination or ligand extraction steps. Yet on calcination the preadjusted NP- and support properties (e.g. crystal structure and faces, defect density etc.) may again be altered rendering independent parametric studies required for developing structure activity correlations more complex and intensive [41].

In order to elude those inconvenient effects a rather novel catalyst preparation technique, namely the laser-based catalyst preparation method has recently been developed. [42] [43] [44] [45] [15]. The main principle as well as the advantages and disadvantages are presented in Fig. 1 C. Similar to the *Bönnemann technique* of colloidal deposition the laser method is usually based on a two step synthesis route, while one step processes are also possible but not always feasible as will be discussed later. At first electrostatically stabilized ligand-free metal [46] [45] [47] [48] or alloy [49] [50] [51] [52] nanoparticles with defined particle size [45] [44] [53] and composition [54] [55] are prepared in liquid without organic additives employing the Pulsed Laser Ablation in Liquid (PLAL) technique. Current state of laser synthesis and processing of colloids (LSPC) has been reviewed recently [1]. In brief, a target material (e.g. metal, oxide, polymer) is immersed in a carrier liquid (usually water or basic organic solvents) and irradiated with a pulsed laser beam focused onto the target material as described by Rehbock et al. and Amendola et al. in more detail [56][57] [58]. Subsequently, these nanoparticles are being adsorbed onto support materials by simple mixing following the electrostatic adsorption principle established by Wagener and Marzun et al. [43] [44] [59] [60]. This method allows a transferability on various support such as oxides, sulfates or carbon-based materials [43] [45] [44]. Following a simple decantation and drying step at moderate temperatures (<<100 °C) the active heterogeneous catalyst is obtained in catalytically relevant quantities (currently in lower kilogram-scale [47] [48]) without applying further calcination steps as demonstrated by Dong et al. [15]. Importantly, the size of the as-prepared ligand-free colloid does not change during preparation of the heterogeneous catalyst. Hence independent parametric studies on the effect of nanoparticle size and loading as well as defect density and morphology of different support materials are possible to be conducted without any preparation induced cross-correlations. This is interesting for up-scaling, but also for fundamental studies.

Due to these given advantages the current research and prospects of laser-generated nanoparticals for catalysis purposes are summarized, by structuring this review into several

chapter relevant for catalysis: purity, functional properties, alloys and the strategy for integration of nanoparticles onto supports. Within this sections, an overview of expedient recommendations for the design of suitable catalysts and a description of their perspectives will be presented.

1.2 High catalytic performance: Purity matters

a. Value of ligand-free nanoparticles

Numerous investigations have been conducted regarding the influence of remaining or intentionally added ligands on the catalytic activity in various reactions [61] [62] [63] [64] [65]. Following the previously introduced *Bönnemann* method ligands are usually used in order to control the nanoparticle size and shape during particle growth as well as binding the nanoparticle to the support material [39] [66]. One of the most extensively studied reactions in this regard is the oxidation of CO-catalyzed by supported noble metals like platinum (PtNP), palladium (PdNP) or gold nanoparticles (AuNP). As shown in Fig. 3 a) a higher onset temperature for CO conversion has been found in case of wet chemically synthesized catalyst [67]. The lower catalytic activity of ligand-loaded catalysts can be ascribed to a preferential depletion of highly active surface sites on the nanoparticle as well as a less developed NP-support interaction. On the other hand, due to the absence of ligands in the case of nanoparticles generated by PLAL, exposed active sites as well as pronounced strong metal to support interaction between AuNP and CeO_2 surface are attributed to the lower onset temperature and hence higher catalytic activity [68] [69] [61] [67].

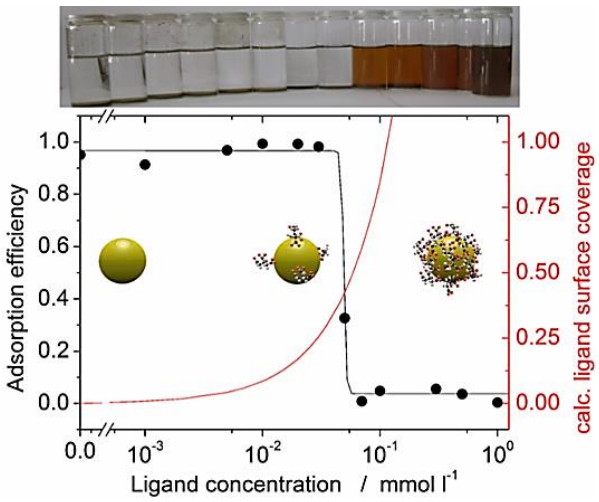

Fig. 2 Ligand (citrate) concentration dependent Adsorption efficiency of AuNP on TiO_2. (Reprinted with permission from [70], Copyright 2012, American Chemical Society).

According to the depletion of nanoparticle adsorption by ligands Wagener et al. investigated the dependency of the nanoparticle adsorption efficiency on the ligand coverage of AgNP during their deposition on $BaSO_4$ as shown in Fig. 2 [43]. On exceeding 50% coverage of the AgNP surface with ligands the authors observed complete inhibition of the deposition process which was assigned to electrostatic or steric repulsion [43]. On the other hand when using ligand-free nanomaterials from PLAL, a quantitative particle adsorption was achieved. The adsorption processes is mainly influenced by energy distribution of different adsorption sites on the support resulting in a Freundlich adsorption isotherm [43] [44]. Hereby the direct contact of support and nanoparticle may also enable symbiotic effects like strong metal to support interactions to occur causing extensively increased catalytic activities [15].

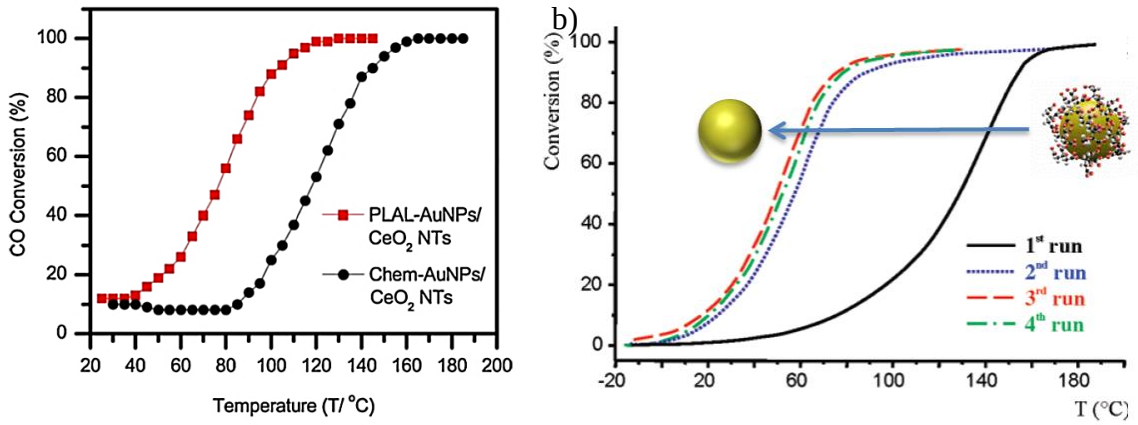

Fig. 3 Effect of ligands shown by: a) comparing the catalytic performance of CeO_2 supported AuNP synthesized by wet chemical technique (in presence of citrate) and ligand-free AuNP from PLAL. (Reprinted from [67] with permission from Elsevier**). b) The increasing catalytic performance of initially glucose-protected supported AuNP on TiO_2 during CO oxidation due to reaction-initiated ligand removal during successive reaction cycles. (**Reprinted with permission from **[68]** Copyright 2006 American Chemical Society.**)**

In case of chemically synthesized AuNPs subsequent calcination steps at increased temperatures or an initial reaction cycle has to usually be applied in order to activate the ligand-contaminated catalyst by ligand decomposition or removal as show in Fig. 3 b) [68]. Yet poisoning due to ligand-degradation products during calcination at increasing temperatures may decrease the overall turnover frequency as reported by Kuhn et al. [69]. Additionally changes in the morphology or the composition (in case of alloy nanoparticles) may occur due to growth or phase segregation processes, respectively, eventually gradually decreasing activity with increasing calcination temperature [71]. Even though alternative purification methods are already established a quantitative ligand removal is often not given. In any case, these additional

a)

purification steps require further ressources and efforts and are (when considering laser-based catalyst preparation) an evitable cost factor during catalyst preparation.

While saving the time and the efforts clear benefits are constituted by laser-generated particles in pure water. Hereby the PLAL technique grants both options of either obtaining pure or modified nanoparticle surfaces after subsequent functionalization. Hence one of the biggest advantages of laser-based catalyst preparation is the accessibility / provision of model materials in various compositions without necessary procedural adaptions or organic additives opening new doors and possibilities to examine, understand and optimize catalytic processes. Following the previous statement, Ballauf et al. conducted a theoretical and experimental work on the kinetics of the common 4-Nitrophenol reduction reaction as shown in Fig. 4 [65] [72].

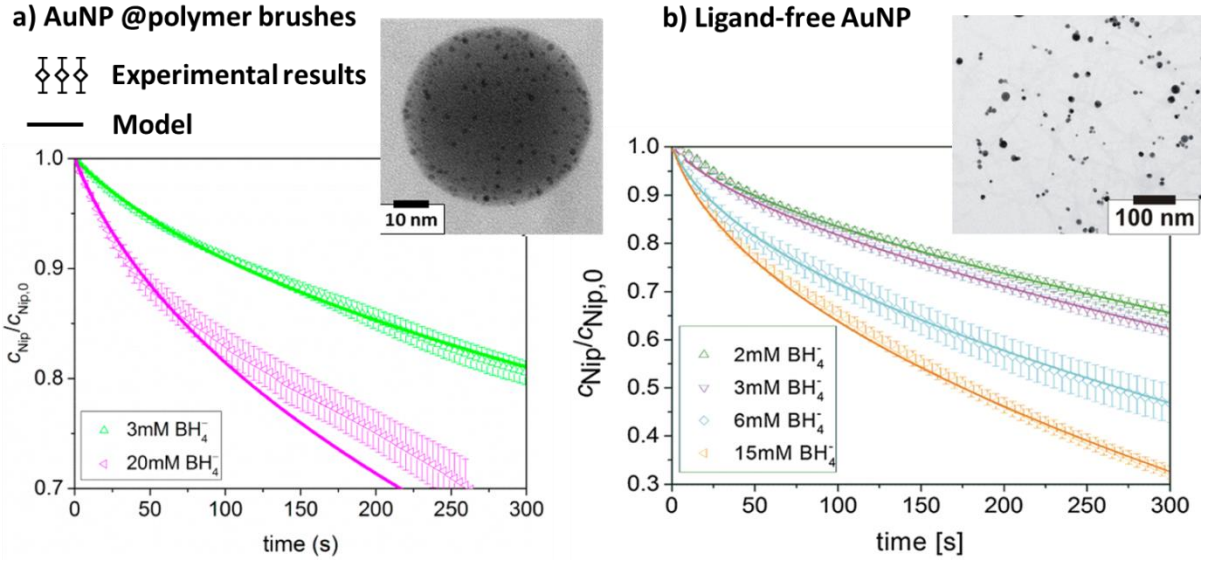

Fig. 4 Exemplary AuNP catalysed nitrophenyl reduction reaction in order to verify a previously developed Langmuir-Hinshelwood based kinetic model using laser-generated AuNP as reference material a) plotted for AuNP fixed inside of polymer brushes. (Adapted with permission from **[72]** Copyright 2014, American Society)**; b) plotted for ligand-free gold nanoparticles. (**Adapted with permission from [65] Springer).

Herein a significant discrepancy between the theoretical kinetic model and experimental data was observed with progressing reaction time in the case that polymer brush supported AuNP had been used during the experiments (Fig. 4 a) [72]. Yet while basic researchers may have traced this effect back to missing or false presumptions during the modeling process indeed a comparison of the given kinetic model (neglecting ligand effects) and the catalytic performance of laser-generated bare AuNP were in outstanding agreement as shown in Fig. 4 b) [65]. Hence ligand-free nanoparticle systems provide an ideal reference system for mechanistic studies in order to develop or verify structure-activity correlations. Additionally, due to the free surfaces

subsequent or *in situ* functionalization of the reference nanomaterials from PLAL can be variably achieved by simple mixing with inorganic supports or organic as well as biomolecular additives [43] [58] [73]. A subsequent targeted functionalization enables parametric studies by maintaining other particles properties e.g. size distribution and morphology. Thus ligand-free nanoparticles may also be used as reference material for other independent investigations of nanoparticle properties in ongoing investigations as will be presented in Section 6 (future prospects).

Before using laser-generated nanoparticles as reference materials, their surface properties need to be investigated. In several independent studies it was verified by X-ray photoelectron spectroscopy (XPS) and zeta potential analysis that laser-generated nanoparticles are partially charged on their surfaces [74]. However measuring zeta potential is not a direct proof of the initial surface charge and gives only an indication on the basis of the electric double layer that the particles are oxidized. Also XPS analysis are performed under vacuum conditions, where drying artefacts and interaction with the sample support can not be excluded and thus can affect the particles' oxidation state. Consequently further in-depth studies (such as *in-situ* X-ray absorption spectroscopy) are needed to verify that laser-generated nanoparticles are charged in their colloidal state. On this basis also the impact of ions and ligands on the nanoparticles' electronic structure should be investigated and compared with wet-chemically synthesized particles.

b. Benefits of ligand-functionalized nanoparticles

While the previous section has mainly been highlighting the advantages of bare nanoparticle surfaces numerous novel approaches aim on intentionally functionalizing the nanoparticle-supported catalysts with organic ligands in order to sterically [75] [62] [63] or electrostatically [76] [77] modify the noble metal surface. Bäumer et al. were investigating the effect of ligands on the catalytic activity of supported PtNP during the CO oxidation reaction after functionalization of ligand free PtNP produced by the ethyleneglycol method [61] [62]. Accordingly, comparing amine and thiole functionalized catalysts using a comprehensive methodology they were able to separately verify a ligand-mediated alternation (mainly decrease) of strong metal to support interactions as well as ligand concentration dependent blocking of specific crystal planes [61] [62]. Pang et al. conducted similar experiments on the (de-)/hydrogenisation and coincident decarbonization of furfural in order to resolve the nature of active sites for each type of reaction. By combining catalytic results of the given reaction and DRIFTS measurements as well as choosing suitable mono- and bifunctionalized thiol ligands the authors could separately probe

the reaction on different crystal planes of previously ligand-free PtNP in order to develop a structure-activity correlation for the given reaction [63]. In consequence, ligand-mediated sterically-limited adsorption configurations of educt molecules occur (e.g. molecule adsorption in upright configuration) preventing side reactions from happening [75] [63]. Additionally to the steric ligand effect Zhou et al. investigated the electrostatic effect of ligands with different functional groups showing a significant improvement of the ORR activity if aryl functionalized platinum nanoparticles with meta oriented- electron depleting functional groups like $–CF_3$, $–OCF_3$ or –Cl were used [77]. Similar electrostatic ligand effects were found in an XPS study conducted by Byindir et al. concluding that thiol-modified surfaces exhibit an electron-depleted surface [76]. As discussed by Wang et al. this effect can however be in superposition with a ligand-induced reduction of metal to support interactions due to the less pronounced contact between nanoparticles and support [61]. Following this concept, the electrostatically mediated ligand functionalization additionally adds a new degree of freedom for controlling adsorption and desorption enthalpies (Sabatier principle) which may in future render intended ligand-functionalization of initially ligand-free nanoparticles to be an alternative strategy compared to developing new alloy compositions for currently existing volcano curves (e.g. for OER or HER).

Yet while the ligand functionalization represents a great chance for the development of novel highly selective catalytic nanomaterials a mandatory prerequisite to avoid impurity induced crossover interactions is constituted by the availability of high purity ligand-free nanoparticles prior to ligand functionalization. The previous statement actually seems easily achievable in wet chemical synthesis of ligand-free nanoparticles, e.g. using the ethylene glycol method given by Bäumer et al. and Kuhn et al [61] [62]. However, regarding the scale of typical nanoparticle concentrations (mg/L) various impurities being present even in *pro analysi* quality chemicals needs to be considered. In fact for a gold colloid with typically $3.7 \cdot 10^{17} \frac{\#AuNP}{L}$ ($@\ 0.1\ \frac{g}{L}, 3\ nm$ spehrical AuNP) dispersed in 99.9% pure ethylene glycol the ratio of impurities and AuNP can roughly be estimated to $2 \cdot 10^4$ potentially ligand-like impurities (like siloxanes) per AuNP. Therefore the purity of all chemicals used would have to be increased by about 3-4 magnitudes (about 99.9999%). Following this request extensive purification and care during wet chemical synthesis of nanomaterials to exclude these impurities from residual components in solvents, precursors, reducing agents or occurring side reactions are required but rarely applied in most research found on this topic. Since nanoparticle

generation by PLAL can be performed in pure water, this method offers great advantages in terms of purity.

Following the previous section high purity nanomaterials generated by PLAL present an excellent reference material for fundamental catalytic research as well as for providing highly active catalyst materials. Additionally, the ligand-free nanoparticle surfaces provide an ideal prerequisite for a systematic study of the influence of ligands in comparison with bare nanoparticles. Apart from that, intented nanoparticle functionalization can be done independently from other additives to modify the particles properties even at sub-monolayer concentrations. Hence, by this technique, precisely designed nanomaterials with increased catalytic activity and selectivity are available for scientific studies as well as potential industrial applications.

1.3 Functional properties

a. Particle size

In order to maximize the density of catalytically active centers and simultaneously reduce the amount of active material, numerous investigations according the minimization of nanoparticle size on heterogeneous catalysts and the activity-size-dependence have been conducted [78] [79] [80] [3] [81] [4] [82] [46] [45] [83] [84]. One of the most surprising results during this endeavor was Masatake Harutas observation in 1987 and Graham Hutchings contemporaneous prediction that AuNP with sizes smaller than 5 nm are highly active catalysts for the oxidation reaction which nowadays took place as common textbook example [78] [79] [71]. Following these insights a manifold of studies on the nature of the catalytic activity of AuNP were conducted especially targeting the size effect [80] [3] [81] [85] [12] [4]. To that end Yang et. al. reviewed several novel preparation methods of atom-doped surfaces and their catalytic activity compared to atom-clusters and nanoparticles showing higher activities and selectivities for single atomic reaction sites [85]. Yet they also conclude that despite the superior activities of the atom-functionalized catalysts during the therein presented variety of reactions (oxidation, hydroformylation, water gas shift) scaling the nanoparticle size down to atomic scales should not be considered as a general rule for high catalyst activity [85]. Accordingly, it is well known that minimizing the particle size causes several simultaneously occurring morphology and property changes of the final catalyst affecting its activity and stability during reaction condition. The most important are given in the following list:

- modification of morphology like predominant crystal surfaces and amount of crystal defects like kinks, edges, steps or twin boundaries [86] [87] [12] [4] [88]
- change of electronic band structure due to depletion of density of states with decreasing particle size [89] [90]
- influence on wetting behavior of the nanoparticle material on the support due to the size-dependent development of strong metal to support interactions and charge transfer effects [88] [91] [92]
- change of physical nanoparticle properties e.g. sintering tendency as well as atomic mobility (ripening tendency) [93] [94]

Peter et al. were able to prove that oxygen has especially high adsorption enthalpies and hence high catalytic activity when being adsorbed on low coordinated surfaces of higher order as well as edges and kinks [87]. The authors performed calorimetric studies on the adsorption enthalpy of oxygen on pristine Pd {111} as well as grown PdNP with various exposed crystal sites [87]. On assuming that the amount of edges and kinks increases with decreasing particle size it may be presumed that the adsorption enthalpy accordingly increases with decreasing the particle size reaching a maximal value for single atom clusters. Yet Peter et al. observed an optimal PdNP size of 4 nm while smaller and bigger particles yielded less activated oxygen species [87]. The authors referred this effect to a decrease in Pd-Pd bonding length which in turn was predicted to result in lower adsorption enthalpies elsewhere [95] as well as an attenuation of van-der-Waals forces on decreasing cluster size [87]. Following cluster sized nanoparticles are (apart from stability issues) not always the favored catalytic system [87]. Similar results were found by Meier et al. when they showed that the particle size is one of the most dominant parameter for the stability, while the specific activity is less influenced by Pt particles in a range of 1-5 nm [10]. Herein the authors verify that heat treatment increases the particle size from 1-2 nm to 3-4 nm in turn significantly enhancing the catalyst cycle stability and overall activity due to a minimization of particle dissolution and detachment from the carbon carrier under reaction conditions. A collection of these different aging mechanisms, particular relevant to design catalysts for fuel cells, is summarized in Fig. 5 A. Following Fig. 5 A the main mechanisms are either based on changes of the carrier surface structure (e.g. carbon corrosion and particle detachment) or changes of the nanoparticles itself (e.g. agglomeration, Ostwald ripening or simple nanoparticle dissolution) [10]. In this case particle dissolution was shown to be predominant in case of particles smaller than 2 nm an subsequently be attributed to the particle curvature and thus the high surface energy, which leads to thermodynamic instable particles (Gibbs–Thomson effect) [10]. The authors further correlate the catalyst stability to the average inter-particle distance (AID). The formula the authors used to calculate the AID as well as a graphical correlation of AID with nanoparticle content and size is shown in Fig. 5 B. According

to this concept as well as Fig. 5 B it was found that Ostwald ripening and coalescence effects were most pronounced for small AID (<25 nm) which usually appears for low specific support surface areas, high nanoparticle loading and cluster sized nanoparticles (< 2 nm). Hence low AID's need to be avoided which especially has to be kept in mind when supporting ligand-free nanoparticles as will be addressed in more detail during section 6 (future prospects). Following the concept of AID, Meier et al. proposed a design rule for electro catalysts used under ambient temperature conditions where highest stability can be achieved if AID values are kept greater than 25 nm [10]. However as comprehensively reviewed by Cuenya this concept is highly biased by the support being used and the resulting nanoparticle support interactions [88]. Additionally, among others Vece et al. and Misty et al. prove that the expressed nanoparticle morphology and stability is further dependent on the chemical atmosphere [94] [4] [88]. Both groups conclude that Pd (Vece et.al.) and Pt (Misty et.al.) undergo restructuring (from 2D to 3D) under H_2 atmosphere due to an increase in atom-atom-bond distance and subsequent strain initiated partial detachment of the nanoparticle from the support [94] [4]. Hence an increased Ostwald-ripening tendency of noble metal nanoparticles has to be expected when working under H_2 [94] [13 Cuenya] as well as CO atmosphere [8].

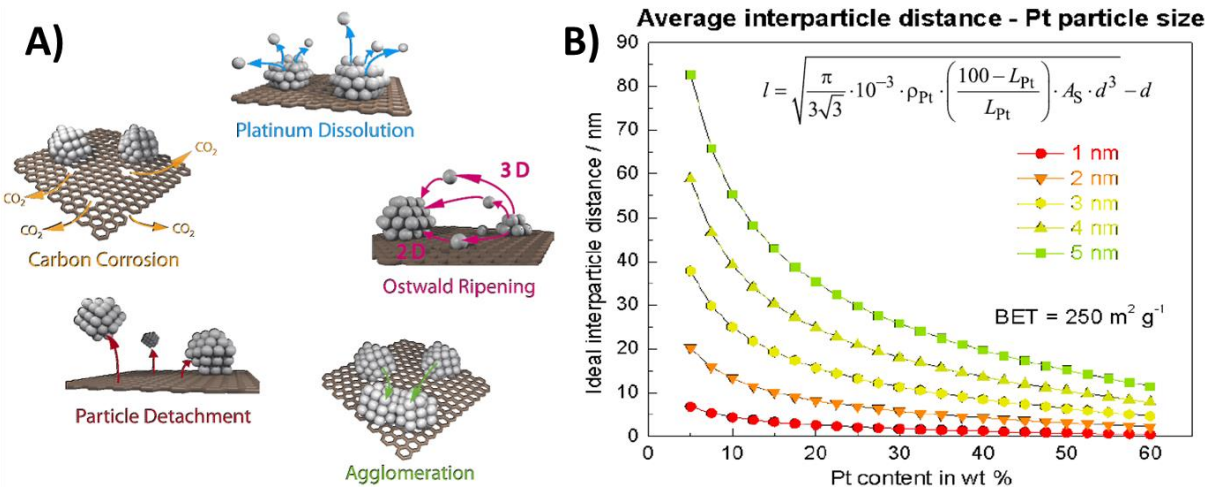

Fig. 5 A) different degradation mechanisms summarized by Schüth et al. as well as B) dependence of the average interparticle distance with nanoparticle size and nanoparticle content. (Reprinted from [10], Beilstein.)

Most size-dependent property changes are in some way related to interactions between nanoparticles and the support. Hence, the development of design rules usually referred to as structure-activity-correlations is mandatory. Yet in order to develop such correlations the independent adjustment of nanoparticle size as well as support properties like crystal structure,

specific surface (and porosity), defect density (e.g. oxygen vacancies on TiO_2, CeO_2, ZnO etc.) are required. Furthermore, ligand-related impurities and residual decomposition products should be avoided. An innovative approach to attend these requirements may be given by using ligand-free nanoparticles generated by pulsed laser ablation in liquids and the subsequent deposition onto supports exhibiting defined preset material properties. Due to the dispensability of subsequent reductive (e.g. H_2) atmospheres or high temperature calcinations steps the aforementioned support and nanoparticle properties are retained during this preparation method. Hence this technique offers the ability of an independent investigation of underlying catalytic mechanisms without biasing crossover effects introduced by calcination or activation steps [15] [96]. Yet a size selective nanoparticle generation is mandatory, since PLAL rarely provide monodisperse, though often monomodal, nanoparticles if no additional additives (i.e., anions, ligands) or steps (re-irradiation) are included.

Following the previous thoughts Rehbock et al. reviewed different techniques for gold nanoparticles in order to control the nanoparticle size during pulsed laser ablation in liquid in a size regime ranging from 2 nm to 100 nm [57] [58]. The following (depicted in Fig. 6) are the most important ones [58]:

- Pulsed laser fragmentation in liquid (PLFL) – by varying laser fluence (100-500 mJ/cm^2) [57] [98] [99] [100]
- *In situ* size quenching by salts – by varying electrolyte concentration (0-100 µm) [53] [45]
- Delayed conjugation in liquid flow – by varying time delay (0-120 s) [101] [53]
- Pulsed laser melting in liquid (PLML) – by varying laser fluence (0-60 mJ/cm^2) 30-130 nm [102] [103] [104]
- *In situ* size quenching by supports [105] [97]

The authors concluded that adjusting the laser parameters alone employs only some degree of size variation but is not solely the solution for nanoparticle size control [58]. Accordingly, an efficient method was developed exploiting the size quenching effect due to anion adsorption on the nanoparticle surface present during laser ablation in diluted electrolyte solutions. These adsorbed anionic species were proven to increase the nanoparticle surface charge density and therby repulsion forces between nanoparticles and clusters retarding subsequent growth processes during nanoparticle genesis [58] [46]. Building on this conclusion Rehbock et al. established a correlation between particle size and the present ion concentration as well as the individual charge density of different anion species [46]. The authors showed that the size quenching effect was following a Hofmeister series and being especially pronounced with chaotropic anions like Br^- or SCN^- but still pronounced with catalytically less problematic ions

like NO_3^-, CO_3^- or PO_3^- [45] [46]. Additionally Marzun et al. concluded that a proper pH-adjustment being guided by the acidity or basicity of the generated nanoparticles presents another efficient strategy for adjusting the resulting nanoparticle size even without adding the aforementioned ionic species [45]. Even though different approaches for size control of laser-generated platinum group elements and gold nanoparticles have been followed, size quenching of other materials such as oxides without using any steric or reducing ligands is less addressed so far.

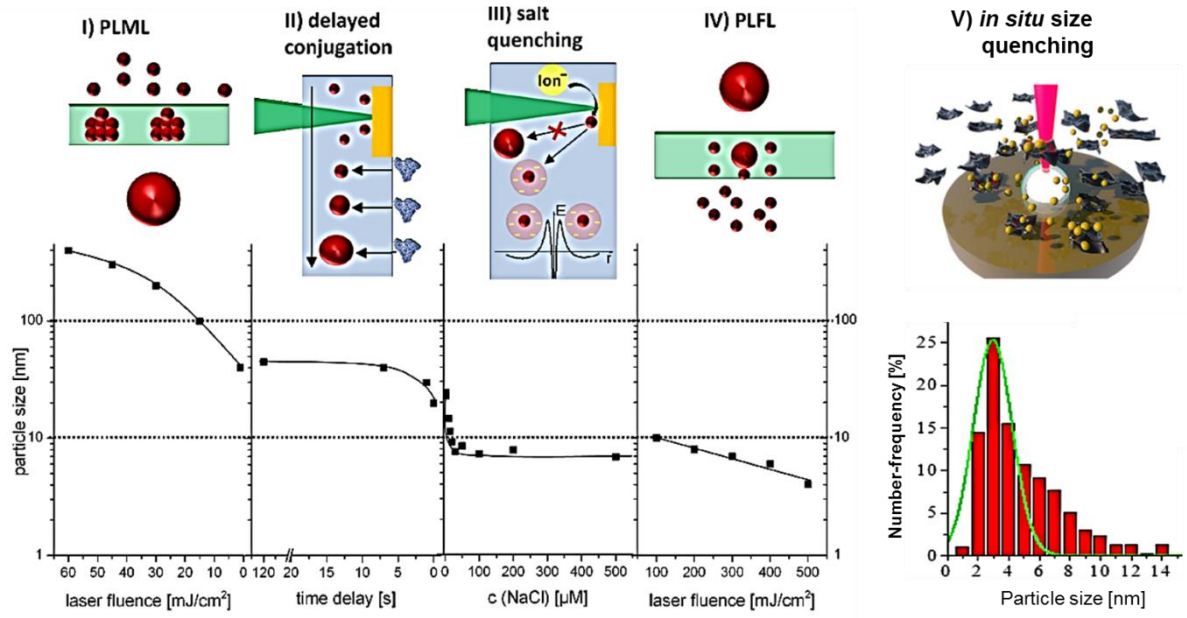

Fig. 6 Size quenching mechanisms for laserbased nanoparticle synthesis following Rehbock et al. (I-IV) and Mendi et al. (I-IV **r**eprinted from **[58]** Beilstein and V from [97] Nature Publishing group.)

In contrast to anion mediated control of growth processes a similar result can be achieved on adding a support material prior to the ablation process as was shown by Mafune et al [105]. Hereby the nanoparticle growth is being quenched by an *in situ* deposition of generated nanoclusters from the plasma plume on the SiO_2 support material inhibiting the coalescence mediated growth process [97] [105]. This *in situ* particle deposition method was firstly introduced by Hashimoto et al. [106] They synthesized AuNP-loaded zeolite crystals ablating Au flakes in a synthesis gel containing $Al_2O_3/SiO_2/K_2O/H_2O$ and could successfully visualized the embedded AuNP with dark field microscopy. Hence this technique provides a one-step synthesis route for heterogeneous catalysts even without subsequent activation steps required due to the ligand-free nature of this method. Besides using oxides also PLAL of metals in a dispersion of carbon-based supports were carried out [107] [97]. Yet as shown by Torres-Mendieta et al. when following this approach an alteration of the carrier properties due to laser-support-interaction can't

generally be excluded [97]. Hereby the authors observed a partial reduction of the graphene oxide which however could not yet undoubtedly be attributed to a laser-graphene oxide interaction or a reducing effect of adsorbed AuNP [97]. Hence further investigations are required to fully clarify the mechanisms if support materials are present during the ablation process. As well as the investigation of support-laser-interactions needtobe considered.

A well-established method for controlled nanoparticle size adjustment with very narrow size distribution in scalable quantities is given by the laser fragmentation in liquid technique (PLFL) [108] [109] [110] [111] [112] [113]. In accordance to PLAL, these fragmentation processes can be realized by re-irradiation of nanoparticle colloids using short laser pulses (femto second to nanosecond pulses) with sufficient laser pulse energy and wavelength [112]. Depending on the applied laser pulse duration, wavelength and hence the absorption cross section of the irradiated nanoparticles, a size-selective fragmentation of nanoparticles is achieved by choosing a appropriate laser pulse energy [114] [110] [112]. Hence nanoparticle sizes down to 2 nm can be generated und ligand-free conditions and subsequently deposited on support materials making them useful in catalytic applications [111].

b. Oxidation state

During laser ablation in liquid surface oxidation processes as well as ion adsorption play an important role in order to electrostatically stabilize the ligand-free nanoparticles [58]. In order to design materials with desired properties exploiting and controlling these oxidation processes can offer a versatile tool for specific material design. In fact a correlation of the amount of oxidized surface atoms with the electrochemical potential of the nanoparticle material and the liquid used can be observed when comparing different publications. In case of AuNP, PtNP and PdNP, XPS studies on laser-generated ligand-free nanoparticles from these materials show that only lesser amounts of oxidation are observed in case of laser-generated AuNP (about 3.3-12% of oxidized surface atoms [58] [115] [46] [116] while PtNP exhibits 20%-73% [96] [117] and PdNP 71% [45] of surface oxidation [1]. This correlation is in good agreement with the theoretical oxidation tendency of these species in water following the series Au ($\approx 1{,}7\ V$) > Pt ($\approx 1{,}2\ V$) > Pd ($\approx 0{,}85\ V$). Furthermore, the laser ablation of base metals like nickel, copper, manganese etc. in water leads to the partial or complete oxidation of the atomic species during laser ablation [47] [118] [119] [120][121][122][123] .While exact mechanisms about the origin of particle oxidation and growth during the nanoparticle nucleation are still under debate a further more detailed understanding of these PLAL processes offers great potential for a defined material design.

However until now there is still not enough data available to develop a generalized model. Hence more investigations focusing on the interaction of nanomaterial and solvent during PLAL especially considering the generation of base metal nanomaterials with defined oxidation state and particle size are required. This also includes the influence of the different oxygen species, which are present during nanoparticle laser synthesis. Due to extreme conditions [124] during PLAL the liquid media might decompose[125], [126] and reactive species of the solvent may affect the particle formation. On the other hand, dissolved molecular oxygen can also cause particle oxidation. Thus the impact of the different oxygen species must be investigated.

c. Crystalline morphology

Nanomaterials generated during laser-based fabrication under ligand-free conditions usually exhibit a spheroidal shape with crystalline morphology [127] [128] [70] [56] [15] [129] [47]. Streubel et al. compared the crystalline morphology of different nanomaterials generated by applying high power picosecond laser pulses under continuous flow conditions [47]. As shown in Fig. 7 a) in addition to the densely packed usually rather inactive {111} crystal faces (in case of fcc structure) catalytically important disclosed {200}, {220} and {311} faces could be found in case of PtNP [47]. Same results were obtained when nanoparticles are produced continuously for 60 minutes, which show a high process stability of PLAL. Similar conclusions were also drawn in case of other noble metals like AuNP, AgNP or PdNP [84] [15] [130] as well as AuPt alloys prepared by Ma et al. [54]. On the other hand if the laser ablation of less noble materials like nickel or copper is conducted in water, oxidation processes occur as shown in Fig. 7 b [47]. Hereby in case of nickel additional crystal faces due to the formation of surface oxides can be found as well as a distinct $NiO/Ni(OH)_2$ shell. Such base metal nanoparticles exhibiting an oxide shell represent interesting structures for the preparation of numerous heterogeneous catalysts like e.g. electro- [131] [132], methanisation- [133], partial oxidation- [134] or water gas shift reaction- [135] catalysts.

While the topic of controlling growth of a specific crystal face is already exhausted in wet chemical approaches and is mainly limited by subsequent calcination and ligand removal steps [136] [137] [138] many opportunities are still to be grasped using the PLAL approach. One of the most important factors in this sense may be the defined modulation of the nanoparticle cooling rate. This is directly linked to the lifecycle and lifespan as well as the pressure development of the cavitation bubble [70] [139] [140] [141]. Hereby the cavitation bubble engineering is a promising approach, although it has not been shown yet if this allows to further increase the amount of high order crystal faces and gain further nanoparticle morphology control. Because of nobel

price winner Gerhard Ertl the huge importance of the exposed crystal faces and structural changes during reactions on the catalytic activity is well known [9] [142] [143]. Hence, the occurrence of these high-order crystal faces ({200}, {220} and {311}) on laser generated ligand-free nanoparticles may provide a promising system for the synthesis of active catalysts.

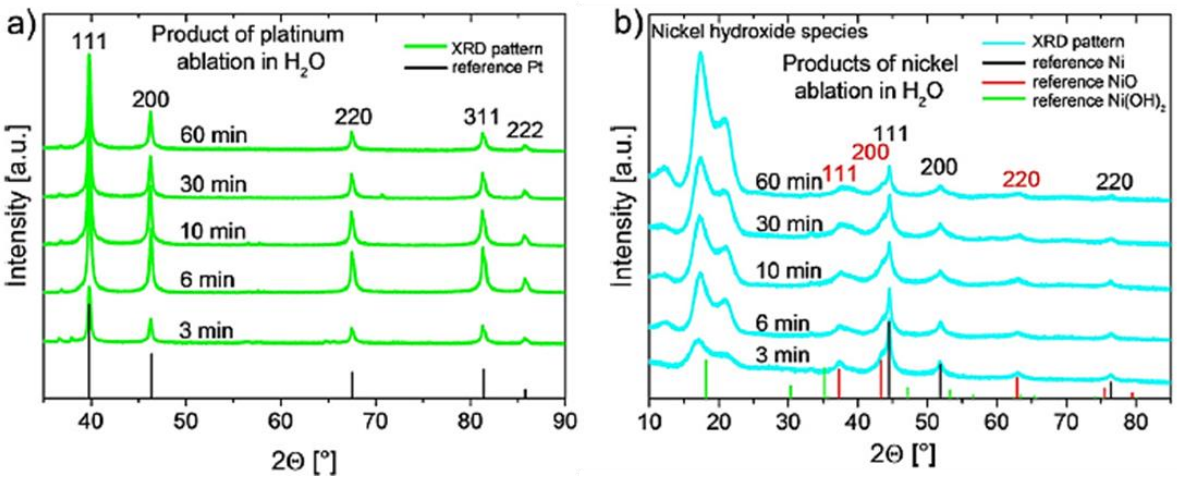

Fig. 7 XRD diffractograms of a) PtNP and b) NiNP after PLAL in water during continuous production taken at different time steps. (Reprinted with permission from [47] IOP science.)

A further generalization based on structure-activity correlations as well as the reaction conditions is still pending. In this sense the application of heterogeneous catalysts made from ligand-free nanoparticles may present an alternative, if not ideal starting point enabling the synthesis of model catalysts with defined nanoparticle size, loadings and readjusted morphologies. Yet in order to prepare these model catalysts a specific material design is a mandatory prerequisite and will therefore be the topic of the next chapter.

1.4 Material design: multi-elemental nanoparticles

While oxidation state and particle size are determining factors in optimizing an already given catalyst, the generation of novel alloy or binary catalysts with predesigned composition and morphology yielding superior properties is a probably even more important material design aspect in modern catalyst research and development. In this context the generation of bi- or multi metallic alloy structures is one of the most important hot topic especially regarding the replacement of expensive and scarce materials like Pt-group metals (Pt, Ir, Pd, Rh, Ru) and its application in sustainable energy generation and storage technologies [144] [145].

Platinum is usually used as a reference standard when comparing catalysts amongst each other since it is the best metal in terms of activity, selectivity and stability in several catalytic reactions. However, besides the fact that platinum is expensive and limited in supply, it is also not located on the presumed peak-top of the volcano plot. Thus in order to optimize the catalyst, studies on fine-tuning the electronic properties of Pt are mainly based on the following strategies [146]:

- Alloying [147] [148] [149]
- layering Pt on surfaces of another cheaper and less active metal [150] [151]
- core-shell particles with Pt shell and cheap metal core [152] [153] [154]
- alloying followed by dealloying- lattice strain of Pt caused by alloying retains while the less noble metal is removed [13] [155] [156] [157]
- numerous other approaches: doped graphene [158], transition metal carbides and nitrides [147] [159]

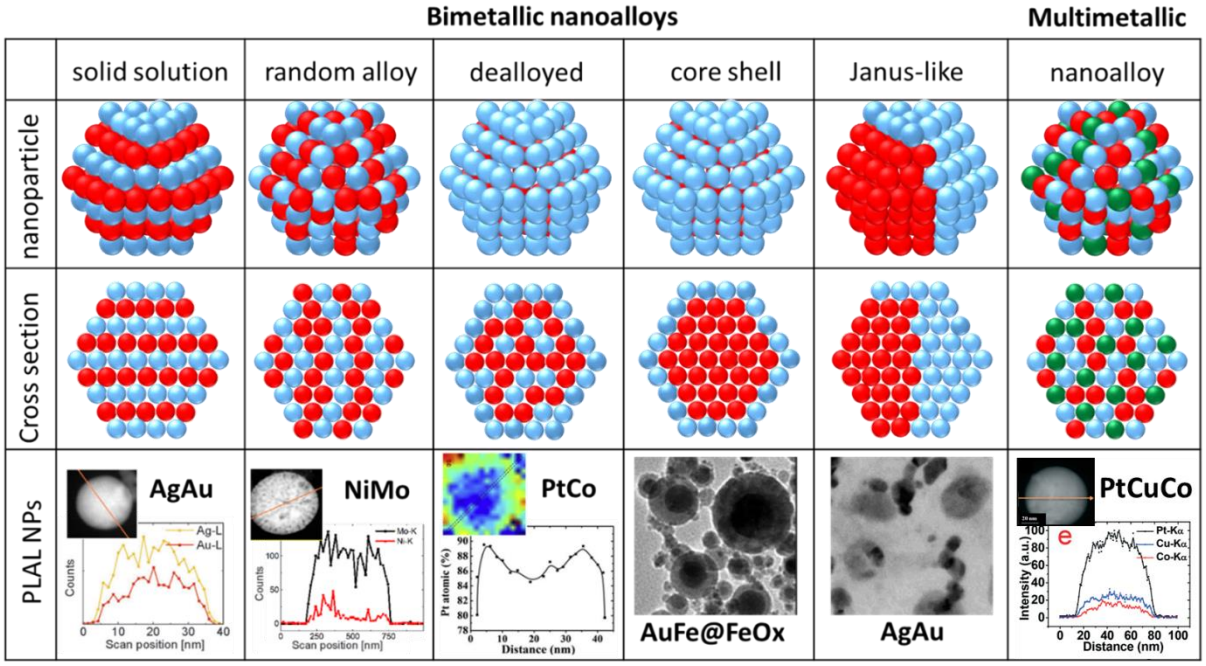

Fig. 8: Scheme of some possible mixing patterns and TEM images with EDX line scans, respectively. (Adapted from [55] Royal Society of Chemistry; Adapted with permission from [51], [167] and [168] Elsevier; Reprinted with permission from [169], Materials Science & Processing; Adapted with permission from [170], Royal Society of Chemistry.)

The term ‘alloy’ is wide ranging. Fig. 8 shows the main types of nanoalloys including examples of laser-generated nanoprticles. So far, catalysis-experts verified the functionality of different kind of structures in wet-chemically synthesized nanomaterials. A common approach is the synthesis of bimetallic alloys of platinum with less noble and less expensive metals such as nickel, cobalt or iron [160] [161] including further innumerable metal combinations depending on

the catalytic reaction. A recent intensively studied concept to increase the catalytic activity is dealloying. Hereby, the less noble metal is dissolved from the surface in a selective corrosion process and leaves a nanoporous structure that is composed of the more noble and active metal (PtCu [13], PtNi [162] [163], CuAu & AgAu [157] [155]). Moreover, outstanding activities were also found for ternary alloys e.g. PtIrCo, PtAuCo [164], PtCuCo [153] [165] PtNiCu [50], $PtNi_3M$ (M-Cu, Co, Cr) [166], to name a few.

The above mentioned alloying approaches affect an improved catalytic activity due to change of the electronic structure of their surfaces and thus the optimization of binding energy affinities between Pt and adsorbates such as oxygen or oxygenated species considering the rate-determining oxygen reduction reaction (ORR, Fig. 9 b). According to the Sabatier principle, the optimal catalyst surface must keep a balance between binding the reagents strong enough to become activated and still weak enough to desorb the product. The so-called Balandin's volcano plot can be helpful in the design of optimized catalysts, since it plots the catalytic activity against adsorption energy (Fig. 9 a). For instance in case of ORR, the exchange current density J is plotted against adsorption energy of O (or OH, since it is a two step reaction). Hammer and Norskov elaborated, that the oxygen adsorption energy on metallic surfaces correlates with the d-band center with respect to the Fermi level of the surfaces [171] [172]. A down-shift of d-band center (Edbc) with respect to that of pure Pt would lead to weaker O adsorption and thus to enhanced activity. By performing DFT-calculations Duan and Wang found that modifying Pt/M(111) surfaces with transition metals (M=Ni, Co or Fe) could down-shift the d-band center of outermost Pt- monolayer and thus weaken the binding of chemical species to Pt/M surfaces compared to a Pt surface [172] (Fig. 9 c,d). The position of the metals in the periodic table enables an orientation: elements on the left-hand side weaken the Pt-O binding and thus facilitate a down-shift of the d-band center, while metals to the right of the group 10 lowers the activation energy for binding oxygen [172]

Because of size-related properties, stable alloy phases may be formed even if bimetallic materials are immiscible in bulk. In this context noteworthy nanometer scaled alloys which were successfully synthesized are AgPt [173]] AuPt [174], AuFe [175] PtRu [176] [149] When the particle size decreases an increasing ratio of the surface energy to the total free energy facilitates the formation of alloy phases between two metals [177]. Using molecule dynamics simulations, it has been calculated that alloy phases are thermodynamically preferred with decreasing number of atoms [178] [179] [180]. Thus a critical value r_c has to be overcome to form challenging alloy nanomaterials.

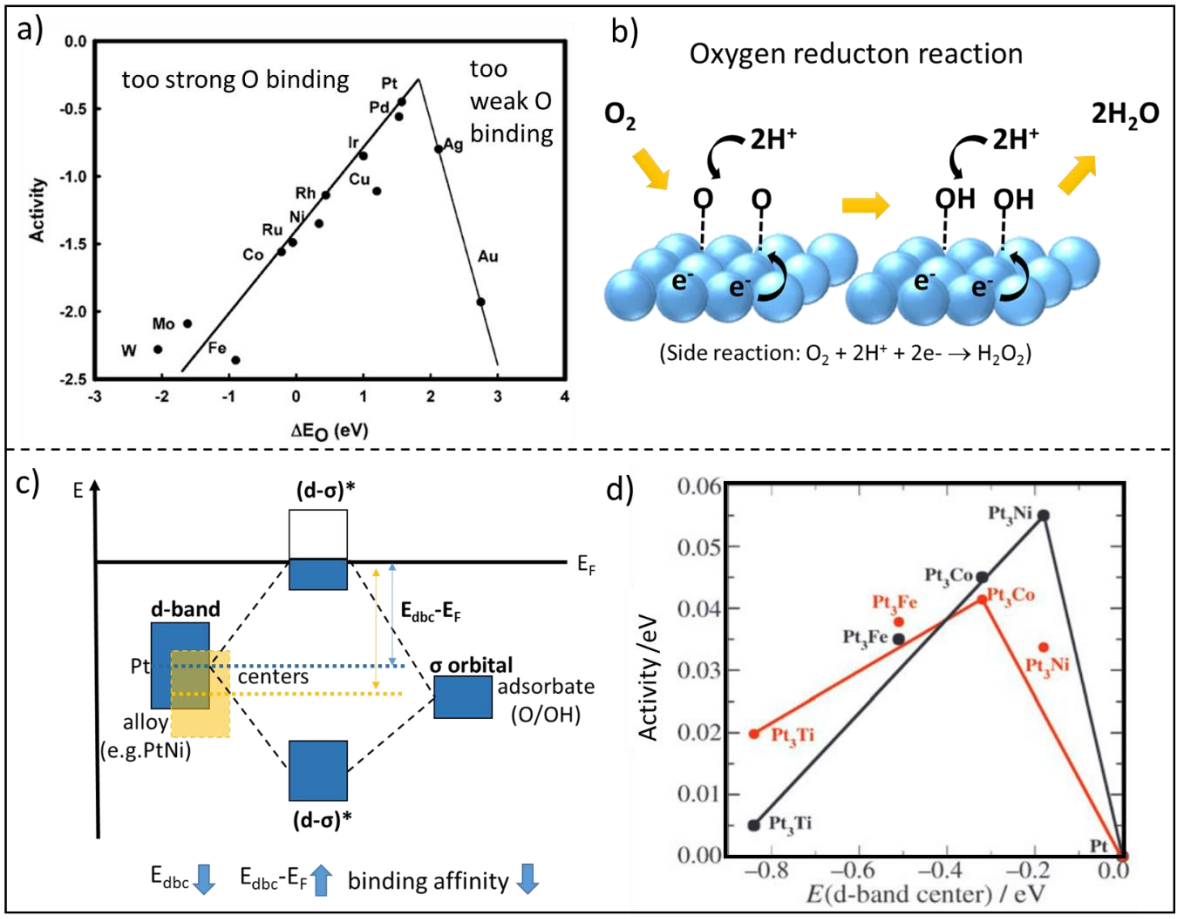

Fig. 9: a) Volcano plot reflects trend on different meal surfaces as a function of calculated oxygen adsorption energy. (Adapted with permission from [181] Copyright 2004, American Chemical Society.) **b) Sketch of the mechanism of oxygen reduction reaction (ORR) on metal surfaces. c) Diagram of the electronic structure showing the role of the d-band center when alloying with transition metals.** (Adapted with permission from [170], Royal Society of Chemistry.) **d) Correlation of the ORR activity against d-band center relative to platinum (black: from DFT simulations, red: measured). (**Adapted with permission from [160] John Wiley & Sons.)

Modification of the electronic structure of Pt by mixing transition metals becomes a favored approach in the field of PEMFCs to increase the catalytic activity. The transferability of PLAL to a variety of metals and liquids enables a high-throughput screening of molar fraction series catalysts [182]. In 2012 Ma and co workers introduced a novel material design strategy by employing pressed mixtures of gold and platinum metal powders during PLAL in order to prepare PtAu alloys over the whole composition range [54]. The authors where able to show the successful nanoparticle alloy series generation from the pressed powder mixture over the whole composition range regardless of the Pt/Au miscibility gap [54]. A summarizing scheme of this principle is summarized in Fig. 10.

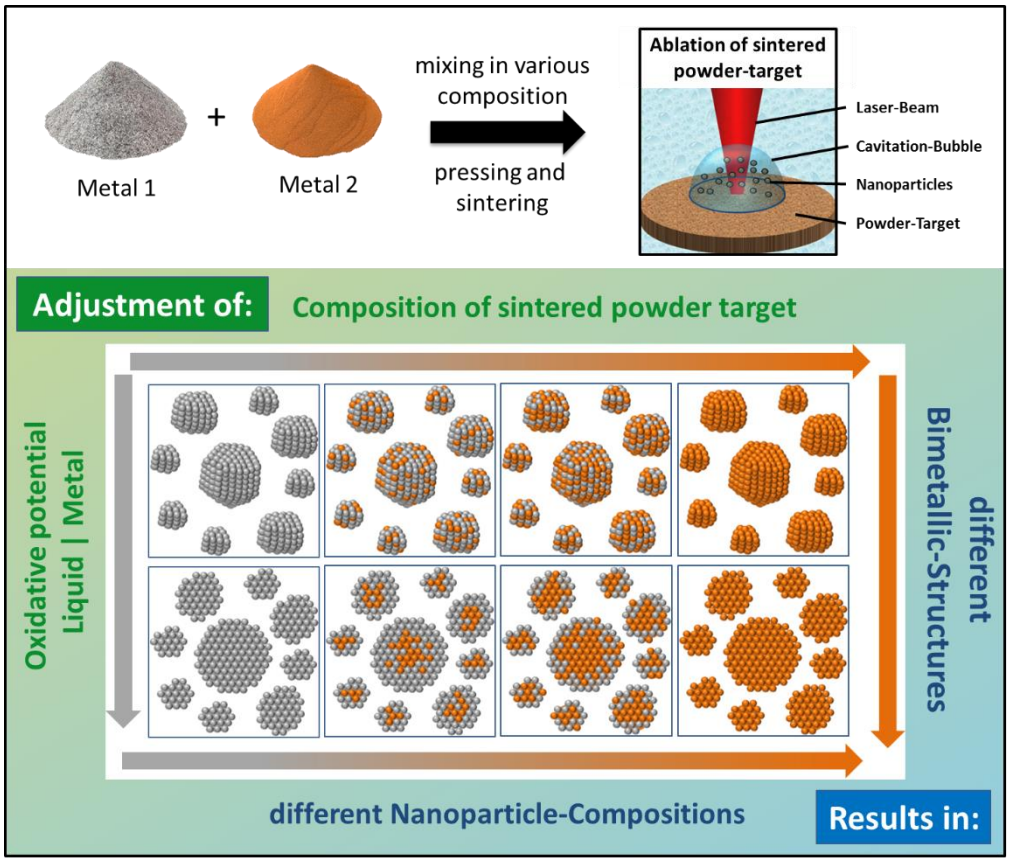

Fig. 10 Scheme on the basic principle for the generation of bimetallic nanoparticles with different structures and compositions by using Pulsed Laser Ablation in Liquid

Particle synthesis by PLAL offers many other possibilities for the synthesis of multi-elemental nanoparticles. Among using alloy or pressed targets of at least two elements in an additive-free solvent, laser ablation synthesis of a target in a metal salt solution can be performed. While the particles are formed in the cavitation bubble a chemical reduction reaction is initiated with metal ions during laser ablation and results in the formation of alloy nanoparticles [183]. The so-called laser ablation synthesis in solution-galvanic replacement reaction (LASis-GRR) technique opens new opportunities to develop a large variety of novel materials with controllable properties, including core-shell alloys. For instance, Hu et al. could successfully laser-synthesize PtCo nanoparticles as remarkable ORR catalysts with controllable size, atomic compositions and alloying degree [167] [184]. As recently in particular in the field of catalysis the interest on ternary nanoalloys increases, initial approaches based on laser irradiation of mixed solutions of metallic ions are taken. Sarker et al. could fabricate RhPdPt alloy nanoparticles with controlled compositions [185] [50]. Following the previously introduced LASisGRR-method, Mottaghi et al. was able to produce AgPt core shell nanoparticles in the presence of colloidal silver nanoparticles and palladium salt solution [186]. Without using any salt precursor, Wagener

et al. conducted laser ablation experiments on iron-gold alloys in water or acetone observing nanoparticles either having a gold enriched core and FeOx shell (in water) or an unoxidized iron rich core and gold shell (in acetone). The authors found that this effect was independent of the laser pulse duration which was varied in the range of femtoseconds up to nanoseconds [52].

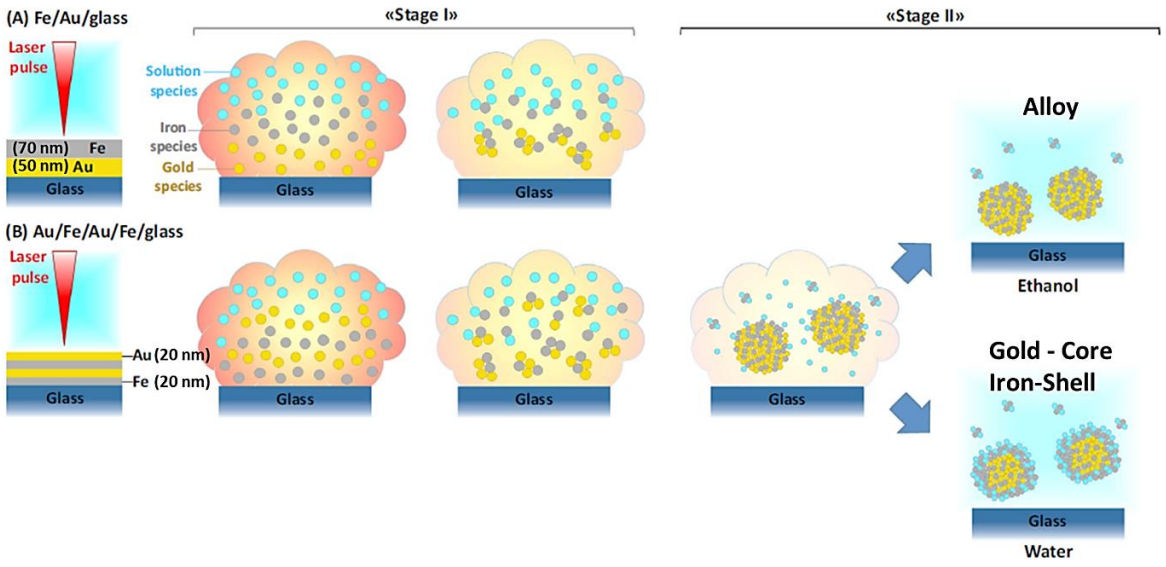

Fig. 11 Two stage growth mechanism occurring on laser ablation of an iron-gold target in water or solvents as proposed by Amendola et al. (Reprinted with permission from [168] Elsevier.)

This hypothesis was confirmed and further established into a mechanistic proposal by Amendola et al. when utilizing a well-conceived experimental setup based on the ablation of layered Au and Fe layers while varying the layer thickness and arrangement order [168]. A sketch of the mechanism proposed by Amendola et al. is shown in Fig. 11. Following, the growth process of the Au/Fe nanoparticles occurs in two steps. As depicted in Fig. 11 A a sacrificial effect of iron occurs during the first stage of the growth process depleting the present active solvent species eventually forming iron oxides in case of water being the solvent. The extent of this depletion effect is dependent on the amount of iron species present in the cavitation bubble [168]. Hence, core-shell structures exhibiting a gold rich core and iron oxide shell are yielded when iron species were present in the cavitation bubble during the first stage of nanoparticle growth. This situation was given when the ablation was performed in water (Fig. 11 B) using either a Fe (70 nm)-Au (50 nm) layered target (Fig. 11 A) or an Au-Fe-Au-Fe layered target obtaining 20 nm thick layers (Fig. 11 B) as well as an Au/Fe alloy target (as it was used by Wagener et al.) [168] [52]. On the other hand, in case of an ablation in ethanol [168] (or acetone [52]) pure Au/Fe alloy nanoparticles can be found (as can be seen in Fig. 11 B). Additionally on using an Au (70 nm)-Fe (50 nm) layered targets AuFe alloys are also being formed in water with an

under-stoichiometric iron content in the core [168]. Therefore, the alloy design is not just tunable by adapting the type of target material and solvent but also by tuning how the individual elemental species are ordered within the target material. When working on the generation of Au-MnOx core-shell nanoparticles Simao et al. just recently provided additional evidence that the core-shell formation is also augmented by re-irradiation of nanoparticle mixtures exhibiting a miscibility gap [119]. For further laser-based strategies for the synthesis of alloy nanoparticles for catalytic application it is refered to the review of Ma et al [84].

Although many studies were performed on laser synthesis technique for nanoalloys, a simultaneous control of the metal composition and size is still challenging and needs further investigations. As the study of laser-generated nanoalloys in the field of catalysis is less explored compared to chemically ones, the effect of nanoalloys should be investigated more systematically on activity, selectivity and stability.

Following the approach of pressed micro particulate metal mixtures it was shown, that the synthesis of alloy particles consisting of noble metals is possible. However, in regards of the use of less expensive materials in catalysis and in order to develop equally active platinum-free electro catalysts, adequate studies on laser-synthesis of non-noble alloy particles are missing. Due to their sensitivity to oxidation in the most preferred and economically meaningful solvent water, it need to be clarified whether the formation of non-noble alloy nanoparticles is feasible and to what extent (solid solution or core-shell) bimetallic nanoparticles can be formed. The literature shows, that the electrochemical potential of the metals as well as the solvent and the metals affinity to carbon (formation of carbides, graphitic shell [187], [188], [189]) plays a major role. While PLAL of an iron-gold containing target in water reveal in the formation of core-shell nanoparticles with Au in the core and Fe_3O_4 on the surface, ablation in acetone lead to a gold shell covering a non-oxidized iron core [52]. In this experiment, the affinity of the metal to the solvent controls the present metals species on the particles surface where noble and non-noble metals were present. However the metal composition of the particles need to be investigated when using only non-noble metals to produce bimetallic nanoparticles, especially if the materials are immiciable according their phase diagram. Obviously a fundamental chemical interaction between nanoparticle surface and the solvent significantly contribute to elemental distribution in the nanoparticles. Thus the impact of different solvents on the particles' properties on non-noble metals need to be clarified. Furthermore a functionality proof of the laser-synthesized alloy particles should be performed in a meaningful selected catalytic reaction.

1.5 Nanointegration

The integration of nanoparticles onto support materials is a key strategy in order to enhance the catalyst applicability as well as to evolve novel material properties from synergetic effects between support and nanoparticle [28] [190] [88] [191] [28]. The typical support materials used in heterogeneous catalysis are generally carbon-based (carbon black, graphene or carbon nanotubes) or oxide-based (MgO, ZnO Al_2O_3, Fe_3O_4, SiO_2, TiO_2, CeO_2 etc.) and mainly used in electro-catalysis [13], photo-catalysis [191], Fischer Tropsch reactions [190] as well as selective oxidation or reduction processes [15] [88]. As it was already deduced in the previous sections especially material gaps arise from calcination and ligand removal due to a simultaneously (but not necessarily equally) occurring alteration of the support- and nanoparticle morphology increasing the difficulty of separately screening specific catalyst properties and their influence on catalyst activity [69] [71] [33] [39]. An attractive strategy to independently adjust defined catalyst properties like particle size, nanoparticle loading, crystallinity or defect density without cross-correlations from e.g. calcination is the successive deposition of laser-generated and ligand-free nanoparticles onto support materials. Hereby the main prerequisite is a quantitative and homogenous nanoparticle deposition onto the support [61] [43] [67] [44] [62]. Hence, in the following section we briefly introduce two basic principles which comply with the previously given prerequisites namely the particle deposition onto macroscopic surfaces and the electrostatic deposition method on particulate supports, as well as diffusion driven particle deposition (Fig. 12).

As the methodology of electrophoresis and dielectrophoresis is already established and well understood for a couple of decades, the electrophoretic nanoparticle deposition (EPD) of charged laser-generated nanoparticles was initially addressed by many researchers working in the area of pulsed laser-ablation in liquids [192] [193] [194] [195] [73] [132] [131]. Accordingly, this technique is based on applying a homogenous electrical field to charged nanoparticles that introduces a directed nanoparticle motion towards the counter electrode resulting in a subsequent deposition [192] [193]. Hereby the same principle is also applicable under constant colloid flow [195]. The electrostatic charge of the nanoparticles results from surface oxidation as well as adsorbed ions or ionic ligands [115] [196] [116] [46]. Typical applications of EPD can be found in research topics on solar cells [193], batteries [132] and supercapacitors [197] as well as catalyst development [192] [131] and performance improvement of certain measurement techniques [194]. Yet while most of these studies are based on ligand-functionalized nanoparticles Streich et al. compared the deposition rate of ligand-free and ligand-coated laser-

generated gold nanoparticles. In contrast to ligand-coated particles, they found an unsuppressed linear deposition kinetic on using ligand-free nanoparticles yielding significantly higher loadings which were investigated up to 70 wt% of deposited gold nanoparticles [73]. Additionally the initial nanoparticle diameter does not change during the deposition process [195] [132]. Yet this method requires either support materials with low impedance or placement of the support material between the electrodes, forcing mass flow through the support.

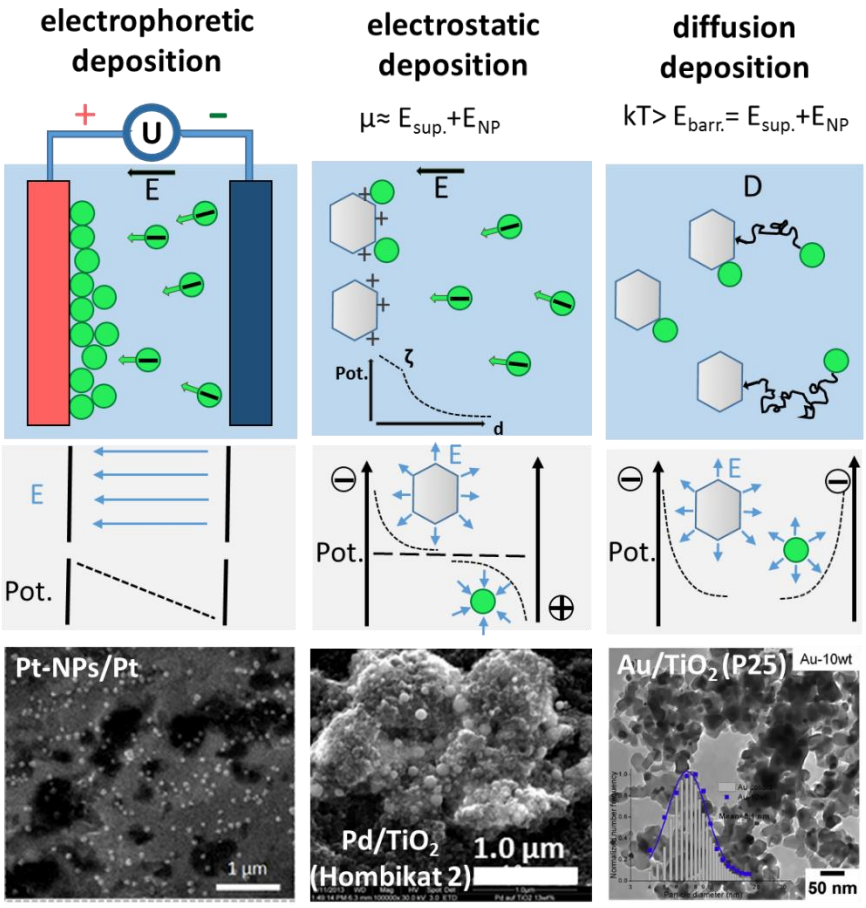

Fig. 12: Principles for deposition of laser-generated nanoparticles and the corresponding SEM/TEM micrographs for Electrophoretic deposition (EPD) (Micrograph reprinted with permission from [73] Elsevier)**, Electrostatic deposition (ESD)** (Micrograph reprinted from [45], Elsevier) **and Diffusion deposition** (Micrograph reprinted with permission from[15], Elsevier)**.**

In order to load nanoparticles onto oxides employing high impediance a second method called electrostatic deposition need to be established exploiting the natural electrostatic charge being present on nearly all nanoparticulate materials. A comprehensive mechanism for the electrostatic nanoparticle deposition was suggested by Wagener et al. [43]. As already shown in Fig. 2 they investigated the dependency of the nanoparticle adsorption efficiency on the ligand coverage of AgNP during their deposition on $BaSO_4$. By this method they where already able to obtain a great variety of nanosupported particle combinations even without further

calcination or annealing steps when working in the electrostatic attraction regime as shown in Fig. 12 [43]. However the mechanism of laser-generated colloidal particle adsorption on supports is yet not fully understood. To clearly proof that particle adsorption is initiated by electrostatic interactions further experiments are needed to demonstrate the effect of the surface charge. By using ligand-free nanoparticles and changing the pH value the electrostatic surface charge causing zeta potential, can be controlled. With this simple investigations the mechanism of the particle adsorption on supports could be clarified.

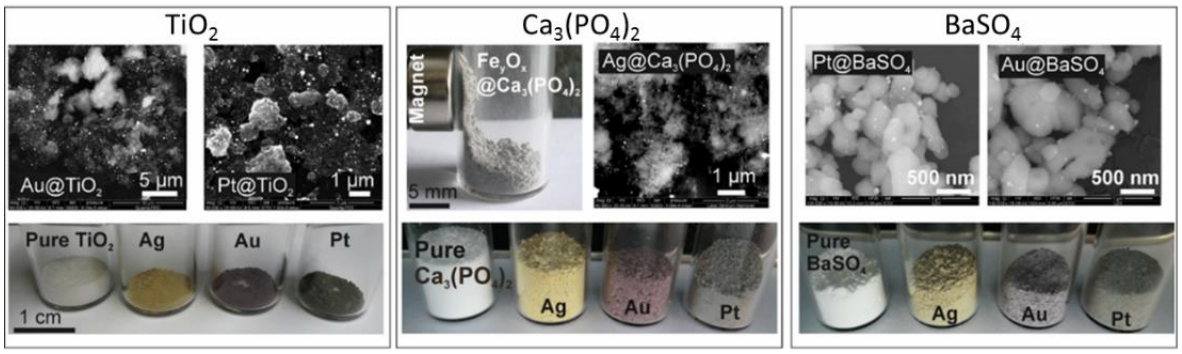

Fig. 13 A collection of supported noble metals on several oxide materials as well as graphene nanosheets produced by electrostatic deposition of laser-generated ligand-free nanoparticles. (Reprinted with permission from [70] Copyright 2012, American Chemical Society).

1.6 Future prospects

Yet while applying these structure-activity-correlations not only the catalyst activity but also its stability (durability) need to be regarded during the design. Some mechanisms found for single oxide catalysts like Fe_2O_3 are usually based on poisoning effects e.g. coking [28]. However, in most scientific works an increased instability is observed in case of decreasing nanoparticle size as well as increased loading, mainly due to an enhanced tendency of Ostwald ripening and coalescence [198] [7] [14] [28] as it was already addressed in chapter 1.4. Following the simplified concept called “average inter-particle distance” which has been proposed by Meier and Schüth et al. based on cyclo-voltammetric testings of PtNP adsorbed onto carbon based carrier materials [10], these aging effects were only observed when alternating the electrical potential while no changes occurred on applying a constant electrical potential [10].

Although this concept was based on electrical potentials it may as well be generalized onto chemical potentials. In general, high local educt concentration- and temperature-shifts are most likely to occur under reactive conditions. Hence, the alternating chemical potential due to limited reaction and diffusion kinetics in a general catalytic reaction presumingly has the same effect on the catalyst stability like the varying electrical potential applied in the experiments of

Schüth et al. [10]. To that end Dong and Reichenberger et al. investigated the influence of AuNP loading on the catalytic activity independent of size and pretreatment effects by using $AuTiO_2$ catalysts in a selective oxidation reaction of ethanol. Hereby, ligand-free AuNP with a size of 7 nm were adsorbed onto P25 (TiO_2) following the electrostatic adsorption process described by Marzun et al. [44]. Subsequently, the catalytic activity and stability of prepared catalysts with different AuNP loadings in the range of 1-10 wt% were investigated and compared to the commercial AUROlite catalyst possessing 3 nm AuNP with 1 wt% as shown in Fig. 15 A [15]. For a detailed discussion of the influence of AuNP loading we refer to the original publication [15]. Following the nanoparticle surface-area-normalized yields (of acetic acid produced) shown in Fig. 15A the AuNP size difference between commercial catalyst and prepared catalyst expectantly causes a higher specific activity of the AUROlite catalyst at low reaction temperatures (80°C). However on increased temperatures a significantly higher catalytic activity (with regard to AuNP number) was observed for both catalysts but with the 7 nm ligand-free AuNP exceeding the performance of the commercial AUROlite catalyst by about 70 % at 180 °C (see Fig. 15 A).

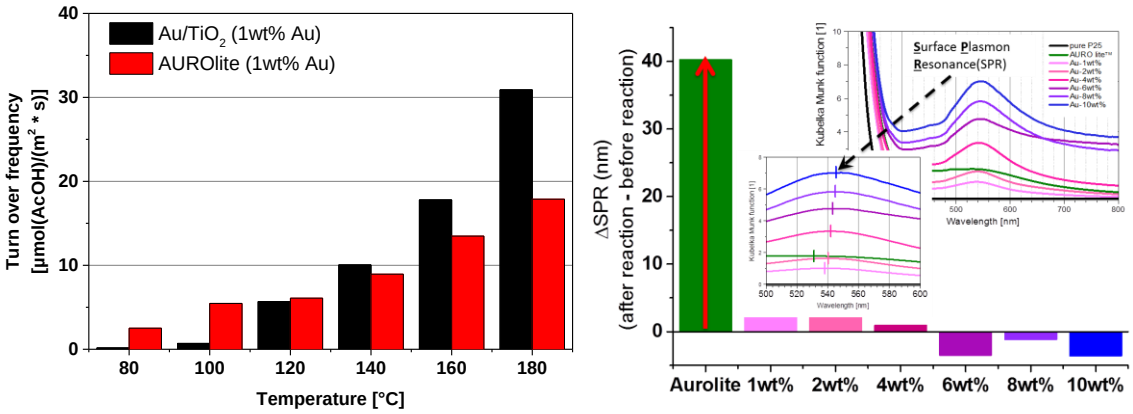

Fig. 15 A: Measured catalytic yield of acetic acid adapted from [15] normalized on the AuNP surface for different reaction temperatures comparing the commercial catalyst AUROlite with the Au/TiO_2 catalyst prepared using ligand-free AuNP. Both catalysts are loaded with 1 wt% AuNP and are supported on the same TiO_2 (P25). B: Ripening plot of the AuNP plasmonresonance shift after the reaction, comparing the commercial AUROlite catalyst as well as the prepared laser-generated catalysts with different AuNP loadings.

As shown in Fig. 15 B the lower specific activity of the AUROlite (3 nm AuNP) at 180°C was found to be connected to a significant aging tendency of the AUROlite correlating with a surface plasmon resonance shift of the AuNP before and after the reaction. When calculating the AID as suggested by Meier and Schüth et al. (formula given in [10]) the unstable AUROlite yields an AID of 36.5 nm while the laser-generated AuNP with the same mass loading exhibits 164.0 nm

AID suggesting an increased stability of the laser-generated nanoparticles. Yet additionally considering the laser-based 10 wt% sample (7 nm AuNP) having an AID of 43.8 nm it is obvious from the small peak-shift of the 10 wt% sample in Fig. 15 B that even with smaller inter-particle distances (in case of 10 wt%) the aging tendencies are significantly reduced. This effect is most likely augmented by the increased particle size and hence lower ripening tendency. Additionally, based on a model calculation, a connection between the AuNP number and the number of oxygen defects on the surface was hypothesized by Dong et al. [15]. Interestingly an optimum in catalytic activity has been found in case of a mass loading of 4 wt% AuNP on P25 and hypothesized (based on an empiric estimation of the oxygen-defect density on P25) to be connected with the coverage of all catalytically relevant oxygen vacancies with AuNP at this optimal loading [15]. Yet while the validation of this hypothesis is still part of an ongoing investigation the prolonged stability of the 7 nm AuNP at 1 wt% loading may hence be attributed to either an enhanced metal to support interaction between ligand-free nanoparticles and TiO_2 supports or only the AuNP particle size itself [15].

Yet due to the exclusion of cross-correlations originating from calcination as well as ligand or ionic residues the laser-based catalyst preparation method exhibits a rather novel and promising tool to develop structure-activity correlations.

While it was successfully demonstrated that laser-generated, oxide-supported nanoparticles are process-stable at high temperatures performing ethanol oxidation reaction, there are no studies on their stability of carbon-based catalyst, yet. Since laser-generated nanoparticles are of great interest for electrocatalytic reactions, investigations on activity and stability of carbon supported laser-generated nanoparticles are essential to assess their application potential for example in fuel cells.

Literature:

[1] D. Zhang, B. Gökce, and S. Barcikowski, “Laser synthesis and processing of colloids: fundamentals and applications,” *Chemical Reviews*, vol. 117, no. 5, pp. 3990–4103, 2017.

[2] J. J. Bravo-Suárez, R. V. Chaudhari, and B. Subramaniam, “Design of heterogeneous catalysts for fuels and chemicals processing: An overview,” in *Novel Materials for Catalysis and Fuels Processing*, pp. 3–68, ACS Publications, 2013.

[3] T. Schalow, B. Brandt, D. E. Starr, M. Laurin, S. K. Shaikhutdinov, S. Schauermann, J. Libuda, and H.-J. Freund, “Particle size dependent adsorption and reaction kinetics on

reduced and partially oxidized Pd nanoparticles," *Phys. Chem. Chem. Phys.*, vol. 9, pp. 1347–1361, 2007.

[4] H. Mistry, R. Reske, Z. Zeng, Z.-J. Zhao, J. Greeley, P. Strasser, and B. R. Cuenya, "Exceptional size-dependent activity enhancement in the electroreduction of CO2 over Au nanoparticles," *Journal of the American Chemical Society*, vol. 136, no. 47, pp. 16473–16476, 2014.

[5] C. L. Kuo and K. C. Hwang, "Does morphology of a metal nanoparticle play a role in ostwald ripening processes?," *Chemistry of Materials*, vol. 25, no. 3, pp. 365–371, 2013.

[6] T. W. Hansen, A. T. DeLaRiva, S. R. Challa, and A. K. Datye, "Sintering of catalytic nanoparticles: particle migration or ostwald ripening?," *Accounts of chemical research*, vol. 46, no. 8, pp. 1720–1730, 2013.

[7] S. B. Simonsen, I. Chorkendorff, S. Dahl, M. Skoglundh, K. Meinander, T. N. Jensen, J. V. Lauritsen, and S. Helveg, "Effect of particle morphology on the ripening of supported Pt nanoparticles," *The Journal of Physical Chemistry C*, vol. 116, no. 9, pp. 5646–5653, 2012.

[8] A. Berko, J. Szökő, and F. Solymosi, "Effect of co on the morphology of Pt nanoparticles supported on TiO2 (110)-(1× n)," *Surface science*, vol. 566, pp. 337–342, 2004.

[9] M. Eiswirth and G. Ertl, "Kinetic oscillations in the catalytic co oxidation on a Pt(110) surface," *Surface Science*, vol. 177, no. 1, pp. 90 – 100, 1986.

[10] J. C. Meier, C. Galeano, I. Katsounaros, J. Witte, H. J. Bongard, A. A. Topalov, C. Baldizzone, S. Mezzavilla, F. Schüth, and K. J. J. Mayrhofer, "Design criteria for stable Pt/C fuel cell catalysts," *Beilstein Journal of Nanotechnology*, vol. 5, pp. 44–67, 2014.

[11] M. D. Argyle and C. H. Bartholomew, "Heterogeneous catalyst deactivation and regeneration: A review," *Catalysts*, vol. 5, no. 1, p. 145, 2015.

[12] H.-J. Freund, N. Nilius, T. Risse, and S. Schauermann, "A fresh look at an old nano-technology: catalysis," *Phys. Chem. Chem. Phys.*, vol. 16, pp. 8148–8167, 2014.

[13] P. Strasser, S. Koh, T. Anniyev, J. Greeley, K. More, C. Yu, Z. Liu, S. Kaya, D. Nordlund, H. Ogasawara, *et al.*, "Lattice-strain control of the activity in dealloyed core–shell fuel cell catalysts," *Nature chemistry*, vol. 2, no. 6, pp. 454–460, 2010.

[14] F. Behafarid and B. R. Cuenya, "Towards the understanding of sintering phenomena at the nanoscale: Geometric and environmental effects," *Topics in Catalysis*, vol. 56, no. 15, pp. 1542–1559, 2013.

[15] W. Dong, S. Reichenberger, S. Chu, P. Weide, H. Ruland, S. Barcikowski, P. Wagener, and M. Muhler, "The effect of the au loading on the liquid-phase aerobic oxidation of ethanol

over Au/TiO2 catalysts prepared by pulsed laser ablation," *Journal of Catalysis*, vol. 330, pp. 497 – 506, 2015.

[16] V. M. Wall, A. Eisenstadt, D. J. Ager, and S. A. Laneman, "The heck reaction and cinnamic acid synthesis by heterogeneous catalysis," *Platinum Metals Review*, vol. 43, no. 4, pp. 138–145, 1999.

[17] H.-U. Blaser, H.-P. Jalett, M. Müller, and M. Studer, "Enantioselective hydrogenation of α-ketoesters using cinchona modified platinum catalysts and related systems: A review," *Catalysis today*, vol. 37, no. 4, pp. 441–463, 1997.

[18] P. Rylander, *Catalytic Hydrogenation Over Platinum Metals*. Academic Press, 1967.

[19] H. Tong, S. Ouyang, Y. Bi, N. Umezawa, M. Oshikiri, and J. Ye, "Nano-photocatalytic materials: Possibilities and challenges," *Advanced Materials*, vol. 24, no. 2, pp. 229–251, 2012.

[20] K. Maeda and K. Domen, "Photocatalytic water splitting: recent progress and future challenges," *The Journal of Physical Chemistry Letters*, vol. 1, no. 18, pp. 2655–2661, 2010.

[21] F. Safizadeh, E. Ghali, and G. Houlachi, "Electrocatalysis developments for hydrogen evolution reaction in alkaline solutions - a review," *International Journal of Hydrogen Energy*, vol. 40, no. 1, pp. 256 – 274, 2015.

[22] R. Singh, R. Awasthi, and C. Sharma, "Review: An overview of recent development of platinum-based cathode materials for direct methanol fuel cells," *Int. J. Electrochem. Sci*, vol. 9, pp. 5607–5639, 2014.

[23] O. Z. Sharaf and M. F. Orhan, "An overview of fuel cell technology: Fundamentals and applications," *Renewable and Sustainable Energy Reviews*, vol. 32, pp. 810 – 853, 2014.

[24] B. M. Hunter, H. B. Gray, and A. M. MuÌˆller, "Earth-abundant heterogeneous water oxidation catalysts," *Chemical Reviews*, vol. just accepted, 2016.

[25] M. A. Abbas and J. H. Bang, "Rising again: opportunities and challenges for platinum-free electrocatalysts," *Chemistry of Materials*, vol. 27, no. 21, pp. 7218–7235, 2015.

[26] H. Xiong, E. Peterson, G. Qi, and A. K. Datye, "Trapping mobile Pt species by PdO in diesel oxidation catalysts: Smaller is better," *Catalysis Today*, vol. 272, pp. 80 – 86, 2016. Jens Rostrup-Nielsen Synthesis Gas Generation and Use.

[27] J. Greeley, I. Stephens, A. Bondarenko, T. P. Johansson, H. A. Hansen, T. Jaramillo, J. Rossmeisl, I. Chorkendorff, and J. K. Nørskov, "Alloys of platinum and early transition metals as oxygen reduction electrocatalysts," *Nature chemistry*, vol. 1, no. 7, pp. 552–556, 2009.

[28] R. Schlögl, "Heterogeneous catalysis," *Angewandte Chemie International Edition*, vol. 54, no. 11, pp. 3465–3520, 2015.

[29] J. Zhang, H. Yang, J. Fang, and S. Zou, "Synthesis and oxygen reduction activity of shape-controlled Pt3Ni nanopolyhedra," *Nano letters*, vol. 10, no. 2, pp. 638–644, 2010.

[30] K. A. Stoerzinger, L. Qiao, M. D. Biegalski, and Y. Shao-Horn, "Orientation-dependent oxygen evolution activities of rutile IrO2 and RuO2," *The journal of physical chemistry letters*, vol. 5, no. 10, pp. 1636–1641, 2014.

[31] A. J. Medford, A. Vojvodic, J. S. Hummelshøj, J. Voss, F. Abild-Pedersen, F. Studt, T. Bligaard, A. Nilsson, and J. K. Nørskov, "From the sabatier principle to a predictive theory of transition-metal heterogeneous catalysis," *Journal of Catalysis*, vol. 328, pp. 36–42, 2015.

[32] S. E. Bozbag and C. Erkey, "Supercritical deposition: Current status and perspectives for the preparation of supported metal nanostructures," *The Journal of Supercritical Fluids*, vol. 96, pp. 298–312, 2015.

[33] R. Siburian, T. Kondo, and J. Nakamura, "Size control to a sub-nanometer scale in platinum catalysts on graphene," *The Journal of Physical Chemistry C*, vol. 117, no. 7, pp. 3635–3645, 2013.

[34] R. Siburian, T. Kondo, and J. Nakamura, "Size control to a sub-nanometer scale in platinum catalysts on graphene," *The Journal of Physical Chemistry C*, vol. 117, no. 7, pp. 3635–3645, 2013.

[35] S. Li, H. Liu, Y. Wang, W. Xu, J. Li, Y. Liu, X. Guo, and Y. Song, "Controlled synthesis of high metal-loading, Pt-based electrocatalysts with enhanced activity and durability toward oxygen reduction reaction," *RSC Advances*, vol. 5, no. 12, pp. 8787–8792, 2015.

[36] M. Behrens, S. Kißner, F. Girsgdies, I. Kasatkin, F. Hermerschmidt, K. Mette, H. Ruland, M. Muhler, and R. Schlögl, "Knowledge-based development of a nitrate-free synthesis route for cu/zno methanol synthesis catalysts via formate precursors," *Chemical Communications*, vol. 47, no. 6, pp. 1701–1703, 2011.

[37] P. Munnik, P. E. de Jongh, and K. P. de Jong, "Recent developments in the synthesis of supported catalysts," *Chemical reviews*, vol. 115, no. 14, pp. 6687–6718, 2015.

[38] H. Bönnemann and W. Brijoux, "Surfactant-stabilized nanosized colloidal metals and alloys as catalyst precursors-chapter 7," *Advanced Catalysts and Nanostructured Materials*, pp. 165–196, 1996.

[39] H. Bönnemann, G. Braun, W. Brijoux, R. Brinkmann, A. Tilling, K. Seevogel, and K. Siepen, "Nanoscale colloidal metals and alloys stabilized by solvents and surfactants preparation and use as catalyst precursors," *Journal of Organometallic Chemistry*, vol. 520, no. 1, pp. 143 – 162, 1996.

[40] H. Bönnemann, W. Brijoux, R. Brinkmann, E. Dinjus, T. Joußen, and B. Korall, "Erzeugung von kolloiden Übergangsmetallen in organischer Phase und ihre Anwendung in der Katalyse," *Angewandte Chemie*, vol. 103, no. 10, pp. 1344–1346, 1991.

[41] Y. Guo, D. Gu, Z. Jin, P.-P. Du, R. Si, J. Tao, W.-Q. Xu, Y.-Y. Huang, S. Senanayake, Q.-S. Song, C.-J. Jia, and F. Schuth, "Uniform 2 nm gold nanoparticles supported on iron oxides as active catalysts for co oxidation reaction: structure-activity relationship," *Nanoscale*, vol. 7, pp. 4920–4928, 2015.

[42] S. Barcikowski, P. Wagener, and A. Schwenke, "Verfahren zur Herstellung von mikro-nanokombinierten Wirksystemen," 2012.

[43] P. Wagener, A. Schwenke, and S. Barcikowski, "How citrate ligands affect nanoparticle adsorption to microparticle supports," *Langmuir*, vol. 28, no. 14, pp. 6132–6140, 2012.

[44] G. Marzun, C. Streich, S. Jendrzej, S. Barcikowski, and P. Wagener, "Adsorption of colloidal platinum nanoparticles to supports: charge transfer and effects of electrostatic and steric interactions," *Langmuir*, vol. 30, no. 40, pp. 11928–11936, 2014.

[45] G. Marzun, J. Nakamura, X. Zhang, S. Barcikowski, and P. Wagener, "Size control and supporting of palladium nanoparticles made by laser ablation in saline solution as a facile route to heterogeneous catalysts," *Applied Surface Science*, vol. 348, pp. 75–84, 2015.

[46] V. Merk, C. Rehbock, F. Becker, U. Hagemann, H. Nienhaus, and S. Barcikowski, "In situ non-dlvo stabilization of surfactant-free, plasmonic gold nanoparticles: Effect of hofmeister's anions," *Langmuir*, vol. 30, no. 15, pp. 4213–4222, 2014.

[47] R. Streubel, G. Bendt, and B. Gökce, "Pilot-scale synthesis of metal nanoparticles by high-speed pulsed laser ablation in liquids," *Nanotechnology*, vol. 27, no. 20, p. 205602, 2016.

[48] R. Streubel, S. Barcikowski, and B. Gökce, "Continuous multigram nanoparticle synthesis by high-power, high-repetition-rate ultrafast laser ablation in liquids," *Opt. Lett.*, vol. 41, pp. 1486–1489, Apr 2016.

[49] S. Barcikowski, T. Baranowski, Y. Durmus, U. Wiedwald, and B. Gokce, "Solid solution magnetic feni nanostrand-polymer composites by connecting-coarsening assembly," *J. Mater. Chem. C*, vol. 3, pp. 10699–10704, 2015.

[50] D. Zhang, B. Gökce, C. Notthoff, and S. Barcikowski, "Layered seed-growth of agge football-like microspheres via precursor-free picosecond laser synthesis in water," *Scientific reports*, vol. 5, pp.1-10, 2015.

[51] G. Marzun, A. Levish, V. Mackert, T. Kallio, S. Barcikowski, and P. Wagener, "Laser synthesis, structure and chemical properties of colloidal nickel-molybdenum nanoparticles for

the substitution of noble metals in heterogeneous catalysis," *Journal of Colloid and Interface Science*, pp. 57–67, 2016.

[52] P. Wagener, J. Jakobi, C. Rehbock, V. S. K. Chakravadhanula, C. Thede, U. Wiedwald, M. Bartsch, L. Kienle, and S. Barcikowski, "Solvent-surface interactions control the phase structure in laser-generated iron-gold core-shell nanoparticles," *Scientific reports*, vol. 6, pp.1-12, 2016.

[53] C. Rehbock, V. Merk, L. Gamrad, R. Streubel, and S. Barcikowski, "Size control of laser-fabricated surfactant-free gold nanoparticles with highly diluted electrolytes and their subsequent bioconjugation," *Physical Chemistry Chemical Physics*, vol. 15, no. 9, pp. 3057–3067, 2013.

[54] J. Zhang, D. N. Oko, S. Garbarino, R. Imbeault, M. Chaker, A. C. Tavares, D. Guay, and D. Ma, "Preparation of ptau alloy colloids by laser ablation in solution and their characterization," *The Journal of Physical Chemistry C*, vol. 116, no. 24, pp. 13413–13420, 2012.

[55] A. Neumeister, J. Jakobi, C. Rehbock, J. Moysig, and S. Barcikowski, "Monophasic ligand-free alloy nanoparticle synthesis determinants during pulsed laser ablation of bulk alloy and consolidated microparticles in water," *Physical Chemistry Chemical Physics*, vol. 16, no. 43, pp. 23671–23678, 2014.

[56] S. Barcikowski and G. Compagnini, "Advanced nanoparticle generation and excitation by lasers in liquids," *Phys. Chem. Chem. Phys.*, vol. 15, pp. 3022–3026, 2013.

[57] V. Amendola and M. Meneghetti, "What controls the composition and the structure of nanomaterials generated by laser ablation in liquid solution?," *Phys. Chem. Chem. Phys.*, vol. 15, pp. 3027–3046, 2013.

[58] C. Rehbock, J. Jakobi, L. Gamrad, S. van der Meer, D. Tiedemann, U. Taylor, W. Kues, D. Rath, and S. Barcikowski, "Current state of laser synthesis of metal and alloy nanoparticles as ligand-free reference materials for nano-toxicological assays," *Beilstein Journal of Nanotechnology*, vol. 5, pp. 1523–1541, 2014.

[59] S. Barcikowski, P. Wagener, and A. Schwenke, "Method for producing micro-nano combined active systems," 12.12 2016. US Patent US20130331257 A1.

[60] S. Barcikowski, P. Wagener, and A. Schwenke, "Verfahren zur Herstellung von mikro-nanokombinierten Wirksystemen," 23.10 2013. EU Patent, EP2651593 A1.

[61] X. Wang, P. Sonström, D. Arndt, J. Stöver, V. Zielasek, H. Borchert, K. Thiel, K. Al-Shamery, and M. Bäumer, "Heterogeneous catalysis with supported platinum colloids: A

systematic study of the interplay between support and functional ligands," *Journal of Catalysis*, vol. 278, no. 1, pp. 143–152, 2011.

[62] L. Altmann, S. Kunz, and M. Bäumer, "Influence of organic amino and thiol ligands on the geometric and electronic surface properties of colloidally prepared platinum nanoparticles," *The Journal of Physical Chemistry C*, vol. 118, no. 17, pp. 8925–8932, 2014.

[63] S. H. Pang, C. A. Schoenbaum, D. K. Schwartz, and J. W. Medlin, "Effects of thiol modifiers on the kinetics of furfural hydrogenation over pd catalysts," *ACS Catalysis*, vol. 4, no. 9, pp. 3123–3131, 2014.

[64] I. Schrader, S. Neumann, R. Himstedt, A. Zana, J. Warneke, and S. Kunz, "The effect of particle size and ligand configuration on the asymmetric catalytic properties of proline-functionalized pt-nanoparticles," *Chem. Commun.*, vol. 51, pp. 16221–16224, 2015.

[65] S. Gu, J. Kaiser, G. Marzun, A. Ott, Y. Lu, M. Ballauff, A. Zaccone, S. Barcikowski, and P. Wagener, "Ligand-free gold nanoparticles as a reference material for kinetic modelling of catalytic reduction of 4-nitrophenol," *Catalysis Letters*, vol. 145, no. 5, pp. 1105–1112, 2015.

[66] M. Ocwieja, Z. Adamczyk, and K. Kubiak, "Tuning properties of silver particle monolayers via controlled adsorption–desorption processes," *Journal of colloid and interface science*, vol. 376, no. 1, pp. 1–11, 2012.

[67] J. Zhang, G. Chen, M. Chaker, F. Rosei, and D. Ma, "Gold nanoparticle decorated ceria nanotubes with significantly high catalytic activity for the reduction of nitrophenol and mechanism study," *Applied Catalysis B: Environmental*, vol. 132-133, pp. 107 – 115, 2013.

[68] M. Comotti, W.-C. Li, B. Spliethoff, and F. Schüth, "Support effect in high activity gold catalysts for co oxidation," *Journal of the American Chemical Society*, vol. 128, no. 3, pp. 917–924, 2006.

[69] J. N. Kuhn, C.-K. Tsung, W. Huang, and G. A. Somorjai, "Effect of organic capping layers over monodisperse platinum nanoparticles upon activity for ethylene hydrogenation and carbon monoxide oxidation," *Journal of Catalysis*, vol. 265, no. 2, pp. 209 – 215, 2009.

[70] P. Wagener, S. Ibrahimkutty, A. Menzel, A. Plech, and S. Barcikowski, "Dynamics of silver nanoparticle formation and agglomeration inside the cavitation bubble after pulsed laser ablation in liquid," *Physical Chemistry Chemical Physics*, vol. 15, no. 9, pp. 3068–3074, 2013.

[71] G. J. Hutchings, "Nanocrystalline gold and gold palladium alloy catalysts for chemical synthesis," *Chem. Commun.*, pp. 1148–1164, 2008.

[72] S. Gu, S. Wunder, Y. Lu, M. Ballauff, R. Fenger, K. Rademann, B. Jaquet, and A. Zaccone, "Kinetic analysis of the catalytic reduction of 4-nitrophenol by metallic nanoparticles," *The Journal of Physical Chemistry C*, vol. 118, no. 32, pp. 18618–18625, 2014.

[73] C. Streich, S. Koenen, M. Lelle, K. Peneva, and S. Barcikowski, "Influence of ligands in metal nanoparticle electrophoresis for the fabrication of biofunctional coatings," *Applied Surface Science*, vol. 348, pp. 92–99, 2015.

[74] D. Zhang and B. Gökce, "Perspective of laser-prototyping nanoparticle-polymer composites," *Applied Surface Science*, vol. 392, pp. 991 – 1003, 2017.

[75] S. T. Marshall, M. O'Brien, B. Oetter, A. Corpuz, R. M. Richards, D. K. Schwartz, and J. W. Medlin, "Controlled selectivity for palladium catalysts using self-assembled monolayers," *Nature materials*, vol. 9, no. 10, pp. 853–858, 2010.

[76] Z. Bayindir, P. N. Duchesne, S. C. Cook, M. A. MacDonald, and P. Zhang, "X-ray spectroscopy studies on the surface structural characteristics and electronic properties of platinum nanoparticles," *The Journal of Chemical Physics*, vol. 131, no. 24, 2009.

[77] Z.-Y. Zhou, X. Kang, Y. Song, and S. Chen, "Ligand-mediated electrocatalytic activity of Pt nanoparticles for oxygen reduction reactions," *The Journal of Physical Chemistry C*, vol. 116, no. 19, pp. 10592–10598, 2012.

[78] M. Haruta, "Size- and support-dependency in the catalysis of gold," *Catalysis Today*, vol. 36, no. 1, pp. 153 – 166, 1997.

[79] M. Haruta, "When gold is not noble: catalysis by nanoparticles," *The chemical record*, vol. 3, no. 2, pp. 75–87, 2003.

[80] S. Hackett, R. Brydson, M. Gass, I. Harvey, A. Newman, K. Wilson, and A. Lee, "High-activity, single-site mesoporous Pd/Al2O3 catalysts for selective aerobic oxidation of allylic alcohols," *Angewandte Chemie*, vol. 119, no. 45, pp. 8747–8750, 2007.

[81] Z. Huang, X. Gu, Q. Cao, P. Hu, J. Hao, J. Li, and X. Tang, "Catalytically active single-atom sites fabricated from silver particles," *Angewandte Chemie*, vol. 124, no. 17, pp. 4274–4279, 2012.

[82] M. Yang, L. F. Allard, and M. Flytzani-Stephanopoulos, "Atomically dispersed Au–(OH) x species bound on titania catalyze the low-temperature water-gas shift reaction," *Journal of the American Chemical Society*, vol. 135, no. 10, pp. 3768–3771, 2013.

[83] Y. Liu, G. Zhao, D. Wang, and Y. Li, "Heterogeneous catalysis for green chemistry based on nanocrystals," *National Science Review*, vol. 2, no. 2, pp. 150–166, 2015.

[84] J. Zhang, M. Chaker, and D. Ma, "Pulsed laser ablation based synthesis of colloidal metal nanoparticles for catalytic applications," *Journal of Colloid and Interface Science*, pp. 138–149, 2016.

[85] X.-F. Yang, A. Wang, B. Qiao, J. Li, J. Liu, and T. Zhang, "Single-atom catalysts: a new frontier in heterogeneous catalysis," *Accounts of chemical research*, vol. 46, no. 8, pp. 1740–1748, 2013.

[86] N. Lopez, T. Janssens, B. Clausen, Y. Xu, M. Mavrikakis, T. Bligaard, and J. NÃ¸rskov, "On the origin of the catalytic activity of gold nanoparticles for low-temperature {CO} oxidation," *Journal of Catalysis*, vol. 223, no. 1, pp. 232 – 235, 2004.

[87] M. Peter, J. M. Flores Camacho, S. Adamovski, L. K. Ono, K.-H. Dostert, C. P. O'Brien, B. Roldan Cuenya, S. Schauermann, and H.-J. Freund, "Trends in the binding strength of surface species on nanoparticles: how does the adsorption energy scale with the particle size?," *Angewandte Chemie International Edition*, vol. 52, no. 19, pp. 5175–5179, 2013.

[88] M. Ahmadi, H. Mistry, and B. Roldan Cuenya, "Tailoring the catalytic properties of metal nanoparticles via support interactions," *The Journal of Physical Chemistry Letters*, vol. 7, no. 17, pp. 3519–3533, 2016.

[89] E. Roduner, "Size matters: why nanomaterials are different," *Chem. Soc. Rev.*, vol. 35, pp. 583–592, 2006.

[90] A. Roldan, J. M. Ricart, and F. Illas, "Origin of the size dependence of au nanoparticles toward molecular oxygen dissociation," *Theoretical Chemistry Accounts*, vol. 128, no. 4, pp. 675–681, 2011.

[91] M. Chen and D. W. Goodman, "Catalytically active gold: from nanoparticles to ultrathin films," *Accounts of chemical research*, vol. 39, no. 10, pp. 739–746, 2006.

[92] M. Haruta, "Spiers memorial lecture role of perimeter interfaces in catalysis by gold nanoparticles," *Faraday Discuss.*, vol. 152, pp. 11–32, 2011.

[93] P. Buffat and J.-P. Borel, "Size effect on the melting temperature of gold particles," *Phys. Rev. A*, vol. 13, pp. 2287–2298, Jun 1976.

[94] M. Di Vece, D. Grandjean, M. J. Van Bael, C. P. Romero, X. Wang, S. Decoster, A. Vantomme, and P. Lievens, "Hydrogen-induced ostwald ripening at room temperature in a pd nanocluster film," *Phys. Rev. Lett.*, vol. 100, p. 236105, Jun 2008.

[95] I. V. Yudanov, M. Metzner, A. Genest, and N. Rösch, "Size-dependence of adsorption properties of metal nanoparticles: A density functional study on palladium nanoclusters," *The Journal of Physical Chemistry C*, vol. 112, no. 51, pp. 20269–20275, 2008.

[96] M. Fischer, J. Hormes, G. Marzun, P. Wagener, U. Hagemann, and S. Barcikowski, "In situ investigations of laser-generated ligand-free platinum nanoparticles by x-ray absorption spectroscopy: How does the immediate environment influence the particle surface?," *Langmuir*, vol. 32, no. 35, pp. 8793–8802, 2016.

[97] R. Torres-Mendieta, D. Ventura-Espinosa, S. Sabater, J. Lancis, G. Mnguez-Vega, and J. A. Mata, "In situ decoration of graphene sheets with gold nanoparticles synthetized by pulsed laser ablation in liquids," *Scientific Reports*, vol. 6, 2016.

[98] V. Amendola and M. Meneghetti, "Controlled size manipulation of free gold nanoparticles by laser irradiation and their facile bioconjugation," *Journal of Materials Chemistry*, vol. 17, no. 44, pp. 4705–4710, 2007.

[99] D. Werner and S. Hashimoto, "Controlling the pulsed-laser-induced size reduction of au and ag nanoparticles via changes in the external pressure, laser intensity, and excitation wavelength," *Langmuir*, vol. 29, no. 4, pp. 1295–1302, 2013.

[100] P. Blandin, K. A. Maximova, M. B. Gongalsky, J. F. Sanchez-Royo, V. S. Chirvony, M. Sentis, V. Y. Timoshenko, and A. V. Kabashin, "Femtosecond laser fragmentation from water-dispersed microcolloids: toward fast controllable growth of ultrapure si-based nanomaterials for biological applications," *Journal of Materials Chemistry B*, vol. 1, no. 19, pp. 2489–2495, 2013.

[101] C. L. Sajti, A. Barchanski, P. Wagener, S. Klein, and S. Barcikowski, "Delay time and concentration effects during bioconjugation of nanosecond laser-generated nanoparticles in a liquid flow," *The Journal of Physical Chemistry C*, vol. 115, no. 12, pp. 5094–5101, 2011.

[102] A. Pyatenko, H. Wang, N. Koshizaki, and T. Tsuji, "Mechanism of pulse laser interaction with colloidal nanoparticles," *Laser & Photonics Reviews*, vol. 7, no. 4, pp. 596–604, 2013.

[103] T. Tsuji, T. Yahata, M. Yasutomo, K. Igawa, M. Tsuji, Y. Ishikawa, and N. Koshizaki, "Preparation and investigation of the formation mechanism of submicron-sized spherical particles of gold using laser ablation and laser irradiation in liquids," *Physical Chemistry Chemical Physics*, vol. 15, no. 9, pp. 3099–3107, 2013.

[104] C. Rehbock, J. Zwartscholten, and S. Barcikowski, "Biocompatible gold submicrometer spheres with variable surface texture fabricated by pulsed laser melting in liquid," *Chemistry Letters*, vol. 43, no. 9, pp. 1502–1504, 2014.

[105] F. Mafuné, T. Okamoto, and M. Ito, "Surfactant-free small ni nanoparticles trapped on silica nanoparticles prepared by pulsed laser ablation in liquid," *Chemical Physics Letters*, vol. 591, pp. 193–196, 2014.

[106] S. Hashimoto, T. Uwada, H. Masuhara, and T. Asahi, "Fabrication of gold nanoparticle-doped zeolite l crystals and characterization by optical microscopy: Laser ablation-and crystallization inclusion-based approach," *The Journal of Physical Chemistry C*, vol. 112, no. 39, pp. 15089–15093, 2008.

[107] H. He, H. Wang, K. Li, J. Zhu, J. Liu, X. Meng, X. Shen, X. Zeng, and W. Cai, "Green and tunable decoration of graphene with spherical nanoparticles based on laser ablation in water: A case of ag nanoparticle/graphene oxide sheet composites," *Langmuir*, vol. 32, no. 7, pp. 1667–1673, 2016.

[108] A. Takami, H. Kurita, and S. Koda, "Laser-induced size reduction of noble metal particles," *The Journal of Physical Chemistry B*, vol. 103, no. 8, pp. 1226–1232, 1999.

[109] P. Boyer, D. Ménard, and M. Meunier, "Nanoclustered co- au particles fabricated by femtosecond laser fragmentation in liquids," *The Journal of Physical Chemistry C*, vol. 114, no. 32, pp. 13497–13500, 2010.

[110] S. Hashimoto, D. Werner, and T. Uwada, "Studies on the interaction of pulsed lasers with plasmonic gold nanoparticles toward light manipulation, heat management, and nanofabrication," *Journal of Photochemistry and Photobiology C: Photochemistry Reviews*, vol. 13, no. 1, pp. 28 – 54, 2012.

[111] M. Lau, I. Haxhiaj, P. Wagener, R. Intartaglia, F. Brandi, J. Nakamura, and S. Barcikowski, "Ligand-free gold atom clusters adsorbed on graphene nano sheets generated by oxidative laser fragmentation in water," *Chemical Physics Letters*, vol. 610, pp. 256–260, 2014.

[112] M. Lau and S. Barcikowski, "Quantification of mass-specific laser energy input converted into particle properties during picosecond pulsed laser fragmentation of zinc oxide and boron carbide in liquids," *Applied Surface Science*, vol. 348, pp. 22–29, 2015.

[113] S. Jendrzej, B. Gökce, V. Amendola, and S. Barcikowski, "Barrierless growth of precursor-free, ultrafast laser-fragmented noble metal nanoparticles by colloidal atom clusters-a kinetic in situ study," *Journal of Colloid and Interface Science*, vol. 463, pp. 299 – 307, 2016.

[114] D. Werner and S. Hashimoto, "Improved working model for interpreting the excitation wavelength-and fluence-dependent response in pulsed laser-induced size reduction of aqueous gold nanoparticles," *The Journal of Physical Chemistry C*, vol. 115, no. 12, pp. 5063–5072, 2010.

[115] J.-P. Sylvestre, S. Poulin, A. V. Kabashin, E. Sacher, M. Meunier, and J. H. Luong, "Surface chemistry of gold nanoparticles produced by laser ablation in aqueous media," *The Journal of Physical Chemistry B*, vol. 108, no. 43, pp. 16864–16869, 2004.

[116] K. M. Hitomi Muto, Kunihiro Yamada and F. Mafune, "Estimation of surface oxide on surfactant-free gold nanoparticles laser-ablated in water," *J. Phys. Chem. C*, vol. 111, pp. 17221–17226, 2007.

[117] W. T. Nichols, T. Sasaki, and N. Koshizaki, "Laser ablation of a platinum target in water. iii. laser-induced reactions," *Journal of applied physics*, vol. 100, no. 11, p. 114911, 2006.

[118] G. Marzun, H. Bönnemann, C. Lehmann, B. Spliethoff, C. Weidenthaler, and S. Barcikowski, "Role of dissolved and molecular oxygen on cu and ptcu alloy particle structure during laser ablation synthesis in liquids," *ChemPhysChem*, 2017.

[119] T. Simao, D. M. Chevrier, J. Jakobi, A. Korinek, G. Goupil, M. Lau, S. Garbarino, P. Zhang, S. Barcikowski, M.-A. Fortin, *et al.*, "Gold-manganese oxide core-shell nanoparticles produced by pulsed laser ablation in water," *The Journal of Physical Chemistry C*, 2016.

[120] T. Tsuji, T. Hamagami, T. Kawamura, J. Yamaki, and M. Tsuji, "Laser ablation of cobalt and cobalt oxides in liquids: influence of solvent on composition of prepared nanoparticles," *Applied Surface Science*, vol. 243, no. 1, pp. 214–219, 2005.

[121] P. Boyer and M. Meunier, "Modeling solvent influence on growth mechanism of nanoparticles (Au, Co) synthesized by surfactant free laser processes," *The Journal of Physical Chemistry C*, vol. 116, no. 14, pp. 8014–8019, 2012.

[122] G. Cristoforetti, E. Pitzalis, R. Spiniello, R. Ishak, F. Giammanco, M. Muniz-Miranda, and S. Caporali, "Physico-chemical properties of Pd nanoparticles produced by pulsed laser ablation in different organic solvents," *Applied Surface Science*, vol. 258, no. 7, pp. 3289 – 3297, 2012.

[123] B. Gökce, D. D. van't Zand, A. Menéndez-Manjón, and S. Barcikowski, "Ripening kinetics of laser-generated plasmonic nanoparticles in different solvents," *Chemical Physics Letters*, vol. 626, pp. 96–101, 2015.

[124] J. Lam, D. Amans, F. Chaput, M. Diouf, G. Ledoux, N. Mary, K. Masenelli-Varlot, V. Motto-Ros, and C. Dujardin, "γ-Al2O3 nanoparticles synthesised by pulsed laser ablation in liquids: a plasma analysis," *Physical Chemistry Chemical Physics*, vol. 16, no. 3, pp. 963–973, 2014.

[125] G. Maatz, A. Heisterkamp, H. Lubatschowski, S. Barcikowski, C. Fallnich, H. Welling, and W. Ertmer, "Chemical and physical side effects at application of ultrashort laser pulses for intrastromal refractive surgery," *Journal of Optics A: Pure and Applied Optics*, vol. 2, no. 1, p. 59, 2000.

[126] M.-R. Kalus, N. Bärsch, R. Streubel, E. Gökce, S. Barcikowski, and B. Gökce, "How persistent microbubbles shield nanoparticle productivity in laser synthesis of colloids–quantification of their volume, dwell dynamics, and gas composition," *Physical Chemistry Chemical Physics*, vol. 19, no. 10, pp. 7112–7123, 2017.

[127] A. Simakin, V. Voronov, N. Kirichenko, and G. Shafeev, "Nanoparticles produced by laser ablation of solids in liquid environment," *Applied Physics A*, vol. 79, no. 4, pp. 1127–1132, 2004.

[128] G. Cristoforetti, E. Pitzalis, R. Spiniello, R. Ishak, F. Giammanco, M. Muniz-Miranda, and S. Caporali, "Physico-chemical properties of pd nanoparticles produced by pulsed laser ablation in different organic solvents," *Applied Surface Science*, vol. 258, no. 7, pp. 3289 – 3297, 2012.

[129] S. Ibrahimkutty, P. Wagener, T. dos Santos Rolo, D. Karpov, A. Menzel, T. Baumbach, S. Barcikowski, and A. Plech, "A hierarchical view on material formation during pulsed-laser synthesis of nanoparticles in liquid," *Scientific reports*, vol. 5, 2015.

[130] Y.-j. Kim, R. Ma, D. A. Reddy, and T. K. Kim, "Liquid-phase pulsed laser ablation synthesis of graphitized carbon-encapsulated palladium core–shell nanospheres for catalytic reduction of nitrobenzene to aniline," *Applied Surface Science*, vol. 357, pp. 2112–2120, 2015.

[131] A. Ahmadi Daryakenari, D. Hosseini, Y.-L. Ho, T. Saito, A. Apostoluk, C. R. Müller, and J.-J. Delaunay, "Single-step electrophoretic deposition of non-noble metal catalyst layer with low onset voltage for ethanol electro-oxidation," *ACS applied materials & interfaces*, vol. 8, no. 25, pp. 15975–15984, 2016.

[132] M. Fayette, A. Nelson, and R. D. Robinson, "Electrophoretic deposition improves catalytic performance of Co3O4 nanoparticles for oxygen reduction/oxygen evolution reactions," *J. Mater. Chem. A*, vol. 3, pp. 4274–4283, 2015.

[133] J. Gao, C. Jia, J. Li, M. Zhang, F. Gu, G. Xu, Z. Zhong, and F. Su, "Ni/Al2O3 catalysts for {CO} methanation: Effect of Al2O3 supports calcined at different temperatures," *Journal of Energy Chemistry*, vol. 22, no. 6, pp. 919 – 927, 2013.

[134] J. Horiguchi, Y. Kobayashi, S. Kobayashi, Y. Yamazaki, K. Omata, D. Nagao, M. Konno, and M. Yamada, "Mesoporous NiO–Al2O3 catalyst for high pressure partial oxidation of methane to syngas," *Applied Catalysis A: General*, vol. 392, no. 1, pp. 86–92, 2011.

[135] P. Djinovic, J. Batista, and A. Pintar, "Calcination temperature and CuO loading dependence on CuO-CeO 2 catalyst activity for water-gas shift reaction," *Ápplied Catalysis A: General*, vol. 347, no. 1, pp. 23–33, 2008.

[136] H. Lee, S. E. Habas, S. Kweskin, D. Butcher, G. A. Somorjai, and P. Yang, "Morphological control of catalytically active platinum nanocrystals," *Angewandte Chemie*, vol. 118, no. 46, pp. 7988–7992, 2006.

[137] Y. Xia, Y. Xiong, B. Lim, and S. Skrabalak, "Shape-controlled synthesis of metal nanocrystals: Simple chemistry meets complex physics?," *Angewandte Chemie International Edition*, vol. 48, no. 1, pp. 60–103, 2009.

[138] A. Zaleska-Medynska, M. Marchelek, M. Diak, and E. Grabowska, "Noble metal-based bimetallic nanoparticles: the effect of the structure on the optical, catalytic and photocatalytic properties," *Advances in Colloid and Interface Science*, vol. 229, pp. 80 – 107, 2016.

[139] A. De Giacomo, M. Dell'Aglio, A. Santagata, R. Gaudiuso, O. De Pascale, P. Wagener, G. Messina, G. Compagnini, and S. Barcikowski, "Cavitation dynamics of laser ablation of bulk and wire-shaped metals in water during nanoparticles production," *Physical Chemistry Chemical Physics*, vol. 15, no. 9, pp. 3083–3092, 2013.

[140] J. Lam, J. Lombard, C. Dujardin, G. Ledoux, S. Merabia, and D. Amans, "Dynamical study of bubble expansion following laser ablation in liquids," *Applied Physics Letters*, vol. 108, no. 7, 2016.

[141] S. Kohsakowski, B. Gökce, R. Tanabe, P. Wagener, A. Plech, Y. Ito, and S. Barcikowski, "Target geometry and rigidity determines laser-induced cavitation bubble transport and nanoparticle productivity–a high-speed videography study," *Physical Chemistry Chemical Physics*, 2016.

[142] S. L. Horswell, A. L. Pinheiro, E. R. Savinova, M. Danckwerts, B. Pettinger, M.-S. Zei, and G. Ertl, "A comparative study of hydroxide adsorption on the (111),(110), and (100) faces of silver with cyclic voltammetry, ex situ electron diffraction, and in situ second harmonic generation," *Langmuir*, vol. 20, no. 25, pp. 10970–10981, 2004.

[143] G. Ertl, "Reactions at surfaces: From atoms to complexity (nobel lecture)," *Angewandte Chemie International Edition*, vol. 47, no. 19, pp. 3524–3535, 2008.

[144] M. G. Walter, E. L. Warren, J. R. McKone, S. W. Boettcher, Q. Mi, E. A. Santori, and N. S. Lewis, "Solar water splitting cells," *Chemical reviews*, vol. 110, no. 11, pp. 6446–6473, 2010.

[145] N. S. Lewis and D. G. Nocera, "Powering the planet: Chemical challenges in solar energy utilization," *Proceedings of the National Academy of Sciences*, vol. 103, no. 43, pp. 15729–15735, 2006.

[146] O. T. Holton and J. W. Stevenson, "The role of platinum in proton exchange membrane fuel cells," *Platinum Metals Review*, vol. 57, no. 4, pp. 259–271, 2013.

[147] E. Antolini, J. R. Salgado, and E. R. Gonzalez, "The stability of Pt–M (M= first row transition metal) alloy catalysts and its effect on the activity in low temperature fuel cells: a literature review and tests on a Pt–Co catalyst," *Journal of Power Sources*, vol. 160, no. 2, pp. 957–968, 2006.

[148] R. Ferrando, J. Jellinek, and R. L. Johnston, "Nanoalloys: from theory to applications of alloy clusters and nanoparticles," *Chemical reviews*, vol. 108, no. 3, pp. 845–910, 2008.

[149] H. You, S. Yang, B. Ding, and H. Yang, "Synthesis of colloidal metal and metal alloy nanoparticles for electrochemical energy applications," *Chemical Society Reviews*, vol. 42, no. 7, pp. 2880–2904, 2013.

[150] S. Sun, G. Zhang, N. Gauquelin, N. Chen, J. Zhou, S. Yang, W. Chen, X. Meng, D. Geng, M. N. Banis, R. Li, S. Ye, S. Knights, G. A. Botton, T.-K. Sham and X. Sun, "Single-atom catalysis using pt/graphene achieved through atomic layer deposition," *Scientific reports*, vol. 3, 2013.

[151] M. Gustavsson, H. Ekström, P. Hanarp, L. Eurenius, G. Lindbergh, E. Olsson, and B. Kasemo, "Thin film Pt/TiO2 catalysts for the polymer electrolyte fuel cell," *Journal of Power Sources*, vol. 163, no. 2, pp. 671–678, 2007.

[152] C.-J. Zhong and M. M. Maye, "Core–shell assembled nanoparticles as catalysts," *Advanced Materials*, vol. 13, no. 19, pp. 1507–1511, 2001.

[153] K. C. Neyerlin, R. Srivastava, and P. Strasser, "Electrochemical stability of PtCu and ptcuco core-shell oxygen reduction reaction electrocatalysts in liquid electrolyte," *ECS Transactions*, vol. 16, no. 2, pp. 509–514, 2008.

[154] K. Tschulik, K. Ngamchuea, C. Ziegler, M. G. Beier, C. Damm, A. Eychmueller, and R. G. Compton, "Core–shell nanoparticles: Characterizing multifunctional materials beyond imaging—distinguishing and quantifying perfect and broken shells," *Advanced Functional Materials*, vol. 25, no. 32, pp. 5149–5158, 2015.

[155] X. Li, Q. Chen, I. McCue, J. Snyder, P. Crozier, J. Erlebacher, and K. Sieradzki, "Dealloying of noble-metal alloy nanoparticles," *Nano letters*, vol. 14, no. 5, pp. 2569–2577, 2014.

[156] I. Dutta, M. K. Carpenter, M. P. Balogh, J. M. Ziegelbauer, T. E. Moylan, M. H. Atwan, and N. P. Irish, "Electrochemical and structural study of a chemically dealloyed PtCu oxygen reduction catalyst," *The journal of physical chemistry. C, Nanomaterials and interfaces*, vol. 114, no. 39, p. 16309, 2010.

[157] J. Erlebacher, M. J. Aziz, A. Karma, N. Dimitrov, and K. Sieradzki, "Evolution of nanoporosity in dealloying," *Nature*, vol. 410, no. 6827, pp. 450–453, 2001.

[158] B. P. Vinayan, R. Nagar, N. Rajalakshmi, and S. Ramaprabhu, "Novel platinum–cobalt alloy nanoparticles dispersed on nitrogen-doped graphene as a cathode electrocatalyst for pemfc applications," *Advanced Functional Materials*, vol. 22, no. 16, pp. 3519–3526, 2012.

[159] D. Susac, A. Sode, L. Zhu, P. Wong, M. Teo, D. Bizzotto, K. Mitchell, R. Parsons, and S. Campbell, "A methodology for investigating new nonprecious metal catalysts for PEM fuel cells," *The Journal of Physical Chemistry B*, vol. 110, no. 22, pp. 10762–10770, 2006.

[160] V. Stamenkovic, B. S. Mun, K. J. Mayrhofer, P. N. Ross, N. M. Markovic, J. Rossmeisl, J. Greeley, and J. K. Nørskov, "Changing the activity of electrocatalysts for oxygen reduction by tuning the surface electronic structure," *Angewandte Chemie*, vol. 118, no. 18, pp. 2963–2967, 2006.

[161] V. R. Stamenkovic, B. S. Mun, M. Arenz, K. J. Mayrhofer, C. A. Lucas, G. Wang, P. N. Ross, and N. M. Markovic, "Trends in electrocatalysis on extended and nanoscale Pt-bimetallic alloy surfaces," *Nature materials*, vol. 6, no. 3, pp. 241–247, 2007.

[162] C. Cui, L. Gan, H.-H. Li, S.-H. Yu, M. Heggen, and P. Strasser, "Octahedral PtNi nanoparticle catalysts: exceptional oxygen reduction activity by tuning the alloy particle surface composition," *Nano letters*, vol. 12, no. 11, pp. 5885–5889, 2012.

[163] C. Cui, L. Gan, M. Heggen, S. Rudi, and P. Strasser, "Compositional segregation in shaped Pt alloy nanoparticles and their structural behaviour during electrocatalysis," *Nature materials*, vol. 12, no. 8, pp. 765–771, 2013.

[164] X. Tan, S. Prabhudev, A. Kohandehghan, D. Karpuzov, G. A. Botton, and D. Mitlin, "Pt–Au–Co alloy electrocatalysts demonstrating enhanced activity and durability toward the oxygen reduction reaction," *Acs Catalysis*, vol. 5, no. 3, pp. 1513–1524, 2015.

[165] K. Neyerlin, R. Srivastava, C. Yu, and P. Strasser, "Electrochemical activity and stability of dealloyed Pt–Cu and Pt–Cu–Co electrocatalysts for the oxygen reduction reaction (orr)," *Journal of Power Sources*, vol. 186, no. 2, pp. 261–267, 2009.

[166] P. Mani, R. Srivastava, and P. Strasser, "Dealloyed binary PtM3 (M= Cu, Co, Ni) and ternary PtNi3M (M= Cu, Co, Fe, Cr) electrocatalysts for the oxygen reduction reaction: performance in polymer electrolyte membrane fuel cells," *Journal of Power Sources*, vol. 196, no. 2, pp. 666–673, 2011.

[167] S. Hu, M. Tian, E. L. Ribeiro, G. Duscher, and D. Mukherjee, "Tandem laser ablation synthesis in solution-galvanic replacement reaction (lasis-GRR) for the production of ptco nanoalloys as oxygen reduction electrocatalysts," *Journal of Power Sources*, vol. 306, pp. 413–423, 2016.

[168] V. Amendola, S. Scaramuzza, F. Carraro, and E. Cattaruzza, "Formation of alloy nanoparticles by laser ablation of Au/Fe multilayer films in liquid environment," *Journal of Colloid and Interface Science*, pp. –, 2016.

[169] A. Simakin, V. Voronov, N. Kirichenko, and G. Shafeev, "Nanoparticles produced by laser ablation of solids in liquid environment," *Applied Physics A: Materials Science & Processing*, vol. 79, no. 4, pp. 1127–1132, 2004.

[170] S. Hu, K. Cheng, E. L. Ribeiro, K. Park, B. Khomami, and D. Mukherjee, "A facile and surfactant-free route for nanomanufacturing of tailored ternary nanoalloys as superior oxygen reduction reaction electrocatalysts," *Catalysis Science & Technology*, vol. 7, no. 10, pp. 2074–2086, 2017.

[171] B. Hammer and J. K. Nørskov, "Theoretical surface science and catalysis-calculations and concepts," *Advances in catalysis*, vol. 45, pp. 71–129, 2000.

[172] Z. Duan and G. Wang, "A first principles study of oxygen reduction reaction on a pt (111) surface modified by a subsurface transition metal M (M= Ni, Co, or Fe)," *Physical Chemistry Chemical Physics*, vol. 13, no. 45, pp. 20178–20187, 2011.

[173] Z. Peng and H. Yang, "Ag–pt alloy nanoparticles with the compositions in the miscibility gap," *Journal of Solid State Chemistry*, vol. 181, no. 7, pp. 1546–1551, 2008.

[174] J. Luo, M. M. Maye, V. Petkov, N. N. Kariuki, L. Wang, P. Njoki, D. Mott, Y. Lin, and C.-J. Zhong, "Phase properties of carbon-supported gold-platinum nanoparticles with different bimetallic compositions," *Chemistry of materials*, vol. 17, no. 12, pp. 3086–3091, 2005.

[175] I.-C. Chiang and D.-H. Chen, "Synthesis of monodisperse feau nanoparticles with tunable magnetic and optical properties," *Advanced Functional Materials*, vol. 17, no. 8, pp. 1311–1316, 2007.

[176] C. W. Hills, N. H. Mack, and R. G. Nuzzo, "The size-dependent structural phase behaviors of supported bimetallic (Pt-Ru) nanoparticles," *The Journal of Physical Chemistry B*, vol. 107, no. 12, pp. 2626–2636, 2003.

[177] K. M. Yeo, S. Choi, R. M. Anisur, J. Kim, and I. S. Lee, "Surfactant-free platinum-on-gold nanodendrites with enhanced catalytic performance for oxygen reduction," *Angewandte Chemie International Edition*, vol. 50, no. 3, pp. 745–748, 2011.

[178] S. Xiao, W. Hu, W. Luo, Y. Wu, X. Li, and H. Deng, "Size effect on alloying ability and phase stability of immiscible bimetallic nanoparticles," *The European Physical Journal B-Condensed Matter and Complex Systems*, vol. 54, no. 4, pp. 479–484, 2006.

[179] J. M. Martinez De La Hoz, R. Callejas Tovar, and P. B. Balbuena, "Size effect on the stability of Cu–Ag nanoalloys," *Molecular Simulation*, vol. 35, no. 10-11, pp. 785–794, 2009.

[180] W. Qi, B. Huang, and M. Wang, "Size and shape-dependent formation enthalpy of binary alloy nanoparticles," *Physica B: Condensed Matter*, vol. 404, no. 12, pp. 1761–1765, 2009.

[181] J. K. Nørskov, J. Rossmeisl, A. Logadottir, L. Lindqvist, J. R. Kitchin, T. Bligaard, and H. Jonsson, "Origin of the overpotential for oxygen reduction at a fuel-cell cathode," *The Journal of Physical Chemistry B*, vol. 108, no. 46, pp. 17886–17892, 2004.

[182] B. M. Hunter, W. Hieringer, J. Winkler, H. Gray, and A. Müller, "Effect of interlayer anions on [NiFe]-LDH nanosheet water oxidation activity," *Energy & Environmental Science*, vol. 9, no. 5, pp. 1734–1743, 2016.

[183] A. Letzel, B. Go?kce, P. Wagener, S. Ibrahimkutty, A. Menzel, A. Plech, and S. Barcikowski, "Size quenching during laser synthesis of colloids happens already in the vapor phase of the cavitation bubble," *The Journal of Physical Chemistry C*, vol. 121, no. 9, pp. 5356–5365, 2017.

[184] S. Hu, G. Goenaga, C. Melton, T. A. Zawodzinski, and D. Mukherjee, "PtCo/CoOx nanocomposites: Bifunctional electrocatalysts for oxygen reduction and evolution reactions synthesized via tandem laser ablation synthesis in solution-galvanic replacement reactions," *Applied Catalysis B: Environmental*, vol. 182, pp. 286–296, 2016.

[185] M. S. I. Sarker, T. Nakamura, and S. Sato, "Composition-controlled ternary Rh–Pd–Pt solid-solution alloy nanoparticles by laser irradiation of mixed solution of metallic ions," *Journal of Materials Research*, vol. 29, no. 07, pp. 856–864, 2014.

[186] N. Mottaghi, M. Ranjbar, H. Farrokhpour, M. Khoshouei, A. Khoshouei, P. Kameli, H. Salamati, M. Tabrizchi, and M. Jalilian-Nosrati, "Ag/Pd core-shell nanoparticles by a successive method: Pulsed laser ablation of ag in water and reduction reaction of PdCl2," *Applied Surface Science*, vol. 292, pp. 892 – 897, 2014.

[187] H. Zhang, C. Liang, J. Liu, Z. Tian, and G. Shao, "The formation of onion-like carbon-encapsulated cobalt carbide core/shell nanoparticles by the laser ablation of metallic cobalt in acetone," *Carbon*, vol. 55, pp. 108–115, 2013.

[188] V. Amendola, G. A. Rizzi, S. Polizzi, and M. Meneghetti, "Synthesis of gold nanoparticles by laser ablation in toluene: quenching and recovery of the surface plasmon absorption," *The Journal of Physical Chemistry B*, vol. 109, no. 49, pp. 23125–23128, 2005.

[189] V. Amendola, S. Polizzi, and M. Meneghetti, "Laser ablation synthesis of silver nanoparticles embedded in graphitic carbon matrix," *Science of Advanced Materials*, vol. 4, no. 3-4, pp. 497–500, 2012.

[190] Y. Cheng, Y. Fan, Y. Pei, and M. Qiao, "Graphene-supported metal/metal oxide nanohybrids: synthesis and applications in heterogeneous catalysis," *Catal. Sci. Technol.*, vol. 5, pp. 3903–3916, 2015.

[191] S. M. Kim, S. W. Lee, S. Y. Moon, and J. Y. Park, "The effect of hot electrons and surface plasmons on heterogeneous catalysis," *Journal of Physics: Condensed Matter*, vol. 28, no. 25, p. 254002, 2016.

[192] J. Jakobi, A. Menéndez-Manjón, V. S. K. Chakravadhanula, L. Kienle, P. Wagener, and S. Barcikowski, "Stoichiometry of alloy nanoparticles from laser ablation of ptir in acetone and their electrophoretic deposition on ptir electrodes," *Nanotechnology*, vol. 22, no. 14, p. 145601, 2011.

[193] W. Guo and B. Liu, "Liquid-phase pulsed laser ablation and electrophoretic deposition for chalcopyrite thin-film solar cell application," *ACS applied materials & interfaces*, vol. 4, no. 12, pp. 7036–7042, 2012.

[194] S.-Q. Zhu, T. Zhang, X.-L. Guo, Q.-L. Wang, X. Liu, and X.-Y. Zhang, "Gold nanoparticle thin films fabricated by electrophoretic deposition method for highly sensitive sers application," *Nanoscale Research Letters*, vol. 7, no. 1, p. 613, 2012.

[195] S. Koenen, R. Streubel, J. Jakobi, K. Schwabe, J. K. Krauss, and S. Barcikowski, "Continuous electrophoretic deposition and electrophoretic mobility of ligand-free, metal nanoparticles in liquid flow," *Journal of The Electrochemical Society*, vol. 162, no. 4, pp. D174–D179, 2015.

[196] T. N. Kunihiro Yamada, Yuki Tokumoto and F. Mafune, "Mechanism of laser-induced size-reduction of gold nanoparticles as studied by nanosecond transient absorption spectroscopy," *J. Phys. Chem. B*, vol. 110, pp. 11751–11756, 2006.

[197] S. D. Perera, X. Ding, A. Bhargava, R. Hovden, A. Nelson, L. F. Kourkoutis, and R. D. Robinson, "Enhanced supercapacitor performance for equal Co–Mn stoichiometry in colloidal Co3-xMn x O4 nanoparticles, in additive-free electrodes," *Chemistry of Materials*, vol. 27, no. 23, pp. 7861–7873, 2015.

[198] S. B. Simonsen, I. Chorkendorff, S. Dahl, M. Skoglundh, J. Sehested, and S. Helveg, "Direct observations of oxygen-induced platinum nanoparticle ripening studied by in situ TEM," *Journal of the American Chemical Society*, vol. 132, no. 23, pp. 7968–7975, 2010.

2. Aims and objectives

The objective of this thesis is to investigate the suitability and usability of laser-generated nanoparticles as a catalyst for several applications – for example, electrocatalytic reactions such as hydrogen and oxygen evolution (HER, OER) as well as oxygen reduction reaction (ORR). Hereby, several aspects starting from a fundamental understanding of the surface properties of the particles up to a functional proof for application-oriented research must be addressed.

In previous work, it was shown that ligand-free nanoparticles have higher catalytic activities than ligand-covered ones; this was attributed to the unhindered accessibility of the particles' surfaces by reactants. However, it is not clear whether laser-generated nanoparticles differ in their properties from wet-chemically synthesised ones – regardless of their surface coverage with ligands. Thus, research is needed to determine whether other reasons can lead to these distinguishing activities by analysing and comparing the particles' surfaces. Consequently, the features of ligand-free – compared to ligand-covered – nanoparticles, which are synthesized by laser ablation in liquids and by a wet-chemical method, need to be examined in detail by surface sensitive analyses, such as *in-situ* x-ray absorption spectroscopy. Since the quantitative removal of ligands or other surfactants on wet-chemically synthesized nanoparticles is impossible without altering the particles' properties (i.e., their size), no differentiated investigations regarding the parameters that influence the particles' surfaces have been feasible so far. Hence, the main goal of the first part of this thesis is to study the nature of the particles' surfaces by investigating the interaction of additives independent of the size distribution or morphology of the particles. Starting from bare surfaces and the same batch, a subsequent functionalisation enables independent studies on the impact of ions and ligands on the particle surfaces.

In view of profitability for future applications, the use of alloys is promising to reduce the demand for noble metals, such as platinum. In the field of PLAL, current research has not yet sufficiently advanced to answer the question of whether this method is suitable to synthesize catalytically active alloy nanoparticles with less noble yet still catalytically relevant metals, such as copper, nickel or molybdenum. Thus, this thesis aims to explore the possibility to form laser-synthesized alloy nanoparticles, to identify the influencing parameter on alloy formation as well as to investigate the properties of noble and less noble metal nanoparticles related to their electrocatalytic relevance. Moreover, the objective is to develop an effective and efficient method to synthesize ligand-free alloy nanoparticles by taking advantage of a novel route that combines consolidated micro-powder-targets and high laser power.

In heterogeneous catalysis, nanoparticles must be deposited on carrier material to ensure their stability and to enhance their activity. The interaction of nanoparticles with supports can be based on several interactions (e.g., Coulomb attractive forces, van der Waals forces, adhesion on oxygen vacancies). Electrostatic interactions are strongly influenced by colloidal properties such as pH, ionic strength and the use of ligands. In order to independently identify the influencing factors, the aim of the last part of this study is to investigate the driving force of the colloidal adsorption of laser-generated nanoparticles on supports and to evaluate the determining factor in a systematic study that benefits from ligand-free surfaces. The stability of the prepared catalysts will be evaluated in order to assess their applicability in catalysis.

3. Analytical instruments

In Table 1 the main characterisation methods including their parameter used in the present studies are summarized. For a better clarity the specific materials and methods are described in in the related section called “Experimental” of each chapter.

Table 1: Overview of the analytical instruments with its details and application.

Instrument	**Manufacture**	**Model**	**Specification**	**Application**
Laser	Edgewave	IS400-1-L INNOSLAB	Nd:YAG laser; λ=1064 nm, τ=8 ns, P=27.5 W, 5 kHz	Nanoparticle synthesis by PLAL
	Rofin-Sinar	RS-Marker D100	Nd:YAG laser; λ=1064 nm, τ=10 ns, P=32 W, 5 kHz	Nanoparticle synthesis by PLAL
Power meter	Gentec EO, Inc.	UP25N-250F-H12-DO	< 250 W	Detection of laser power
Profilometer	Coherent	LaserCam-HR	USB 2.0, Software: BeamView^{TM}-USB	Detection of laser beam profile
UV-Vis spectrometer	Thermo Scientific	Evolution 201	λ=190-900 nm, 1 cm pathway cuvette	Extinction analysis of colloids
Fiber UV-Vis spectrometer	Agilent	Cary 6000	λ=200-900 nm, 0.5 cm pathway cuvette	Extinction analysis of the oxygen-free colloid
pH meter	PCE Instruments	PCE-PHD 1		pH setting for particle adsorption
Particle size and potential analyser	Malvern Instruments	Zetasizer ZS90	0.3nm-10 µm, λ=622.8 nm, Hückel-regime	Analysis of zeta potential and hydrodynamic particle size
Analytical disc centrifuge	CPS Instruments	DC 24000	N_{max}=24000 RPM, d_{NP}>3 nm, λ=405 nm,	Determination of particle size distribution
Benchtop centrifuge	Hettich	Universal 320	Nmax=18.000 RPM (2 ml); Nmax=5.000 RPM (50 ml)	Nanoparticle size separation by centrifugation
Scanning electron microscope (SEM)	FEI	ESEM Quanta 400 FEG	Equipped with EDS detector (Quantax 70)	Structural and elemental analysis of the alloy targets

Table 2: Overview of the analytical instruments with its details and application.

Instrument	**Manufacture**	**Model**	**Specification**	**Application**
Transmission electron microscope (TEM)	FEI	Tecnai F20	Acceleration voltage: 200 kV	Determination of particle size and distribution on supports
	JEOL	JEOL 2200FS	Acceleration voltage: 200 kV; with EDS detector type SSD X-MaxN 80 TLE	Determination of particle size, distribution on supports as well as elemental analysis
	Hitachi	HF2000	Acceleration voltage: 200 kV; with EDS detector type Si(Li) Noran Instruments	Determination of particle size, distribution on supports and, elemental analysis
	Philips	Philips CM12	Acceleration voltage: 120 kV	Determination of particle size as well as distribution on supports
Scanning electron microscope (SEM)	FEI	ESEM Quanta 400 FEG	Equipped with EDS detector (Quantax 70)	Structural and elemental analysis of the alloy targets
X-ray photoelectron spectroscope (XPS)	Physical Electronics	ULVAC-PHI VersaProbe II	Al Kα X-ray source	Surface analysis of oxidation state
XRD	Panalytical	X'Pert Pro	with grazing incidence, graphite monochromator, CuK_{α} radiation	Phase analysis of nanoparticles and targets
	STOE & Cie GmbH	Stoe STADI P	Transmission diffractometer, Ge(111) monochromator, MoK_{α} radiation	Quantitative phase analysis of colloids
Potentiostat	Princeton Applied Research	VersaSTAT F3	scan rate: 100 mV/s potential range: -0.9 – 0.75 V NP loading/ electrode surface: 5.52 µg/cm^2	Electrochemical analysis: surface characterization and catalytic activity

4. Laser-induced surface properties on precious and non-perecious metal nanoparticles

The surface properties of a heterogeneous catalyst are most important factors that influence the conversion, selectivity and kinetics of catalytical reactions[1]. Hereby, the accessibility of the surface by the reactants is mandatory. Hence, ligand-free, laser-generated nanoparticles possess an aspiring potential for any application, where pure nanomaterials are essential. As described in chapter 1, the importance of pure particle surfaces has been previously demonstrated in the literature[2], [3], [4], [5]. When comparing experiment and theory for a kinetic modelling reaction, excellent matching has been found for laser-generated ligand-free nanoparticles, where wet-chemically produced particles did not behave as predicted[3], [6]. So far, it is not fully understood whether the particles only differ by the absence of ligands or if other properties play a role as well. Therefore, deeper scientific research and study on the nature of their surfaces is needed.
Hence, the following chapter describes the surface structure of laser-generated nanoparticles that have been intensively studied by several methods. The surface of laser-generated noble nanoparticles was investigated by conducting XPS of dried samples and showed a positive surface charge due to partial oxidation[7]. The zetapotential of these colloidal particles exhibit negative potentials at pH ≥ 3. Therefore, the Pt-O^- and Pt-OH groups are likely present on the surface of laser-generated nanoparticles surrounded by counter-ion adsorption in aqueous solution, and they may be influenced by other ions and ligands as well. However, a clear evidence of the particle surface oxidation present in their colloidal native state is missing; also, investigations of their surface properties after deposition on a support are needed.

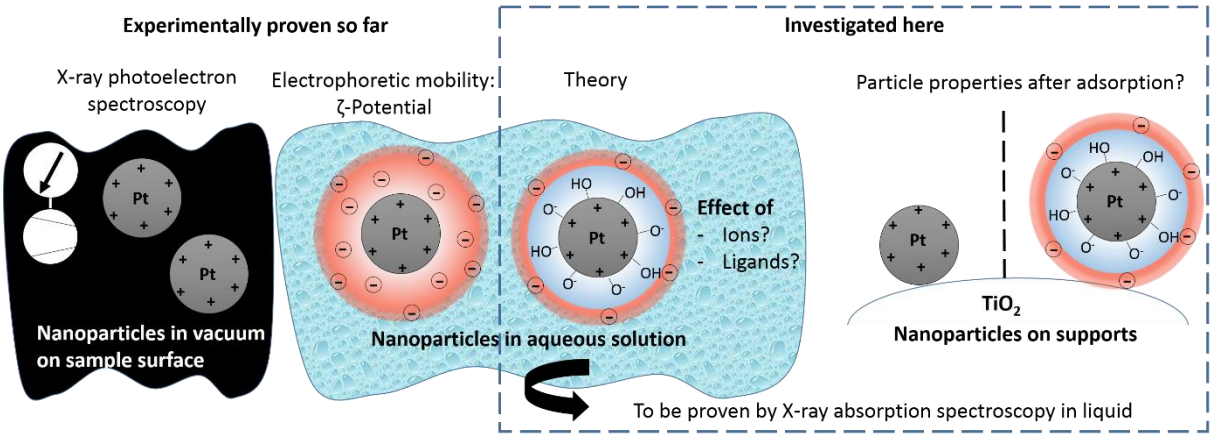

Fig. A1: Schematic illustration of the issues concerning the electronic structure of particles, showing that surface oxidation and anion adsorption were proven indirectly, while a direct proof by an *in-situ* method such as X-ray absorption spectroscopy is missing.

In the first part of this thesis results (section 4.1), colloidal platinum nanoparticles will be investigated by X-ray absorption spectroscopy in their original state. The interaction between laser-synthesized nanoparticles and additives such as ions, ligands and an oxide support material will be examined and compared with the surface of wet-chemically synthesized particles. Based on the electronic structure of the particles' surfaces, conclusions about the impact of the surrounding media will be given. It will be shown that a significant influence can be exerted on the electronic structure by ions and ligands, while the particle properties remain unaltered after adsorption on a support. A comparison of these nanoparticles with wet-chemically synthesized ones implies different types of Pt-O bonds.

In section 4.2, the particle surface will be considered from a different perspective. The origin of the surface oxidation of laser-generated nanoparticles will be studied. Hereby, the main focus of the catalyst development is set on the role of dissolved molecular oxygen and of oxygen bound in solvent molecules on the particle oxidation during laser processing.

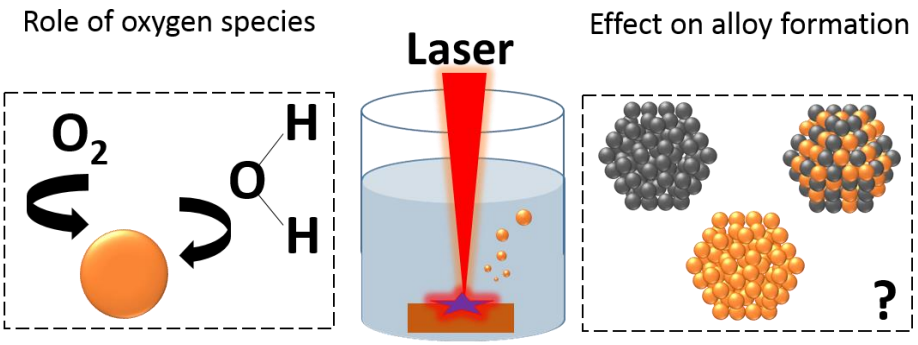

Fig A2: Schematic illustration of the questions concerning the role of oxygen on particle oxidation and alloy formation.

The investigations are conducted in acetone, air-saturated and oxygen-free water in order to differentiate the influence of oxygen species on the nanoparticle properties and formation mechanism. Although ignoble metals maintain a major role in catalysis, very few studies on the surface finish of metals that are sensitive to oxidation have been conducted in the research area of PLAL. Furthermore, since compared to pure Pt, bimetallic Pt catalysts using transition metals like Cu, Mo, Ni are known to exhibit higher economic efficiencies, the impact of the solvent properties on the synthesis of Cu and $PtCu_3$ alloy nanoparticles will be studied. The findings show a distinctive influence of the oxygen bound in water molecules on the surface oxidation. A remarkable impact of the solvent on alloy formation will be demonstrated.

Literature

[1] F. Schüth, "Heterogene Katalyse," *Chem. Unserer Zeit*, vol. 40, pp. 92–103, **2006**.

[2] H. Zhang, C. Liang, J. Liu, Z. Tian, and G. Shao, "The formation of onion-like carbon-encapsulated cobalt carbide core/shell nanoparticles by the laser ablation of metallic cobalt in acetone," *Carbon*, vol. 55, pp. 108–115, **2013**.

[3] S. Gu, J. Kaiser, G. Marzun, A. Ott, Y. Lu, M. Ballauff, A. Zaccone, S. Barcikowski, and P. Wagener, "Ligand-free gold nanoparticles as a reference material for kinetic modelling of catalytic reduction of 4-nitrophenol," *Catalysis Letters*, vol. 145, no. 5, pp. 1105–**1112**, **2015**.

[4] P. Wagener, A. Schwenke, and S. Barcikowski, "How citrate ligands affect nanoparticle adsorption to microparticle supports," *Langmuir*, vol. 28, no. 14, pp. 6132–6140, **2012**.

[5] J. Zhang, M. Chaker, and D. Ma, "Pulsed laser ablation based synthesis of colloidal metal nanoparticles for catalytic applications," *Journal of Colloid and Interface Science*, vol. 489, pp. 138–149, **2017**.

[6] S. Gu, S. Wunder, Y. Lu, and M. Ballauff, "Kinetic analysis of the catalytic reduction of 4-nitrophenol by metallic nanoparticles," *J. Phys. Chem. C*, vol. submitted, **2014**.

[7] D. Zhang, B. Goekce, and S. Barcikowski, "Laser synthesis and processing of colloids: fundamentals and applications," *Chemical Reviews*, vol. 117, no. 5, pp. 3990–4103, **2017**.

4.1. In situ investigations of laser-generated ligand-free platinum nanoparticles by x-ray absorption spectroscopy: How does the immediate environment influence the particle surface?

Reprinted with permission from Langmuir 32, Mathias Fischer, Josef Hormes, Galina Marzun, Philipp Wagener, Ulrich Hagemann, Stephan Barcikowski, "In situ investigations of laser-generated ligand-free platinum nanoparticles by x-ray absorption spectroscopy: How does the immediate environment influence the particle surface?" 8793-8802, 2016. *Copyright 2016 American Chemical Society*.

IV

Abstract

Pulsed laser ablation in liquid (PLAL) has proven its usefulness as a nanoparticle (NP) synthesis method alternative to traditional chemical reduction methods, where the absence of any molecular ligands or residual reactants makes laser-generated nanoparticles ideal reference materials for charge transfer experiments.

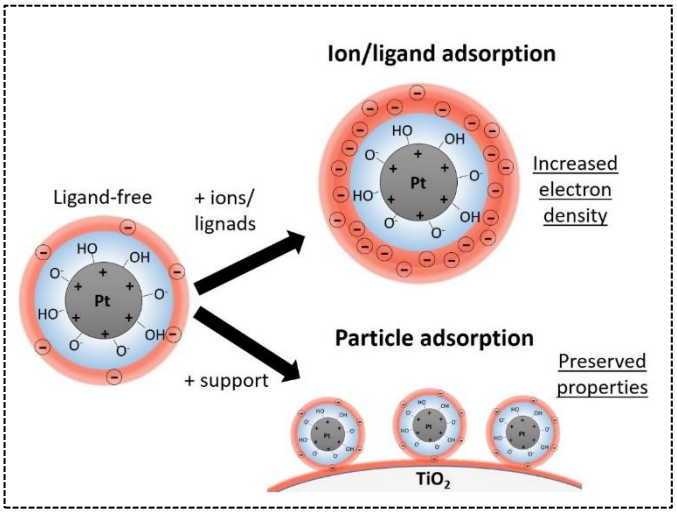

We synthesized additive-free platinum nanoparticles by PLAL and characterized *in situ* their interaction with H_2O, a sodium phosphate buffer and sodium citrate as well as a TiO_2 support by x-ray absorption fine structure (XAFS), i.e. x-ray absorption near-edge structure (XANES) and extended x-ray absorption fine structure (EXAFS). Differences in whiteline intensity between the colloidal particles in the three liquids indicate that the respective NP-solvent interaction varies in strength. The ions added *ex situ* diffuse through the particles' electric double layer and interact electrostatically with the Stern plane. Consequently, these ions weaken the interaction of the functional OH-groups which are bound to the partially oxidized platinum surfaces and cause their partial reduction. Comparing XAFS spectra of laser-generated Pt NPs in citrate with wet-chemically synthesized ones (both ligand-covered) indicate different types of Pt-O-bonds: a $Pt(IV)O_2$-type in case of wet-chemical and a Pt(II)O-type in case of laser-generated NPs. A comparison of unsupported laser-generated platinum NPs in H_2O with TiO_2-supported ones shows no whiteline intensity differences and also an identical number of Pt-O bonds in both cases. This suggests that in the deposition process at least part of the double layer coating stays intact and that the ligand-free particle properties are preserved.

1. Introduction

Metal and semiconductor nanoparticles were given considerable attention in the last decades in various fields like biology, chemistry and material science. They find application e.g. as markers [1], catalysts [2] or gas sensors [3]. Compared to their bulk counterpart they have the advantage of a much higher surface-to-volume ratio and for small particles a high number of step, edge and corner sites which lead, for example, to a higher catalytic activity [2]. Their reduced size is accompanied by an altered electronic structure of atoms in the outermost layers due to under-coordination which gives nanoparticles physico-chemical properties different from bulk, leading to e.g. advanced catalytic effects. Further examples are adsorption behaviour [4] and the quantum size effect [5]. Yet, this higher surface-to-volume ratio also makes nanoparticles prone to aggregation and growth which ultimately decreases said ratio. To prevent unwanted aggregation nanoparticles are either "anchored" to supports [6], [7] or coated with a surfactant layer to provide steric or electro-sterical stabilization [8]. Especially latter has a major impact on the macroscopic properties of nanoparticles, e.g. their magnetic properties [9]. These properties can now be tailored to a given application using traditional wet-chemical synthesis routes by choosing an appropriate stabilizer. Yet, there is a downside when this protective coating has to be removed. A complete removal is very difficult when conventional chemical synthesis routes were used even if extensive "purification steps" are applied [10]. Moreover, these additional procedures bear the risk of unwanted particle growth [11].

In contrast to this, pulsed laser ablation in liquid (PLAL) is a novel route to produce additive-free and colloidal stable nanoparticles without the necessity for any post-synthesis treatment. Hereby a target gets immersed in an organic or inorganic solution [12 - 14]. NP formation then gets initiated by absorption of a pulsed laser beam hitting the target. Advantages of this compared to other techniques are e.g. the facile variation of chemical compositions of NPs that can be synthesized via PLAL and that the products are ligand-free. In particular, PLAL gives access to purely electrostatically stabilized NPs in water without any electro-sterically or sterically effective surface adsorbates. The term "ligand-free" is used here to differentiate the interaction of NPs generated by PLAL with their immediate environment from those generated wet-chemically. The surface of latter is usually covered by various additives such as ligands, surfactants or ions. A disadvantage being that no accurate investigations regarding the influence of nanoparticle functionalization on their properties were possible so far. Surely by wet-chemical methods ligands can be applied on particle surfaces selectively, however the problem

with wet-chemical synthesis routes is that ligands always change particle properties such as size. PLAL now enables such investigations by generating ligand-free nanoparticles. Their surfaces in an aqueous solution are partially oxidized which is an inherent characteristic of this synthesis technique. This was shown by x-ray photoelectron spectroscopy (XPS) analysis [15 - 17]. The surface charge is overcompensated by adsorption of negative ions as described by the Stern model [16]. Here, particles have an electrical double layer consisting of a stationary one with ions adsorbed on the particle surface surrounded by a diffuse layer where ions are loosely attached. Latter can be described as a dynamical shell due to the thermal motions of the ions [18]. This double layer is formed in order to neutralize the surface charge. Thus, the electric potential decreases linearly from the particle surface to outside of the immobile Stern plane. It then decays exponentially to zero through the diffuse layer. The zeta potential is defined as the electrokinetic potential at the shear plane and is determined by the electrophoretic mobility of the particles [19]. Since nanoparticle agglomeration is prevented due to electrostatic repulsion the zeta potential is commonly used to determine particle stability.

To investigate the influence of various ions and ligands on the particles' surfaces we can synthesize colloidal nanoparticles just in water without using any additives and treat the particles in a subsequent step with no impact on size but just on their surface character. Also: *in situ* or *ex situ* functionalization is possible directly onto ligand-free NP surfaces. Since those are always "shielded" by a layer of stabilizing molecules in case of wet-chemical synthesis routes this is the major advantage of laser-generated particles. For more information about NP formation mechanisms, examples of products as well as strengths and limitations of this synthesis technique see e.g. [12 - 14].

In this paper we are trying to answer three questions of fundamental importance for a better understanding of laser-generated nanoparticles and their potential practical applications:

- What is the influence of various additives such as ions and ligands on the electronic and geometric structure of NPs?
- Are there significant differences in the surface properties of laser-generated NPs as compared to those wet-chemically synthesized?
- How do NPs interact with a typical support such as TiO_2?

To address those questions we synthesized additive-free platinum nanoparticles (Pt NPs) via pulsed laser ablation and characterized their solvent-interaction in water by means of x-ray absorption spectroscopy. To examine if this interaction is altered by different ions, sodium citrate and sodium phosphate were added separately. Furthermore, the potential impact of depositing Pt NPs onto TiO_2 NPs on their electronic/geometric structure was studied. In order

to investigate potential differences, all results are compared to unsupported and TiO_2-supported Pt NPs which were synthesized wet-chemically.

So far, XPS and zeta potential measurements were conducted to gain information about the particle-solvent interaction of laser-generated nanoparticles [17]. Former gives information about charge density directly at the particle surfaces (oxidation states of surface atoms, qualitatively and quantitatively); latter is used to determine the potential in the diffuse layer but is "relatively insensitive to specific ion adsorption at the fixed stern layer" [17]. In this study, x-ray absorption spectroscopy (XAS) was applied to gain additional information about the NP surface-solvent as well as -support interaction. XAS has the main advantage of being the only technique with which the electronic and geometric structure of a given element in a sample can be examined simultaneously *in situ* (particles in their common environment). While both, XPS and XANES, are element-specific latter is also sensitive to the specific bonding environment of the element of interest. In general, EXAFS gives information about type, number and distance of neighbouring atoms and for at least small NPs also information about atoms bound to the NP surfaces.

XAS analysis of wet-chemically synthesized ligand-free nanoparticles (e.g. FePt [20]) and cluster (e.g. NiFe [21]) was done by several researchers. However, this is the first time, to the best of our knowledge, that laser-generated ligand-free nanoparticles were characterized *in situ* in their native liquid environment. XAS enables investigations of colloidal particle surfaces in their original state without affecting them due to drying methods, which is usually carried out for other surface-sensitive techniques such as XPS.

1. Experimental section

1.1.Synthesis

Ligand-free Pt nanoparticles were synthesized by pulsed laser ablation of a Pt target (99.99%, Alfa Aesar) in Milli-Q water (Millipore). Details of this process are described e.g. in [22]. Smaller particle sizes increase XAFS sensitivity for surface-related effects due to a higher relative number of surface atoms contributing to the XAFS signal. To remove particles > 10nm, 25ml of the colloidal solution were centrifuged at 5000rpm for 4h using a Hettich320 centrifuge (for more information explaining why particles below 10nm were used see supporting information). Subsequently, the solution was split into three parts. To one part sodium citrate and to another one sodium phosphate buffer (pH 7, both Sigma Aldrich) was added up to a concentration of 0.1mM each. In case of latter an equilibrium between dihydrogen and

hydrogen phosphate ($H_2PO_4^-$/ HPO_4^{2-}) is present. For clarity's sake it will be addressed as "phosphate" henceforth. The addition of citrate or phosphate was done *ex situ*, i.e. after particle synthesis by PLAL, to guarantee a uniform particle size distribution among the three samples. Both stabilizers interact with the Pt NP surfaces, increasing its negative surface charge compared to H_2O thus providing for a higher stability against aggregation through electrostatic repulsion [22, 23]. In addition, Pt NPs were deposited on commercial anatase TiO_2 nanoparticles (HOMBIKAT Type II, Sachtleben, [24]) based on a procedure reported previously [22]. In brief, after TiO_2 was re-dispersed in Milli-Q water Pt NPs suspended in H_2O were added dropwise until a loading of 2wt-% was achieved and the mixture shaken for 20 minutes. After storing it overnight the mixture sedimented. The clear supernatant was removed and the sediment dried at 50°C.

For comparison with corresponding laser-generated samples wet-chemically synthesized unsupported as well as TiO_2-supported Pt NPs (co-doped with 1at-% Ta and 3at-% Nb) were synthesized by Wang et al. - former without an additional stabilizer. Complete synthesis details as well as some of the properties of these materials are given in the corresponding publication[25].

1.2.Experimental

1.2.1. TEM

Particle size distributions were determined by transmission electron microscopy (TEM) using a Philipps CM12 with a LaB_6 cathode at 120kV operating acceleration voltage. Analyses were performed after the colloid was dropped on a carbon-coated copper grid and dried in air at room temperature.

1.2.2. UV/vis extinction spectroscopy

Extinction measurements were carried out to determine the adsorption efficiency of Pt onto TiO_2 NPs via UV/vis (ultraviolet/visible) spectroscopy. A Thermo Scientific Evolution 201 was used in the spectral range between 190-900nm and a glass cuvette with a 10mm path length for the samples. First, Pt NPs in H_2O were measured. After adding the TiO_2 solution the colloid changed its colour. Subsequent to sedimentation the clear supernatant was measured. Since the concentration of freestanding Pt nanoparticles is proportional to the absorption band at 300 nm [26, 27], the adsorption efficiency of Pt NPs onto the TiO_2 support was calculated using this point before (Pt colloid) and after (supernatant) adding TiO_2 to the colloid. For more detailed information regarding this procedure see e.g. [22].

1.2.3. XPS

The colloid was dropped on a Si wafer and dried in air. X-ray photoelectron spectroscopy (XPS) of laser-generated Pt NPs in water was done by using a hemispherical electron energy analyser (Phoibos 100 by SPECS) in a fixed analyser transmission mode with a pass energy of 20 eV. An Al K_α x-ray source (1486.6 eV) served as a non-monochromatic x-ray source. The background was corrected by applying the Shirley-Algorithm. Oxidic species were fitted with symmetric and elemental Pt with asymmetric peaks.

1.2.4. XANES / EXAFS

Unsupported PLAL Pt nanoparticle samples were available in three solutions (H_2O, 0.1mM sodium citrate, 0.1mM sodium phosphate buffer). To increase the NP concentration and thus the XAFS signal-to-noise ratio Pt NPs in H_2O and citrate were centrifuged for up to 5min at up to 5000rpm. After the respective solution was decanted the pellet was scratched from the walls of the vials with a spatula, mixed with deionized water and poured onto filter paper for the measurements. Since no NPs were detected in the pellet after centrifuging, the Pt in phosphate sample from the supernatant was pipetted into a special sample holder; sealed with Scotch tape on both sides. Comparison of Pt LIII XANES spectra taken before and after centrifuging doesn't show any differences except the improved signal-to-noise ratio (Fig. S1a and b). Since the samples weren't dried under vacuum conditions before the measurements they still contained a significant amount of water. Thus, it is safe to assume that the particle-solvent interaction didn't change and only the data quality improved. TiO_2-supported Pt NPs were available in powder form and rubbed onto a glass fiber filter. Unsupported wet-chemical Pt NPs were present in solution (ethylene glycol containing 0.15M NaOH) and poured onto filter paper for the measurements. Pt NPs supported on doped TiO_2 were mixed with BN and prepared into a sample holder with Kapton tape on both sides.

Pt LIII edge (11,564eV) XANES & EXAFS spectra of the PLA samples were recorded at the IDEAS bending magnet beamline at the Canadian Light Source Inc. (CLS) operating at an electron energy of 2.9 GeV. A double crystal monochromator (DCM) of the Lemonnier type [28] equipped with a Ge(220) crystal pair was used without detuning. Pt LIII XANES & EXAFS spectra of the wet-chemical samples were recorded at the HXMA wiggler beamline at the same facility. A Si(111) crystal pair for monochromatizing and Rh-coated collimating mirrors for focussing the x-ray beam were used. Detuning of the monochromator was done by 50% to suppress higher harmonics. All samples were measured in air at ambient conditions. At both beamlines beam intensities before and after the sample as well as the absorption signal from a Pt reference foil were monitored by three 30cm long ionization chambers (Oxford). At IDEAS all chambers were filled with air at ambient pressure; at HXMA they were flushed with N_2 at a

low flow throughout the experiments. For all samples except the reference foils transmission and fluorescence data were recorded simultaneously. Samples were placed at a 45° angle to the incoming beam. For fluorescence detection either a single-element Si drift detector (Vortex, IDEAS) or a 32 element Ge detector (Canberra, HXMA) placed at a 45° angle to the sample, i.e. perpendicular to the beam, was used. Pt $L_{\alpha 1,2}$ emission lines were recorded. Scan parameters are summarized in table 1 (energies are given relative to the respective edge energies as determined by the inflection point method):

Table 1: summary of XAFS scan parameters ("f" refers to "function". The intensity and thus signal-to-noise ratio of the EXAFS signal decreases gradually for increasing energy. To improve that ratio the integration time in the post-edge region was gradually increased from 2 to a maximum of 10s using an empirical function.)

Pt LIII edge (11,564eV)

Pre-edge region	Energy range [eV]	-200 to -30
	Step size [eV]	10
	Integration time [s]	1
Edge region	Energy range [eV]	-30 to +40
	Step size [eV]	1
	Integration time [s]	2
Post-edge region	Energy range	+40eV to 9$Å^{-1}$
	Step size [eV]	0.1$Å^{-1}$
	Integration time [s]	2 (f)

All recorded spectra were processed using ATHENA (version 0.8.061) from the IFFEFIT software package. In short: all reference scans were first energy-calibrated and their respective sample spectra shifted accordingly. Then the reference scans were aligned to the respective first one of the series (between 16 and 50 individual scans) and their respective sample spectra shifted accordingly again. Next, all sample and reference scans were averaged. A linear function was manually adjusted to the pre-edge region and subtracted from the data ("background"). Last, a cubic spline was manually adjusted to the post-edge for normalization.

For EXAFS analysis the program ARTEMIS from the same software package was used (version 0.8.014). Pt foil reference spectra were fitted including the first Pt-Pt single-scattering path. All sample spectra had an additional Pt-O path. In the structural file N was used instead

of O since calculating scattering paths for a bulk Pt structure worked with N atoms in the 1st shell but not with O atoms. This approach is reasonable since N and O atoms have almost identical back-scattering properties. Amplitude reduction factor S_0^2 values between 0.54-0.57 were taken from fits of the respective reference foils and kept fixed subsequently. To reduce the number of fitting parameters one mean-square displacement parameter σ^2 was fitted for each path, kept fix and then the fits repeated. This resulted in a total of 6 fitting parameters (two numbers of next neighbours N, two next neighbour distances R, one ΔE for both paths (see e.g. [29]) and one third order cumulant-expansion parameter σ^3 for the Pt-N path). All fits were done in R-space with a simultaneous k-weighting of 1 and 3. For more detailed information about XANES and EXAFS data handling see e.g. [30].

2. Results and discussion

2.1.TEM / XPS

PLAL Pt nanoparticles in water were characterized by TEM. Fig. 1a shows a representative TEM image of spherical nanoparticles and the corresponding histogram where a cut-off is clearly seen. The corresponding histogram shows a mean particle size of about 7nm which proves the success of centrifuging after the synthesis. Note that PLAL of noble metals may produce monodisperse particles if size-quenched anions are used during the particle synthesis [17] which was intentionally avoided in the present study. Wet-chemically synthesized particles have an average size of 5.4nm (Fig. 1b). Since the relative number of surface atoms is similar for particles synthesized wet-chemically and via PLAL (~20%) comparing XAS results of both groups of samples is feasible (Fig. S2).

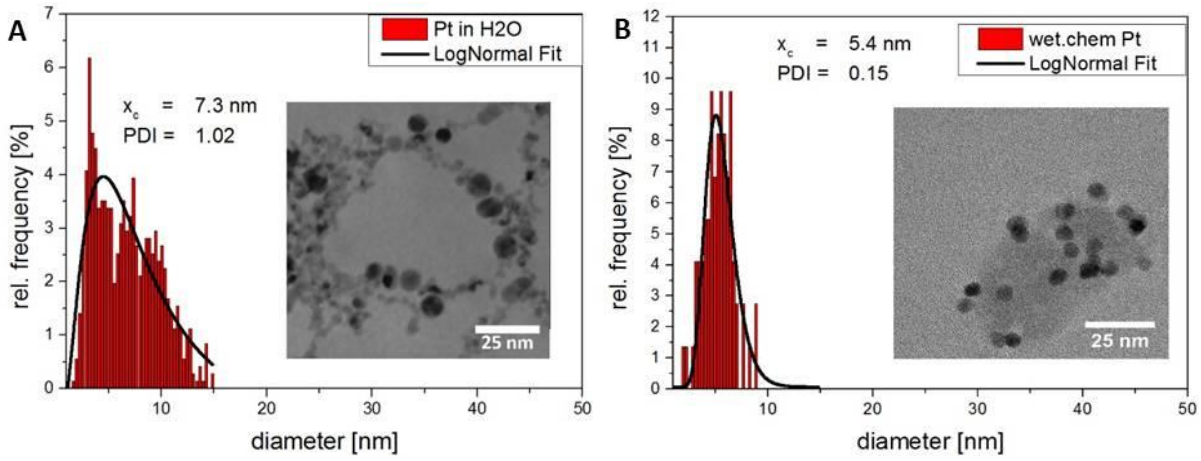

Fig. 1: (a) Particle size distributions of laser-generated Pt nanoparticles in water and (b) wet-chemically synthesized Pt nanoparticles in ethylene glycol as determined by TEM.

When analysing the wet-chemically synthesized particles by XPS a higher amount of Pt^0 was found compared to the particles in all three laser-generated unsupported samples (Fig. 2a). However, a better correlation of Pt4f and O1s peaks was found for a fit with PtO_2 and thus a Pt(IV) peak instead of PtO and thus a Pt(II) peak as is the case for laser-generated particles Fig. 2b and d). This suggests that mainly Pt(IV)-type bonds are present on the surfaces of wet-chemically synthesized and Pt(II)-type bonds on the surfaces of PLAL Pt NPs. The issue of different type of bonds will be revisited in chapter 3.4 when evaluating XAS data. Nevertheless, the oxidative peaks are quite small and thus significant changes are difficult to evaluate.

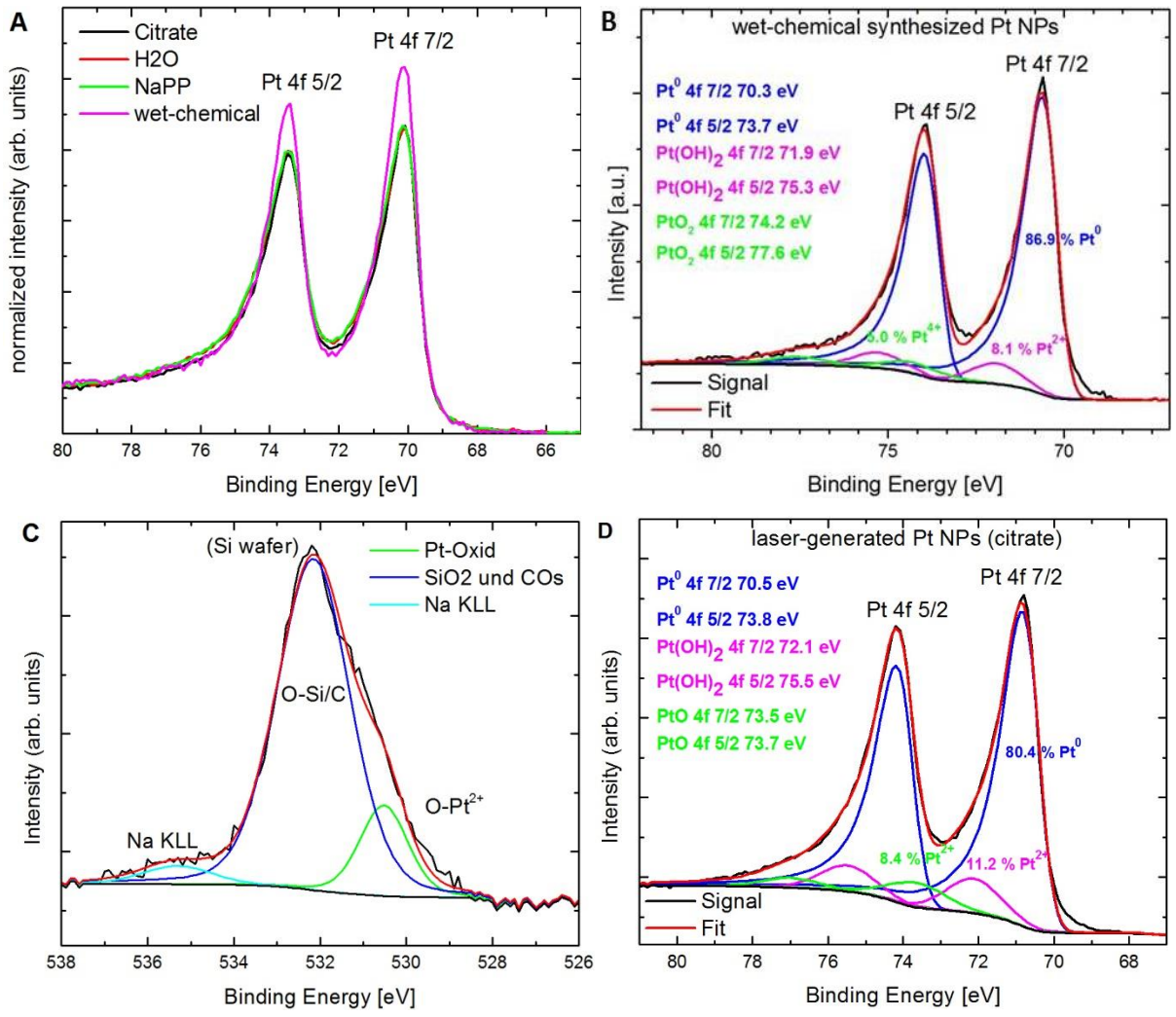

Fig. 2: (a) Comparison of XPS spectra of laser-generated Pt nanoparticles in H_2O, a sodium phosphate buffer and sodium citrate as well as wet-chemically synthesized Pt NPs. Fitting curves for (b) wet-chemically synthesized and (d) laser-generated Pt NPs. (c) shows the oxygen peak corresponding to (d) that was used to clarify the nature of the Pt-O peaks [31].

Based on these XPS results, where the oxygen peaks were carefully evaluated (Fig. 2c), we corrected the fit parameter for the XPS analysis considering $Pt(OH)_2$ and PtO. The results now

stronger correlate with the corresponding oxygen peak at about 530 eV and are in agreement with literature, where Pt-OH groups were verified on laser-generated particles surfaces [14, 32, 33].

Assessing these results and comparing them to the results obtained by x-ray absorption spectroscopy (cf. chapter 3.4) one should keep in mind that XPS experiments are carried out using dried particles under ultrahigh vacuum conditions whereas x-ray absorption experiments are carried out *in situ* (see chapter 2.2.4). Moreover, one has to consider that XPS is very surface-sensitive, providing information about a few atomic layers whereas the information depth of XAS at the Pt LIII edge is several micrometers.

2.2.UV/vis spectroscopy

Fig. 3 shows a typical extinction spectrum of Pt NPs in H_2O before and after mixing with TiO_2:

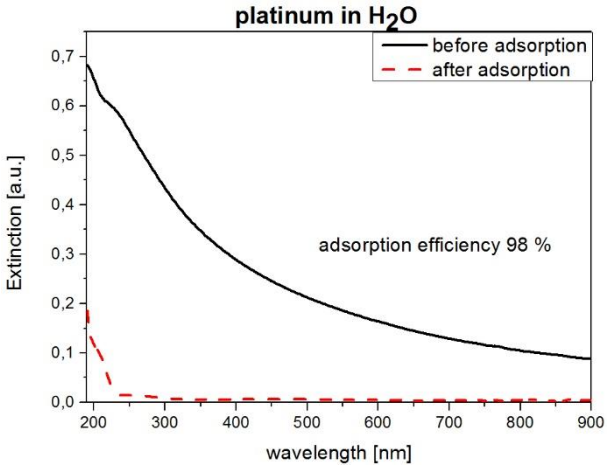

Fig. 3: extinction spectrum of Pt NPs before (black) and after (red) mixing with TiO_2. Adsorption efficiency was calculated from extinction measurements at 300nm wavelength before and after nanoparticle adsorption, according to [34], to 98%.

2.3.XANES / EXAFS: PLAL samples (unsupported)

In this section, the Pt nanoparticle surface-solvent interaction in water and the impact of adding the ions citrate and phosphate is discussed. Fig. 4a compares the normalized XANES spectra of Pt NPs in H_2O, sodium citrate, sodium phosphate buffer and a Pt reference foil. The inset shows just the whiteline region. Fig. 4b shows the k^1-weighted EXAFS Fourier transform magnitudes of all four samples. Data are not phase-corrected, i.e. peak positions are at lower distances than actual bond lengths.

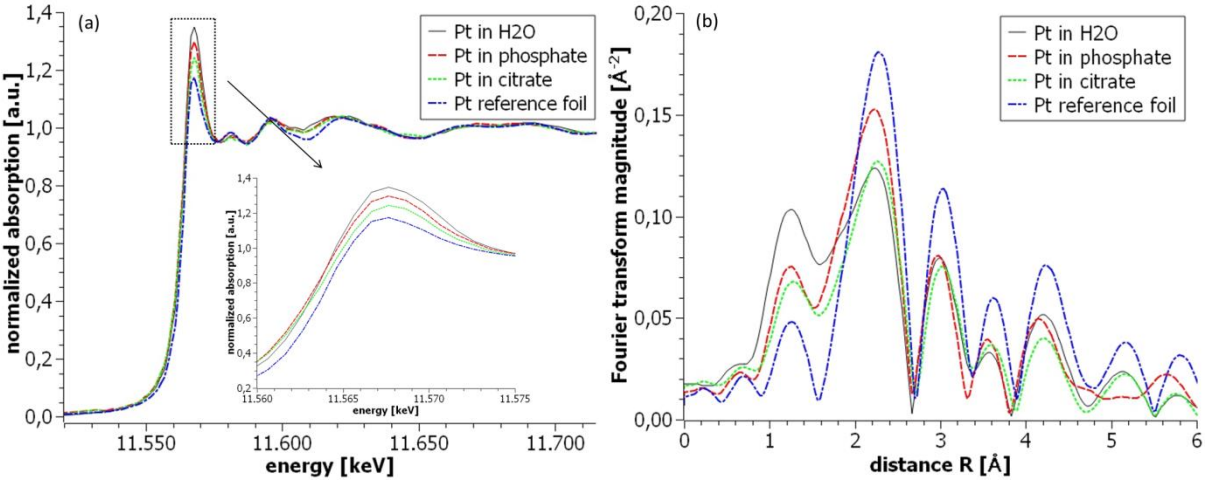

Fig. 4: (a) normalized Pt LIII edge XANES spectra of ligand-free Pt NPs in H_2O, sodium phosphate buffer, sodium citrate and a Pt reference foil. Inset: whiteline region. (b) k^1-weighted EXAFS Fourier transform magnitudes (dk = 1.0; dr = 0.0; Hanning window); not phase-corrected

The whiteline intensity in Fig. 4a increases in the following order:

Pt foil < Pt in citrate < Pt in phosphate < Pt in H_2O

The Pt LIII edge whiteline is caused by transitions from $2p_{3/2}$ to unoccupied $5d_{3/2}$ and $5d_{5/2}$ states [35]. Its intensity is determined by density of unoccupied final states, i.e. for NPs two factors could contribute to the observed differences: a different ratio of surface-to-bulk-atoms (particle size effect) [36, 37] or unequal charge transfer, i.e. different bond strengths due to different binding partners. In the present study particles are rather large and they were taken from the same batch before sodium citrate or phosphate was added. Hence, a particle size effect can be ruled out. Thus, the different interaction with the solvent molecules and ionic additives is the only possible reason for the differences in the whiteline intensity. A comparison with literature (e.g. [35]) shows that Pt-H bonds are highly unlikely, i.e. the whiteline intensity differences are caused by bonds between Pt atoms and one or more O-containing species. As can be seen by XPS analysis in Fig. 2, surfaces of nanoparticles prepared by laser ablation in an aqueous solution are partially positively charged due to oxidized species which in our case are Pt^{2+} and Pt^{4+}. These can now attract water molecules or dissolved oxygen and form Pt-OH/Pt-O^- species on the surfaces [15, 16]. This oxidation is the reason for the strong whiteline of laser-generated Pt NPs in H_2O. We assume that ions added *ex situ* interact electrostatically with the Stern plane thus directly influencing the Pt-OH bonds. Citrate and phosphate ions are Brønsted bases, i.e. proton acceptors. Therefore, the interaction between those and (most likely) OH weakens the Pt-OH bonds. Similarly, surface charge delivery of ligand-free, laser-generated Au NPs was recently studied for a Hofmeister series of anions with a different number of hydration and polarizability showing that anion adsorption causes an increase in surface charge

density [17]. Both effects (Lewis and Brønsted base) cause a higher electron density at the particle surface and hence its partial reduction is observed by a decrease of Pt LIII edge whiteline intensities. This assumption is supported by measuring the zeta potential of the three samples. While its value is -23.7 ± 1.7mV for Pt NPs in H_2O it increased by adding phosphate or citrate ions up to a value of -31.8 ± 7.1mV and -43.8 ± 0.8mV respectively (Fig. S4) at the same pH value. As can be seen in the inset of Fig. 4a the widths of the whitelines increase in the same order as their intensities. This is due the overlap of the Pt 5d band with O 2π* orbitals "forming an antibonding state above the Fermi level" [38] which gets more pronounced for a stronger NP-solvent interaction. The post-edge regions of all nano-samples closely resemble the one of the Pt foil indicating that the NPs have the same geometric structure, i.e. fcc (face-centered cubic). The NP peaks are shifted to slightly different energies and are wider compared to the reference foil. This indicates different Pt-Pt distances and larger mean-square displacements respectively. One possible explanation for that are surface relaxation effects due to the small particle size. NP surface atoms have fewer neighbours than core atoms. To minimize the surface energy next-neighbour bond lengths are contracted [39].

The EXAFS Fourier transform magnitudes of the NP samples (Fig. 4b) show features very similar to the ones of the reference foil, i.e. same number of peaks at similar positions with similar widths but lower intensities. This confirms the XANES finding that all nano-samples have fcc structure. The peak at 1.2 Å mainly results from the photo-electrons backscattering off a low-Z element like C, N or O. Given the molecules or ions the NPs came in contact with during the synthesis O is of course the most probable candidate. The peak intensity at 1.2Å is proportional to the number of Pt-O bonds and follows the same trend as the whiteline intensities. The peaks at about 2.2 and 3.0Å result from photo-electrons backscattering off Pt atoms. Thus, their intensities are proportional to the number of Pt-Pt bonds. For distances > 4.7Å the spectrum of Pt in phosphate is different from all other ones. Since the post-edge regions of all spectra shown in Fig. 4a are very similar regarding peak positions, widths and intensities one would expect also similar Fourier transforms. Thus, we assume that the differences are due to the lower date quality of the spectrum of Pt in phosphate, which was not concentrated by centrifugation. Table 2 summarizes the EXAFS fit results of the samples shown in Fig. 4a+b:

Table 2: summary of Pt LIII edge EXAFS fit results of laser-generated Pt NPs in H_2O, sodium citrate, sodium phosphate buffer and a Pt reference foil. N(Pt)/N(O) is the number of Pt-Pt/Pt-O bonds, ΔE aligns the experimentally determined ionization energy with the one used in the calculation, R(Pt-Pt)/R(Pt-O) is the average Pt-Pt/Pt-O bond length, σ^2 Pt-Pt/σ^2 Pt-O is the mean square displacement of the Pt/O atom in a Pt-Pt/Pt-O bond, σ^3 Pt-O is the third cumulant-expansion parameter of the Pt-O bonds, "f" refers to the parameter kept fixed for the final fit

Δk: 2 – 8.5, ΔR = 0.7 – 3.4Å, number of variables = 10.1-10.9, number of fit parameters = 6				
	Pt foil	**Pt in H_2O**	**Pt in citrate**	**Pt in phosphate**
N (Pt)	12	12.0 ± 0.7	12.1 ± 0.7	13.1 ± 1.0
N (O)	0	2.0 ± 0.2	1.5 ± 0.3	1.7 ± 0.5
ΔE [eV]	7.9 ± 0.4	5.6 ± 0.8	7.0 ± 0.7	5.4 ± 1.2
R(Pt-Pt) [Å]	2.75 ± 0.01	2.73 ± 0.01	2.75 ± 0.01	2.73 ± 0.01
R(Pt-O) [Å]	/	2.15 ± 0.03	2.12 ± 0.04	2.16 ± 0.07
σ^2 [10^3 Å^2] Pt-Pt	5.1 ± 0.1	5.7 ± 1.9$_f$	6.1 ± 1.9$_f$	4.4 ± 2.9$_f$
σ^2 [10^3 Å^2] Pt-O	/	4.6 ± 6.1$_f$	12.1 ± 13.4$_f$	9.6 ± 19.2$_f$
σ^3 [10^3 Å^2] Pt-O	/	7.9 ± 1.2	5.3 ± 2.6	7.9 ± 3.6

Differences between samples are quite small and in most cases within error margins which are quite large due to the short data sets. However, the EXAFS fit results indicate that by adding the various buffers the geometric structure of the NPs and their surfaces is not changed.

2.4.XANES / EXAFS: wet-chemical synthesis vs. PLAL (unsupported)

In order to understand if there is a difference between chemically synthesized and PLAL-prepared NPs, the surface of the latter was covered by organic and steric ligands such as citrate. Fig. 5a compares the XANES spectra of wet-chemically synthesized Pt NPs (5.4nm) in ethylene glycol with laser-generated (7.3 nm) ones in citrate. The inset shows just the whiteline region. Fig. 5b shows the k^1-weighted EXAFS Fourier transform magnitudes of both samples. Data are again not phase-corrected.

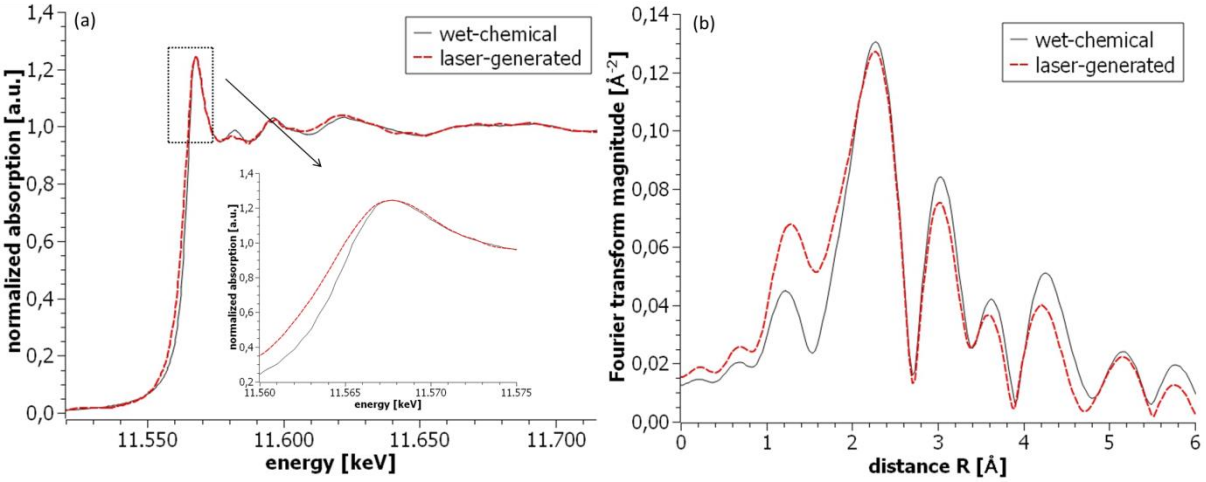

Fig. 5: (a) normalized Pt LIII edge XANES spectra of wet-chemically synthesized Pt NPs in ethylene glycol and laser-generated Pt NPs in citrate. Inset: whiteline region. (b) k^1-weighted EXAFS Fourier transform magnitudes (dk = 1.0; dr = 0.0; Hanning window); not phase-corrected

Within the error margins the whiteline intensities are identical indicating that the NP-solvent interaction is equally strong in both samples. This is surprising since for the wet-chemical sample one would expect it to be stronger and thus a stronger whiteline, assuming that there is only a negligible difference of the binding partner citrate, which was added to laser-generated NPs, and ethylene glycol, which is present on the particle surface of wet-chemical synthesized NPs. For citrate it was proposed, that carboxylic groups are attached to the particle surface [40, 41]. Ethylene glycol only has hydroxyl functional group, which attach to the particle surface. Thus in both cases oxygen binds to the particle surfaces. One aspect to explain the observations in Fig. 5 could be the absence of an additional stabilizer during synthesis of these wet-chemically synthesized NPs. As can be seen in the inset of Fig. 5a the whiteline of the wet-chemical sample is narrower on the low-energy side. This is due to the fact that the two samples were measured at different beamlines with a different energy resolution. The post-edge regions of both spectra closely resemble each other indicating that the wet-chemical NPs have fcc structure as well. No significant shifts or widening can be observed indicating a similar degree of crystallinity, i.e. similar Pt-Pt distances and respective mean-square displacements. Since peaks in the post-edge region amongst laser-generated samples vary in intensity (Fig. 4a) due to experimental reasons differences observed here are not considered significant.

EXAFS spectra > 2.0Å (Fig. 5b) closely resemble each other confirming the XANES finding that Pt NPs in both samples have very similar geometric structure as well as a similar degree of crystallinity. The peak at 1.2Å is significantly lower in case of the wet-chemical sample indicating a lower number of Pt-O bonds. This is supported by EXAFS fitting results as summarized in table 3:

Table 3: summary of Pt LIII edge EXAFS fit results of wet-chemical and laser-generated Pt NPs. "f" refers to the parameter kept fixed for the final fit

Δk: 2 – 9.8, ΔR = 0.7 – 3.4Å, number of variables = 10.1-10.9, number of fit parameters = 6		
	wet-chemical	**laser-generated (Pt in citrate)**
N (Pt)	10.9 ± 0.5	12.1 ± 0.7
N (O)	0.5 ± 0.1	1.5 ± 0.3
ΔE [eV]	7.4 ± 0.5	7.0 ± 0.7
R(Pt-Pt) [Å]	2.75 ± 0.01	2.75 ± 0.01
R(Pt-O) [Å]	2.11 ± 0.05	2.12 ± 0.04
σ^2 [10^3 Å^2] Pt-Pt	$5.5 \pm 1.5_f$	$6.1 \pm 1.9_f$
σ^2 [10^3 Å^2] Pt-O	$2.2 \pm 11.0_f$	$12.1 \pm 13.4_f$
σ^3 [10^3 Å^2] Pt-O	7.8 ± 2.5	5.3 ± 2.6

The fit results indicate that the average number of Pt-O bonds seems to be higher for PLAL-generated NPs after citrate addition than for the wet-chemically synthesized NPs though the intensities of the corresponding whitelines in the XANES spectra are about the same (cf. Fig. 5a). As there is hardly any shift in energy for the LIII whitelines of various potential Pt oxides (PtO, PtO_2, Pt_3O_4) [42] the seeming inconsistency between XANES and EXAFS results can be explained assuming mainly Pt(IV)O_2-type bonds on the surface of the wet-chemical NPs and mainly Pt(II)O-type bonds on the surface of the PLAL NPs. Because of the much more intense whiteline of PtO_2 this assumption leads with less Pt(IV)-O-bonds to the same whiteline intensity as a larger number of weaker Pt(II)-O-bonds. This assumption is confirmed by XPS analysis (Fig. 2). However, the influence of the different ligands cannot be excluded.

2.5.XANES / EXAFS: unsupported vs. TiO_2-supported Pt NPs

Fig. 6a compares the normalized XANES spectra of laser-generated unsupported with TiO_2-supported Pt NPs in H_2O. Fig. 6b shows the k^1-weighted EXAFS Fourier transform magnitudes of both samples. Data are again not phase-corrected. The bump at about 11,530eV in the XANES spectra of the TiO2-supported sample is due to experimental reasons.

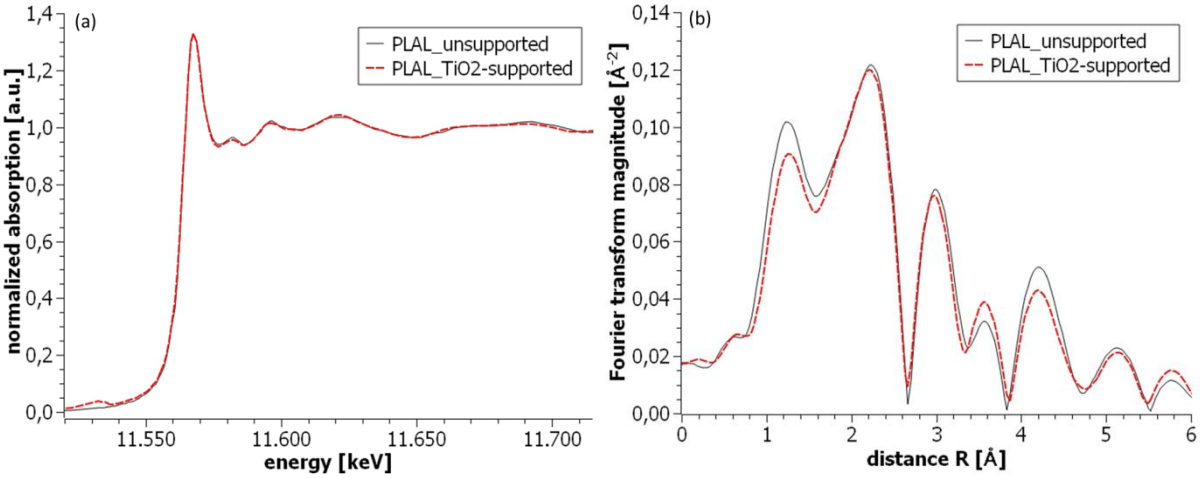

Fig. 6: (a) normalized Pt LIII edge XANES spectra of Pt in H_2O and 2wt-% Pt on TiO_2. (b) k^1-weighted EXAFS Fourier transform magnitudes (dk = 1.0; dr = 0.0; Hanning window); not phase-corrected

Both spectra are identical within error margins. This means that without proper high temperature calcination the deposition process has no measurable impact on the electronic and geometric structure of the Pt nanoparticles. The finding that depositing Pt on TiO_2 without following calcination does not change the Pt LIII edge whiteline seems to be a common situation (see e.g. [43]). Fig. 7a compares the normalized XANES spectra of wet-chemically synthesized unsupported with doped TiO_2-supported Pt NPs. Fig. 7b shows the k^1-weighted EXAFS Fourier transform magnitudes of both samples. Data are again not phase-corrected.

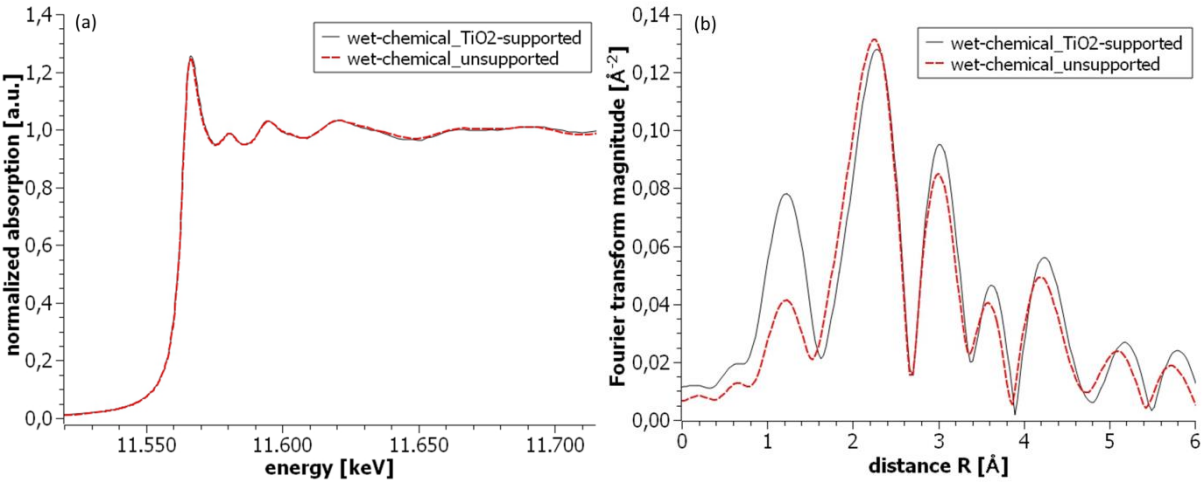

Fig. 7: (a) normalized Pt LIII edge XANES spectra of wet-chemically synthesized unsupported and doped TiO_2-supported 20wt-% Pt NPs. (b) k^1-weighted EXAFS Fourier transform magnitudes (dk = 1.0; dr = 0.0; Hanning window); not phase-corrected

As with the laser-generated particles no whiteline intensity differences can be seen despite a significantly higher loading (2 and 20wt-%). This means that depositing Pt onto TiO_2 NPs does not change the electronic structure of the catalyst. In a previous work, a net charge transfer from

laser-generated Pt nanoparticles to titania was observed by measuring the zeta potential and a shift of the isoelectric points (IEP) [22]. It should be noted that by means of zeta potential measurements it cannot be distinguished if the IEP shift of titania toward the nanoparticle IEP is related to an electron charge transfer or to an ion transfer by adsorbed Pt nanoparticles causing a neutralization of the TiO_2 surface. XAS enables investigations of the electronic structure and gives information e.g. about neighbouring atoms and bond lengths. Our assumptions that (i) after particle adsorption the Gouy-Chapman layer of the particles and the support are combined as well as (ii) the electronic structure of both the Pt and TiO_2 atoms is preserved are confirmed by XAS.

EXAFS data (Fig. 7b) show that, as with the laser-generated particles, the deposition process does not have a significant impact on the geometric structure of the Pt nanoparticles either. However, two differences can be noted. The spectrum of the supported sample shows slightly higher intensity for peaks > 3.0Å. This speaks for a slightly increased particle size and thus some agglomeration (20 wt-% Pt on TiO_2). Also the peak at 1.2Å is more intense in case of the supported sample indicating either a higher number or a change in character of the Pt-O bonds.

3. Conclusions and outlook

Interaction of nanoparticles with their environment is largely controlled by their surface chemistry. Understanding how different additives influence their surface, a suitable model system for the investigations of the electronic structure is needed, where the effects of influential additives such as a shell of ligands can be excluded. Thus we refer to ligand-free colloidal particles, where than the influence of various additives could be studied separately by a subsequent adsorption.

During the past few decades a synthesis of ligand-free particles technique emerged which has proven to be a promising alternative to traditional chemical reduction methods: pulsed laser ablation in liquid (PLAL). Its most outstanding advantage is that stable NPs can be prepared in a desired solvent without using any stabilizing additives. In this study, we synthesized additive-free Pt nanoparticles via pulsed laser ablation in water and characterized their interaction with H_2O, a sodium citrate and a sodium phosphate buffer solution as well as a commercial TiO_2 support. UV/vis extinction spectroscopy data gave an adsorption efficiency of Pt NPs onto TiO_2 NPs of 98%. Pt LIII edge XANES spectra show that all Pt nanoparticles have fcc structure. Its whiteline intensity follows the order Pt in H_2O > Pt in phosphate > Pt in citrate. We explain this in accord with the Stern model describing the interaction of particles in an aqueous medium. In our model, predominantly OH groups chemically bind to the partially oxidized Pt NP surfaces

forming an impenetrable Stern plane. Upon addition of citrate or phosphate molecules interact electrostatically with this OH-group forming a hydration shell on top. These bonds between (most likely) OH and citrate or phosphate molecules weaken the Pt-OH interaction. This increases the electron density of the Pt atoms at the particle surface causing the observed decrease in whiteline intensity which is supported by zeta potential measurements. Our results indicate that the surfaces of chemically synthesized and laser-generated ligand-free particles are different; a situation that changes as soon as Pt NP surfaces are covered by ligands. Comparing XANES spectra of laser-generated ligand-covered Pt NPs (in citrate) with wet-chemically synthesized ones shows no whiteline intensity differences. However, EXAFS results of the wet-chemically synthesized NPs indicate a lower number of Pt-O as compared to the laser-generated ones. This seeming contradiction can be explained by assuming different types of Pt-O-bonds: a Pt(IV)O_2-type in case of wet-chemical and a Pt(II)O-type in case of laser generated NPs. A comparison of unsupported laser-generated Pt nanoparticles in H_2O with TiO_2-supported ones shows no whiteline intensity differences and an identical number of Pt-O bonds in both cases. This suggests that in the deposition process part of the Stern layer is preserved and that the electronic structure of ligand-free Pt NPs is preserved as well during the supporting process. Similar results were obtained when comparing unsupported wet-chemically synthesized Pt NPs with TiO_2-supported ones. However: an indication for a change in character of the Pt-O bonds after particle adsorption was found for which additional investigations are be required. In this study we were interested in the commonly used additives citrate and phosphate using PLAL for particle synthesis [7, 14, 22, 23, 34, 44]. But also further comparisons of laser-generated nanoparticles and wet-chemical synthesized nanomaterials are needed. For instance, further studies with additives such as non-ionic surfactants and other catalytically relevant supports such as carbon could be done.

This is the first time, to the best of our knowledge, that x-ray absorption spectroscopy was used to characterize laser-generated nanoparticles *in situ* in their native environment. XAS is a powerful tool to gain information about the electronic and geometric structure of NPs regardless of the nature of their synthesis. Ligand-free colloidal NPs could act as a reference material since surface chemistry and ligand effects can be studied from bare building blocks. Future investigations will give a deeper insight into the particle-solvent interaction of laser-generated particles and differences to particles synthesized by traditional chemical reduction methods.

Literature

[1] Klein, S.; Petersen, S.; Taylor, U.; Rath, D.; Barcikowski, S. Quantitative visualization of colloidal and intracellular gold nanoparticles by confocal microscopy. *J. Biomed. Opt*. **2010**, *15*, 036015–036015.

[2] Cuenya, B. R. Synthesis and catalytic properties of metal nanoparticles: Size, shape, support, composition and oxidation state effects. *Thin Solid Films* **2010**, *518*, 3127–3150.

[3] Anukunprasert, T.; Saiwan, C.; Traversa, E. The development of gas sensor for carbon monoxide monitoring using nanostructure of Nb-TiO2. *Science and Technology of Advanced Materials* **2005**, *6*, 359–363.

[4] Haruta, M. Size- and support-dependency in the catalysis of gold. *Catalysis Today* **1997**, *36*, 153–166.

[5] Brus, L. E. Electron–electron and electron-hole interactions in small semiconductor crystallites: The size dependence of the lowest excited electronic state. *J. Chem. Phys*. **1984**, *80*, 4403–4409.

[6] Sharma, S.; Pollet, B. G. Support materials for PEMFC and DMFC electrocatalysts – A review. *Journal of Power Sources*, **2012**, *208*, 96–119.

[7] Wagener, P; Schwenke, A.; Barcikowski, S. How Citrate Ligands Affect Nanoparticle Adsorption to Microparticle Supports. *Langmuir*, **2012**, *28*, 6132–6140.

[8] Schmidt, H.; Relevance of Sol-Gel Methods for Synthesis of Fine Particles. *KONA* **1996**, *14*, 92–103.

[9] Hormes, J.; Modrow, H.; Boennemann, H.; Kumar, C.S.S.R. The influence of various coatings on the electronic, magnetic and geometric properties of Cobalt – nanoparticles. *J. Appl. Physics* **2005**, 97, 10R102-1–10R102-6.

[10] Lopez-Sanchez, J. A.; Dimitratos, N.; Hammond, C.; Brett, G. L.; Kesavan, L.; White, S.; Miedziak, P.; Tiruvalam, R.; Jenkins, R. L.; Carley, A. F.; Knight, D.; Kiely, C. J.; Hutchings, G. J. Facile removal of stabilizer-ligands from supported gold nanoparticles. *Nature Chemistry* **2011**, *3*, 551–556.

[11] Beck, A.; Horváth, Z; Stefler, G.; Koppány, Z.; Sajó, I.; Geszti, O.; Guczi, L. Sol derived gold-palladium bimetallic nanoparticles on TiO_2: structure and catalytic activity in CO oxidation. *Topics in Catalysis* **2007**, *44 (1-2)*, 115–121.

[12] Zeng, H.; Du, X.-W.; Singh, S. C.; Kulinich, S. A.; Yang, S.; He, J.; Cai, W.; Nanomaterials via Laser Ablation/Irradiation in Liquid: A Review. *Adv. Funct. Mater*. **2012**, *22*, 1333–1353.

[13] Amendola, V.; Meneghetti, M. What controls the composition and the structure of nanomaterials generated by laser ablation in liquid solution? *Phys. Chem. Chem. Phys*. **2013**, *15*, 3027–3046.

[14] Rehbock, C.; Jakobi, J.; Gamrad, L.; van der Meer, S.; Tiedemann, D.; Taylor, U.; Kues, W.; Rath, D.; Barcikowski, S. Current state of laser synthesis of metal and alloy nanoparticles as ligand-free reference materials for nano-toxicological assays. *Beilstein J. Nanotechnol.*, **2014**, *5*, 1523–1541.

[15] Nichols, W. T.; Sasaki, T.; Koshizaki, N. Laser ablation of a platinum target in water. III. Laser-induced reactions. *Journal of applied physics* **2006**, *100*, 114913-1–114913-7.

[16] Muto, H.; Yamada, K.; Miyajima, K.; Mafune, F. Estimation of surface oxide on surfactant-free gold nanoparticles laser-ablated in water *The Journal of Physical Chemistry C* **2007** *111*, 17221–17226.

[17] Merk, V.; Rehbock, C.; Becker, F.; Hagemann, U.; Nienhaus, H.; Barcikowski, S. In situ non-DLVO stabilization of surfactant-free, plasmonic gold nanoparticles: Effect of Hofmeister's anions. *Langmuir* **2014**, *30*, 4213–4222.

[18] Cosgrove, T.; Colloid Science: Principles, Methods and Applications; 2nd edition; *Wiley*; **2010.**

[19] Hiemenz, P. C.; Rajagopalan R.; Dekker, M. The electrical double layer and double-layer interactions, Principles of colloid and surface chemistry; 3rd edition, *Inc., New York*; **1997**; 499–533.

[20] Boyen, H.-G.; Fauth, K.; Stahl, B.; Ziemann, P.; Kästle, G.; Weigl, F.; Banhart, F.; Hessler, M.; Schütz, G.; Gajbhiye, N. S.; Ellrich, J.; Hahn, H.; Büttner, M.; Garnier, M. G.; Oelhafen, P. Electronic and Magnetic Properties of Ligand-Free FePt Nanoparticles. *Advanced Materials* **2005**, *17 (5)*, 574–578.

[21] Ozin, G. A.; Mitchell, S. A. Ligand-free metal clusters. *Angewandte Chemie International Edition in English* **1983**, *22 (9)*, 674–694.

[22] Marzun, G.; Streich, C.; Jendrzej, S.; Barcikowski, S; Wagener, S. Adsorption of Colloidal Platinum Nanoparticles to Supports: Charge Transfer and Effects of Electrostatic and Steric Interactions. *Langmuir* **2014**, *30*, 11928–11936.

[23] Marzun, G.; Nakamura, J.; Zhang, X.; Barcikowski, S.; Wagener, P. Size control and supporting of palladium nanoparticles made by laser ablation in saline solution as a facile route to heterogeneous catalysts. *Applied Surface Science* **2015**, *348*, 75–84.

[24] Sachtleben Chemie GmbH/ Huntsman product information: http://www.sachtleben.de/fileadmin/pdf_dateien/titandioxid/HOMBIKAT_TYPE_II.pdf (accessed Jan 23, **2016**)

[25] Bock, C.; Paquet, C.; Couillard, M.; Botton, G. A.; MacDougall, B. R. Size-Selected Synthesis of PtRu Nano-Catalysts: Reaction and Size Control Mechanism. *J. Am. Chem. Soc*. **2004**, *126*, 8028–8037.

[26] Henglein, A.; Ershov, B. G.; Malow, M. Absorption spectrum and some chemical reactions of colloidal platinum in aqueous solution. *J. Phys. Chem.* **1995**, *99*, 14129–14136.

[27] Weaver, J. H.; Krafka, C.; Lynch, D. W.; Koch, E. E. Optical Properties of Metals; Fachinformationszentrum Karlsruhe: Weinheim, **1981.**

[28] Lemonnier, M.; Collet, O.; Depautex, C.; Esteva, J.-M.; Raoux, D. High Vacuum Two Crystal Soft X-ray Monochromator. *Nuclear Instruments and Methods* **1978**, *152*, 109–111.

[29] Newville, M. Data processing with IFFEFIT, ATHENA & ARTEMIS *Consortium for Advanced Radiation Sources*, University of Chicago; July 24, **2007**.

[30] Ravel, B.; Newville, M; ATHENA, ARTEMIS, HEPHASESTUS: data analysis for x-ray absorption spectroscopy using IFEFFIT. *J. Synchrotron Rad*. **2005**, *12*, 537–541.

[31] Drawdy, J. E.; Hoflund, G. B.; Gardner, S. D.; Yngvadottir, E.; Schryer, D. R. Effect of pretreatment on a platinized tin oxide catalyst used for low-temperature Co oxidation. *Surface and Interface Analysis* **1990**, *16*, 369–374.

[32] Sylvestre, J.-P.; Poulin, S.; Kabashin, A. V.; Sacher, E.; Meunier, M.; Luong, J. H. T. Surface Chemistry of Gold Nanoparticles Produced by Laser Ablation in Aqueous Media. *J. Phys. Chem. B* **2004**, *108*, 16868–16869.

[33] Pfeiffer, C.; Rehbock, C.; Hühn, D.; Carillo-Carrion, C.; Jimenez, D.; De Aberasturi, D. J.; Merk, V.; Barcikowski, S.; Parak, W. J. Interaction of colloidal nanoparticles with their local environment: the (ionic) nanoenvironment around nanoparticles is different from bulk and determines the physico-chemical properties of the nanoparticles. *J. R. Soc., Interface* **2014**, *11*, 20130931.

[34] Rehbock, C.; Merk, V.; Gamrad, L.; Streubel, R.; Barcikowski, S. Size control of laser-fabricated surfactant-free gold nanoparticles with highly diluted electrolytes and their subsequent bioconjugation. *Phys. Chem. Chem. Phys*. **2013**, *15*, 3057–3067.

[35] Ramaker, D. E.; Mojet, B. L.; Garriga Oostenbrink, M. T.; Miller, T.; Koningsberger, D. C. Contribution of shape resonance and Pt-H EXAFS in the Pt L2,3 x-ray absorption edges of supported Pt nanoparticles: Application and consequences for catalyst characterization. *Phys. Chem. Chem. Phys*. **1999**, *1*, 2293–2302.

[36] Bayindir, Z; Duchesne, P. N.; Cook, S. C.; MacDonald, M. A.; Zhang, P. X-ray spectroscopy studies on the surface structural characteristics and electronic properties of platinum nanoparticles. *The Journal of Chemical Physics* **2009**, *131*, 244716-1–244716-7.

[37] Lei, Y.; Jelic, J.; Nitsche, L. C.; Meyer, R.; Miller, J. Effect of Particle Size and Adsorbates on the L3, L2 and L1 X-ray Absorption Near Edge Structure of Supported Pt Nanoparticles. *Top Catal* **2011**, *54*, 334–348.

[38] Safonova, O. V.; Tromp, M.; van Bokhoven, J. A.; de Groot, F. M. F.; Evans, J.; Glatzel, P. Identification of CO Adsorption Sites in Supported Pt Catalysts Using high-energy-resolution fluorescence detection X-ray spectroscopy. J. *Phys. Chem. B* **2006**, *110*, 16162–16164.

[39] Ankudinov, A. L.; Rehr, J. J.; Low, J. J.; Bare, S. R. Sensitivity of Pt x-ray absorption near edge structure to the morphology of small Pt clusters. *J. Chem. Phys*. **2002**, *116*, 1911–1919.

[40] Park, J. W.; Shumaker-Parry, J. S. Strong Resistance of Citrate Anions on Metal Nanoparticles to Desorption under Thiol Functionalization. *ACS nano* **2015**, *9*, 1665–1682.

[41] Park, J. W.; Shumaker-Parry, J. S. Structural study of citrate layers on gold nanoparticles: role of intermolecular interactions in stabilizing nanoparticles. *Journal of the American Chemical Society* **2014**, *136*, 1907–1921.

[42] Friebel, D.; Miller, D.J.; O'Grady C.P.; Anniyev, T.; Bargar, J.; Bergmann, U.; Ogasawara H.; Wikfeldt, K.T.; Petterson, L.G.M.; Nilson, A. In situ X-ray probing reveals fingerprints of surface Platinum oxide. *Phys. Chem. Chem. Phys*. **2011**, *13*, 262–266.

[43] Gonzalez, I.D.; Navarro, R.M.; Wen, W.; Marinkovic, N.; Rodriguez, J.A.; Rosa, F.; Fierro, J.L.G. A comparative study of the water gas shift reaction over platinum catalysts supported on CeO2, TiO2 and Ce-modified TiO2. *Catalysis Today* **2010**, *149*, 372–379.

[44] Tsuji, T.; Yahata, T.; Yasutomo, M.; Igawa, K.; Tsuji, M.; Ishikawa, Y.;Koshizaki, N. Preparation and investigation of the formation mechanism of submicron-sized spherical particles of gold using laser ablation and laser irradiation in liquids. *Phys. Chem. Chem. Phys.* **2013**, *15*, 3099–3107.

1.1. Role of dissolved and molecular oxygen on Cu and PtCu alloy particle structure during laser ablation synthesis in liquids

Reprinted with permission from ChemPhysChem in Special issue 'Laser Synthesis of Nanoparticles and Colloids' 18, Galina Marzun, Helmut Bönnemann, Christian Lehmann, Bernd Spliethoff, Claudia Weidenthaler, Stephan Barcikowski, "Role of dissolved and molecular oxygen on Cu and PtCu alloy particle structure during laser ablation synthesis in liquids" 1-11, 2017.

Abstract

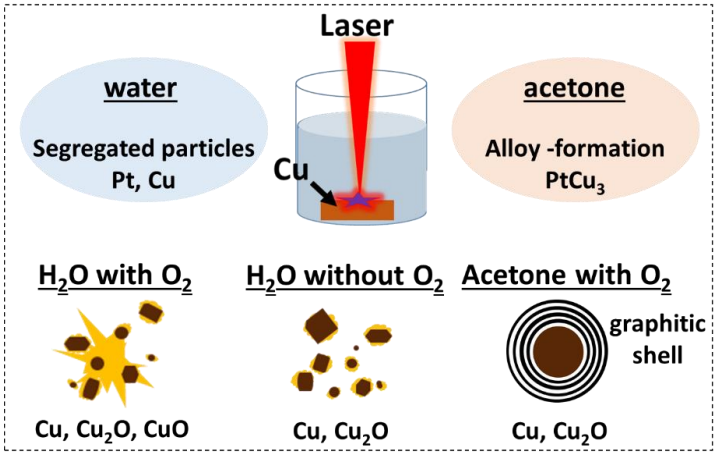

The role of the molecular oxygen dissolved in the solvent is often discussed as being an influencing factor on particle oxidation during pulsed laser ablation in liquids. However, the formation of the particles during laser synthesis takes place under such extreme conditions that enable the decomposition of the liquid media. Reactive species of the solvent may then affect the particle formation due to a chemical reaction in the reactive plasma. Experimental results show a difference between the role of the dissolved molecular oxygen and the contribution of oxygen bound in water molecules. Using a metallic Cu target in air-saturated water, laser ablation led to 20.5 wt% Cu, 11.5 wt% Cu_2O and 68 wt% CuO nanoparticles, according to X-ray diffraction. In contrast to particles in air-saturated water no CuO was observed in the colloid synthesized in a Schlenk ablation chamber in completely oxygen-free water. Under these conditions, less oxidized nanoparticles (25 wt% Cu and 75 wt% Cu_2O) were synthesized. The results show that nanoparticle oxidation during laser synthesis is mainly caused by reactive oxygen species due to the decomposition of water molecules. However, adding molecular oxygen promotes the particle oxidation. Storage of the Cu colloid in the presence of dissolved oxygen leads, due to aging, to nanostructures in a higher oxidation state than the freshly prepared colloid. The XRD pattern of the sample prepared in air-saturated acetone shows no crystalline phases, which is possibly due to small crystallites or low particle concentration. Concentration of particles by centrifugation show that in the large fraction (> 20 nm) even less oxidized nanoparticles (46 wt% Cu and 54 wt% Cu_2O) are present, although the solubility of molecular oxygen in

acetone is higher than in water. The nanoparticles in acetone are stable due to a Cu-catalysed graphite layer formation on their surface. The influence of the solvent on alloy synthesis is crucial as well. Laser ablation of $PtCu_3$ in air-saturated water lead to separated large CuO and Pt-rich spherical nanoparticles, while homogeneous $PtCu_3$ alloy nanoparticles were formed in acetone.

Introduction

The use of light as a tool for manufacturing many metal components has been around for a long time. A laser is a powerful light source that can be used for a variety of applications, typically including welding [1], cutting [2],[3], surveying [4], barcode scanners [5] and medical applications [6]. Also in research, the usage of lasers is indispensable as many analytical methods are based on light detection. Pulsed laser ablation in liquids (PLAL) is a quite recent approach for the production of ligand-free nanoparticles in liquid media and is a research field attracting continuously growing interest.[7],[8],[9],[10] Besides the simple handling of the nanoparticles dispersed in liquids, the advantage of PLAL are the tuneable experimental parameters. Influencing factors that affect the particle properties are primarily laser characteristics (fluence, pulse duration, wavelength), target materials and the ablation environment.[8] Compared to other conventional techniques, one appropriate advantage of particle synthesis by PLAL is the option to use nearly any desired solvent. The variety of the materials and laser properties opens up new dimensions of synthesis routes for nanomaterials which enables new findings in e.g. catalysis research.[11]

By now, there are already many studies on laser-generated noble metal nanoparticles e.g. Pt, Au or Pd dealing with surface characterization[12],[13],[14], particle size control[15],[16],[17],[18] and synthesis of alloy nanoparticles such as PtAu, AuAg and PtIr[19],[20],[21],[22]. At the same time several studies on laser synthesis of less noble metals are available, but a control of the particles properties is still challenging due to the sensitivity to oxidation.[23],[24],[25],[26] Thus, the knowledge about the influence of the surrounding media is crucial. Since copper reveals interesting properties in catalysis, the adjustability of the particle properties is of great interest. For instance, this semi-precious metal is used for methanol synthesis or partial oxidation of methanol to formaldehyde where Cu surfaces activate molecular oxygen, which has a high activation energy barrier for the non-catalysed oxidation reaction.[27],[28],[29]

Several groups have worked on laser ablation of Cu in liquids and have shown different interesting results. The group of Astrid Müller synthesized Cu nanoparticles by PLAL (355 nm) in water and obtained a mixture of metallic Cu and CuO nanoparticles.[30] In comparison to that,

more complex mineral nanoparticles such as $Cu_2(NO_3)(OH)_3$, and $Cu_2Cl(OH)_3$ were formed when PLAL was performed in an appropriate aqueous salt solutions. Tyurnuna et al. have reported that ablation of Cu in H_2O using a laser with a wavelength of 1064 nm lead to spherical CuO nanoparticles.[31] Particle size reduction is possible by subsequent laser fragmentation. Intensive studies on laser fragmented µm-sized Cu precursors (suspension) such as CuO, Cu_3N, $Cu(N_3)_2$, and Cu_2C_2 were carried out by Schaumberg et al.[32] They have reported that small metallic Cu nanoparticles were formed in several organic liquids, even if an oxide was used as a precursor. They have attributed this observation due to fact that chemical reduction takes place during formation of primary particles by a nucleation process. Overall the investigations show, that the solvent plays a crucial role for the final chemical composition and particle structure. Compared to particles in water (~30 nm), Tilaki et al. synthesized much smaller nanoparticles in acetone (~3 nm).[33] Amikura et al. laser-ablated a Cu target at 532 nm in pure water and found micrometer large crystalline paramelaconite Cu_4O_3 particles with a variety of shapes, whereas amorphous Cu species were found in decane.[34] This work already associated the oxidation of copper with oxygen species in water molecules due to the observations of multi-twin particles. They argue that spherical particle could only be produced in absence of oxygen. However, no consideration was given to the fact, that molecular oxygen is dissolved in solvents, which could influence particle oxidation during PLAL.[25],[26]

The group of David Amans investigated the laser synthesis of ϒ-Al_2O_3 in water and characterized the nucleation of the particles by plasma emission spectroscopy.[35] In agreement with DFT calculations they could show convincingly, that oxidation of Al atoms to aluminium oxides takes places within a few microseconds. However, the ablation led to a synthesis of ϒ-Al_2O_3 nanoparticles, thus they raised the question of the influence of water on the control of the stoichiometry, because the oxygen from water was not considered in the DFT calculations. So far no distinction could be made, whether the oxidation can be traced back to the molecular oxygen or the oxygen from water molecules. Recently we have reported that several indications were found that the oxygen from decomposition of water might influence the formation of alloy nanoparticles due to oxidation.[25] Although ablation was performed in degassed water under air atmosphere, the amount of residual oxygen (~1.5 mg/l ±0.4 mg/l) was still enough to oxidize the prepared nanoparticles (with surface atoms of ~$2.2 * 10^{-5}$ $mmol/l_{colloid}$). A clear evidence of the role of oxygen in water on the particle oxidation and alloy formation is still outstanding. To prove the role of oxygen in the solvent during particle synthesis, we performed pulsed laser ablation of copper in different solvents, namely entirely oxygen-free and air-saturated water, as well as air-saturated acetone.

Experimental details

Nanoparticle synthesis by pulsed laser ablation in liquids

Pulsed laser ablation of copper was carried out in acetone, air-saturated (H_2O_{air}) and oxygen-free (H_2O_{Ar}) water. Oxygen-free water was prepared by distillation of water under an argon atmosphere (Figure S1). We developed an ablation chamber, where laser ablation in liquids can be performed under inert gas atmosphere (Figure 1). A Schlenk flask was build using a three-way valve for a gas-flow control and a cuvette, where laser light can penetrate through to reach the target. Furthermore, the quartz cuvette with a 0.5 cm path length allows UV-Vis analysis of the non-aerated colloid.

For particle synthesis, a copper target was placed in the self-made Schlenk-ablation chamber, which was filled with the solvent. In case of the oxygen-free sample distilled water was purged continuously with argon during particle synthesis. Pulsed laser ablation of the target was carried out using an Nd:YAG nanosecond laser (Rofin-Sinar RS-Marker 100D, pulse duration 40 ns) at a fundamental wavelength of 1064 nm with a repetition rate of 5 kHz and a pulse energy of 5.5 mJ (36 A). In this process a focused laser beam (f-Theta lens of 63 mm focal length) was scanned in a spiral pattern over the copper target.

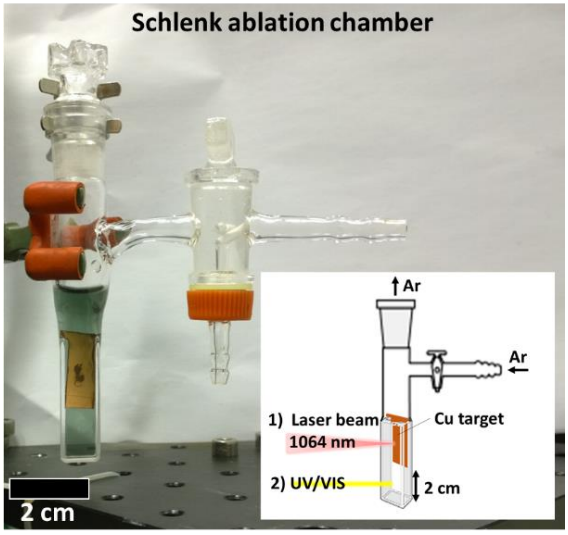

Figure 1: Ablation chamber for laser ablation in liquids under exclusion of oxygen.

Characterization methods

Laser-generated nanoparticles were characterized by UV-Vis extinction spectroscopy in the spectral range of λ = 200-900 nm on a fiber optic spectrometer (USB-650 UV) using a deuterium/tungsten light source (emission 20-2000 nm).

The colloids were characterized by transmission electron microscopy (TEM) and energy dispersive X-ray spectroscopy (EDX) employing a Hitachi HF2000 transmission electron microscope (TEM). It was equipped with a 200 kV cold field emission gun and an EDX spectrometer with a Si (Li) detector from Noran Instruments for point-resolved elemental analysis. EDX mapping of alloy nanoparticles were performed using JEOL 2200FS HR-TEM (Acceleration voltage of 200 kV) and an SSD-MaxN 80 TLE detector. For the investigations, a colloidal solution was deposited onto a carbon coated nickel lacey grid under inert gas atmosphere in a glove box. The particle size was determined by measuring the diameter using iTEM software.

The X-ray powder patterns for quantitative phase analysis were collected on a Stoe STADI P transmission diffractometer using Mo radiation (0.7093 Å). The instrument is equipped with a primary Ge (111) monochromator (MoKα_1) and a position sensitive Mythen1K detector. Data were collected in the range between 5 and 65° 2θ with a step width of 0.015° 2θ. Measuring times per step were varied between 50 and 100 s. For each sample, 8 scans were collected and summed after data collection. For the measurements, the colloidal solutions were concentrated by solvent evaporation and filled into glass capillaries (∅ 0.5 or 0.7 mm). For the analysis of the oxygen-free sample, the solvent was removed by condensation under Ar atmosphere. The capillary was sealed to avoid the contamination with oxygen during XRD measurements. Further samples for XRD were prepared from the sediment after centrifuging the air containing colloid solutions. Rietveld refinements were performed with the Program TOPAS, crystal structure data were taken from the ICSD database. [36]

Results

Ablating a copper target in the three liquids results in different colouration of the colloids. Nanoparticles synthesized in air-saturated water (H_2O_{air}) show a green-yellow colouration of the liquid, whereby the colour of acetone turned into brown after laser ablation of the copper target under ambient air. Interestingly, the colour of nanoparticles in oxygen-free water (H_2O_{Ar}) is blue-green (Figure 2), which differs from the colloid with molecular oxygen. This observation might give rise to the assumption, that particles with different properties are obtained. Zooming into the nanoscale, the particles show a different structure. TEM analysis of

the particles in H_2O_{air} show needle-like ~106 nm big nanostructures, which consist of smaller (~32 nm) agglomerated rectangular shaped crystallites surrounded by an amorphous part. In contrast to this, no large structures were found in H_2O_{Ar}, but only similar rectangular-shaped particles with an average size of 18 nm surrounded by a thin amorphous layer were found. Laser ablation of copper in acetone resulted in round small monodispersed nanoparticles (3 nm). However, larger particles (~ 40 – 100 nm) can be found sporadically in all samples.

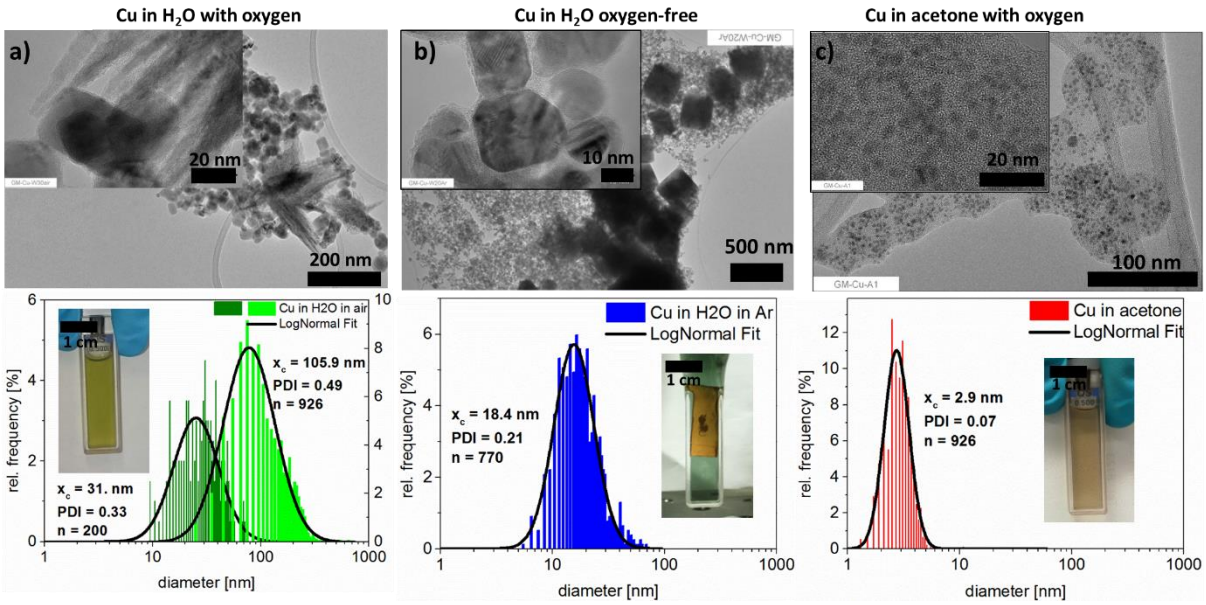

Figure 2: TEM micrographs, size histograms derived from TEM images and sample cuvettes of nanoparticles laser-synthesized in water under air (a), oxygen-free water (b) and acetone under air (c). Size distribution of the needle-like structures in (a) is shown in light green, while the histogram of the rectangular shaped nanoparticles is dark green.

Note that counting nanoparticles by TEM analysis is not representative for the entire sample, since only a small amount is analysed by this method. Also the different phases (Cu, Cu_2O or CuO) were not distinguished in the evaluation of the particle size. Only in case of nanoparticles in H_2O_{air}, the size (long side) of the needle-like structures were measured separately (Figure 2a, light green histogram). TEM-EDX analysis of this needle-like structures in H_2O_{air} suggests amorphous CuO (TableS1). However, a clear allocation of the mineral phases by EDX is not possible, since the formation of $Cu(OH)_x$ on the particles' surface may influence the Cu:O ratio signal. Furthermore, the analysis is performed on a small area that can lead to statistical inaccuracies. Thus, X-ray diffraction (XRD) that gives clear information of the amount of the present crystalline phases was carried out to obtain further structural information.

Rietveld refinement enables a quantitative analysis of the crystalline phases. To investigate the environmental impact on the particles' chemical composition, we calculated the amount of the

crystalline phases by Rietveld refinements, respectively. Figure 3 shows that nanoparticles in H_2O_{Ar} reveal a phase composition of Cu (25 wt%) and Cu_2O (75 wt%), whereas nanoparticles in H_2O_{air} have a lower content of elemental Cu (20.5 wt%) and are oxidized to Cu_2O (11.5 wt%) as well as to a higher oxidation state in CuO (68 wt%). These results show that particle oxidation is possible without the presence of molecular oxygen dissolved in water. Particles synthesized in acetone do not show Bragg reflections indicative of crystalline phases, which can be due to the low particle concentration of the sample or due to the small crystallites as shown by TEM (Figure 2). The colloidal solutions were concentrated by centrifugation (15000 RPM, Cut-Off 20 nm) and the fraction with larger crystallites was-measured by XRD. The particles do not show reflections of Cu (II), but only Cu_2O (54 wt%) and a higher Cu (46 wt%) content compared to the particles synthesized in aqueous solutions (Figure S9). Though molecular oxygen is present in acetone, the particles are less oxidized than in H_2O_{air} due to a stabilization by acetone molecules.

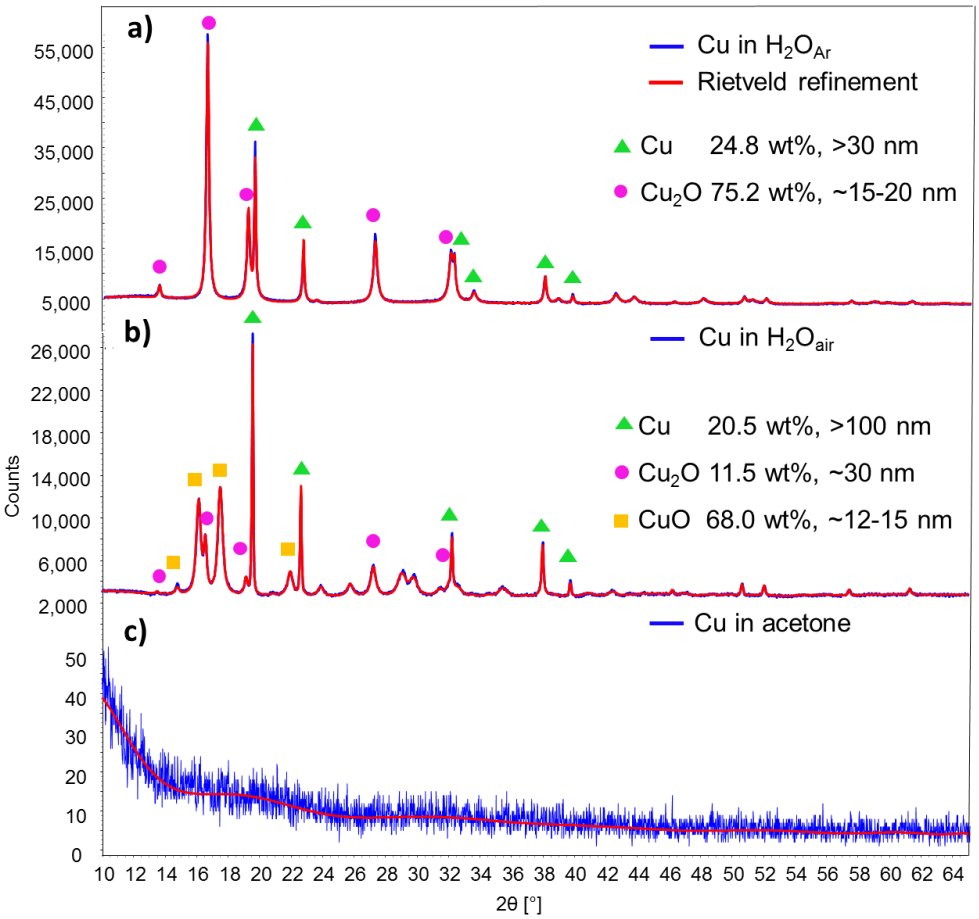

Figure 3: Rietveld refinement plots of the samples synthesized by laser ablation in in oxygen-free water (a), air-saturated water (b) and acetone (c). Blue curve: measured data, red curve: refined data in a) and b).

Our results show that particles synthesized in H_2O_{air} as well as in H_2O_{Ar} differ in their size and structure, as additionally to the rectangular-shaped nanoparticles also amorphous structures were detected, which are probably formed due to an ageing process (Figure S5, S6). The analyses show that molecular oxygen plays a minor role during particle synthesis. This is supported by the observations that Cu in acetone is less oxidized although the solubility of oxygen is much higher than in water.[37] However acetone molecules can be an issue as carbon atoms can be released in the plasma and act as a scavenger of oxygen. Furthermore, acetone molecules can be an issue as they can participate in the reactions and act as trapping agents during PLAL while the particles are formed. Since XRD analysis is a technique to study crystalline materials, other species such as amorphous materials or thin shells (e.g. of carbon on the particles' surface) cannot be detected with this method.

The detection of the three phases Cu, Cu_2O and CuO by XRD is in good agreement with UV-Vis spectroscopy in water, as well as the detection of Cu and Cu_2O in acetone. Laser-synthesized nanoparticles in acetone show a typical Cu extinction peak at ~575 nm (Figure 4). The extinction peak at about ~575 nm is well known for elemental Cu nanoparticles, which is due to the surface plasmon resonance (SPR) of the particles.[38],[39],[40] Furthermore an increase of a broad extinction in the UV region (<500 nm) is visible, that is often reported to be caused by charge transitions in Cu_2O, that must be formed on the particle surface.[41], [41], [42]

Main factors determining the peak position are the particle species e.g. metallic copper or oxidic particles and the particle size as well as their shape. Comparing the extinction spectra of particles in acetone with particles synthesized in water, the peaks of both -particles in H_2O_{air} and particles in H_2O_{Ar}- show a read-shift and broadening. This peak shift is probably caused by the presence of CuO and much larger and rectangular-shaped nanoparticles in water compared to the particles in acetone (Figure 2). Khashan et al. observed CuO particles (3-40 nm) by XRD analysis, which exhibit absorption peaks in UV-Vis spectra at ~ 275 nm and ~645 nm. This is in good agreement with the optical extinction spectra of the particles in H_2O_{air} .[43] The particles in H_2O_{Ar} do not show an extinction band in the UV-Vis region, indicating no CuO is optically detected, similarly to the XRD results. However a broadening of the spectra may occur due to the instability of the particles, which hamper the characterization. Furthermore, amorphous CuO species in XRD can not be excluded.

We could observe that the particles synthesized in oxygen-free water were less colloidal stable than particle in H_2O_{air} and thus forming agglomerates, which explains the broader extinction

band of Cu in H_2O_{Ar}. While nanoparticles in H_2O_{Ar} agglomerated shortly after ablation, nanoparticles in H_2O_{air} tend to agglomerate after a few days. The higher stability of particles synthesized in H_2O_{air} means, that the presence of molecular oxygen is favourable for colloidal stability due to the higher oxidation state on the particles surface causing electrostatic repulsion.[44]

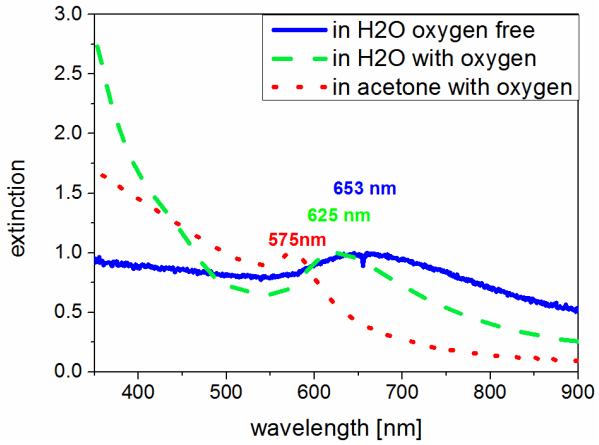

Figure 4: UV-Vis extinction spectra of laser-generated nanoparticles in oxygen-free water (blue solid line), air-saturated water (green dashed line) and acetone (red dotted line).

Moreover, Cu_2O can also cause a peak broadening in the IR region. Chang et al. studied plasmonic properties of copper nanoparticles.[38] Simulations and experimental analysis have shown, that a replacement of a 2 nm thin layer of Cu by Cu_2O results in a peak broadening and red-shift of the SPR-peak of copper, which is similar to the spectra observed in the current study. Similar finding were reported by Rice et al. They have synthesized metallic nanoparticles by wet-chemistry in an inert environment in toluene and monitored the effect of oxidation on the optical properties by means of adding a solvent containing dissolved oxygen.[39] By accurate acquisition of the extinction spectra with time, they have observed that the SPR peak of Cu disappears and an extinction peak of Cu_2O appears at ~715 nm. Due to a similar peak position and shape of the extinction spectra of particles in water our extinction spectra indicate the presence of Cu and Cu_2O. However, there is no clear evidence of core-shell particles but rather a mixture of both particle species, metals and oxides species.

In this study we investigate the role of oxygen in water on the particle oxidation. All methods clearly show different results in the particle structure when comparing the samples in different solvents. The question arises: What happens during laser ablation in liquids that leads to these different particles?

Discussion

If a laser hits a target, the material absorbs the laser pulse leading to a rapid heating and the formation of a plasma.[45] The target material evaporates and nuclei are formed already in a short time-scale, followed by a growth process which continues for hundreds of nanoseconds after the laser pulse. [45], [46], [47] Experimental studies show that nanoparticles are already formed in the vapour filled cavitation bubble, which then can grow further to larger structures.[48],[49] The formation of much smaller particles in acetone compared to the ones in water (Figure 2) suggests that the particle growth was quenched during the particle synthesis or within a short time scale, while particles in water were able to grow.

Ibrahimkutty and Wagener et al. examined dynamics of particle formation inside the cavitation bubble during pulsed laser synthesis. [48], [49]. A hemispherically shaped cavitation bubble is formed after the emission of a shockwave and starts to oscillate and finally collapses after a few hundred of microseconds.[50],[51] After the contraction of the bubble, a jet of outward moving material is formed which is clearly observed after the second collapse. Lam et al. recently calculated that the predominant portion of the cavitation bubble consists of solvent molecules rather than the ablated material. [52] The presence of solvent molecules in the cavitation bubble enables a reaction during the particle formation between acetone molecules, which decomposed previously in the plasma at high temperatures.

Boyer and Meunier, who performed a systematic study with several alcohols and ketones, investigated the influence of the solvent during PLAL on the particle size.[53] They could observe that the particle size decreased with decreasing solvent polarity. This was attributed to a stronger weakening of the particle surface charge in polar solvents than in less polar ones. Rehbock et al, who investigated the influence of several anions on the particle size and stability, also demonstrated the significance of the anions polarization.[17] They have shown that the presence of chaotropic anions, which have high polarizability, results in smaller and more stable particles compared to particles synthesized in the presence of small anions with a low polarizability (cosmotropes). Hence low solvent polarity alone cannot explain why nanoparticles synthesized in acetone are much smaller than those synthesized in water. However, in case of acetone the adsorption of molecules and the effect, that they can be subjected to carbonisation at high temperature, is notable. Our observations indicate that the adsorption of acetone enolate groups or pyrolyzed carbonic species on the particle surfaces prevents particle agglomeration (Figure S10). The existence of enolate groups bounded on metal oxide surfaces[54],[55] or on organometallic complexes[56] of Pt and Pd was reported in the literature on the basis of infrared spectroscopy measurements of acetone. Also in case of laser synthesized particles (1064 nm), Giorgetti et al. characterized gold nanoparticles in acetone by

Raman spectroscopy and could observe vibration signals of enolate groups on the particles' surface.[57] Furthermore they could show that graphitic carbon is present if the particles are re-irradiated with a wavelength of 532 nm. Cristoforetti et al. observed different colloidal stability tendencies if working with acetone or toluene, which was also assigned to the different solvent polarities. They have synthesized Pd nanoparticles using 1064 nm and noticed a stronger formation of an amorphous carbon shell on the particles by using solvents with a high carbon content such as toluene or n-hexane.[58] Obviously not only the laser parameter such as the wavelength, but also the type of the solvent plays a crucial role. In the current work, we ablated Cu with 1064 nm in acetone, a solvent containing a low carbon content compared to toluene. However, similar to the previous work a matrix surrounding the Cu nanoparticles in acetone is visible by TEM indicating the presence of amorphous carbon (Figure 2).[58] Furthermore, we could observe that some particles exhibit a thin graphitic layer on the particle surface, which is more pronounced for larger particles, similar to what was observed by Amendola et al. after irradiation of Au in toluene.[59] On the other hand, when synthesizing gold nanoparticles in acetone no graphitic layer was observed.[57] Obviously, Cu features certain properties that triggers the formation of carbon-encapsulated Cu nanoparticles at 1064 nm PLAL in acetone. We think that Cu catalyses the formation of graphite, because Cu is an efficient catalyst to form carbon-carbon bonds for reactions e.g. such as Ullmann reactions and Diels-Alder reaction.[60],[61] Furthermore, Cu and Ni are the most widely used catalysts in chemical vapour deposition for graphene formation.[62],[63] In literature a formation of onion-like carbon-encapsulated Co_3C nanoparticles by laser ablation in acetone was explained by a catalytic cracking of the solvent molecules.[64] The authors explain that the carbon layer growth is initiated by the supersaturation of carbon atoms in the carbide core. However the layers observed in our study are much smaller if comparing similar particle sizes and furthermore no Cu-carbides could be analysed by XRD (Figure 4, Figure S9). Hence the formation of the graphite layer around Cu nanoparticles in acetone is likely due to the decomposition of the solvent on Cu and CuO surfaces at high temperatures and a subsequent catalysed formation of graphitic structures. Alternative hypothesis according Nakamura is that carbon species are formed after segregation from the bulk to the particles' surface. [65] The appearance of the carbon layers may result from the generation of carbon ions and atoms as well as CH_3 and CO radicals[64] at extreme conditions provided by the PLAL induced plasma. The inter-shell distance between the carbon shells ranges from 0.38 to 0.44 nm. In comparison to graphite, which has an inter-shell spacing of 0.34 nm[66], the distances of the graphitic shells on laser-generated nanoparticles correspond to an expanded graphite lattice. This can be explained by

the fact, that the particles have a high curvature, due to the small particle size. Kiang et al. studied the size effect in carbon nanotubes and concluded that an increased curvature results in an increased repulsive force, associated with a decreased shell diameter.[67] For validation of a graphitic species on laser-generated nanoparticles, we performed Raman spectroscopy. The results clearly show the presence of graphitic species (Figure S11). In relation to catalysis, a graphitized carbon-layer structure can facilitate hydrogenation reactions, as shown by Kim et al. on the example of a model reaction. In this case, the reduction of nitrobenzene to aniline on carbon-encapsulated palladium particles revealed higher conversion efficiencies than their bare palladium counterparts.[68]

Since no dissolved oxygen was present in H_2O_{Ar} and copper nanoparticles are readily oxidized, reactive oxygen species due to the decomposition of water molecules in the reactive plasma during laser ablation must be responsible for the oxidation.[69] The ionization and vaporization of water at the plume-liquid interface takes place due to the high temperature of a plasma plume. This plasma plum arises if the laser beam hits a target with a fluence higher than the threshold of the target material. This results in ablation of the material, where water is converted into vapour, molecular and atomic hydrogen or oxygen. Consequently, chemical reactions between the reactive water species and the ablated material can take place. Possible reactive species as a product of the decomposition of water are OH radicals.

Comparing the ionization energy threshold of H_2O (12.62 eV) with the electron energy (~ 0.65 eV, SI), the direct ionization of water is unlikely, as well as of the predominantly present gases nitrogen (14.53 eV) and oxygen (13.62 eV) in air in case of H_2O_{Air}. In case of H_2O_{Ar}, argon was purged before and during particle synthesis. The gas dissolved in water may influence the formation mechanism of reactive $OH^{\cdot}$. Argon can generate water ions through Penning ionization, which refers to an ionization of a molecule by an electronically excited atom. [70], [71]:

$$\boldsymbol{Ar^* + H_2O \rightarrow Ar + H_2O^+ + e^-} \qquad \textbf{Eq. 1}$$

A dissociative recombination of water ions then can lead to the formation of $OH^{\cdot}$.

$$e^- + H_2O^+ \rightarrow OH^{\cdot} + H^{\cdot} \qquad \textbf{Eq. 2}$$

Alternatively and most likely in H_2O_{Air}, water splitting into O_2 and H_2 at high temperatures could have an effect on the particle oxidation. A direct thermal dissociation of water requires about 1300-1900K[72], which is easily to reach in the laser induced plasma with ~ 5000 K.[35] Evidence of H_2 formation by (femtosecond) laser ablation of water has been given by Maatz et al.[69]

In summary, Figure 5 shows a scheme of the possible mechanisms for the PLAL particle synthesis in H_2O_{air}, H_2O_{Ar} and acetone. In both aqueous solvents, oxygen from the decomposition of H_2O molecules is responsible for the oxidation of laser-generated nanoparticles. As H_2O_{air} contains dissolved oxygen, the oxidation potential is higher compared to the oxygen-free water H_2O_{Ar}, leading to a post-oxidation after laser ablation. The rectangular shaped 30 nm large Cu and Cu_2O particles disappeared while ~109 nm amorphous large nanostructures are observed (Figure S6). Observation by TEM/EDX in H_2O_{air} of small (~5 nm) sized crystallites within the amorphous structures (Figure S7) strengthens the thought, that the larger rectangular particles (31 nm) somehow degrade with time.

The ripening process of these structures is already observed on the freshly prepared particles, where a thin amorphous layer on the particle surface is formed (Figure S5). These observations clearly show that particle oxidation in H_2O_{air} continues, which is favoured due to the presence of molecular oxygen, since oxidation of nanoparticles in H_2O_{Ar} seems to be less pronounced (Figure S2).

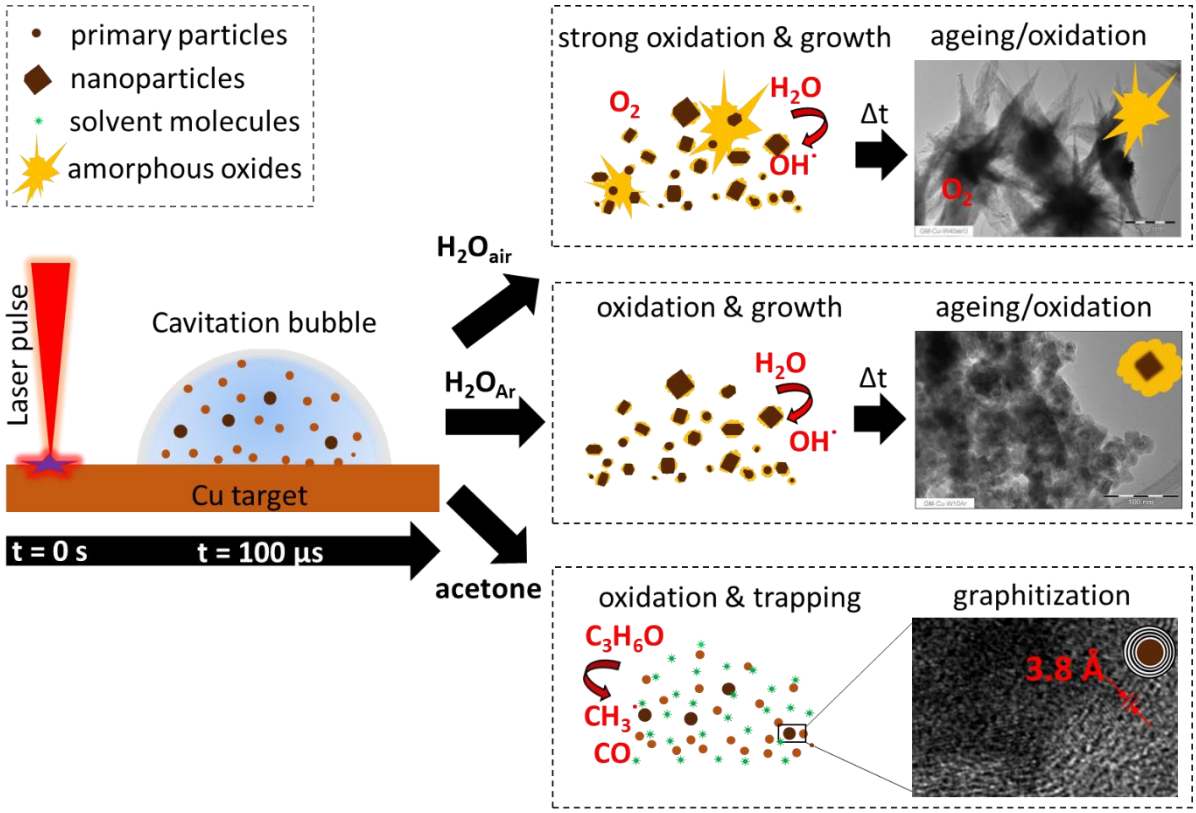

Figure 5: Scheme of the synthesis of Cu_xO_y and $PtCu_3$ nanoparticles during laser synthesis in H_2O_{air}, H_2O_{Ar} and acetone.

We exposed the nanoparticles synthesized in H_2O_{Ar} to air for one day and re-measured them in TEM. The images (in Figure S4) show that the particles did not significantly change after one

day. Comparing these particles with the freshly prepared colloid in H_2O_{air}, where large amorphous needle like structures where found, it is suggested that their formation was favoured by the high temperatures during PLAL additionally to the molecular oxygen. As soon as needle-shaped $Cu(OH)_2$ formation takes place, a continuous oxidation and restructuring proceeds, as nanoparticles in H_2O_{air} form these structures directly after PLAL. Nevertheless, it should be noted that no kinetic studies were done here, thus clear evidences to kinetics are needed to confirm this hypothesis, not being focus of our study.

By means of TEM analysis the formation of the needle- like structures can be concluded. Different kind of particle species were observed in $H_2O_{air.}$ As can be seen in Figure 6 large spherical particles seem to dissolve and form smaller irregular shaped nanoparticles. Finally they decompose and grow to needles.

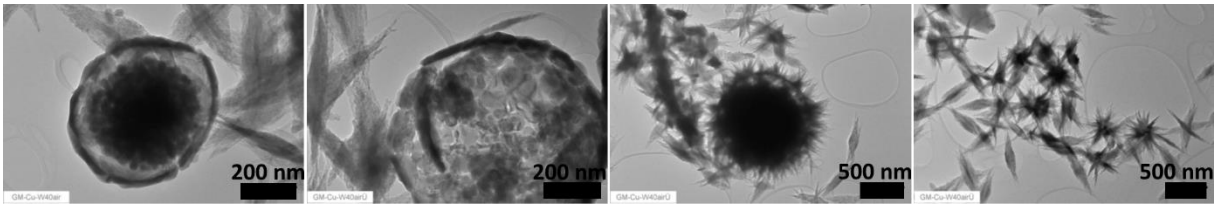

Figure 6: TEM images of several particle species synthesized by PLAL of Cu in air-saturated water suggests the development of the formation of needle structures.

In case of laser ablation of Cu in acetone, we have observed small Cu and Cu_2O nanoparticles (Figure 2 and Figure S8). Having a closer look on the reactions in Eq.2 and Eq. 3, one can see that the presence of water provides the reactive OH species. Since acetone usually contains water (although less than the other used solvents here), oxidation of the particles is conceivable as shown by UV-Vis and XRD. However, acetone seems to have a stabilizing effect and leads to less oxidized nanoparticles. In addition the particle growth is impeded due to the presence of stabilizing groups - probably carbonyl groups or other carbonic species due to solvent pyrolysis.[59],[62],[63],[64] For instance a graphitic shell was observed around some larger nanoparticles, that can prevent further oxidation of the particles (Figure S10). However, further investigations would be necessary to statistically identify the size dependence of the nature of the carbonaceous shell.

To demonstrate the significance of the solvent on further studies, e.g. towards catalysis, we investigated the influence of the solvent on alloy formation. We prepared a $PtCu_3$ target according to a previous approach [25] and laser-generated nanoparticles in H_2O_{air} and acetone.

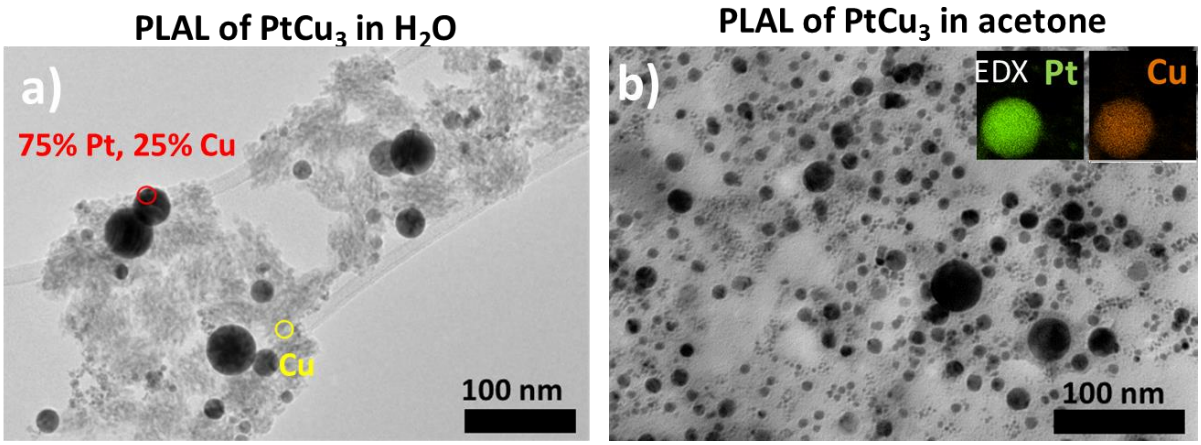

Figure 7: TEM images and EDX mapping of nanoparticles synthesized by PLAL of a $PtCu_3$ target in air-saturated water (a) and acetone (b), respectively.

TEM images clearly show the analogy between Cu nanoparticles produced in the respective solvents (Figure 2, Figure 7 and S5). Similar to the Cu particles synthesized in acetone, carbon-encapsulated $PtCu_3$ nanoparticles were found in acetone (Figure S12). While more uniformly distributed, spherical nanoparticles were formed in acetone, we found two different nanostructures in water. EDX analysis revealed that platinum rich spherical particles are formed in H_2O_{air}. The larger needle-like structures with a lower contrast consist of CuO. In contrast to this, homogeneous $PtCu_3$ alloy formation of nanoparticles in acetone (Figure 7, Figure S12). Obviously, the oxygen in water molecules does not only influence the oxidation of the particles, but also the alloy formation as a consequence of the alloy's Cu oxidation. Thus, these results illustrate the importance of the choice of the solvent when synthesizing Cu-based nanoparticles by PLAL.

Conclusion

We precisely differentiated the influence of molecular oxygen and oxygen from water molecules on the particle oxidation during laser-ablation of Cu in oxygen-free water, air-saturated water and acetone. A mixture of metallic copper and copper oxide nanoparticles were analysed in air-saturated water and in water under exclusion of oxygen. Our observations show that nanoparticle oxidation during laser synthesis is mainly caused by reactive oxygen species due to the decomposition of water molecules. On a longer time-scale after synthesis, molecular oxygen may influence the subsequent particle ageing, as continuing oxidation and change in the particle structure in air-saturated water were observed. The number weighted size distribution (TEM) of nanoparticles in acetone were much smaller (3 nm) than in water since their growth was quenched due to the presence of acetone molecules. Due to the extreme conditions during PLAL in the plasma, decomposition of the organic solvent to reactive carbon

species can take place and result in nanoparticles surrounded by a carbon matrix. The formation of a graphitic layer on the particles' surface, in particular on larger particles (>20 nm), is probably due to a copper-catalysed reaction to form carbon-carbon bonds. The significant effect of the solvent was confirmed for synthesizing copper-based alloy nanoparticles. While separated or segregated nanoparticles were formed in air-saturated water, homogeneous $PtCu_3$-alloy particle formation was obtained in acetone. Hence, it is the chemical reaction with the solvent molecules that determines final nanoparticle composition and oxidation, rather than dissolved gas. In future works the influence of the different particle surface, e.g. effect of the carbidic shell, on catalytic properties should be investigated.

Acknowledgements

The authors gratefully acknowledge the financial support of the German Federal Ministry of Education and Research (BMBF) within the young investigator competition NanoMatFutur (project INNOKAT, FKZ 03X5523). We are grateful to Nicolas Wöhrl for the measurements and discussion of the Raman spectra. Thanks to Prof. Junji Nakamura for discussing the formation of the carbon shell. We also thank Dr. Michael Felderhoff for preparing the oxygen-free water and giving us the instructions. For the EDX mapping analysis of alloy nanoparticles we would like to thank Dr. Markus Heidelmann from the Team of Interdisciplinary Center for Analytics on the Nanoscale (ICAN) at the University of Duisburg-Essen.

Literature

[1] R. T. Kung, R. B. Stewart, and M. Rosenberg, "Laser welding system," Sept. 2 **1997**. *US Patent* 5, 662,643.

[2] M. Yamada, "Laser cutting process," Dec. 20 **1994**. US Patent 5,374,803.

[3] D. Zhang, B. Gökce, S. Sommer, R. Streubel, and S. Barcikowski, *Appl. Surf. Sci.* **2016**, *367*, 222–230

[4] J. G. Dunne, "Laser surveying instrument," Mar. 1 **1994**. US Patent 5,291,262.

[5] C.-C. Hou, S. Cao, W.-F. Fu, and Y. Chen, *ACS Appl. Mater. Interfaces* **2015**, *7*, 51, 28412–28419

[6] H. Lubatschowski, A. Heisterkamp, F. Will, J. Serbin, T. Bauer, C. Fallnich, H. Welling, W. Mueller, B. Schwab, A. I. Singh, W. Ertmer, *SPIE Proc.* **2002**, *4633*, 38–49

[7] S. Barcikowski and G. Compagnini, *Phys. Chem. Chem. Phys.* **2013**, *15*, 9, 3022–3026.

[8] C. Rehbock, J. Jakobi, L. Gamrad, S. van der Meer, D. Tiedemann, U. Taylor, W. Kues, D. Rath, and S. Barcikowski, *Beilstein J. Nanotechnol.* **2014**, *5*, 1, 1523–1541

[9] R. Streubel, S. Barcikowski, and B. Gökce, *Opt. Lett.* **2016**, *41*, 7, 1486–1489

[10] R. Streubel, G. Bendt, and B. Gökce, *Nanotechnology* **2016**, *27*, 20, 205602

[11] J. Zhang, M. Chaker, and D. Ma, *J. Colloid Interface Sci.* **2016**, *489*, 138–149

[12] H. Muto, K. Yamada, K. Miyajima, and F. Mafune, *J. Phys. Chem. C*, **2007**, *111*, 17221–17226

[13] J. P. Sylvestre, S. Poulin, A. V. Kabashin, E. Sacher, M. Meunier, and J. H. T. Luong, *J. Phys. Chem. B*, **2004**, *108*, 43, 16864–16869

[14] M. Fischer, J. Hormes, G. Marzun, P. Wagener, U. Hagemann, and S. Barcikowski, *Langmuir* **2016**, *32*, 35, 8793–8802

[15] F. Mafune, J. Y. Kohno, Y. Takeda, T. Kondow, and H. Sawabe, *J. Phys. Chem. B*, **2000**, *104*, 39, 9111–9117

[16] V. Amendola and M. Meneghetti, *J. Mater. Chem.*, **2007**, *17*, 4705–4710

[17] C. Rehbock, V. Merk, L. Gamrad, R. Streubel, and S. Barcikowski, *Phys. Chem. Chem. Phys.*, **2013**, *15*, 3057–3067

[18] G. Marzun, J. Nakamura, X. Zhang, S. Barcikowski, and P. Wagener, *Appl. Surf. Sci.* **2015**, *348*, 75–84

[19] J. Jakobi, A. Menendez-Manjon, V. S. K. Chakravadhanula, L. Kienle, P. Wagener, and S. Barcikowski, *Nanotechnology*, **2011**, *22*, 145601

[20] J. Zhang, D. N. Oko, S. Garbarino, R. Imbeault, M. Chaker, A. C. Tavares, D. Guay, and D. Ma, *J. Phys. Chem. C*, **2012**, *116*, 13413–13420

[21] D. N. Oko, J. Zhang, S. Garbarino, M. Chaker, D. Ma, A. C. Tavares, and D. Guay, *J. Power Sources*, **2014**, *248*, 273–282

[22] A. Neumeister, J. Jakobi, C. Rehbock, J. Moysig, and S. Barcikowski, *Phys. Chem. Chem. Phys.*, **2014** , *16*, 23671–23678

[23] J. Jakobi, S. Petersen, A. Menendez-Manjon, P. Wagener, and S. Barcikowski, *Langmuir*, **2010** , *26*, 6892–6897

[24] S. Barcikowski, T. Baranowski, Y. Durmus, U. Wiedwald, and B. Gökce, *J. Mater. Chem. C*, **2015**, *3*, 41, 10699–10704

[25] G. Marzun, A. Levish, V. Mackert, T. Kallio, S. Barcikowski, and P. Wagener, *J. Colloid Interface Sci.* **2016**, *489*, 57–67

[26] P. Wagener, J. Jakobi, C. Rehbock, V. S. K. Chakravadhanula, C. Thede, U. Wiedwald, M. Bartsch, L. Kienle, and S. Barcikowski, *Sci. Rep.* **2016** , *6*, 1–12

[27] G. Ertl, H. Knozinger, F. Schuth, and J. Weitkamp, "Handbook of heterogeneous catalysis," *Wiley-VCH*, **2008**, 8 volumes.

[28] BASF Aktiengesellschaft, "Verfahren" Mar. 2 **1980**, *Patent* EP0033880, DE3004436A1, US4354045.

[29] S. Sá, H. Silva, L. Brandão, J. M. Sousa, and A. Mendes, *Appl.Catal., B.* **2010**, *99*, 1, pp. 43–57

[30] C. W. Roske, J. W. Lefler, and A. M. Müller, *J. Colloid Interface Sci.* **2016**, *489*, 68–75

[31] A. Tyurnina, V. Y. Shur, R. Kozin, D. Kuznetsov, V. Pryakhina, and G. Burban, *Phys. Solid State*, **2014**, *56*, 7, 1431–1437

[32] C. A. Schaumberg, M. Wollgarten, and K. Rademann, *J. Phys. Chem. A.* 2014, *118*, 37, 8329–8337

[33] R. Tilaki, A. Iraji zad, S. Mahdavi, *Appl. Phys. A.* **2007**, *88*, 2, 415–419

[34] K. Amikura, T. Kimura, M. Hamada, N. Yokoyama, J. Miyazaki, and Y. Yamada, *Appl. Surf. Sci.* **2008**, *254*, 21, 6976–6982

[35] J. Lam, D. Amans, F. Chaput, M. Diouf, G. Ledoux, N. Mary, K. Masenelli-Varlot, V. Motto-Ros, and C. Dujardin, *Phys. Chem. Chem. Phys.* 2014, *16*, 3, 963–973

[36] B. AXS, "Topas v5: General profile and structure analysis software for powder diffraction data.- user's manual." Karlsruhe, Germany, **2014**.

[37] H. L. Clever, R. Battino, H. Miyamoto, Y. Yampolski, C. L. Young, *J. Phys. Chem. Ref. Data*, **2014**, *43*, 3, 033102

[38] G. H. Chan, J. Zhao, E. M. Hicks, G. C. Schatz, and R. P. Van Duyne, *Nano Lett.* 2007, *7*, 7, 1947–1952

[39] K. P. Rice, E. J. Walker Jr, M. P. Stoykovich, and A. E. Saunders, J. *Phys. Chem. C*, **2011**, *115*, 5, 1793–1799

[40] B. Gökce, D. D. van't Zand, A. Menéndez-Manjón, and S. Barcikowski, *Chem. Phys. Lett.* **2015**, *626*, 96–101

[41] M. Zahmakran, S. Özkar, T. Kodaira, and T. Shiomi, *Mater. Lett.* **2009**, *63*, no. 3, pp. 400–402

[42] M. D. Susman, Y. Feldman, A. Vaskevich, and I. Rubinstein, "Chemical deposition and stabilization of plasmonic copper nanoparticle films on transparent substrates," *Chem. Mater.* **2012**, *24*, no. 13, pp. 2501–2508

[43] K. S. Khashan, G. M. Sulaiman, and F. A. Abdulameer, *Arabian J. Sci. Eng.* **2016**, *41*, no. 1, pp. 301–310

[44] N. Bärsch, J. Jakobi, S. Weiler, and S. Barcikowski, *Nanotechnology*, **2009**, *20*, 44, 445603

[45] V. Amendola and M. Meneghetti, *Phys. Chem. Chem. Phys.* **2013**, *15*, 3027–3046

[46] C.-Y. Shih, C. Wu, M. V. Shugaev, and L. V. Zhigilei, *J. Colloid Interface Sci.* **2016**, *489*, 3–17

[47] V. Amendola and M. Meneghetti, *Phys. Chem. Chem. Phys.* **2009**, *11*, 20, 3805–3821

[48] P. Wagener, S. Ibrahimkutty, A. Menzel, A. Plech, and S. Barcikowski, *Phys. Chem. Chem. Phys.***2013**, *5*, 3068–3074

[49] S. Ibrahimkutty, P. Wagener, T. dos Santos Rolo, D. Karpov, A. Menzel, T. Baumbach, S. Barcikowski, and A. Plech, *Sci. Rep.* **2015**, *5*, 1–11

[50] A. Vogel, W. Lauterborn, and R. Timm, *J. Fluid Mech.* **1989**, *206*, 299–338

[51] K. Sasaki, T. Nakano, W. Soliman, and N. Takada, *Appl. Phys. Express*, **2009**, *2*, p. 046501

[52] J. Lam, J. Lombard, C. Dujardin, G. Ledoux, S. Merabia, and D. Amans, *Appl. Phys. Lett.* **2016**, *108*, 7, 074104

[53] P. Boyer and M. Meunier, *J. Phys. Chem. C* **2012**, *116*, 14, 8014–8019

[54] B. E. Hanson, L. F. Wieserman, G. W. Wagner, and R. A. Kaufman, *Langmuir* **1987**, *3*, 4, 549–555

[55] M. Zaki, M. Hasan, F. Al-Sagheer, and L. Pasupulety, *Langmuir* **2000**, *16*, 2, 430–436

[56] J. Vicente, J. A. Abad, M.-T. Chicote, M.-D. Abrisqueta, J.-A. Lorca, and M. C. Ramrez de Arellano, *Órganometallics* **1998**, *17*, 8, 1564–1568

[57] E. Giorgetti, M. Muniz-Miranda, P. Marsili, D. Scarpellini, and F. Giammanco, *J. Nanopart. Res.* **2012**, *14*, 1, 1–13

[58] G. Cristoforetti, E. Pitzalis, R. Spiniello, R. Ishak, F. Giammanco, M. Muniz-Miranda, and S. Caporali, *Appl. Surf. Sci.* **2012**, *258*, 3289– 3297

[59] V. Amendola, G. A. Rizzi, S. Polizzi, and M. Meneghetti, *J. Phys. Chem. B.* **2005**, *109*, 23125–23128

[60] I. P. Beletskaya and A. V. Cheprakov, *Coord. Chem. Rev.* **2004**, *248*, 21, 2337–2364

[61] S. Reymond and J. Cossy, *Chem. Rev.* **2008**, *108*, no. 12, pp. 5359–5406

[62] M. Kalbac, O. Frank, and L. Kavan, *Carbon* **2012**, *50*, 10, 3682–3687

[63] X. Li, W. Cai, J. An, S. Kim, J. Nah, D. Yang, R. Piner, A. Velamakanni, I. Jung, E. Tutuc, *et al.*, *Science*, **2009**, *324*, 5932, 1312–1314

[64] H. Zhang, C. Liang, J. Liu, Z. Tian, and G. Shao, *Carbon*, **2013**, *55*, 108–115

[65] L. Ni, K. Kuroda, L.-P. Zhou, T. Kizuka, K. Ohta, K. Matsuishi, and J. Nakamura, "Kinetic study of carbon nanotube synthesis over mo/co/mgo catalysts," *Carbon*, **2006**, *44*, 11, 2265–2272

[66] M. J. McAllister, J.-L. Li, D. H. Adamson, H. C. Schniepp, A. A. Abdala, J. Liu, M. Herrera-Alonso, D. L. Milius, R. Car, R. K. Prud'homme, I.. Aksay, *Chem. Mater.* **2007**, *19*, 18, 4396–4404

[67] C.-H. Kiang, M. Endo, P. Ajayan, G. Dresselhaus, and M. Dresselhaus, *Phys. Rev. Lett.* **1998**, *81*, 9, 1869

[68] Y.-j. Kim, R. Ma, D. A. Reddy, and T. K. Kim, *Appl. Surf. Sci.* **2015**, *357*, 2112–2120

[69] G. Maatz, A. Heisterkamp, H. Lubatschowski, S. Barcikowski, C. Fallnich, H. Welling, and W. Ertmer, *J. Opt. A: Pure Appl. Opt.* **2000**, *2*, 1, 59

[70] N. Srivastava and C. Wang, *J. Appl. Phys.* **2011**, *110*, 5, 053304

[71] D.-X. Liu, P. Bruggeman, F. Iza, M.-Z. Rong, and M. G. Kong, *Plasma Sources Sci. Technol.* **2010**, *19*, 2, 025018

[72] R. T. Jongma, M. G. Boogaarts, I. Holleman, and G. Meijer, *Rev. Sci. Instrum.* **1995**, *66*, 4, 2821–2828

1. Synthesis and functionality of laser-generated alloy nanoparticles for electrochemical catalysis

Even though platinum is the most effective electrocatalyst, it is a scarce and expensive noble metal. Finding an inexpensive and efficient replacement of platinum offers enormous possibilities for clean energy[1], [2], [3], [4]. The adsorption enthalpy of an elementary step during a catalytic reaction depends on the electronic structure of the catalyst and can be tuned by doping or alloying at least two metals to trigger synergetic effects. Due to an optimization of binding energies between catalyst and adsorbates, according to the Sabatier principle, alloy nanoparticles show outstanding catalytic activities, and they are therefore promising materials in electro catalysis[5], [6], [7]. Synthesizing alloy nanoparticles by wet-chemical routes such as wet-impregnation enables a fine control of the metal composition. However, the synthesis parameters are often difficult to transfer to other metals, and changing metals usually requires a great deal of time and effort[8]. In the following chapter, an alternative to wet-chemical methods for the synthesis of alloy nanoparticles will be demonstrated. Due to the novelty of Pulsed Laser Ablation in Liquids (PLAL) in the area of bimetallic nanoparticles[9], a new efficient and convenient method for the synthesis of alloy nanoparticles needs to be further established and verified by catalytic functionality. So far, the subsequently described method was applied only for noble metals (e.g., PtAu), which do not show a tendency to oxidation. To draw economic benefits from supplementary active materials, the investigation of such non-noble metals is essential.

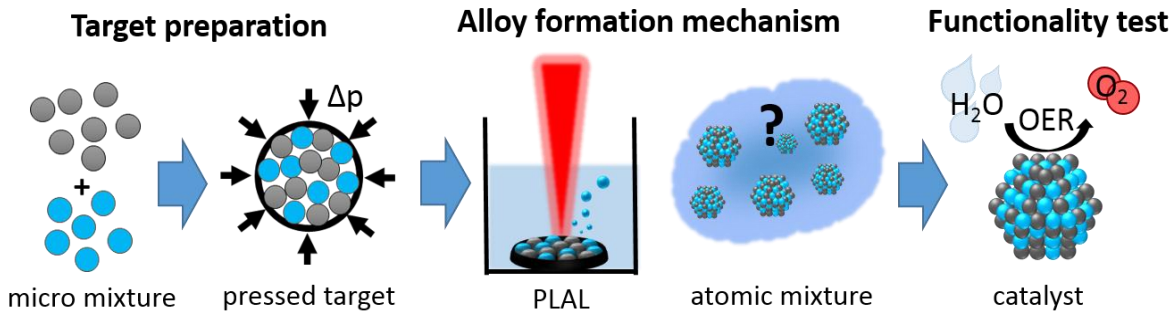

Fig. A3: Schematic illustration of issues that need to be explored for the defined synthesis of cost-efficient active catalysts

Chapter 5.1 demonstrates that PLAL is a useful method to synthesize active nanoalloys from cheap starting materials. For this, targets consisting of a mixture of two metals' powders are used instead of more expensive bulk alloy targets. This novel approach can be readily extended

to the preparation of other alloys, whose bulk targets are not available; therefore, this is of great technical importance for the synthesis of nanoalloys with exotic compositions and metals. After extensive studies on the surface of laser-generated nanoparticles and a demonstration of the solvent effect on $PtCu_3$ alloy formation in chapter 4, the influence of the solvent on alloy formation consisting of the non-noble metals nickel and molybdenum will be presented in this chapter. This chapter will show that segregated alloys synthesized in pure water exhibit superior catalytic activities that are higher than their monometallic counterparts due to synergetic effects. Furthermore, as already shown and discussed in chapter 4.2, using examples of nickel-molybdenum nanoparticles, pulsed laser ablation in acetone will be shown to provide smaller and more monodisperse nanoparticles.

Literature

[1] O. T. Holton and J. W. Stevenson, "The role of platinum in proton exchange membrane fuel cells," *Platinum Metals Review*, vol. 57, no. 4, pp. 259–271, **2013**.

[2] F. Safizadeh, E. Ghali, and G. Houlachi, "Electrocatalysis developments for hydrogen evolution reaction in alkaline solutions–a review," *international journal of hydrogen energy*, vol. 40, no. 1, pp. 256–274, **2015**.

[3] R. Bashyam and P. Zelenay, "A class of non-precious metal composite catalysts for fuel cells," *Nature*, vol. 443, no. 7107, pp. 63–66, **2006**.

[4] M. G. Walter, E. L. Warren, J. R. McKone, S. W. Boettcher, Q. Mi, E. A. Santori, and N. S. Lewi, "Solar water splitting cells," *Chem. Rev.*, vol. 110, pp. 6446–6473, **2010**.

[5] E. Antolini, "Carbon supports for low-temperature fuel cell catalysts," *Applied Catalysis B: Environmental*, vol. 88, no. 1, pp. 1–24, **2009**.

[6] J. C. Meier, C. Galeano, I. Katsounaros, J. Witte, H. J. Bongard, A. A. Topalov, C. Baldizzone, S. Mezzavilla, F. Schüth, and K. J. Mayrhofer, "Design criteria for stable pt/c fuel cell catalysts," *Beilstein journal of nanotechnology*, vol. 5, no. 1, pp. 44–67, **2014**.

[7] B. Hammer and J. K. Nørskov, "Theoretical surface science and catalysis—calculations and concepts," *Advances in catalysis*, vol. 45, pp. 71–129, **2000**.

[8] B. M. Hunter, H. B. Gray, and A. M. Muller, "Earth-abundant heterogeneous water oxidation catalysts," *Chemical reviews*, vol. 116, no. 22, pp. 14120–14136, **2016**.

[9] J. Zhang, M. Chaker, and D. Ma, "Pulsed laser ablation based synthesis of colloidal metal nanoparticles for catalytic applications," *Journal of Colloid and Interface Science*, vol. 489, pp. 138–149, **2016**.

1.1. Laser synthesis, structure and chemical properties of colloidal nickel-molybdenum nanoparticles for the substitution of noble metals in heterogeneous catalysis

Reprinted from Journal of Colloid and Interface Science, 489, Galina Marzun, Alexander Levish, Viktor Mackert, Tanja Kallio, Stephan Barcikowski, Philipp Wagener, "Laser synthesis, structure and chemical properties of colloidal nickel-molybdenum nanoparticles for the substitution of noble metals in heterogeneous catalysis", 57-67, *Copyright (2017), with permission from Elsevier.*

Abstract

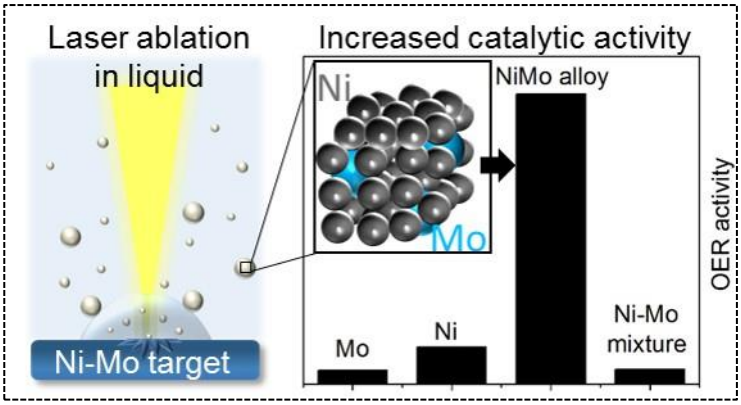

Platinum and iridium are rare and expensive noble metals that are used as catalysts for different sectors including in heterogeneous chemical autocatalysis and electrochemical energy conversion. Nickel and its alloys are promising materials to substitute noble metals. Nickel based materials are cost-effective with good availability and show comparable catalytic performances. The nickel-molybdenum system is a very interesting alternative to platinum in water electrolysis. We produced ligand-free nickel-molybdenum nanoparticles by laser ablation in water and acetone. Our results show that segregated particles were formed in water due to the oxidation of the metals. X-ray diffraction shows a significant change in the lattice parameter due to a diffusion of molybdenum atoms into the nickel lattice with increasing activity in the electrochemical oxygen evolution reaction. Even though the solubility of molecular oxygen in acetone is higher than in water, there were no oxides and a more homogeneous metal distribution in the particles in acetone as seen by TEM-EDX. This showed that dissolved molecular oxygen does not control oxide formation. Overall, the laser ablation of pressed micro particulate mixtures in liquids offers a combinational synthesis approach that allows the screening of alloy nanoparticles for catalytic testing and can convert micro-mixtures into nano-alloys.

Introduction

About 90% of all chemical production processes require a catalyst on their synthesis pathway to allow targeted production of many products; the major part is heterogeneously catalysed [1]. Heterogeneous catalysis is not only important in the chemical industry (e.g. ammonia synthesis by Haber-Bosch process or production of nitric acid by Ostwald process) but also in exhaust cleaning or energy conversion. Hydrogen is an essential energy carrier and can be produced from renewable energy sources by water electrolysis or from fossil resources during steam reforming. The use of hydrogen as a green energy carrier offers many energy applications.

For example, hydrogen from solar production can be stored on site and used at night. The hydrogen produced by wind or solar power is a clean energy carrier and can be stored cost-effectively in large quantities for long periods. Electrolysers can be placed at hydrogen refuelling stations to facilitate the generation of fuel. In addition, hydrogen can be supplied to the industry as a feedstock or used in households as seasonal energy storage, heat, or backup power [2]. Electrolysers can operate with fluctuating electrical input and can be performed intermittently, and they are well suited to being coupled with variable sources of renewable energies. Alkali electrolysers convert water into hydrogen and oxygen following the cathodic hydrogen evolution reaction (HER, $2H_2O + 2e^- \rightarrow H_2 + 2OH^-$) and anodic oxygen evolution reaction (OER, $4OH^- \rightarrow O_2 + 2H_2O + 4e^-$), respectively [3] . Finally, using hydrogen in fuel cells eliminates greenhouse gases over the entire cycle: hydrogen reacts with oxygen to produce water and releases the stored energy. However, to make water splitting viable on the industrial level, the stability of the electrodes and the high overpotential of HER and OER must be improved. Typically, the efficiency of water electrolysis is limited by OER, which requires the transfer of four electrons to form one oxygen molecule. This results in slow kinetics i.e. high over-potential [4], [3], [5]. Over-potentials can be lowered using bimetallic alloy catalysts and their intrinsic activity.

Alloy nanoparticles have altered properties relative to mono-metal nanoparticles. Hence, they are of interest and are important for several applications including biomedicine, microelectronics and catalysis—these are spread over a large range of sub-areas [6], [7], [8]. Several studies have shown that alloy bulky electrodes or catalysts containing binary oxide nanoparticles improve the catalytic activities for the electro-oxidation of water to oxygen (OER) [9], [10], [11]. Precious metals such as RuO_2 and IrO_2 are the most commonly used catalysts for OER due to their high activities; however, their large-scale applications are hampered predominantly by their high costs and scarcity[3], [12], [13].

Platinum is well-known as an essential material for electrocatalysts in fuel cells and water electrolysis [14], [15], [16], [17]. It is the most effective elemental catalyst for the oxidation of hydrogen and the reduction of oxygen (HOR, ORR) [18], [19]. In the hydrogen evolution reaction (HER; critical in electro- and photocatalysis [20]), platinum has the highest catalytic activity [21], but it is also expensive and rare. Volcano plots graph the exchange currents of the HER vs. the strength of the metal-hydrogen bond; nickel is the most active non-noble metal [21], [22].

Nickel could be used to produce highly active electro-catalysts for both HER as Ni and OER as Ni-oxide. It has high current densities, considerably lower price and better availability. In 1979, the BP company found that substrates coated with NiMo are highly stable and active electrocatalyst for HER [23]. McKone et al. studied hydrogen evolution with platinum, nickel and nickel-molybdenum electro-deposited on silicon substrates. They found that nickel-molybdenum-alloy (NiMo) has very similar catalytic activity to platinum, which makes NiMo a promising alternative [24]. Furthermore, McKone carried out electrochemical investigations on unsupported Ni-Mo nanopowders and reported a higher mass-activity than pure Ni particles and high long-term stability of these materials under alkaline conditions [25]. Raj compared the electro-catalytic activities for HER with several nickel-based binary-composites and showed that a cathode coated with nickel-molybdenum has the lowest hydrogen-over-potential values [26].

High catalyst purity is important because minor impurities can impact electrocatalytic reactions[27]. In case of chemically synthesized nanoparticles, extensive purification methods such as thermal treatment, centrifugation and solvent extraction are required to remove ligands and other stabilizing agents from their surfaces [28], [29], [30]. This applicability of this follow-up treatment is limited because quantitative removal cannot be achieved and often results in sintering or agglomeration. This modifies the nanoparticle properties. Nanoparticle generation by pulsed laser ablation in liquid (PLAL) is a scalable technology with a high future impact on technical applications [31], [32], [33]. This method does not require any precursors [32], which often contribute to impurities in colloids. It is a fast method and a variety of solvents [34], [35], [36] and materials [37], [38], [39] can be used for nanoparticle production. Both mono-metallic materials and alloy nanoparticles can be produced by ablating an alloy target [6], a powder of mixed materials as a suspension [40] or micro powder pressed into a pellet [39], [41], [42]. The pellet method allows precise control of composition, and the resulting alloy nanoparticles are easily tuned by changing the molar ratio of the metals in the powder. Nanoparticle fabrication with the bulk alloy method needs the desired alloy, which is much more challenging to get in each compositions and usually much more expensive.

To date, there are only a few studies on nickel alloy nanoparticles fabricated by PLAL. In one example, Zhang et al. synthesized cobalt-rich NiCo particles stabilized by PVP [43]. Gökce et al. recently published results on magnetic FeNi-polymer composites [44] based on the work of Jakobi et al. on FeNi fabrication in cyclopentanone [45]. Poondi and Liu et al. produced AgNi nanoparticles in the presence of a precursor [46], [47]. However, to the best of our knowledge, the formation of NiMo nanoparticles by PLAL and a pressed mixture of Ni and Mo micro powder in pure water without using any stabilizer has not yet been reported. Recently we have shown that perfectly monophasic alloy nanoparticle formation is possible by laser ablation of noble metals such as AgAu in pure water [42]. These non-precious metals are important in electrocatalysis, and the impact of oxidation on the formation non-precious alloys remains to be studied.

Here, we synthesized and characterized bimetallic nickel/molybdenum nanoparticles as an electrocatalyst for energy applications. We studied the effect of oxidation on alloy formation and the nanoparticle composition by pulsed laser ablation in liquid. Nanoparticles were synthesized by pulsed laser ablation of a pressed micro powder immersed in pure water. Their properties were characterized by several methods such as UV-VIS, XRD, TEM and EDX. Finally, electrochemical investigations were done to prove its catalytic properties and prospects in water electrolysis.

Experimental Details

Preparation of pellets

Nickel (> 99%, 10 µm) and molybdenum (>99%, 5 µm) micro powders from Merck at different molar ratios were mortared for 5-10 minutes. The mixed powder (1 mg) was then placed in a 13-cm diameter steel die and pressed at 100 kN for 6 minutes using a hydraulic laboratory press (PW 10 from P/O/weber company). For higher mechanical stability, the formed pellets were sintered at 800 °C for 1 hour in an argon atmosphere with a tube furnace from Nabertherm (R 50/500/11).

Colloidal nanoparticle production by laser ablation

Pulsed laser ablation of the pellets with several compositions were carried out in a self-made flow-through chamber using an Nd:YAG nanosecond laser (Rofin-Sinar RS-Marker 100D, pulse duration 40 ns) at a fundamental wavelength of 1064 nm with a repetition rate of 5 kHz and a pulse energy of 6.4 mJ. The laser beam was focused with a f-Theta lens of 63 mm focal length and was scanned in a spiral pattern on the pellet during Milli-Q water (resistivity of 18.2

MΩ·cm at 25 °C). This flowed through the chamber with a flow rate of 13.5 ml/min (pump Ismatec ISM321C). The nanoparticle mass was determined by weighing the target prior and after ablation using a microbalance (PESA Weighting Systems) with 10 µg accuracy. Figure 1 shows a sketch of the synthetic route of nickel-molybdenum nanoparticles.

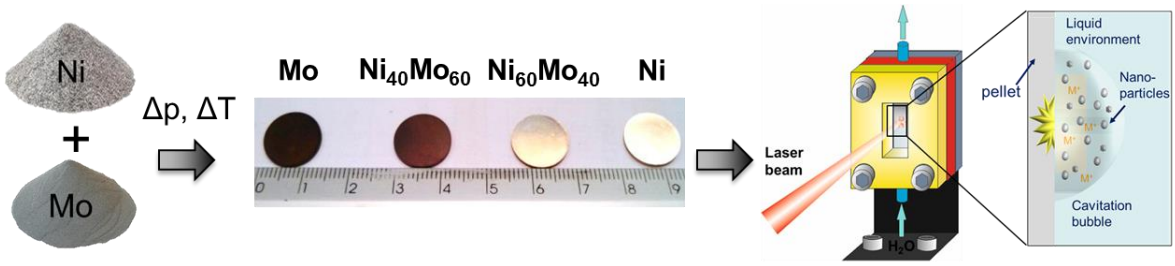

Figure 1: Synthesis of nickel-molybdenum nanoparticles: 1) pressing powders into a pellet; 2) generating nanoparticles by pulsed laser ablation in liquids.

Characterization methods

Laser-generated nanoparticles were characterized by UV-VIS absorption spectroscopy in the spectral range of λ = 200-800 nm on a Thermo Scientific Evolution 201 spectrometer using a quartz cuvette with a 1 mm path length. The pressed pellets were characterized by scanning electron microscopy (SEM) with a Hitachi TM3000 and energy-disperse X-ray spectroscopy (EDX) spectrometer Quantax 70 from Bruker Nano GmbH (Fig. S1). Transmission electron microscopy (TEM) and EDX were performed on nanoparticles with a FEI Tecnai F20 (acceleration voltage of 200 kV). A freshly prepared colloidal solution was deposited onto a carbon-coated copper grid and dried on air. The particle size was determined by measuring the diameter of more than 600 particles using ImageJ software.

X-ray diffraction (XRD) on pellets and grazing incidence X-ray (GIXRD) on nanoparticles were carried out on an X'Pert Pro diffractometer from Panalytical in Bragg-Brentano geometry at a grazing incidence angle of 0.5°. The analysis was performed by dropping the colloid solution onto a fresh single crystalline (111) silicon substrate (from Crystec) and drying in air.

Electrochemical measurements were carried out in a three-electrode electrochemical cell at room temperature using a VersaSTAT F3 from Princeton Applied Research. An adequate volume of the colloid solutions—corresponding to a nanoparticle loading of 5.52 $\mu g_{NPs}/cm_{electrode}^2$—was deposited on a glassy carbon (GC) disc electrode (5 mm diameter). After solvent evaporation, 5 µl of 5 wt% Nafion was pipetted onto the electrode. Prior to the measurements, the working electrode was ultrasonicated in ethanol and in deionized water for 5 minutes. The bare electrode was electrochemically pre-treated by 10 CV cycles at the same conditions as the electrochemical measurements. Cyclic voltammograms were recorded at 100

mV/s from -0.9 V to 0.75 V using an Ag/AgCl-reference electrode in a saturated KCl solution and a platinum wire as the counter electrode. The electrolyte was 1 M NaOH (pH=14) purged with nitrogen for at least 30 min followed by a continuous gas flow over the solution throughout the electrochemical measurements. The electrolyte and the electrode were not stirred during the electrochemical studies so that diffusion limitation artefacts can be excluded.

Results and discussion

Analysing colloidal nanoparticles by optical methods can reveal much information on their chemical properties. Pulsed laser ablation of the pellets produces target-dependent colloid colours. Figure 2 shows that the UV-VIS spectra of the nanoparticles depend on the molar ratio. The absorption spectra of pure nickel colloid have broad absorption in the UV region, which is consistent with chemically-prepared nickel nanoparticles [48]. There were no absorption peaks at 300 nm (band gap peaks) despite this being common for oxidized nanoparticles [49]. However, a broad absorption peak below 350 nm was seen. Thus, oxidized nickel species cannot be excluded due to the broad absorption band in this region.

Creighton calculated the absorption spectra for several metals according the Mie-theory [50]. The absorption spectrum of elemental, colloidal nickel correlates well with our results. In the molybdenum nanoparticles spectrum (d=10 nm), there was a broad absorption band from 300-500 nm, but this was not observed in our study [50]. In our study, the UV-VIS spectrum of the molybdenum colloids shows a strong absorption peak at about 215 nm corresponding to MoO_3. This is caused by interband transitions in the $(MoO_6)^{6-}$ octahedron where Mo^{5+} is generated by capturing an electron by Mo^{6+} [51], [52]. The absorption shoulder at 240 nm indicates the presence of MoO_4^{2-} and $HMoO_4^-$ [53], [54] (Figure 2 right). After a few weeks, the colour of the molybdenum colloid turns blue, and two absorption bands from 500 to 900 nm appear. The UV absorption also increases and becomes broader versus the freshly prepared colloid (Figure 2, right). This indicates continuous oxidation after ablation in water.

Molybdenum blue is well known in the literature. Tao et al. and Zheng et al. studied the photochromism of molybdenum oxide where the blue colour was attributed to the semi-conductive properties of MoO_3 ($E_g \geq 2.9$ eV) [55], [56]. The characteristic coloration of molybdenum oxide indicates the Mo(IV) species. This is caused when the energy of the excitation light is larger than the bandgap of molybdenum oxide. Oxide formation cannot be attributed to oxygen inclusion into the pressed micro powder pellets because the UV-VIS spectra show the same absorption band after ablation of molybdenum with bulk metal targets (Figure S4).

The binary colloids show a composition-dependent optical behaviour. By decreasing the molar fraction of nickel in the pressed micro powder, the broad extinction in the colloids due to nickel decreases and moves to a molybdenum-like extinction spectra. There is no clear tendency for the extinction when changing the molar fraction, although there is a linear correlation between the colloidal concentration of pure nickel and the extinction at 400 nm was found. This can be due to different particle sizes found in the mixed colloids, which influences the extinction spectra or indicates that the colloid contains a mixture of metals.

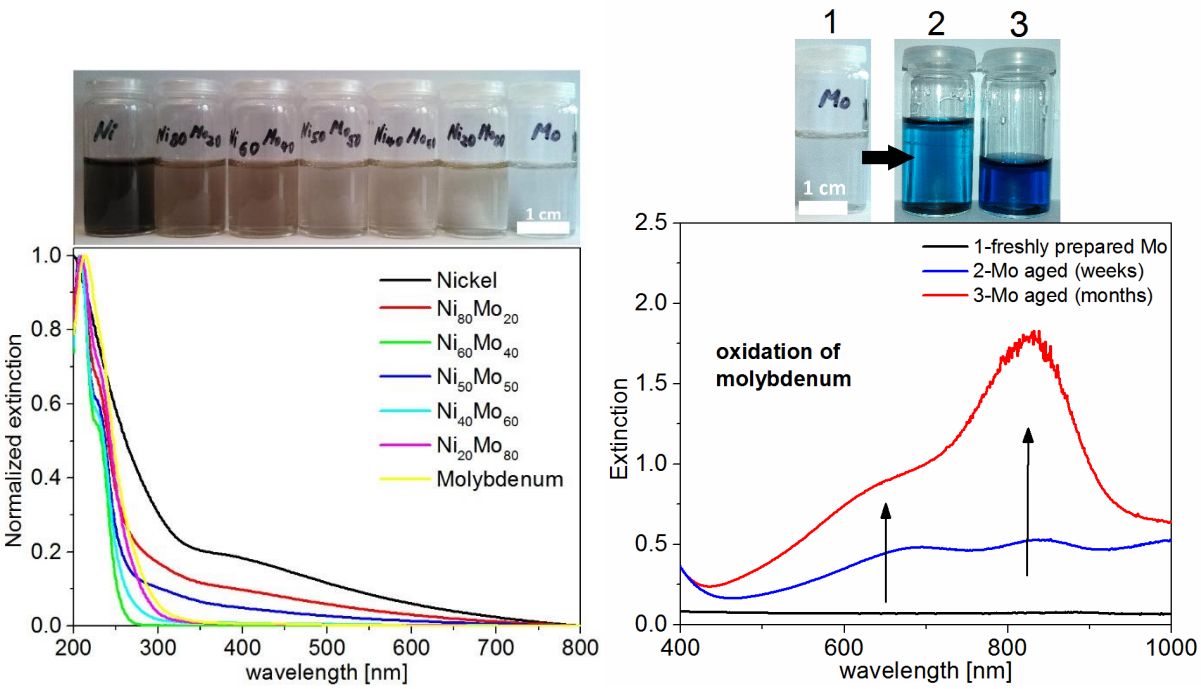

Figure 2: UV-VIS extinction spectra of colloidal NiMo nanoparticles (left) and long-term UV-VIS spectra of molybdenum colloids (right).

TEM analyses measured the average size and morphology of the nanoparticles. Figure 3 shows that the nanoparticles are spherical with a log-normal size distribution, which agrees with the literature on laser-generated nanoparticles [57], [33], [58]. The average nanoparticle diameter fluctuates with the metal ratio set in the ablated pellets; the bimetallic colloids contain larger nanoparticles compared to the monometallic colloids. Similar observations were made by Sarker et al. where the size of binary and ternary alloy nanoparticles varied with the molar ratios of metals produced by laser irradiation values [59], [60]. The results have not yet been described in detail, but they suppose that this tendency is due to differences in surface energy, interatomic distance and atomic ratio [60], [61].

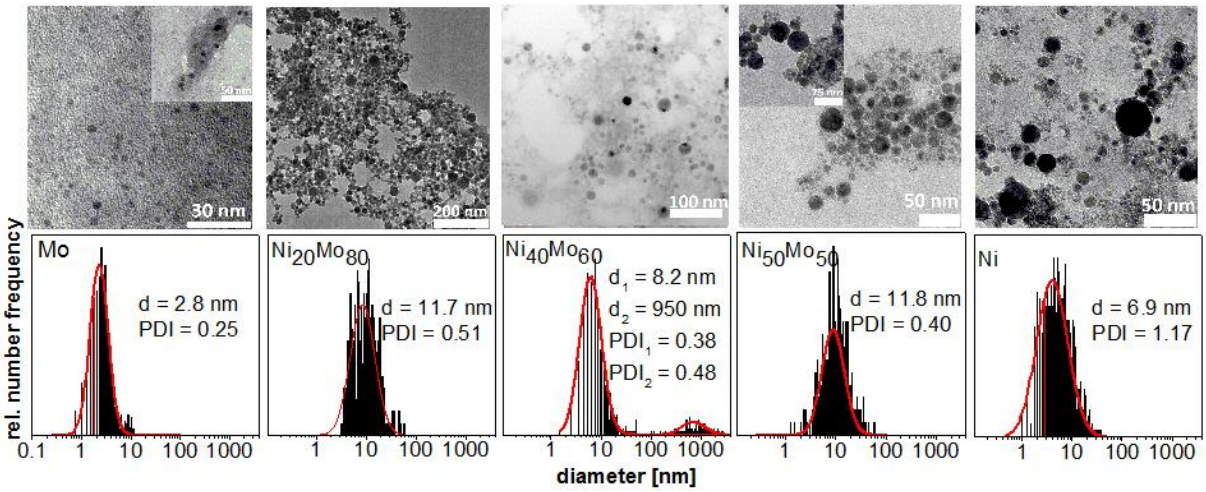

Figure 3: TEM-micrographs and size histograms of pure Mo, Ni and the colloids ablated from the NiMo pellets with molar fractions of 20:80, 40:60 and 50:50.

V

To analyse the elemental distribution of the nanoparticles, EDX line scans were carried out with the $Ni_{40}Mo_{60}$ colloid from randomly chosen nanoparticles, and a bimodal size distribution was obtained. Both elements were detected in the spectra. The elemental composition is not consistent for all the nanoparticles and varied with nanoparticle size (Figure 4). The large nanoparticles (2nd mode at 950 nm diameter) are molybdenum-rich, and smaller nanoparticles (1st mode at 8.2 nm diameter) consist of nickel. Deviation in the stoichiometry of laser-generated Cu/Zn nanoparticles has been observed by Koch et al. where the use of a nanosecond laser and higher laser fluences yielded to an increased formation of polydisperse particles up to the micrometer range [62]. The mechanism of nanoparticle formation by laser ablation is not completely understood. Different simultaneous ablation processes may lead to deviations in the composition of the laser-generated nanoparticles, where the energy density deposited on the target plays an important role in nanoparticle formation [63], [64], [33]. Due to the high laser fluences (81 J/cm^2) applied here, we assume that multiple ablation mechanisms like fragmentation, vaporisation and phase explosion are responsible for nanoparticle formation and led to a broad size distribution [33]. Note that a bimodal nanoparticle size distribution has been clearly detected inside the laser-induced cavitation bubble (vapour-filled) before its collapse [65]. This indicates that the formation of polydisperse and distributed particles cannot be attributed solely to particle growth after the particles are released in the liquid.

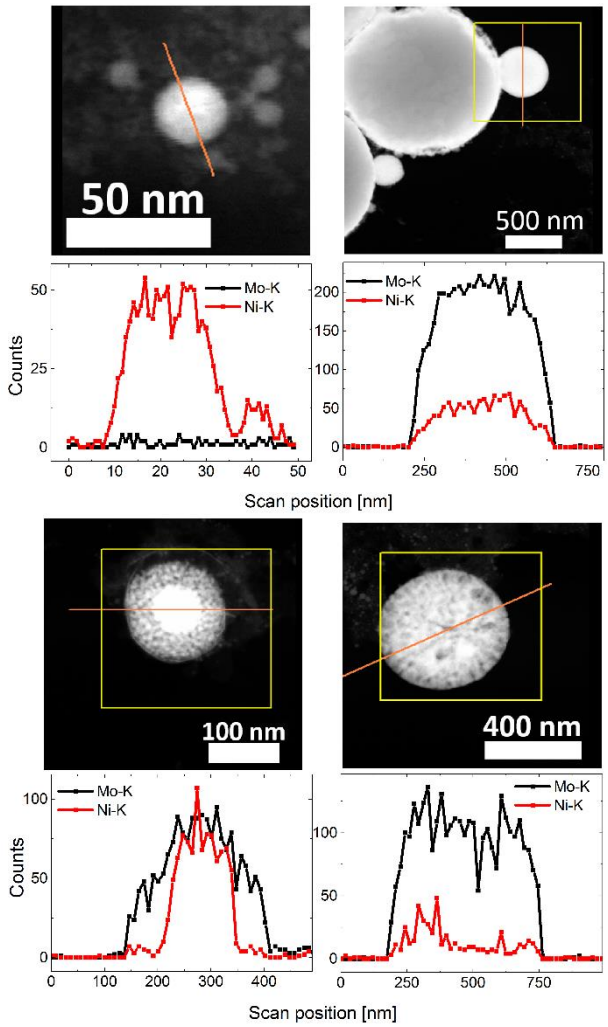

Figure 4: TEM-EDX line scans of nanoparticles laser ablated in water from a NiMo pellet with a molar fraction of 40:60 nickel-molybdenum.

There is good agreement on the nanoparticle's elemental composition with respect to target composition for noble metal alloy nanoparticles like PtAu, AuAg and PtIr [39], [42], [66]. However, it was reported, that the stoichiometry of alloys like SmCo differs from the target due to large differences in the heat of evaporation of both metals [45]. The difference between the heat of evaporation of molybdenum (598 kJ/mol) and nickel (370 kJ/mol) is larger than other metals that have good correlation of the elemental composition with the target composition [42], [39]. This might give rise to the assumption that the inhomogeneous elemental composition in NiMo particles is attributed to their different heat of evaporation (Δ_H). This serves as a measure of atomic interaction in the cavitation bubble. The Ni and Mo atoms released from the target are homogeneously mixed because of the hot plasma. The initial atomic composition inside the cavitation bubble is dominated by the target composition.

However, Amendola et al. concluded that the stoichiometry of alloy nanoparticles is influenced by different reactivity with the solvent and oxygen molecules [33]. This is because the

stoichiometry of laser-generated FePt alloy nanoparticles were not maintained as in the target and varies with the chosen solvent in [67] and [33]. In our study, we used water as a solvent during laser ablation. The non-noble metal nanoparticles oxidize because oxygen is soluble in water. But does the molecular oxygen or maybe even decomposed solvent rule oxidation?

Oxidized nanoparticles were seen in the UV-VIS spectra of the colloids (Figure 2). The oxidation of molybdenum can minimize the solubility of molybdenum in the nickel lattice [68]. It could be assumed that the dissolved molecular oxygen in the water is responsible for the particle oxidation during pulsed laser ablation in liquids. This can be validated by laser ablation of molybdenum in degassed water. Preliminary results indicate that oxidation takes place even in water with low oxygen content (Figure S5 and S6). Nearly the same extinction spectra as in Figure 2 were measured indicating molybdenum oxidation (Figure S5). This indicates that either there is still enough residually dissolved oxygen in degassed water to oxidize the particles, or more likely, that the oxygen from H_2O molecules is responsible for the oxidation due to decomposition of water molecules during laser ablation. In this case, reactive oxygen species can be formed in the plasma during laser ablation, and this reactive species can oxidize the particles.

For clear evidence of the influence of decomposed water molecules, laser ablation of a $Ni_{40}Mo_{60}$ target was evaluated in acetone. Although not uniform, most particles has a more homogeneous elemental distribution via TEM-EDX (Figure 5). It should be noted that the homogeneity in the pellet composition plays an important role in terms of alloy formation. The metal distribution in the pellets was confirmed by SEM-EDX analysis, which shows that both metals are present in the spot area and thus can be ablated at the same time (Fig. S1 and S2). Furthermore, EDX analysis of the NiMo target after ablation clearly indicates alloy formation on the ablated crater (Fig. S3).

The solubility of oxygen in acetone is much higher than in water (solubility of oxygen in water: 5.99 cm^3/L; in acetone: 45 cm^3/L [69, 70]). Thus, the dissolved molecular oxygen is probably not the main influencing factor responsible for particle oxidation. In contrary to synthesis in water, XRD analysis of Ni, Mo and $Ni_{40}Mo_{60}$ particles in acetone do not show any oxidation peaks in the respective diffractograms (Figure S8). The formation of carbides indicates that a protective carbidic shell prevents particle oxidation. Consequently our results show that a metal segregation is caused by oxidation of metals, which is likely due to oxygen from water molecules and not molecular oxygen in the liquid. In a similar work, Wagener et al. synthesized Au@FeOx in water, and elemental Fe@Au in acetone were observed [70].

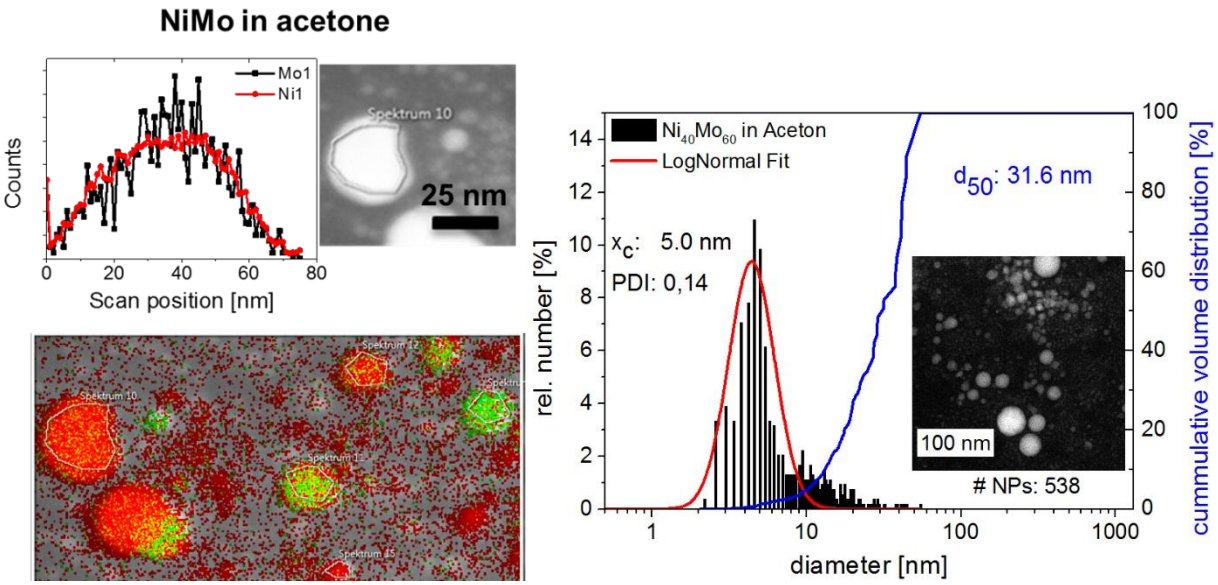

Figure 5: TEM-EDX (left) and size histogram (right) of nanoparticles in acetone ablated from a NiMo pellet with a molar fraction of 40:60.

XRD measurements of the particles synthesized in water were performed for further structural analysis. Figure 6 shows the typical diffractograms. The characteristic fcc-peaks of nickel and obvious nickel oxide (NiO)-peaks were detected in the nickel colloid. A pure molybdenum colloid reveals diffraction peaks of molybdenum as well as of molybdenum oxide (MoO_2). The diffraction patterns of NiMo colloids contain characteristic peaks for elemental molybdenum and nickel as well as additional small peaks of MoO_2. We assume that the Mo oxides observed in UV-VIS are either amorphous or only a layer at the particles' surface, and metallic Mo is dominant in the core after laser ablation. The particles seem to corrode because further oxidation takes place over time. This assumption is supported by XPS analyses, which show that small particles (< 20 nm) were completely oxidized to Mo^{5+} and Mo^{6+}, but large particles (>20 nm) were oxidised; metallic Mo was also detected (Figure S10). In contrast to this, no size dependence of oxidation state was found for the nickel nanoparticles.

The XRD data show a gradual shift in the nickel diffraction peaks for the NiMo alloy nanoparticles. These correspond to the {111} and {200} planes toward larger 2θ values as measured by increased molar fraction of molybdenum (Figure 6 A and B). The lattice parameters were calculated from the position of the Ni {111} and {200} peak using equation (Eq. 1).

$$a = d_{hkl} \cdot \sqrt{h^2 + k^2 + l^2} \qquad \textbf{Eq. 1}$$

a = lattice constant

d_{hkl} = lattice plane according to Bragg's equation

h, k, l= Miller indices

Figure 6D plots the average lattice constant of both the peaks and the resulting standard deviation plotted as a function of the pellet composition. The nickel lattice constant increases with molybdenum content corresponding to a lattice expansion of nickel due to tensile stress. This can be explained by the diffusion of the larger molybdenum atoms (136.2 pm) in the fcc lattice with the smaller nickel atoms (124.6 pm). On the other hand, the molybdenum diffraction peaks of the {110}, {200} planes do not shift indicating that nickel does not noticeably diffuse into molybdenum.

One can estimate the concentration of molybdenum diffused in nickel lattice according to following equation and the calculated lattice constant; this is also plotted in Figure 6 D as red rectangles [68].

$$\text{Mo} - \text{portion [At. \%]} = \frac{\text{a}_{\text{Ni(ss)}}\,[\text{nm}] - \text{a}_{\text{Ni}}\,[nm]}{0{,}000409} \qquad \textbf{Eq. 2}$$

$a_{Ni(ss)}$ = lattice constant according to Eq. 1

a_{Ni} = lattice constant of nickel bulk (3.52394 Å) [71]

The calculated concentration of molybdenum in the nickel lattice is below the maximum soluble concentration of 27 at. % [68], which suggests possible diffusion of molybdenum into the nickel lattice (Figure 6D).

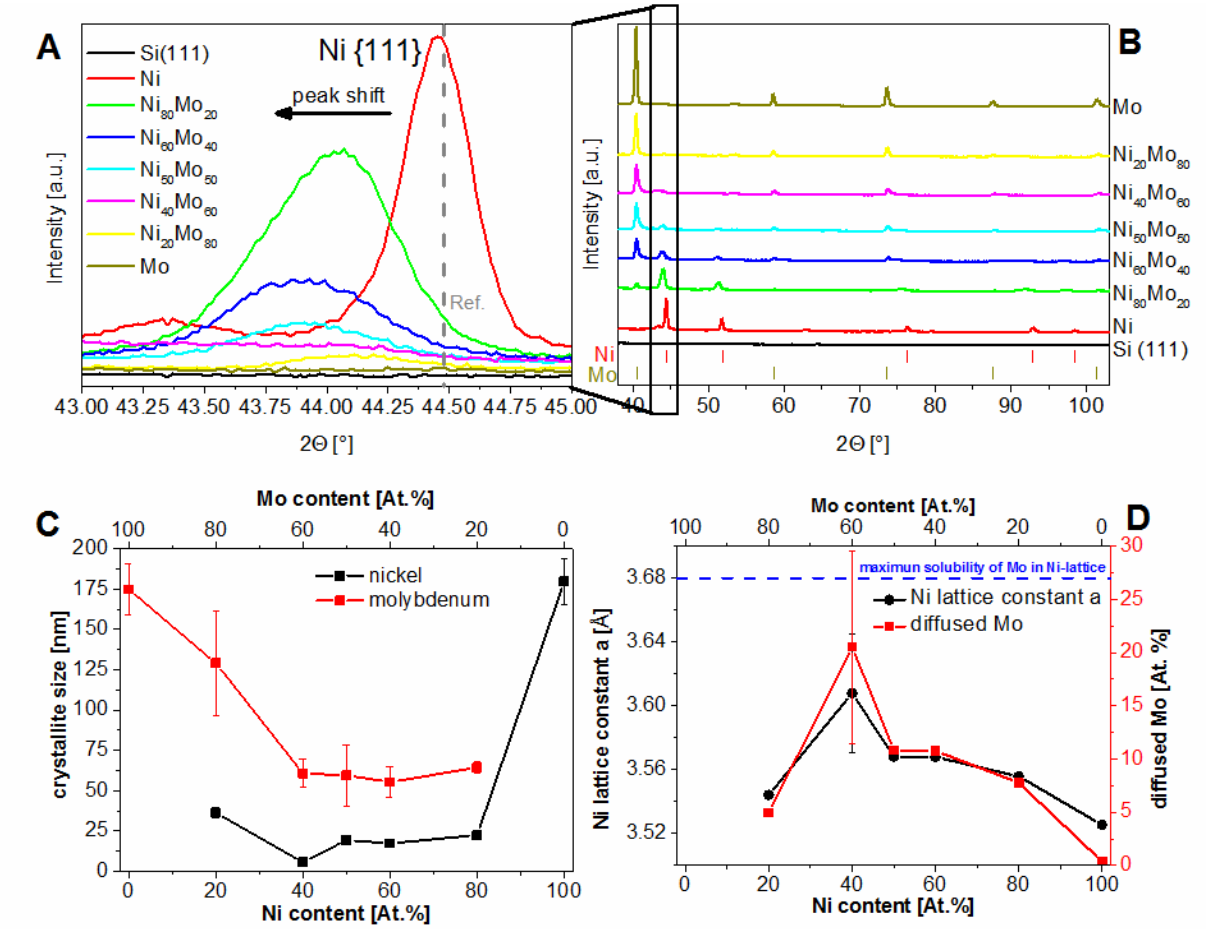

Figure 6: Crystal structure of the NiMo nanoparticles depending on molar fraction of the target. A) X-ray diffraction {111} peak shift of nickel and B) XRD patterns of pure Ni, Mo and NiMo colloids. C) Crystallite size. D) Lattice constant and the fraction of Mo diffused in the Ni lattice as a function of the Ni molar fraction.

The crystallite size of the molybdenum and nickel nanoparticles was calculated from Scherrer equation for full width at half maximum (FWHM) of {111} and {200} reflections. A significant decrease in the crystallite size was found with an increased fraction of molybdenum (Figure 6 C). The formation of smaller crystallites and a change in the lattice constant of laser-generated nanoparticles were observed for PtAu alloys by Zhang et al [39]. The crystallite size and their TEM analysis of the nanoparticles had similar values. They concluded that single crystals were formed. In our study, the crystallite size differs from the average nanoparticle size measured by TEM. Some large particles (~950 nm) are also clearly present in the colloids (Figure 3). Large values in crystallite sizes were found because XRD is a volume-weighted technique and over-represents larger nanoparticles.

We observed a structural change in the NiMo alloy particles as indicated by the variation of the lattice constant observed by XRD (Figure 6). Because the particle's structural changes influence the surface catalytic activity, we electrochemically investigated the catalytic activity of the particles. Cyclic voltammetry was carried out with the monometallic molybdenum and nickel

colloids as well as with the $Ni_{40}Mo_{60}$ nanoparticles and mixture of nickel and molybdenum colloids to investigate synergistic effects (Figure 7).

The cyclic voltammogram of the nickel colloid in 1 M aqueous NaOH was reminiscent of those reported earlier in the literature [72], [73], [74]. As soon as metallic nickel is immersed in an aqueous solution, it forms a $Ni(OH)_2$ layer on the top of a NiO layer that was previously formed in air [10] as shown by XPS analysis (Fig. S9) [10]. In the first cycle, no pronounced peaks are observed in Figure 7 b; only a small peak in the range of -0.10 V to 0.20 V (see insert). This wave is attributed to a reversible $Ni(OH)_2$/NiOOH oxidation reaction:

$$Ni(OH)_2 + OH^- \rightleftarrows NiOOH + H_2O + e^- \quad \textbf{Eq.3}$$

The corresponding reduction peak can be observed during the cathodic scan—the nickel oxohydroxide is reduced to hydroxide (Eq. 4) from 0.10…0.38 V vs. Ag/AgCl [75], [73]. As a consequence of successive sweeps to low potential range (where hydroxide reduction occurs), an active surface is generated and the nickel colloid is activated [69]. This activation increases the anodic current peaks and shifts the small peak observed in the first scan to a more positive potential of 0.38…0.65 V. This current results from formation of nickel oxohydroxide in a quasi-reversible reaction (Eq 4) whereas shifts in the peak position are attributed to α-$Ni(OH)_2$ conversion to (β)-$Ni(OH)_2$ upon sample aging [76], [77], [73], [72].

When the electrode containing the nickel colloid is further polarized to more positive potentials of the $Ni(OH)_2$/NiOOH oxidation reaction, there is a drastic increase in the current induced by oxygen evolution . This agrees with earlier studies showing that nickel-based oxides are good catalyst materials for oxygen evolution reaction in alkaline media [72], [78]. At the negative potential, hydration waterof nickel hydroxide is reduced prior to the solvent water[74]. This is observed as the current increases to -0.60 V and follows a peak attributed to hydrogen evolution at 0.30 V more negative potential (Eq. 4).

$$2H_2O + 2e^- \rightarrow 2OH^- + H_2 \quad \textbf{Eq.4}$$

The cyclic voltammograms of colloids containing molybdenum suffer from somewhat poor reproducibility because of the ongoing changes in the composition of various molybdenum species due to exposure to light as discussed above. On first observation, currents obtained with the molybdenum colloid are clearly lower than those for the nickel, even though the diameter

of the molybdenum particles is some 2.5 times lower than the nickel particles (see Figure 3). The notable difference in surfaces areas—combined with the higher currents—indicate that the nickel colloid has a higher intrinsic activity.

In the first cycle, it is clear that the pure molybdenum colloid (Figure 7a) anodic peaks at -0.25…0.20 V (peak current at 45 mV), 0.20…0.45 V (peak current at 330 mV) and 0.45…0.67 V vs. Ag/AgCl are observed. The two first anodic peaks are attributed to the formation of molybdenum oxides MoO_2 and further oxidation to MoO_3 [79], [80], [81], [82].

$$Mo + 4OH^- \rightarrow MoO_2(s) + 2H_2O + 4e^- \quad \textbf{Eq.5}$$

$$MoO_2 + 2OH^- \rightarrow MoO_3(s) + H_2O + 2e^- \quad \textbf{Eq.6}$$

It is well known that molybdenum oxides are unstable in alkaline environments [63]; therefore, the wave flowing the formation is attributed to oxide dissolution. The complex reaction path involves chemical and electrochemical steps and is not known in detail. It depends on the pH and exact composition of the surface oxide [83]. However, surface passivation during successive scans suggests that molybdenum dissolution from colloids under the selected experimental conditions is slow.

The peak at the highest potential range is assigned to an oxygen evolution reaction because different molybdenum containing oxides have been reported earlier as active oxygen evolution catalysts in alkaline environments [84], [11].

$$4OH^- \rightarrow 2H_2O + O_2 + 4e^- \quad \textbf{Eq.7}$$

Thus, the resulting molybdenum oxide layer functions as an efficient catalyst for oxygen evolution. Activation upon cycling likely results from increases in the surface area as a result of oxide layer formation and molybdenum dissolution (see 150th cycle at Figure 7 a). However, post-mortem experiments to confirm these results are beyond of the scope of the current study. At the cathodic scan, only a small peak at -0.40…-0.70 V is observed resulting from reduction of molybdenum oxide (Eq 8).

$$MoO_3 + H_2O + 2e^- \rightarrow MoO_2 + 2OH^- \quad \textbf{Eq 8}$$

The notably lower charge involved in this reduction relative to the oxidation reactions indicates that molybdenum reactions are irreversible either because of the molybdenum dissolution or kinetic limitations.

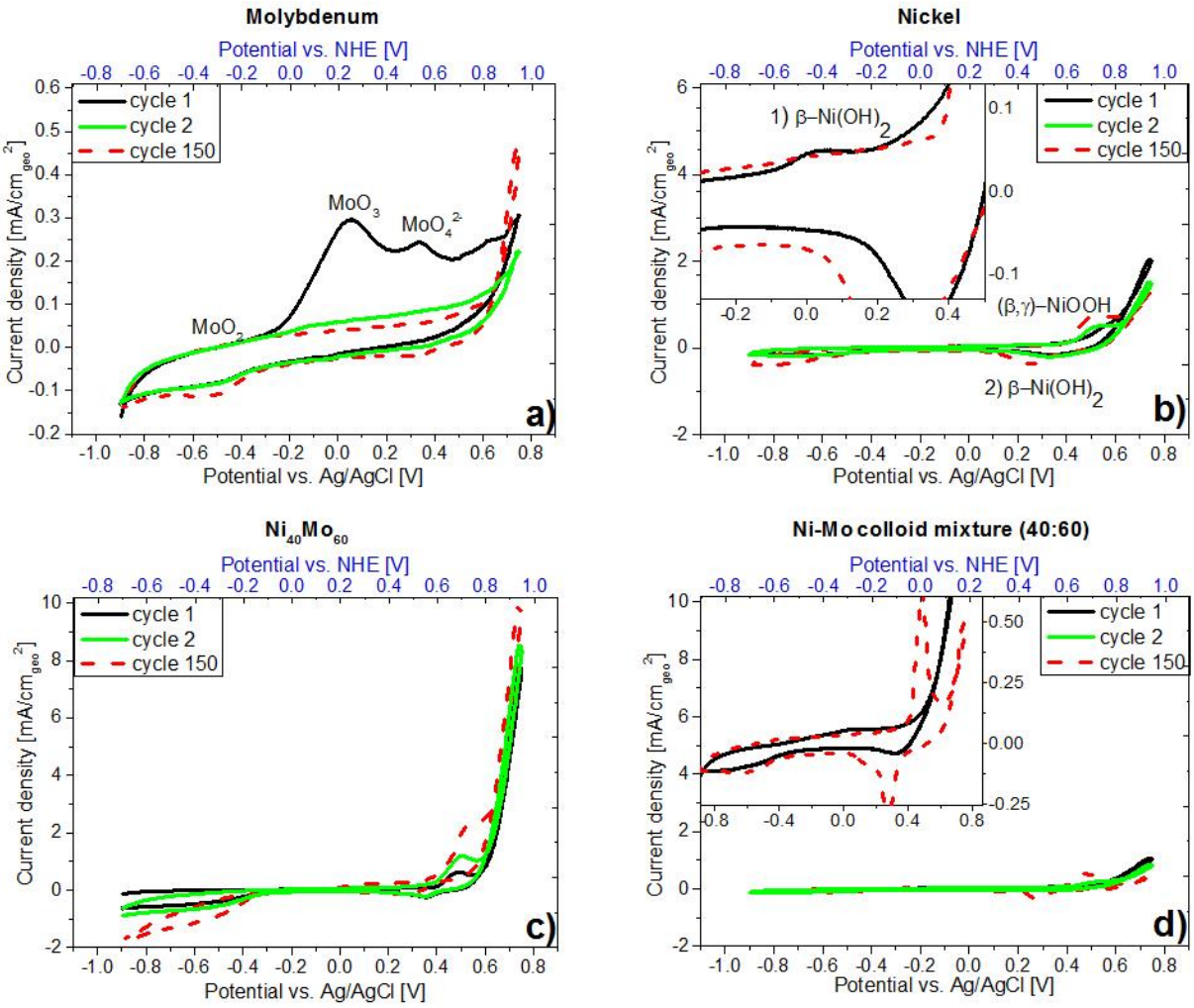

Figure 7: Cyclic voltammograms of Mo, Ni and $Ni_{40}Mo_{60}$ alloy colloid as well as a 40:60 mixture of nickel with molybdenum colloid.

To compare alloying effects with particle mixtures, a NiMo colloid was studied relative to a mixture of Ni and Mo colloids at the same molar ratio as the $Ni_{40}Mo_{60}$ alloy. The cyclic voltammograms of $Ni_{40}Mo_{60}$ and the particle mixture show similar features as the pure nickel colloid but with higher currents measured for the elemental nickel colloid relative to molybdenum. The oxidation and reduction peaks at 0.4...0.6 V and 0.2…0.4 V vs. Ag/AgCl are assigned to the reversible $Ni(OH)_2$/NiOOH redox reaction (Eq. 3). The increase in the current at the potential end of the cyclic voltammogram is assigned to an oxygen evolution reaction. Clear synergistic effects are observed when comparing the currents obtained with the alloy and metal mixture suggesting that the former is a good catalyst for an oxygen evolution reaction. This is even more evident when considering that the surface area of the alloy is clearly higher than the elemental nickel colloid (see diameters in Figure 3).

Ni-Mo alloys are good catalysts for hydrogen evolution reactions as well [25] [75]. The cyclic voltammograms of all studied alloys and metal mixtures increase the cathodic current with concomitant bubble formation at potentials more negative than -0.80 V vs. Ag/AgCl. Thus, this current is attributed to hydrogen evolution reaction [81], [79], [77]. Those peaks at -0.4…-0.8 V can be attributed either to reduction of hydrated water in nickel hydroxide or reduction of molybdenum.

A closer look at the cyclic voltammogram of the mixture of nickel with molybdenum colloid (see inset in Figure 7d) also reveals features related to molybdenum oxidation from 0…0.2 vs. Ag/AgCl (Eq. 6). We concluded that molybdenum is active, but its contribution to the total current is lower as expected on the basis of the cyclic voltammograms of pure nickel and molybdenum colloids.

The electrocatalytic properties of the $Ni_{40}Mo_{60}$ colloid shows a clear increase in the current (Figure 8) There is a small shift of the onset potential to more positive potentials in the oxygen evolution region indicating higher activity. Moreover, the activity of the colloidal solution is enhanced during the 150 potential cycles.

We performed at least three repeat measurements to ensure data reproducibility. We evaluated the OER activity of the voltammograms of Mo, Ni, $Ni_{40}Mo_{60}$ and the colloidal mixture, respectively, with error bars. Figure 8 shows the mean current density at 0.75 V vs Ag/AgCl with the corresponding error bars.

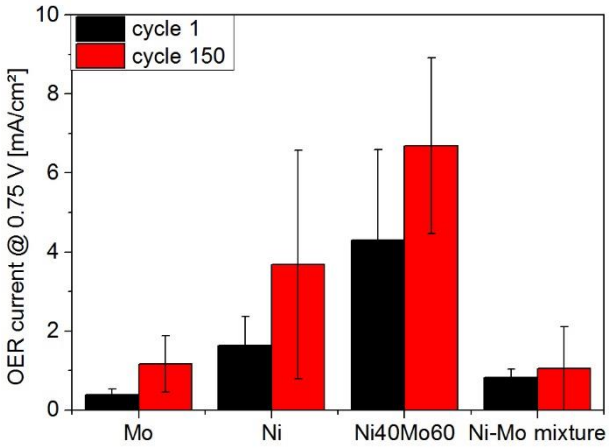

Figure 8: Comparison of the OER activity of Mo, Ni and $Ni_{40}Mo_{60}$ alloy colloid as well as a 40:60 mixture of nickel with molybdenum colloid.

The cyclic voltammograms of $Ni_{40}Mo_{60}$ and Ni-Mo colloid mixture change shape during the measurements. The changes induced with time of the colloidal mixture resemble those taking place on pure Ni colloid. However, the prepared bimetallic $Ni_{40}Mo_{60}$ sample shows a somewhat different behaviour. A potential explanation for these observations is dealloying of this colloidal

sample, i.e. molybdenum dissolution resulting in formation of more active porous nickel surface. Strasser et al. showed that dealloying could improve the electro-catalytic activity due to the removal of a less noble component from the surface of a bimetallic alloy [86], [87]. This explains the observed surface activation of the $Ni_{40}Mo_{60}$ in this study; further measurements are needed to confirm this.

The monometallic particles are even smaller and have larger surfaces relative to their mass versus alloyed $NiMoO_x$ particles. However the alloys show higher activities, thus we assume that intrinsic activities affect the OER reaction. However, the influence of particle size is not negligible (compare CVs in SI). In contrast to this, adding molybdenum to nickel was not traced back on intrinsic activities but is related to HER [85]. For further evidences, electrochemical investigations such as impedance spectroscopy and other techniques such as in-situ Raman or FTIR measurements are needed.

Laser-generated NiMoOx particles are more suitable as active materials for oxygen evolution reaction because oxides are formed in water. In case of carbidic NiMo particles that are formed in acetone, hydrogen evolution is favourable [88], [89] (not investigated in the current study).

In any case, we concluded that there is a clear synergistic effect of alloying Ni with Mo. It results in higher activity during all of the electrochemical measurements. There was significantly improved performance for the oxygen evolution reaction. Furthermore, there was direct correlation between the crystal size and electrocatalytic performance as reported by Huot et al. [90]. They showed that the average crystal size is linearly proportional to the overpotential of the hydrogen evolution reaction. Therefore—even if a partially inhomogeneous composition and a bimodal size distribution of the nanoparticles is evident—changes in the electrical properties or a higher electrocatalytic activity can be achieved due to synergetic effects of the NiMo alloy nanoparticles.

Conclusion

We fabricated nickel-molybdenum nanoparticles by pulsed laser ablation in water and acetone. For this purpose, targets of desired composition were formed by pressing and subsequent sintering of mixed nickel and molybdenum micro-powders. This method allows simple and fast synthesis of alloy-based catalysts and enables screening test of desired metals and their composition.

The resulting colloids show a formation of alloyed nanoparticles even though precise control of stoichiometry was not seen in TEM-EDX. Particle synthesis in acetone offered 7-fold more molecular oxygen and results in non-oxidized NiMo nanoparticles. Thus, we hypothesize that

molecular oxygen is not the influencing parameter in oxide formation but rather reactive oxygen species. These are formed by water decomposition. A significant increase in the lattice constant for nickel—due to diffusion of molybdenum into nickel lattice—was seen in molybdenum-rich colloids. This results in smaller crystallites. In contrast to mixed Ni and Mo colloids, alloy nanoparticles ablated from mixed nickel-molybdenum targets show enhanced electrochemical activity for the oxygen evolution reaction indicating a clear synergetic effect.

These materials catalyse water splitting are attractive catalysts for large-scale OER production. They could replace precious metal oxides in alkaline electrolysers, but need further studies in terms of metal composition, size control and electrochemical stability under real operating conditions. In future works, HER performances of the non-oxidized particles in acetone should be elaborated and quantitatively compared to reference materials such as Pt or NiMo materials synthesized by other methods to confirm the features of the laser-generated particles.

Acknowledgements

The authors gratefully acknowledge the financial support of the German Federal Ministry of Education and Research (BMBF) within the young investigator competition NanoMatFutur (project INNOKAT, FKZ 03X5523). Cyclic voltammetry studies have been supported by Max Buchner Research Foundation (DECHEMA, MBFSt-Kennziffer: 3354). The authors thank to Prof. Dr. Markus Winterer for the access to the X-ray diffractometer, tube furnace and the hydraulic press. Furthermore, we would like to thank Thomas Winter for the fruitful discussion regarding evaluations of the XRD patterns. For the XPS and TEM analyses we thank Dr. Ulrich Hagemann and Dr. Markus Heidelmann from the Team of Interdisciplinary Center for Analytics on the Nanoscale (ICAN) at University of Duisburg-Essen.

Literature

[1] F. Schüth, "Heterogene Katalyse. Schlüsseltechnologie der chemischen Industrie," *Chemie in unserer Zeit*, vol. 40, no. 2, pp. 92–103, **2006**.

[2] J. M. Plc, "Water electrolysis & renewable energy systems," *Fuel Cell Today*, pp. 1–44, **2013**.

[3] J. Ryu, N. Jung, J. H. Jang, H.-J. Kim, and S. J. Yoo, "In situ transformation of hydrogen-evolving cop nanoparticles: Toward efficient oxygen evolution catalysts bearing

dispersed morphologies with co-oxo/hydroxo molecular units," *ACS Catalysis*, vol. 5, no. 7, pp. 4066–4074, **2015**.

[4] C.-C. Hou, S. Cao, W.-F. Fu, and Y. Chen, "Ultrafine cop nanoparticles supported on carbon nanotubes as highly active electrocatalyst for both oxygen and hydrogen evolution in basic media," *ACS applied materials & interfaces*, vol. 7, no. 51, pp. 28412–28419, **2015**.

[5] R. Subbaraman, D. Tripkovic, K.-C. Chang, D. Strmcnik, A. P. Paulikas, P. Hirunsit, M. Chan, J. Greeley, V. Stamenkovic, and N. M. Markovic, "Trends in activity for the water electrolyser reactions on 3d M (Ni, Co, Fe, Mn) hydr (oxy) oxide catalysts," *Nature materials*, vol. 11, no. 6, pp. 550–557, **2012**.

[6] D. Tiedemann, U. Taylor, C. Rehbock, J. Jakobi, S. Klein, W. A. Kues, S. Barcikowski, and D. Rath, "Reprotoxicity of gold, silver, and gold-silver alloy nanoparticles on mammalian gametes," *Analyst*, vol. 139, pp. 931–942, **2014**.

[7] J. A. Rodriguez and D. W. Goodman, "The nature of the metal-metal bond in bimetallic surfaces," *Science*, vol. 257, no. 5072, pp. 897–903, **1992**.

[8] M. Oezaslan, M. Heggen, and P. Strasser, "Size-dependent morphology of dealloyed bimetallic catalysts: linking the nano to the macro scale," *Journal of the American Chemical Society*, vol. 134, no. 1, pp. 514–524, **2011**.

[9] X. Li, F. C. Walsh, and D. Pletcher, "Nickel based electrocatalysts for oxygen evolution in high current density, alkaline water electrolysers," *Physical Chemistry Chemical Physics*, vol. 13, no. 3, pp. 1162–1167, **2011**.

[10] E. Fabbri, A. Habereder, K. Waltar, R. Kötz, and T. Schmidt, "Developments and perspectives of oxide-based catalysts for the oxygen evolution reaction," *Catalysis Science & Technology*, vol. 4, no. 11, pp. 3800–3821, **2014**.

[11] A. A. El-Moneim, N. Kumagai, K. Asami, and K. Hashimoto, "Nanocrystalline manganese-molybdenum-tungsten oxide anodes for oxygen evolution in acidic seawater electrolysis," *Materials transactions*, vol. 46, no. 2, pp. 309–316, **2005**.

[12] S. Buller and J. Strunk, "Nanostructure in energy conversion," *Journal of Energy Chemistry*, vol. 25, no. 2, pp. 171–190, **2016**.

[13] T. Reier, M. Oezaslan, and P. Strasser, "Electrocatalytic oxygen evolution reaction (oer) on Ru, Ir, and Pt catalysts: a comparative study of nanoparticles and bulk materials," *Acs Catalysis*, vol. 2, no. 8, pp. 1765–1772, **2012**.

[14] C. Song, "Fuel processing for low-temperature and high-temperature fuel cells: Challenges, and opportunities for sustainable development in the 21st century," *Catalysis Today*, vol. 77, pp. 17–49, **2002**.

[15] J. T. M. M. H. A. D. Peter M. Urban, Anett Funke, "Catalytic processes in solid polymer electrolyte fuel cell systems," *Applied Catalysis A: General*, vol. 221, pp. 459–470, **2001**.

[16] G. Acres, J. Frost, G. Hards, R. Potter, T. Ralph, D. Thompsett, G. Burstein, and G. Hutchings, "Electrocatalysts for fuel cells," *Catalysis Today*, vol. 38, no. 4, pp. 393–400, **1997**.

[17] H. A. Gasteiger, S. S. Kocha, B. Sompalli, and F. T. Wagner, "Activity benchmarks and requirements for Pt, Pt-alloy, and non-pt oxygen reduction catalysts for pemfcs," *Applied Catalysis B: Environmental*, vol. 56, no. 1, pp. 9–35, **2005**.

[18] N. Tian, Z.-Y. Zhou, S.-G. Sun, Y. Ding, and Z. L. Wang, "Synthesis of tetrahexahedral platinum nanocrystals with high-index facets and high electro-oxidation activity," *science*, vol. 316, no. 5825, pp. 732–735, **2007**.

[19] W. Sheng, H. A. Gasteiger, and Y. Shao-Horn, "Hydrogen oxidation and evolution reaction kinetics on platinum: acid vs alkaline electrolytes," *Journal of The Electrochemical Society*, vol. 157, no. 11, pp. B1529–B1536, **2010**.

[20] M. G. Walter, E. L. Warren, J. R. McKone, S. W. Boettcher, Q. Mi, E. A. Santori, and N. S. Lewi, "Solar water splitting cells," *Chem. Rev.*, vol. 110, pp. 6446–6473, **2010**.

[21] S. Trasati, "Work function, electronegativity, and electrochemical behaviour of metals: Iii. electrolytic hydrogen evolution in acid solutions," *J. Electroanal. Chem.*, vol. 39, pp. 163–184, **1972**.

[22] M. H. Miles, "Evaluation of electrocatalysts for water electrolysis in alkaline solutions," *Journal of Electroanalytical Chemistry and Interfacial Electrochemistry*, vol. 60, pp. 89–96, **1975**.

[23] Int. J. Hydrogen Energy 1982, 7, 405; Brown, D.; Mahmood, M. Method of preparing active electrodes. **1982**; U.S. Patent 4,358,475; Electrochim. Acta 1984, 29, 1551

[24] J. R. McKone, E. L. Warren, M. J. Bierman, S. W. Boettcher, B. S. Brunschwig, N. S. Lewis, and H. B. Gray, "Evaluation of pt, ni, and ni–mo electrocatalysts for hydrogen evolution on crystalline si electrodes," *Energy & Environmental Science*, vol. 4, no. 9, pp. 3573–3583, **2011**.

[25] J. R. McKone, B. F. Sadtler, C. A. Werlang, N. S. Lewis, and H. B. Gray, "Ni–Mo nanopowders for efficient electrochemical hydrogen evolution," *ACS Catalysis*, vol. 3, no. 2, pp. 166–169, **2013**.

[26] I. A. Raj, "Nickel-based, binary-composite electrocatalysts for the cathodes in the energy-efficient industrial production of hydrogen from alkaline-water electrolytic cells," *Journal of materials science*, vol. 28, no. 16, pp. 4375–4382, **1993**.

[27] I. Katsounaros, J. C. Meier, and K. J. Mayrhofer, "The impact of chloride ions and the catalyst loading on the reduction of H2O2 on high-surface-area platinum catalysts," *Electrochimica Acta*, vol. 110, pp. 790–795, **2013**.

[28] Y. Liu, C.-J. Jia, J. Yamasaki, O. Terasaki, and F. Schuth, "Highly active iron oxide supported gold catalysts for co oxidation: How small must the gold nanoparticles be?," *Angew. Chem. Int. Ed.*, vol. 49, pp. 5771–5775, **2010**.

[29] S. K. Balasubramanian, L. Yang, L. L. Yung, C. N. Ong, W. Y. Ong, and L. E. Yu, "Characterization, purification, and stability of gold nanoparticles," *Biomaterials*, vol. 31, pp. 9023–9030, **2010**.

[30] J. A. Lopez-Sanchez, N. Dimitratos, C. Hammond, G. L. Brett, L. Kesavan, S. White, P. Miedziak, R. Tiruvalam, R. L. Jenkins, A. F. Carley, D. Knight, C. J. Kiely, and G. J. Hutchings, "Facile removal of stabilizer-ligands from supported gold nanoparticles," *Nature Chem.*, vol. 3, pp. 551–556, **2011**.

[31] S. Barcikowski, F. Devesa, and K. Moldenhauer, "Impact and structure of literature on nanoparticle generation by laser ablation in liquids," *J. Nanopart. Res.*, vol. 11, pp. 1883–1893, **2009**.

[32] S. Barcikowski and G. Compagnini, "Advanced nanoparticle generation and excitation by lasers in liquids," *Physical Chemistry Chemical Physics*, vol. 15, no. 9, pp. 3022–3026, **2013**.

[33] V. Amendola and M. Meneghetti, "What controls the composition and the structure of nano-materials generated by laser ablation in liquid solution?" *Phys. Chem. Chem. Phys.*, vol. 15, pp. 3027–3046, **2013**.

[34] F. Mafune, J. Kohno, Y. Takeda, and T. Kondow, "Growth of gold clusters into nanoparticles in a solution following laser-induced fragmentation," *J. Phys. Chem. B*, vol. 106, pp. 8555–8561, **2002**.

[35] G. Compagnini, A. Scalisi, and O. Puglisi, "Production of gold nanoparticles by laser ablation in liquid alkanes," *Journal of applied physics*, vol. 94, no. 12, pp. 7874–7877, **2003**.

[36] Y. Kimura, H. Takata, M. Terazima, T. Ogawa, and S. Isoda, "Preparation of gold nanoparticles by the laser ablation in room-temperature ionic liquids," *Chemistry Letters*, vol. 36, no. 9, pp. 1130–1131, **2007**.

[37] T. Tsuji, K. Iryo, N. Watanabe, and M. Tsuji, "Preparation of silver nanoparticles by laser ablation in solution: influence of laser wavelength on particle size," *Applied Surface Science*, vol. 202, no. 1, pp. 80–85, **2002**.

[38] S. Barcikowski, A. Hahn, A. V. Kabashin, and B. Chichkov, "Properties of nanoparticles generated during femtosecond laser machining in air and water," *Appl. Phys. A*, vol. 87(1), p. 47–55, **2007**.

[39] J. Zhang, D. N. Oko, S. Garbarino, R. Imbeault, M. Chaker, A. C. Tavares, D. Guay, and D. Ma, "Preparation of ptau alloy colloids by laser ablation in solution and their characterization," *J. Phys. Chem. C*, vol. 116, pp. 13413–13420, **2012**.

[40] D. N. Oko, J. Zhang, S. Garbarino, M. Chaker, D. Ma, A. C. Tavares, and D. Guay, "Formic acid electro-oxidation at PtAu alloyed nanoparticles synthesized by pulsed laser ablation in liquids," *Journal of Power Sources*, vol. 248, pp. 273–282, **2014**.

[41] D. Kil, Y. Suh, H. Jang, J. Lee, C. Song, and W. Kim, "Nanosize particles of ZrVFe alloy by pulsed laser ablation in ethanol," *Materials transactions*, vol. 46, no. 11, pp. 2509–2513, **2005**.

[42] A. Neumeister, J. Jakobi, C. Rehbock, J. Moysig, and S. Barcikowski, "Monophasic ligand-free alloy nanoparticle synthesis determinants during pulsed laser ablation of bulk alloy and consolidated microparticles in water," *Phys. Chem. Chem. Phys.*, pp.23671 –23678, **2014**.

[43] J. Zhang and C. Q. Lan, "Nickel and cobalt nanoparticles produced by laser ablation of solids in organic solution," *Materials Letters*, vol. 62, no. 10, pp. 1521–1524, **2008**.

[44] S. Barcikowski, T. Baranowski, Y. Durmus, U. Wiedwald, and B. Gökce, "Solid solution magnetic FeNi nanostrand–polymer composites by connecting-coarsening assembly," *Journal of Materials Chemistry C*, vol. 3, no. 41, pp. 10699–10704, **2015**.

[45] J. Jakobi, S. Petersen, A. Menendez-Manjon, P. Wagener, and S. Barcikowski, "Magnetic alloy nanoparticles from laser ablation in cyclopentanone and their embedding into a photoresist," *Langmuir*, vol. 26, p. 6892–6897, **2010**.

[46] D. Poondi, T. Dobbins, and J. Singh, "A novel laser-liquid-solid interaction technique for synthesis of silver, nickel and immiscible silver-nickel alloys from liquid precursors," *Journal of materials science*, vol. 35, no. 24, pp. 6237–6243, **2000**.

[47] W. Liu, O. Kosareva, I. S. Golubtsov, A. Iwasaki, B. A., V. P. Kandidov, and S. L. Chin, "Femtosecond laser pulse filamentation versus optical breakdown in H2O," *Appl. Phys. B*, vol. 76, pp. 215–229, **2003**.

[48] K. Nouneh, M. Oyama, R. Diaz, M. Abd-Lefdil, I. Kityk, and M. Bousmina, "Nanoscale synthesis and optical features of metallic nickel nanoparticles by wet chemical approaches," *Journal of Alloys and Compounds*, vol. 509, no. 19, pp. 5882–5886, **2011**.

[49] K. Chandrappa, T. Venkatesha, K. Nayana, and M. Punithkumar, "Generation of nanocrystalline nio particles by solution combustion method and its Zn? NiO composite coating for corrosion protection," *Materials and Corrosion*, vol. 63, no. 5, pp. 445–455, **2012**.

[50] J. A. Creighton and D. G. Eadont, "Ultraviolet-visible absorption spectra of the colloidal metallic elements," *J. Chem. Soc. Faraday Trans.*, vol. 87, pp. 3881–3891, **1991**.

[51] K. Krishnamoorthy, M. Veerapandian, K. Yun, and S. J. Kim, "New function of molybdenum trioxide nanoplates: Toxicity towards pathogenic bacteria through membrane stress," *Colloids and Surfaces B: Biointerfaces*, vol. 112, pp. 521–524, **2013**.

[52] H. Sinaim, A. Phuruangrat, S. Thongtem, and T. Thongtem, "Synthesis and characterization of heteronanostructured Ag nanoparticles/MoO3 nanobelts composites," *Materials Chemistry and Physics*, vol. 132, no. 2, pp. 358–363, **2012**.

[53] J. Cruywagen and J. Heyns, "Equilibria and uv spectra of mono-and polynuclear molybdenum (VI) species," *Inorganic Chemistry*, vol. 26, no. 16, pp. 2569–2572, **1987**.

[54] R. S. Weber, "Effect of local structure on the uv-visible absorption edges of molybdenum oxide clusters and supported molybdenum oxides," *Journal of Catalysis*, vol. 151, no. 2, pp. 470–474, **1995**.

[55] T. He and J. Yao, "Photochromism of molybdenum oxide," *Journal of Photochemistry and Photobiology C: Photochemistry Reviews*, vol. 4, no. 2, pp. 125–143, **2003**.

[56] L. Zheng, Y. Xu, D. Jin, and Y. Xie, "Novel metastable hexagonal MoO3 nanobelts: Synthesis, photochromic, and electrochromic properties," *Chemistry of Materials*, vol. 21, no. 23, pp. 5681–5690, **2009**.

[57] G. Cristoforetti, E. Pitzalis, R. Spiniello, R. Ishak, and M. Muniz-Miranda, "Production of palladium nanoparticles by pulsed laser ablation in water and their characterization," *J. Phys. Chem. C*, vol. 115, p. 5073–5083, **2011**.

[58] W. T. Nichols, T. Sasaki, and N. Koshizaki, "Laser ablation of a platinum target in water. ii. ablation rate and nanoparticle size distributions," *J. Appl. Phys.*, vol. 100, p. 114912, **2006**.

[59] M. S. I. Sarker, T. Nakamura, Y. Herbani, and S. Sato, "Fabrication of rh based solid-solution bimetallic alloy nanoparticles with fully-tunable composition through femtosecond laser irradiation in aqueous solution," *Applied Physics A*, vol. 110, no. 1, pp. 145–152, **2013**.

[60] M. S. Islam Sarker, T. Nakamura, and S. Sato, "Composition-controlled ternary Rh–Pd–Pt solid-solution alloy nanoparticles by laser irradiation of mixed solution of metallic ions," *Journal of Materials Research*, vol. 29, no. 07, pp. 856–864, **2014**.

[61] K. Yuge, "Concentration effects on segregation behavior of Pt-Rh nanoparticles," *Physical Review B*, vol. 84, no. 8, p. 085451, **2011**.

[62] J. Koch, A. Von Bohlen, R. Hergenröder, and K. Niemax, "Particle size distributions and compositions of aerosols produced by near-IR femto-and nanosecond laser ablation of brass," *Journal of Analytical Atomic Spectrometry*, vol. 19, no. 2, pp. 267–272, **2004**.

[63] L. J. Lewis and D. Perez, "Laser ablation with short and ultrashort laser pulses: Basic mechanisms from molecular-dynamics simulations," *Applied Surface Science*, vol. 255, no. 10, pp. 5101–5106, **2009**.

[64] H. Dang, Z. Han, Z. Dai, and Q. Qin, "Characterization of laser ablated species from a La–Ca–Mn–O target by angle-and time-resolved mass spectrometry," *International journal of mass spectrometry*, vol. 178, no. 3, pp. 205–212, **1998**.

[65] P. Wagener, S. Ibrahimkutty, A. Menzel, A. Plech, and S. Barcikowski, "Dynamics of silver nanoparticle formation and agglomeration inside the cavitation bubble after pulsed laser ablation in liquid," *Phys. Chem. Chem. Phys.*, vol. 5, pp. 3068–3074, **2013**.

[66] J. Jakobi, A. Menendez-Manjon, V. S. K. Chakravadhanula, L. Kienle, P. Wagener, and S. Barcikowski, "Stoichiometry of alloy nanoparticles from laser ablation of PtIr in acetone and their electrophoretic deposition on ptir electrodes," *Nanotechnology*, vol. 22, p. 145601, **2011**.

[67] Y. Ishikawa, K. Kawaguchi, Y. Shimizu, T. Sasaki, and N. Koshizaki, "Preparation of Fe–Pt alloy particles by pulsed laser ablation in liquid medium," *Chemical physics letters*, vol. 428, no. 4, pp. 426–429, **2006**.

[68] R. Schulz, J. Huot, M. Trudeau, L. Dignard-Bailey, Z. Yan, S. Jin, A. Lamarre, E. Ghali, and A. Van Neste, "Nanocrystalline ni-mo alloys and their application in electrocatalysis," *Journal of materials research*, vol. 9, no. 11, pp. 2998–3008, **1994**.

[69] H. L. Clever, R. Battino, H. Miyamoto, Y. Yampolski, C. L. Young, *et al.*, "Iupac-nist solubility data series. 103. oxygen and ozone in water, aqueous solutions, and organic liquids (supplement to solubility data series volume 7)," *Journal of Physical and Chemical Reference Data*, vol. 43, no. 3, p. 033102, **2014**.

[70] P. Wagener, J. Jakobi, C. Rehbock, V. S. K. Chakravadhanula, C. Thede, U. Wiedwald, M. Bartsch, L. Kienle, and S. Barcikowski, "Solvent-surface interactions control the phase structure in laser-generated iron-gold core-shell nanoparticles," *Scientific Reports*, vol. 6, **2016**.

[71] ICSD-Database, "http://icsd.fiz-karlsruhe.de," **2013**.

[72] L. Trotochaud, J. K. Ranney, K. N. Williams, and S. W. Boettcher, "Solution-cast metal oxide thin film electrocatalysts for oxygen evolution," *Journal of the American Chemical Society*, vol. 134, no. 41, pp. 17253–17261, **2012**.

[73] H. M. French, M. J. Henderson, A. R. Hillman, and E. Vieil, "Ion and solvent transfer discrimination at a nickel hydroxide film exposed to lioh by combined electrochemical quartz crystal microbalance (EQCM) and probe beam deflection (pbd) techniques," *Journal of Electroanalytical Chemistry*, vol. 500, no. 1, pp. 192–207, **2001**.

[74] A. Seghiouer, J. Chevalet, A. Barhoun, and F. Lantelme, "Electrochemical oxidation of nickel in alkaline solutions: a voltammetric study and modelling," *Journal of Electroanalytical Chemistry*, vol. 442, no. 1, pp. 113–123, **1998**.

[75] N. Krstajic, V. Jovic, L. Gajic-Krstajic, B. Jovic, A. Antozzi, and G. Martelli, "Electrodeposition of ni–mo alloy coatings and their characterization as cathodes for hydrogen evolution in sodium hydroxide solution," *Ínternational Journal of Hydrogen Energy*, vol. 33, no. 14, pp. 3676–3687, **2008**.

[76] M. R. O. Riyanto and J. Salimon, "Analysis of ethanol using copper and nickel sheet electrodes by cyclic voltammetry," *Malaysian Journal of Analytical Sciences*, vol. 11, no. 2, pp. 379–387, **2007**.

[77] M. Dmochowska and A. Czerwinski, "Behavior of a nickel electrode in the presence of carbon monoxide," *Journal of Solid State Electrochemistry*, vol. 2, no. 1, pp. 16–23, **1998**.

[78] C. C. McCrory, S. Jung, J. C. Peters, and T. F. Jaramillo, "Benchmarking heterogeneous electrocatalysts for the oxygen evolution reaction," *Journal of the American Chemical Society*, vol. 135, no. 45, pp. 16977–16987, **2013**.

[79] F. Endres and G. Schwitzgebel, "Cyclic voltammetry of polyethylene stabilized hydrogen molybdenum bronzes," *Journal of Electroanalytical Chemistry*, vol. 415, no. 1, pp. 23–26, **1996**.

[80] T. Heumann and M. Klimmeck, "Elektrochemische untersuchungen an molybdän, "*Materials and Corrosion*, vol. 22, no. 2, pp. 115–120, **1971**.

[81] W. Badawy, H. Feky, N. Helal, and H. Mohammed, "Cathodic hydrogen evolution on molybdenum in naoh solutions," *International Journal of Hydrogen Energy*, vol. 38, no. 23, pp. 9625–9632, **2013**.

[82] W. Badawy, H. Fekry, N. Helal, and H. Mahmmed, "Hydrogen production on molybdenum in H2SO4 solutions," *Journal of Power Sources*, **2014**.

[83] V. S. Saji and C.-W. Lee, "Molybdenum, molybdenum oxides, and their electrochemistry," *ChemSusChem*, vol. 5, no. 7, pp. 1146–1161, **2012**.

[84] V. K. V. P. Srirapu, C. S. Sharma, R. Awasthi, R. N. Singh, and A. S. K. Sinha, "Copper–iron–molybdenum mixed oxides as efficient oxygen evolution electrocatalysts," *Physical Chemistry Chemical Physics*, vol. 16, no. 16, pp. 7385–7393, **2014**.

[85] L. Birry and A. Lasia, "Studies of the hydrogen evolution reaction on raney nickel—molybdenum electrodes," *Journal of applied electrochemistry*, vol. 34, no. 7, pp. 735–749, **2004**.

[86] P. Strasser, "Dealloyed core-shell fuel cell electrocatalysts," *Reviews in Chemical Engineering*, vol. 25, no. 4, pp. 255–295, **2009**.

[87] P. Strasser, S. Koh, T. Anniyev, J. Greeley, K. More, C. Yu, Z. Liu, S. Kaya, D. Nordlund, H. Ogasawara, *et al.*, "Lattice-strain control of the activity in dealloyed core–shell fuel cell catalysts," *Nature Chemistry*, vol. 2, no. 6, pp. 454–460, **2010**.

[88] H. Vrubel and X. Hu, "Molybdenum boride and carbide catalyze hydrogen evolution in both acidic and basic solutions," *Angewandte Chemie*, vol. 124, no. 51, pp. 12875–12878, **2012**.

[89] L. Liao, S. Wang, J. Xiao, X. Bian, Y. Zhang, M. D. Scanlon, X. Hu, Y. Tang, B. Liu, and H. H. Girault, "A nanoporous molybdenum carbide nanowire as an electrocatalyst for hydrogen evolution reaction," *Energy & Environmental Science*, vol. 7, no. 1, pp. 387–392, **2014**.

[90] J. Huot, M. Trudeau, and R. Schulz, "Low hydrogen overpotential nanocrystalline ni-mo cathodes for alkaline water electrolysis," *Journal of The Electrochemical Society*, vol. 138, no. 5, pp. 1316–1321, **1991**.

1. Synthesis of heterogeneous catalysts – method, mechanism and challenges of colloidal nanoparticle deposition

In the previous chapters, the synthesis and properties of colloidal nanoparticles have been examined in detail. However, in order to synthesize a heterogeneous catalyst, the previously prepared nanoparticles need to be immobilized on support material. Until now, investigations on the mechanism of particle deposition of laser-generated nanoparticles have been missing. Due to the ligand-free surfaces of these particles, the adsorption onto carriers is free of steric barriers. Concerning this matter, Koenen et al. showed that during electrophoretic deposition, ligands on the particle's surface as well as free ligands in the solvent act as a barrier in front of the electrode and thus shield the electrode's charge and prevent particle deposition[1]. Similar observations were made with respect to particle adsorption on micrometer-sized supports. Wagener et al. investigated the particle adsorption efficiency on ligand coverage and hypothesized that the adsorption process is initiated by inducing electrostatic interactions between the ligand and support[2]. Since the charge of the nanoparticles strongly depends on ligand functionalization, the authors observed an inhibition of the deposition process on exceeding 50% coverage of the particles surface with ligands that were assigned to electrostatic repulsion. However, in this study, mechanism of particle adsorption and its influential parameters were not examined. The authors has assumed, that also the influence of the pH value play a role but was not further investigated. Thus, in the present study, the basic principle is to investigate the mechanism for particle adsorption by individually adjusting the ligand coverage, pH and ionic strength to control the adsorption kinetics and efficiency. Because of the separation of the nanoparticle-generation step and subsequent adsorption, the particle size distribution can be adjusted independently from the nanoparticle loading. This enables individual comparative studies of nanoparticle properties and loading.

Motivated by the possibilities of ligand-free nanoparticles, the adsorption mechanism of laser-generated colloidal nanoparticles on supports will be elaborated in the first section (6.1) of this chapter. It will be shown that the electrostatic interactions, which can be controlled by the pH of the colloid, determine particle adsorption. Based on the results, a mechanistic proposal as well as a set of experimental design criteria for a quantitative particle adsorption will be suggested.

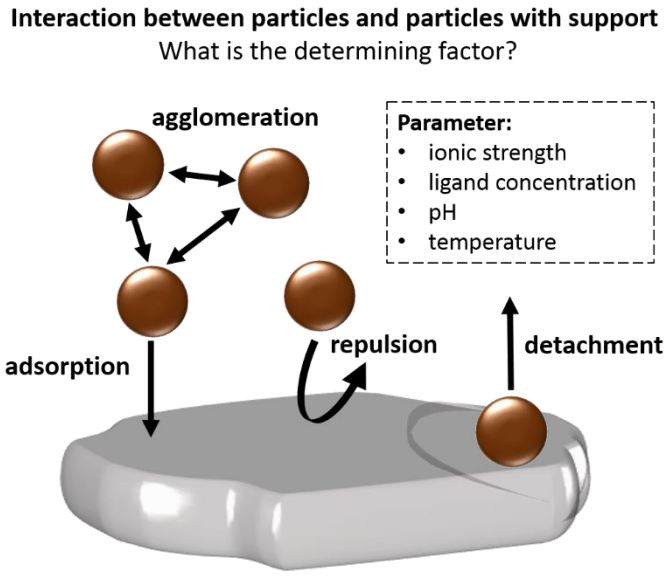

Fig. A4: Schematic illustration of current investigations on particle interactions.

Hence, in section 6.2, the stability of supported nanoparticles will be evaluated. $PtCu_3$-functionalized supports were chosen as model materials because of their promising usability in fuel cell reactions[3], [4]. Subsequently, the prepared catalysts (PtCu/CB and $PtCu/TiO_2$) were tested for their apparent chemical and thermal stability under application-relevant conditions. The results show that there is still room for improvement, since evident particle detachment has been observed under thermal conditions. These first insights may be used as an inspiration for future catalyst design – especially when designing heterogeneous catalysts that contain bimetallic alloys.

Literature

[1] C. Streich, S. Koenen, M. Lelle, K. Peneva, and S. Barcikowski, "Influence of ligands in metal nanoparticle electrophoresis for the fabrication of biofunctional coatings," *Applied Surface Science*, vol. 348, pp. 92–99, 2015.

[2] P. Wagener, A. Schwenke, and S. Barcikowski, "How citrate ligands affect nanoparticle adsorption to microparticle supports," *Langmuir*, vol. 28, no. 14, pp. 6132–6140, 2012. PMID: 22417054.

[3] M. Oezaslan, F. Hasché, and P. Strasser, "Ptcu3, ptcu and pt3cu alloy nanoparticle electrocatalysts for oxygen reduction reaction in alkaline and acidic media," *Journal of The Electrochemical Society*, vol. 159, no. 4, pp. B444–B454, 2012.

[4] N. Hodnik, C. Jeyabharathi, J. C. Meier, A. Kostka, K. L. Phani, A. Recnik, M. Bele, S. Hocevar, M. Gaberšček, and K. J. Mayrhofer, "Effect of ordering of ptcu 3 nanoparticle structure on the activity and stability for the oxygen reduction reaction," *Physical Chemistry Chemical Physics*, vol. 16, no. 27, pp. 13610–13615, 2014.

1.1. Adsorption of colloidal platinum nanoparticles to supports: Charge transfer and effects of electrostatic and steric interactions

Reprinted with permission from Langmuir, 30 (40), Galina Marzun, Carmen Streich, Sandra Jendrzej, Stephan Barcikowski and Philipp Wagener, "Adsorption of colloidal platinum nanoparticles to supports: Charge transfer and effects of electrostatic and steric interactions" 11928-11936, 2014.

Abstract

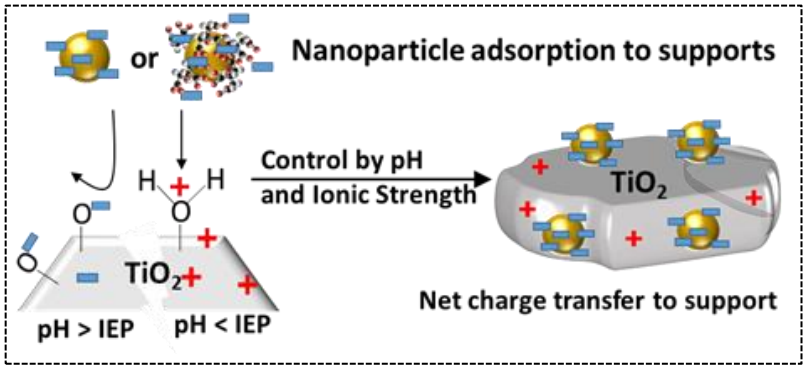

Adsorption of colloidal nanoparticles to surfaces and supports is a convenient approach to heterogeneous catalysts, polymer additives or waste water treatment. We investigated the adsorption of laser-generated and initially ligand-free platinum nanoparticles to TiO_2 supports as function of pH, ionic strength and ligand surface coverage. The nanoparticle adsorption is dominantly controlled by electrostatic interactions: if the pH of the suspension is between the isoelectric point of the nanoparticles and the support, nanoparticles are adsorbed and transfer a net charge to the support. This charge-driven adsorption is not affected by steric repulsion due to various ligands attached to the nanoparticle surface. In addition to electrostatic interactions, colloidal stability given by moderate ionic strengths and pH values above the isoelectric point of nanoparticles are prerequisites for colloidal deposition.

1. Introduction

The adsorption of colloidal nanoparticles to surfaces and supports is essential in diverse fields of research. Such colloidal deposition is usually applied in the synthesis of nanoparticle-functionalized materials (e.g. heterogeneous catalysts[1,2], polymer additives[3]) but is also helpful in the removal of nanoparticles from the liquid phase (e.g. waste water treatment[4,5]). In heterogeneous catalysis, the traditional synthesis protocol includes a wet impregnation of the

supporting material with metal salts and subsequent reduction to nanostructures[6]. Due to the inherent simplicity of this protocol, itis successful for both lab scale and industrial scale production of catalysts. But it does not provide satisfactory control of particle size. In their pioneering work, Bönneman et al. established a method for the production of heterogeneous catalysts from chemically synthesized nanoparticle precursors ("precursor concept") which allowed a superior control of nanoparticle properties[7]. In a first step of this method, colloidal nanoparticles are prepared through chemical reduction of metal salts in the presence of stabilizing agents which allows a good control of nanoparticle properties. The second step consists of the adsorption of the colloidal particles on the support, resulting in an "egg-shell" structured catalyst. Because the produced thin film of active metal species at the support surface is protected by a surfactant shell, thermal treatment and calcination is required to remove most of the protecting layer and activate the catalyst[8].

In addition to catalysis, supported nanoparticles are also useful as polymer or ceramic additives in biomedical application[3,9] or processing of semiconductors[10]. Furthermore, environmental scientists are concerned about the appearance of metal nanoparticles in waste water and other aquatic environmental systems[11,12]. A deeper understanding of the nanoparticle adsorption processes under various conditions is highly demanded and may result in new techniques for water purification and cleaning or synthesis of nanoparticle-functionalized materials.

In the literature, the interaction of nanoparticles with surfaces and supports is usually described by means of Coulomb attractive forces between charged colloidal particles and solid surfaces[13–16], but other contributions like van-der-Waals-forces[17] or adhesion at oxygen vacancies[18] are also discussed. Since it is well known that especially electrostatic interactions are strongly influenced by colloidal properties, like pH[2], ionic strength[19] or use of (charged) ligands[14], one has to understand all individual parameters. Unfortunately, the investigation of nanoparticle adsorption is complicated by the fact, that colloids usually contain a manifold of additives like surfactants, ligands and ions which handicap a differentiated investigation of the influencing parameters. To reduce the complexity of the system, laser ablation in liquid is a versatile approach to pure and ligand-free nanoparticles[20–22] which are a suitable model system for the investigation of colloidal deposition[23]. Those laser-generated nanoparticles are born in a plasma-filled cavitation bubble[24,25] resulting in charged and electrostatically stable crystalline nanoparticles with a surface free of ligands and monodisperse size[26–28]. Starting from this clean colloid, one can individually adjust ligand surface coverage[29,30], pH and ionic strength of the suspension[28].

The scope of this paper is to identify and qualify the parameters which control the nanoparticle

adsorption to suspended supports using ligand-free nanoparticles made by laser ablation. As a model system platinum nanoparticles and TiO_2 support which have broad application in catalysis and photocatalysis[31,32], water splitting reactions[33,34] and biomedical application[35] are chosen.

2. Experimental

2.1 Laser-generation of colloids

Platinum nanoparticles were produced by pulsed laser ablation in liquid of a Pt target (99.99 % Alfa Aesar). We used a Nd:YAG nanosecond-laser (Rofin-Sinar RS-Marker 100D, pulse duration 40 ns) at a fundamental wavelength of 1064 nm with a repetition rate of 5 kHz and a pulse energy of 6.4 mJ. The laser beam was focused with an f-theta lens of 63 mm focal length and was scanned by coupling it into a scanner optic in a spiral pattern. Nanoparticles were synthesized in a self-constructed flow-through chamber (liquid layer 5 mm) made of steel with a continuous flow of Milli-Q water (resistivity of 18.2 MΩ·cm at 25 °C) using a flow rate of 28.2 ml/min (pump Ismatec ISM321C). The concentration of colloidal platinum (120.7 µg/ml corresponding to a productivity of 0.2 g/h) was determined by weighting the target before and after ablation with a microbalance (Sartorius M235S). Ligand-functionalized nanoparticles using polyvinylpyrrolidone (PVP, Sigma-Aldrich), and lipoic acid (LA, Sigma-Aldrich) were fabricated using a Nd:YAG nanosecond-laser (Rofin Powerline E, pulse duration 8 ns, f-theta lens of 130 mm focal length) operated at a repetition rate of 10 kHz and a pulse energy of 0.385 mJ in a self-designed batch-chamber (more details on used laser systems can be found within the Supporting Information). Ligands were added to the colloid after laser ablation (ex situ). The samples were allowed to stand for 16 hours at room temperature to obtain a chemical equilibrium between ligands attached to the nanoparticle surface and dissolved ligands.

2.2 Nanoparticle adsorption experiments

Platinum colloids were mixed with the carrier material TiO_2 (Hombikat Type II (Sachtleben), primary particle diameter < 15 nm, BET surface 90-120 m^2/g) with a nanoparticle-to-support ratio of 1 wt%. The colloidal-support suspension was shaken and stored overnight. After sedimentation of TiO_2 the supernatant was pipetted out and used for further analysis on adsorption efficiency (UV/Vis spectroscopy and pH measurements). The platinum-loaded TiO_2 (Pt/TiO_2) were dried at 50° C (drying oven Binder ED115) for further analysis (SEM). To study the effect of the ionic strength and the pH on adsorption efficiency, aqueous trisodium citrate

solution (c=0.01–100 mmol/l, Sigma-Aldrich), sodium phosphate buffer at pH=7 (PB, c=0.1–100 mmol/l, Sigma-Aldrich), sodium carbonate buffer (CB, c=0.5-6 mmol/L, Merck) and sodium hydroxid solution (NaOH, c=0.1–1 mmol/l, VWR) were added in various concentration to the platinum colloid. Ligand functionalization of platinum nanoparticles was also done by adding PVP (MW=58,000 g/mol, c=0.001-1000 µmol/l) or LA (c=0.01–1000 µmol/l) to freshly prepared ligand-free nanoparticles. Before and after adsorption of the platinum nanoparticles, the pH value of the colloids and the supernatant was measured with a pH-meter (PCE-PHD1). The adsorption efficiency was determined by extinction measurements using UV/Vis spectroscopy in a spectral range of λ = 190-900 nm using a Thermo Scientific Evolution 201 in a glass cuvette with 10 mm path length. The UV-Vis spectra of the platinum colloid was measured before the adsorption experiments. The spectra of the supernatant was measured after the added support material sedimented. When the TiO_2 support was added to the colloidal solution, the typical brown color of the Pt colloid disappeared and a clear supernatant was obtained after sedimentation of the hybrid Pt/TiO_2. The concentration of colloidal platinum nanoparticles is linear proportional to the interband extinction at λ = 300 nm (S1)[36,37] which is shown in more detail within the Supporting Information (see Figure S1). Hence, the adsorption efficiency of nanoparticle deposition to support was calculated using equation 1:

$$\text{Adsorption efficiency} = \frac{Ext@300nm_{\text{before}} - Ext@300nm_{\text{after}}}{Ext@300nm_{\text{before}}} \qquad (1)$$

$Ext@300nm_{before}$ = Extinction at 300 nm before adding TiO_2 (colloid)

$Ext@300nm_{after}$ = Extinction at 300 nm after adding TiO_2 (supernatant)

If platinum nanoparticles are completely adsorbed to the TiO_2 support (adsorption efficiency=1), the supernatant is clear and the UV/Vis spectra does not indicate any absorption at 300 nm. When no adsorption takes place at a certain pH or ionic strength, a certain amount of TiO_2 is dispersed together with the platinum nanoparticles in the supernatant, which yields to an additional absorption band at 300 nm. In this case, the calculated adsorption efficiency is based on a superposition of both platinum nanoparticle and TiO_2 extinction values and may even result in a negative value. Nevertheless, a negative value means no adsorption took place which is shown in more detail within the Supporting Information.

2.3 Characterization of colloidal and supported platinum nanoparticles

The hydrodynamic diameter of the nanoparticles were determined by analytical disc

centrifugation (ADC) using a DC 24000 from CPS instruments. A volume of 0.1 ml of the sample was analyzed against a saccharose gradient and an external standard (PVC particles at 0.239 μm) while the disc was operated at 24000 rpm.

The colloidal solution was dropped on a carbon-coated copper grid, dried in air and imaged with Transmission Electron Microscopy (TEM) using a Philips CM12. Scanning Electron Microscopy (SEM) measurements of Pt/TiO_2 deposited on a polished graphite carrier were carried out with a Quanta 400FEG and are shown within the Supporting Information (Figure S5).

For studying the particle surface charge and the isoelectric point (IEP) zeta-potential measurements in a titration mode with an autotitrator (MPT-2-Malvern) were performed with a Malvern Zetasizer "Nano ZS" in a capillary cell (750 μl).

3. Results and discussion

3.1. Electrostatic-controlled adsorption of ligand-free nanoparticles

Ligand-free platinum nanoparticles were obtained by laser ablation in liquid and characterized in their colloidal state. Figure 1 shows the particle size distributions which were measured using disc centrifugation and electron microscopy. Laser-generated platinum nanoparticles have a diameter in the range of 3–5 nm showing a monomodal particle size distribution in the particle number-weighted histograms. As there are a few nanoparticles > 5 nm, the mass-weighted particle size analysis shows a weak second mode around 10 nm. UV/Vis spectra shown in Figure 2 reveal the characteristic extinction spectra of colloidal platinum nanoparticles[36,38]. The zeta potential of platinum nanoparticles was measured to be –36 mV resulting in an electrostatically stable colloid that could be stored for days without any significant change. Surface charge characterization of nanoparticles and support was done by measuring the zeta potential as a function of pH which is shown in Figure 3. The isoelectric point (neutral particles) is about 2.8 for platinum nanoparticles and 6.3 for TiO_2 support, respectively.

For adsorption experiments, the colloid was mixed with TiO_2 as described in the experimental section. To quantify adsorption, the concentration of colloidal nanoparticles was measured by UV/Vis spectroscopy before and after the mixing. If nanoparticle adsorption takes place, the liquid gets clear and the absorption band (at 300 nm) disappears in the UV/Vis spectra which is shown in Figure 2. Using this simple method one can easily calculate nanoparticle adsorption efficiency to the support[9, 24]. Please note that negative values correspond to the given calculation method (see experimental section). In this case, some TiO_2 is dispersed and contributes to the

UV/Vis extinction after mixing with the colloid. Thus, equation 1 results in a negative value. However, no adsorption of platinum nanoparticles takes place in this case which was checked by centrifugation and subsequent size analysis by ADC (data shown in the Supporting Information, Figure S4-S6).

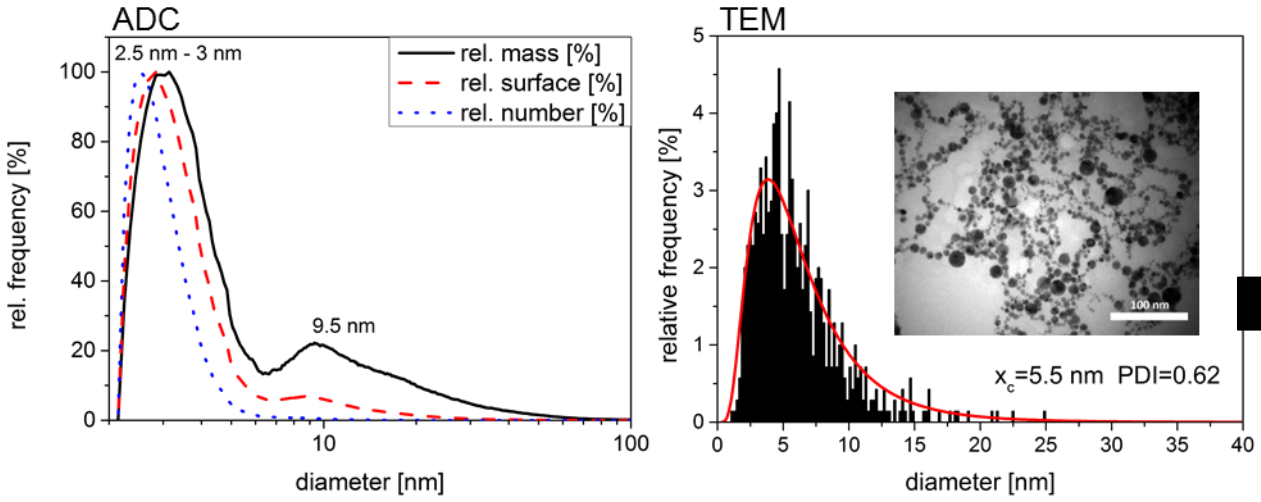

Figure 1: Particle size of platinum nanoparticles measured by analytical disc centrifugation (ADC) and transmission electron microscopy (TEM).

As can be seen from Figure 2, all colloidal nanoparticle quantitatively (adsorption efficiency > 95%) adsorb to the white support resulting in a transparent supernatant and grey-colored TiO_2 support with platinum nanoparticles (more information on this can be found in the Supporting Information).

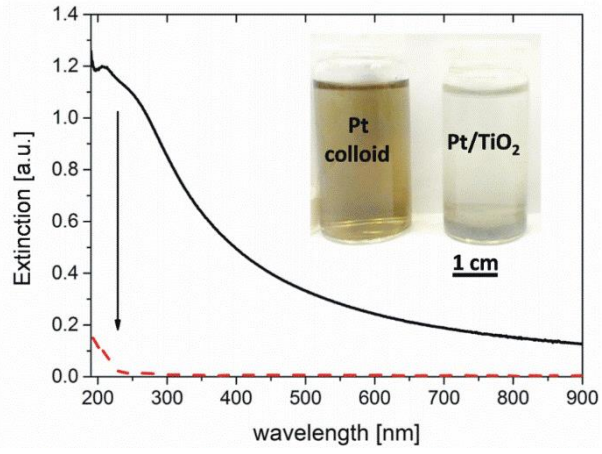

Figure 2: UV/Vis spectra of colloidal platinum nanoparticles before (black line) and after mixing with TiO_2 support (red dotted line).

For further use like for catalysis, the supported nanoparticles only have to be filtrated and dried. According to literature, the nanoparticle adsorption can be considered as an electrostatic adsorption[2]. The mixture of platinum nanoparticles and TiO_2 support show a pH of 5.0 which

means that platinum nanoparticles are negatively charged (IEP 2.3-2.8) and TiO_2 support is positively charged (IEP 6.3-6.4) resulting in an attractive Coulomb force which initiates adsorption. By adsorption of negatively charged nanoparticles to suspended support, we can clearly observe a net charge transfer to the support. This net charge transfer is caused by a shift of IEP of the TiO_2 support in Figure 3. The IEP shifts from 6.4 to a lower value of 5.0 which means that a negative charge is transferred by ions after platinum nanoparticles are adsorbed on TiO_2-support. In a microscopic view, this should be connected to an initial neutralization of the surface charge of TiO_2. Consequently, the net-charge-transfer to the support results in less positively charged support and should margin the maximal load of nanoparticles. Accordingly, Figure 3 (bottom) demonstrates the impact of nanoparticle load on IEP of the TiO_2 support (raw data can be found within the Supporting Information, Fig. S8): A higher nanoparticle load lowers the IEP of the TiO_2 until it converges with the IEP of platinum nanoparticles. At this point, the charges of nanoparticles and support are almost identical to prevent further electrostatic-controlled nanoparticle adsorption. For the given system, we observe a maximal nanoparticle load up to 65 wt% which is shown within the Supporting Information (Figure S8).

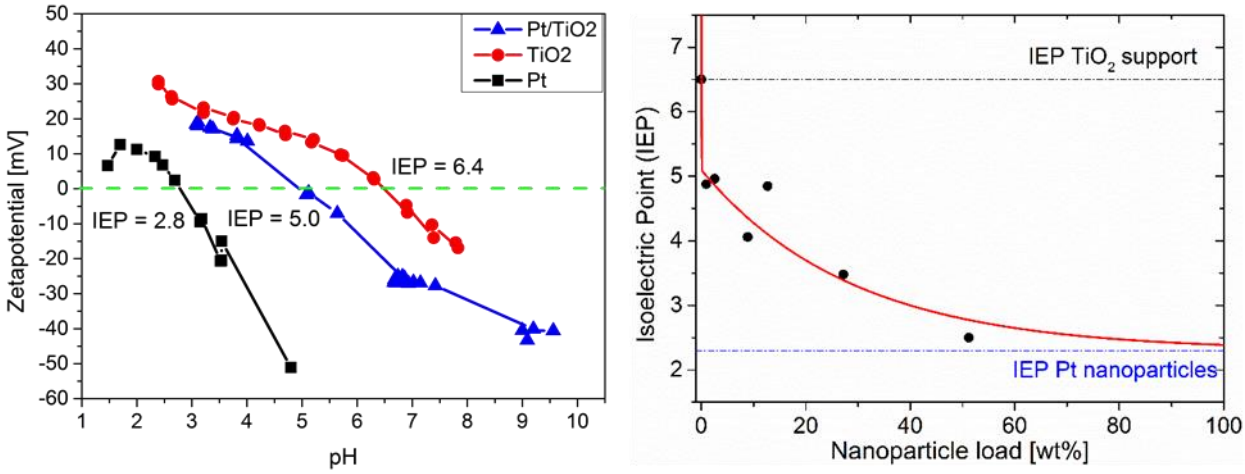

Figure 3: Top: Zeta potentials and isoelectric points of colloidal platinum nanoparticles, TiO_2 support and Pt/TiO_2 catalyst (1 wt%). Bottom: Isoelectric point of Pt/TiO_2 as a function of nanoparticle load (the line is just to guide the eyes).

Due to electrostatic interaction, the adsorption process is very sensitive to the pH of the dispersion. Figure 4 shows the adsorption efficiency as a function of pH using different electrolytes like phosphate buffer, carbonate buffer and citrate or sodium hydroxide solution. Low pH values (< 5.5) result in a complete adsorption of platinum nanoparticles which is initiated by an attraction between positively charged support and negatively charged platinum nanoparticles. Since the particle surface gets protonated at low acidity (pH<4), too low pH values close to the IEP of platinum nanoparticles (IEP 2.7) have to be avoided. Thereby, the negative surface charge is compensated and results in critically low zeta potential values < *kT/e*

that cause agglomeration. If the pH exceeds the IEP of the support (IEP 6.4), the charge of the support is reversed from positive to negative, causing electrostatic repulsion of negatively charged nanoparticles and negative support. Overall, this clearly reveals that adsorption of metal nanoparticles is efficient only if pH is higher than the IEP of the nanoparticle adsorbate and lower than the IEP of the adsorbent.

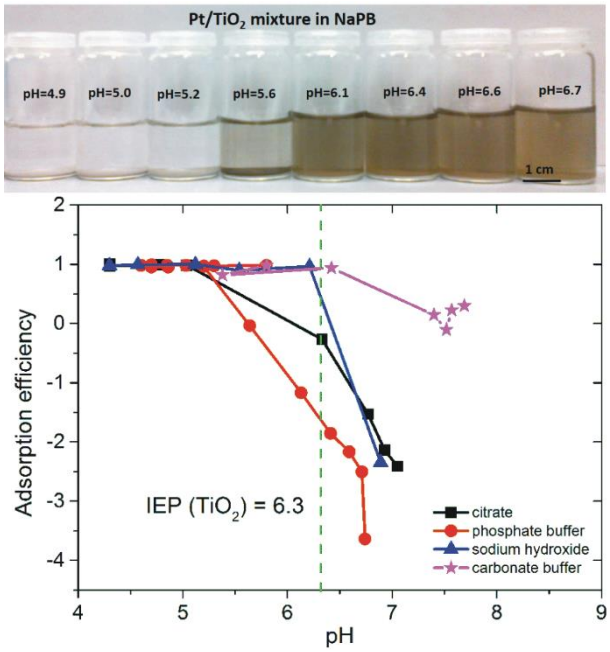

Figure 4: Adsorption efficiency of platinum nanoparticles to TiO_2 as a function of pH. Negative values result from dispersion of TiO_2 (no nanoparticle adsorption, see Supporting Information).

In addition to electrostatic interactions, attractive forces like van der Waals forces also play a distinct role. In a recent work, we demonstrated that negatively charged silver nanoparticles could also adsorb to a slightly negatively charged barium sulfate support[23]. In this case, a support with lower surface charge density like a sulfate[39] shows only a weak repulsive force to the colloidal nanoparticle that may be overcompensated by van der Waals forces. However, when using an oxide with high surface charge density like TiO_2 as a support, electrostatic interactions are the dominant force in the adsorption process. Hence, adsorption is triggered by adjusting the pH between IEP of the nanoparticles and IEP of the support which result in oppositely charged particle species and subsequent electrostatic attraction.

To identify the adsorption mechanism, we modelled the adsorption process using Henry, Langmuir, Freundlich und Temkin isotherms which can be found within the Supporting Information (Tab. S4-5, Fig. S10). Linear regression of experimental data showed that isotherms by Henry, Freundlich and Temkin result in the best fitting result with high correlation coefficients of $R^2 > 0.95$. This is in good agreement with recent work, where we have shown that silver nanoparticle adsorption to barium sulfate supports clearly follows a Freundlich

adsorption isotherme[23]. Consequently, the Freundlich model of adsorption should be the most appropriate model for adsorption of ligand-free nanoparticles to support surfaces. The failure of the Langmuir model indicates that there are interactions between adsorbed nanoparticles and differences in adsorption sites also might play a role.

3.2. Impact of ligands

Ligands, stabilizers and surfactants are omnipresent additives in chemical synthesis of nanoparticles and play an important role in colloidal deposition. Since it is necessary to stabilize colloidal nanoparticles by ligands it is hard to investigate their distinct impact on nanoparticle adsorption due to a missing reference of ligand-free nanoparticles. This reference is provided by bare nanoparticles made by laser ablation of solids in liquid. Laser-generated nanoparticles are electrostatically-stable without the use of stabilizers[40] and ligands but can be ligand-functionalized easily after the laser-based synthesis. Because of the partial oxidation of their surface atoms[41] and high surface charge density[40], laser-generated nanoparticles can act as electron acceptors with unparalleled high affinity[42]. Therefore, they attract molecules containing electron donor moieties. In particular, ligands with functional groups such as -NH_2, -SH, -COOH coordinate to the noble metal nanoparticle surface. Ligands representing typical molecule classes relevant for particle coating were chosen for functionalization of nanoparticles. The group of ligands consisted of the sterically stabilizing PVP or electrosterically stabilizing citrate and LA. Moreover, these ligands feature different affinities for nanoparticle adsorption (physisorption: citrate, PVP; chemisorption: LA). Conjugation experiments revealed that the footprints vary depending on the type of the ligand due to their different sizes, further information on this can be found in the supporting information including tables that summarize the derived ligand footprints and maximal number of ligands on the platinum nanoparticle surface (Tab. S2-S3). Using this information one can calculate ligand surface coverage as a function of ligand concentration which is done in the following sections. As expected, PVP as a high molecular weight ligand, resulting a comparable large footprint (PVP: 27 nm^2) and a low ligand numbers per nanoparticle. Citrate and LA are smaller molecules, resulting in smaller footprints (Citrate: 0.09 nm^2, LA: 0.04 nm^2) and higher ligand numbers per nanoparticle.

Since ligands are known to acquire charges (PVP) or bear charges themselves (citrate, LA) the functionalization of platinum nanoparticles with ligands has also a certain impact on nanoparticle charge. Figure 5 shows the zeta potential and IEP of ligand-functionalized nanoparticles. Exchange of anions that stabilize ligand-free nanoparticles in solution[40] by

charged ligands like citrate do not alter the zeta potential too much. In contrast to this, the amphophilic PVP macromolecule results in lower charge after functionalization of the nanoparticles.

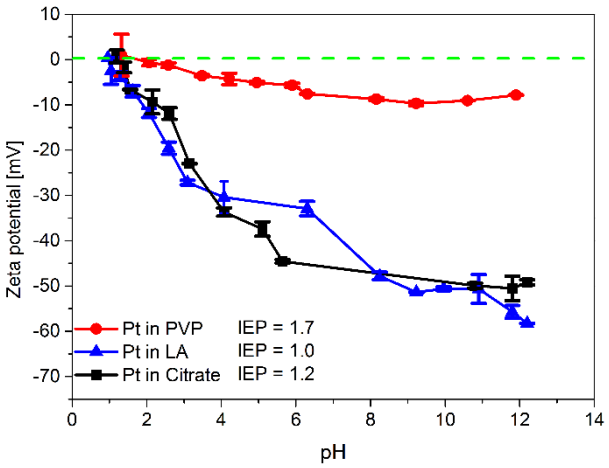

Figure 5: Zeta potentials and isoelectric points of colloidal platinum nanoparticles functionalized with sodium citrate, polyvinylpyrrolidone (PVP) and lipoic acid (LA).

3.2.1. Steric ligands

3.2.1.1 Physisorbed ligands

As a model system for sterically stabilizing ligands we applied the commonly-used polymer PVP. PVP is water soluble, non-charged and non-toxic which results in a broad application range from medical use[43] to nanoparticle synthesis and stabilization[44]. Mdululi et al. investigated the selective adsorption of PVP on the surface of silver nanoparticles through molecular dynamics. They predicted that each monomer of the PVP macromolecule is weakly coordinated by the carbonyl end to the nanoparticle with an adsorption enthalpy of about 5 kJ/mol[45]. Thus, the PVP adsorption may be regarded as physisorption process and should be a good model for other physisorbed, high molecular weight like polymers.

Figure 6 depicts the adsorption efficiency of platinum nanoparticles to TiO_2 as a function of PVP concentration. The adsorption efficiency is almost complete at low concentrations and starts only slightly to decrease at concentrations > 100 µM. These data are in good agreement with the electrostatically-controlled adsorption of ligand-free nanoparticles shown in section 3.1. In comparison to ligand-free nanoparticles, PVP-coated nanoparticles have a lower, but still negative zeta potential (see Figure 5) which results in an attraction to the suspended, positively charged TiO_2 support. The decrease of adsorption efficiency starting at 100 µM is not related to steric hindrance but to a shift of the pH. As can be seen from Figure 6, at concentrations > 100 µM the pH value of the suspension increases towards the IEP of TiO_2

support which results in the compensation of the charge attraction by the support and lower adsorption efficiency. Note that the monolayer coverage of the platinum nanoparticle surface with PVP is reached at a ligand concentration of three orders of magnitude lower when no effect on adsorption efficiency is observed. Hence, the result indicates that the electrostatic interaction rule the nanoparticle adsorption even at high steric hindrance.

3.2.1.2 Chemisorbed ligands

In general, thiolated ligands are considered to have the highest affinity to noble metal surfaces, as shown in the high dissociation energies for Au-S bonds of 200 kJ/mol reported for self-assembled monolayers (SAMs)[46,47].

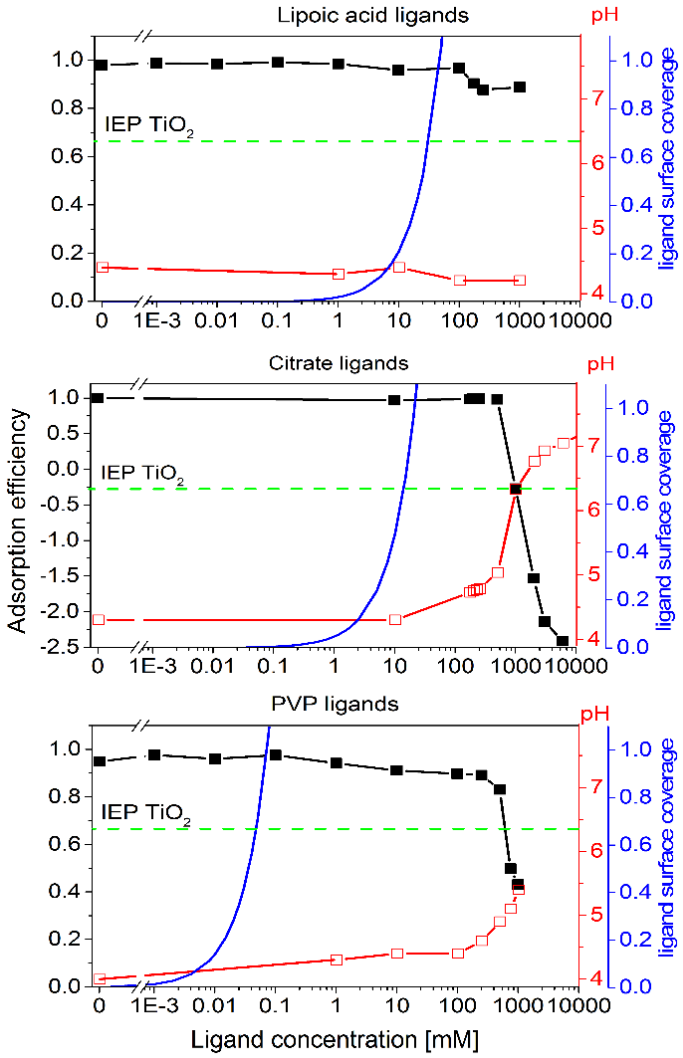

Figure 6: Adsorption efficiency (left axis) of platinum nanoparticles to TiO_2 supports as a function of ligand concentration (black solid squares). For comparison, calculated values of ligands surface coverage (blue lines, right axis) and pH of suspension (red hollow squares, right axis) are given in the same diagram. Green-dashed horizontal line marks the isoelectric point of TiO_2 support.

Thereby, the adsorption of thiolated ligands on nanoparticle surfaces can be regarded as

chemisorption. We used lipoic acid (LA) for ligand functionalization. Because the disulfide-terminated LA bears another carboxylic acid group (pKa = 4.7)[48], its speciation depends on the pH. At pH > 4.7 the deprotonated LA- dominates; at pH < 4.7 the protonated LA is primarily present. In addition to a small sterically stabilizing effect, LA may thus act as an electrostatic stabilizer at pH > 4.7.

Figure 6 depicts the impact of chemisorbed ligands on nanoparticle adsorption to supports. As can be seen, there is almost no impact of ligand surface coverage on nanoparticle adsorption. This again indicates that steric repulsion does not play a role in the adsorption process. The zeta potential of LA-coated nanoparticles is about -35 to -40 mV (see Figure 5), a value close to the ligand-free nanoparticles. Therefore, negative nanoparticles are attracted by a positively charged TiO_2 support. As there is no shift of the pH by ligand concentration (see Figure 6), the electrostatic attraction is dominant over steric repulsion and high nanoparticle adsorption efficiency is achieved fully independent from ligand concentration.

3.2.2. Protic ligands

The use of protic ligands such as organic acids and corresponding salts has a distinct impact on the pH of the solution and may influence nanoparticle adsorption as discussed in section 3.1. One of the most common ligand is citrate as chemical synthesis is typically carried out through a citric acid reduction reaction. Citric acid is a water soluble triprotic acid (pK_{a1} = 3.13, pK_{a2} = 4.76, pK_{a3} = 6.40)[49]. For citrate-coated nanoparticles, stabilization arises from the repulsion between particles caused by the negative charge of the citrate layer adsorbed to the particles. Because citrate is only weakly bound to the surface, its adsorption can be regarded as physisorption with a bond energy of ~8 kJ/mol for Au-COO[50]. However, stronger adsorption of citrate may occur through the intermolecular interaction of hydrogen bonds between carboxylic acid groups (~59 kJ/mol bond energy in carboxylic acid dimers)[50,51]. The adsorption mechanism of SAMs on Au(111) has been studied by Nichols et al.. They proposed that citric acid deprotonates fully upon adsorption and coordinates with the gold surface via all three carboxylate groups, adopting a tilted orientation[52]. A recent overview of citrate adsorption to gold nanoparticles was given by Park and Shumaker-Parry[51].

Figure 6 depicts the adsorption efficiency of citrate-functionalized nanoparticles to TiO_2 support as a function of citrate concentration. At low citrate concentrations the adsorption of platinum nanoparticles on the TiO_2 support is almost complete. At higher citrate concentrations (> 1000 μM), the adsorption efficiency of platinum nanoparticles steadily decreases. Obviously,

there is no correlation between ligand surface coverage and adsorption efficiency indicating that steric repulsion is not the dominant force to control adsorption in water. However, pH of the suspension is also altered by addition of citrate and correlates with nanoparticle adsorption efficiency. At a citrate concentration of 1000 µmol/l, the pH exceeds the IEP of the TiO_2 support and results in a positively charged support and nanoparticle attraction turns into repulsion.

Consequently, electrostatic interactions control the adsorption of nanoparticles independently from ligand surface coverage. The influence of ligands on nanoparticle adsorption efficiency is limited to a ligand-induced pH shift which can alter the charge of the support and prevent adsorption.

3.3. Ionic strength

Ionic strength of nanoparticle dispersion is an important parameter known to directly affect the electrostatic stability. So the dissolved ions may affect the adsorption efficiency as well. The addition of electrolytes and the specific adsorption of ions can reduce the electrochemical double layer thickness. This results in a decrease of the maximum energy barrier and may cause coagulation of the particles. Changes in the pH value can also have an impact on the range and magnitude of electrostatic forces, when protons or hydroxide ions compensate or contribute to nanoparticle surface charge. It is noted that the traditional DLVO model is unable to fully describe colloidal behavior because effects such as Lewis acid/base interactions, hydrogen bonding and steric interactions are not considered[53]. According to the classical DLVO theory high ionic strength destabilizes the colloid by decreasing the electrochemical double layer and the associated repulsive potential. Nevertheless, low ionic strength is also capable of stabilizing the colloidal nanoparticles since adsorption of specific anions such as chloride or bromide causes additional electrostatic stabilization[28].

Figure 7 shows the adsorption efficiency of platinum nanoparticles to TiO_2 support as a function of ionic strength using phosphate buffer and carbonate buffer, citrate, and sodium hydroxide solution. At low ionic strength there is a complete adsorption of the nanoparticles corresponding to a pH below the IEP of the support. As soon as the pH exceeds the IEP due to the increased base concentration, nanoparticle adsorption is prevented. For all used electrolytes, adsorption efficiency drops if the pH reaches the IEP of the support and reverses the charge of the support similar to the pH-effect caused by ligands (see section 3.2).

To control whether this is a pure pH effect or if it is also influenced by ion concentration, we added hydrochloric acid to the electrolyte solutions to decrease the pH level to pH 4 (below $IEP_{Support}$). Notably, nanoparticle adsorption in citrate solution recovered to an adsorption

efficiency > 90% (see Figure 7 (red points)). However, this adjustment of pH to initiate adsorption is limited to a maximum ionic strength. When the platinum nanoparticles get unstable at high ionic strength and precipitate, colloidal deposition is prevented. Accordingly, further addition of acid did not result in successful colloidal deposition. Consequently, there is a maximum ionic strength of the suspension which correspondes to the nanoparticle stability. Typically, this threshold limit value of ionic strength is in a regime of tens of milimolar salinity (1–40 mM) and are marked by dashed lines in the diagrams of Figure 7.

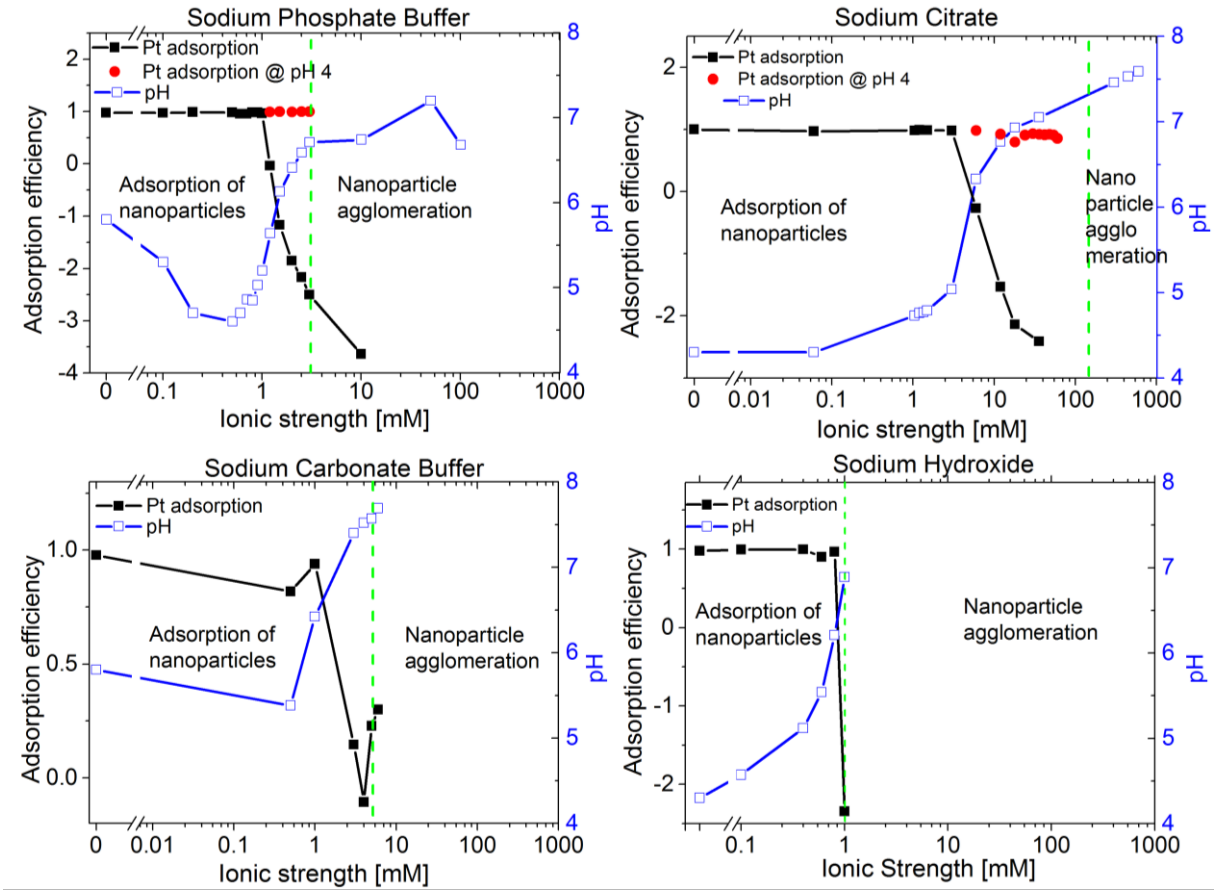

Figure 7: Adsorption efficiency (left axis) of platinum nanoparticles to TiO_2 supports as a function of ionic strength (black solid squares). For comparison, pH of suspension (open blue squares, right axis) is given in the same diagram. Green-dashed vertical line marks the limit of ionic strength for nanoparticle agglomeration, negative values result from dispersion of TiO_2 (no nanoparticle adsorption, see Supporting Information). Note: Solid red dots give the adsorption efficiency after adjusting pH to a value of 4 to identify the pH as the key parameter for supporting.

Overall, the supporting of colloidal nanoparticles can be done by simple mixing of colloid and support and is a fast and an almost complete process under well-chosen conditions (pH, ionic strength). Figure 8 shows a suggestion for a general scheme for successful nanoparticle adsorption in colloidal solutions. Important characteristics are the IEP of the nanoparticles and the support, the pH, the ionic strength and the surface coverage of the nanoparticles with

ligands. For both ionic strength and pH, there is a process "window" which is marked blue in Figure 8. As colloidal stability is required for deposition of nanoparticles, the pH must exceed IEP of the nanoparticle as well as the ionic strength has to be below a concentration that results in precipitation. In addition, electrostatic-controlled adsorption is only achieved if the pH is below the IEP of the support (see section 3.1). Ligand surface coverage only plays a role in case of weak electrostatic interactions, i.e.close to the IEP of support or slightly above, or van-der-Waals interactions[4,23]. In this transition area there is only nanoparticle adsorption in case of weak steric repulsion due to low ligand surface coverage[23].

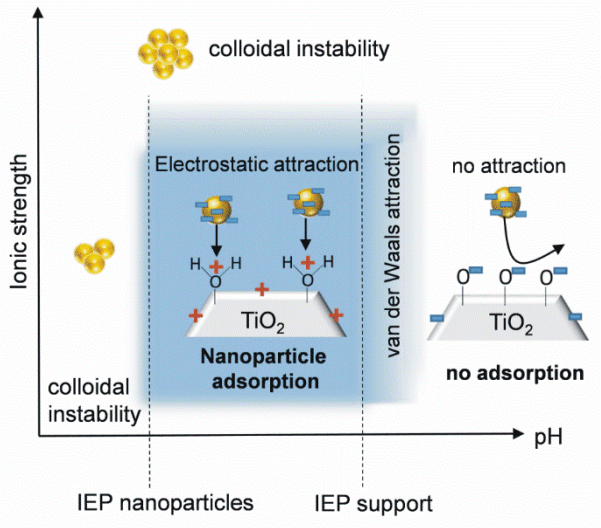

Figure 8: Scheme of nanoparticle adsorption to supports as a function of pH and ionic strength.

4. Conclusion

Adsorption of colloidal nanoparticles is a versatile technique to be applied in the synthesis of heterogeneous catalysts, polymer additives or waste water treatment. Using laser-generated and initially ligand-free nanoparticles allows high-yield nanoparticle adsorption from colloidal solution and individual adjustment of parameters like ligand coverage or ionic strength.

Adsorption of platinum nanoparticles to a dispersed TiO_2 support is characterized by the isoelectric point (IEP) of the nanoparticles and the support, the pH, the ionic strength and the ligand surface coverage of the nanoparticles. Prerequisite for successful colloidal deposition is a sufficient colloidal stability of the dispersed nanoparticles. This is given for pH values higher than the IEP of the nanoparticles (IEP_{Pt} = 2.2-2.8) and at micromolar ionic strength (< 40 mM). At the same time, the pH has to be adjusted below the IEP of the support (IEP_{TiO2} = 6.3) to result in a positively charged support which attracts the negatively charged nanoparticles. If there is a sufficient electrostatic interaction even nanoparticle surface coverage with ligands

(citrate, LA, PVP) does not prevent adsorption. During adsorption, a net charge is transferred by the nanoparticles to the support changing its IEP towards the nanoparticle IEP. The nanoparticle adsorption follows a Freundlich isotherme, the maximum nanoparticle load was shown to be about 65 wt% for the given system Pt/TiO_2.

Literature

[1] Astruc, D.; Lu, F.; Aranzaes, J. Nanoparticles as recyclable catalysts: The frontier between homogeneous and heterogeneous catalysis. *Angew. Chem. Int. Ed.* **2005**, *44*, 7852–7872.

[2] Grunwaldt, J. D.; Kiener, C.; Wogerbauer, C.; Baiker, A. Preparation of supported gold catalysts for low-temperature co oxidation via "size-controlled" gold colloids. *J. Catal.* **1999**, *181*, 223–232.

[3] Schwenke, A.; Wagener, P.; Weiss, A.; Klimenta, K.; Wiegel, H.; Sajti, L.; Barcikowski, S. Laserbasierte Generierung matrixbinderfreier Nanopartikel-Polymerkomposite für bioaktive Medizinprodukte. *Chem. Ing. Tech.* **2013**, *85*, 740–746.

[4] Gicheva, G.; Yordanov, G. Removal of citrate-coated silver nanoparticles from aqueous dispersions by using activated carbon. *Colloids Surf. A* **2013**, *431*, 51–59.

[5] Lin, S.; Cheng, Y. C.; Bobcombe, Y.; Jones, K. L.; Liu, J.; Wiesner, M. R. Deposition of silver nanoparticles in geochemically heterogeneous porous media: Predicting affinity from surface composition analysis. *Environ. Sci. Technol.* **2011**, *45*, 5209–5215.

[6] Yang, C. M.; Liu, P. H.; Ho, Y. F.; Chiu, C. Y.; Chao, K. J. Highly dispersed metal nanoparticles in functionalized SBA-15. *Chem. Mater.* **2003**, *15*, 275–280.

[7] Boennemann, H.; Braun, G.; Brijoux, W.; Brinkmann, R.; Schulze Tilling, A.; Seevogel, K.; Siepen, K. Nanoscale colloidal metals and alloys stabilized by solvents and surfactants: Preparation and use as catalyst precursors. *J. Organomet. Chem.* **1996**, *520*, 143–162.

[8] Richards, R.; Moertel, R.; Boennemann, H. Precursor concept for fuel cell catalysts. *Fuel Cells Bull.* **2002**, *37*, 7–10.

[9] Bergmann, C.; Schwenke, A.; Sajti, L.; Chichkov, B.; Fischer, H. Temperature-dependent morphology changes of noble metal tricalcium phosphate-nanocomposites. *Ceram. Int.* **2014**, *40*, 7931–7939.

[10] Lau, M.; Niemann, R. G.; Bartsch, M.; O'Neill, W.; Barcikowski, S. Near-field-enhanced, off-resonant laser sintering of semiconductor particles for additive manufacturing of dispersed Au–ZnO-micro/nano hybrid structures *Appl. Phys. A* **2014**, *114*, 1023–1030.

[11] Wiesner, M. R.; Lowry, G. V.; Alvarez, P.; Dionysiou, D.; Biswas, P. Assessing the risks of manufactured nanomaterials. *Environ. Sci. Technol.* **2006**, *40*, 4336–4345.

[12] Abraham, P. M.; Barnikol, S.; Baumann, T.; Kuehn, M.; Ivleva, N. P.; Schaumann, G. E. Sorption of silver nanoparticles to environmental and model surfaces. *Environ. Sci.*

Technol. **2013**, *47*, 5083–5091.

[13] Dokoutchaev, A.; James, J. T.; Koene, S. C.; Pathak, S.; Prakash, G. K. S.; Thompson, M. E. Colloidal metal deposition onto functionalized polystyrene microspheres. *Chem. Mater.* **1999**, *11*, 2389–2399.

[14] Mori, K.; Kumami, A.; Tomonari, M.; Yamashita, H. A pH-induced size controlled deposition of colloidal Ag nanoparticles on alumina support for catalytic application. *J. Phys. Chem. C* **2009**, *113*, 16850–16854.

[15] Downard, A.; Tan, E.; Yu, S. Controlled assembly of gold nanoparticles on carbon surfaces. *New J. Chem.* **2006**, *30*, 1283–1288.

[16] Matthey, D.; Wang, J. G.; Wendt, S.; Matthiesen, J.; Schaub, R.; Laegsgaard, E.; Hammer, B.; Besenbacher, F. Enhanced bonding of gold nanoparticles on oxidized TiO_2(110). *Science* **2007**, *315*, 1692–1696.

[17] Zhang, Y.; Franklin, N. W.; Chen, R. J.; Dai, H. Metal coating on suspended carbon nanotubes and its implication to metal tube interaction. *Chem. Phys. Lett.* **2000**, *331*, 35–41.

[18] Lopez, N.; Norskov, J. K.; Janssens, T. V. W.; Carlsson, A.; Puig-Molina, A.; Clausen, B. S.; Grunwaldt, J.-D. The adhesion and shape of nanosized au particles in a Au/TiO2 catalyst. *J. Catal.* **2004**, *225*, 86–94.

[19] Thio, B. J. R.; Lee, J. H.; Meredith, J. C.; Keller, A. A. Measuring the influence of solution chemistry on the adhesion of Au nanoparticles to mica using colloid probe atomic force microscopy. *Langmuir* **2010**, *26*, 13995–14003.

[20] Amendola, V.; Meneghetti, M. What controls the composition and the structure of nanomaterials generated by laser ablation in liquid solution? *Phys. Chem. Chem. Phys.* **2013**, *15*, 3027–3046.

[21] Zeng, H.; Du, X. W.; Singh, S. C.; Kulinich, S. A.; Yang, S.; He, J.; Cai, W. Nanomaterials via laser ablation/irradiation in liquid: A review. *Adv. Funct. Mater.* **2012**, *22*, 1333–1353.

[22] Barcikowski, S.; Compagnini, G. Advanced nanoparticle generation and excitation by lasers in liquids. *Phys. Chem. Chem. Phys.* **2013**, *15*, 3022–3026.

[23] Wagener, P.; Schwenke, A.; Barcikowski, S. How citrate ligands affect nanoparticle adsorption to microparticle supports *Langmuir* **2012**, *28*, 6132–6140.

[24] Wagener, P.; Ibrahimkutty, S.; Menzel, A.; Plech, A.; Barcikowski, S. Dynamics of silver nanoparticle formation and agglomeration inside the cavitation bubble after pulsed laser ablation in liquid. *Phys. Chem. Chem. Phys.* **2013**, *5*, 3068–3074.

[25] De Giacomo, A.; Dell'Aglio, M.; Santagata, A.; Gaudiuso, R.; De Pascale, O.;

Wagener, P.; Messina, G. C.; Compagnini, G.; Barcikowski, S. Cavitation dynamics of laser ablation of bulk and wire-shaped metals in water during nanoparticles production. *Phys. Chem. Chem. Phys.* **2013**, *15*, 3083–3092.

[26] Menendez-Manjon, A.; Jakobi, J.; Schwabe, K.; Krauss, J. K.; Barcikowski, S. Mobility of nanoparticles generated by femtosecond laser ablation in liquids and its application to surface patterning. *J. Laser Micro/Nanoeng.* **2009**, *4*, 95–99.

[27] Sylvestre, J. P.; Poulin, S.; Kabashin, A. V.; Sacher, E.; Meunier, M.; Luong, J. H. T. Surface chemistry of gold nanoparticles produced by laser ablation in aqueous media. *J. Phys. Chem. B* **2004**, *108(43)*, 16864–16869.

[28] Rehbock, C.; Merk, V.; Gamrad, L.; Streubel, R.; Barcikowski, S. Size control of laser-fabricated surfactant-free gold nanoparticles with highly diluted electrolytes and their subsequent bioconjugation. *Phys. Chem. Chem. Phys.* **2013**, *15*, 3057–3067.

[29] Mafune, F.; Kohno, J. Y.; Takeda, Y.; Kondow, T.; Sawabe, H. Formation and size control of silver nanoparticles by laser ablation in aqueous solution. *J. Phys. Chem. B* **2000**, *104(39)*, 9111–9117.

[30] Sajti, C.; Barchanski, A.; Wagener, P.; Klein, S.; Barcikowski, S. Delay time and concentration effects during bioconjugation of nanosecond laser-generated nanoparticles in a liquid flow. *J. Phys. Chem. C* **2011**, *115*, 5094–5101.

[31] Wang, X.; Yu, J. C.; Yip, H. Y.; Wu, L.; Wong, P. K.; Lai, S. Y. A mesoporous Pt/TiO_2 nanoarchitecture with catalytic and photocatalytic functions. *Chem. Eur. J.* **2005**, *11*, 2997–3004.

[32] Sonstrom, P.; Baeumer, M. Supported colloidal nanoparticles in heterogeneous gas phase catalysis: on the way to tailored catalysts. *Phys. Chem. Chem. Phys.* **2011**, *13*, 19270–19284.

[33] Osterloh, F. E. Inorganic materials as catalysts for photochemical splitting of water. *Chem. Mater.* **2008**, *20*, 35–54.

[34] Walter, M. G.; Warren, E. L.; McKone, J. R.; Boettcher, S. W.; Mi, Q.; Santori, E. A.; Lewi, N. S. Solar water splitting cells. *Chem. Rev.* **2010**, *110*, 6446–6473.

[35] Mallik, A.; Bryan, S.; Puukila, S.; Chen, A.; Khaper, N. Efficacy of Pt-modified TiO_2 nanoparticles in cardiac cells *Exp. Clin. Cardiol.* **2011**, *16*, 6–10.

[36] Henglein, A.; Ershov, B. G.; Malow, M. Absorption spectrum and some chemical reactions of colloidal platinum in aqueous solution. *J. Phys. Chem.* **1995**, *99*, 14129–14136.

[37] Weaver, J. H.; Krafka, C.; Lynch, D. W.; Koch, E. E. *Optical Properties of Metals;* Fachinformationszentrum Karlsruhe, 1981.

[38] Creighton, J. A.; Eadont, D. G. Ultraviolet-visible absorption spectra of the colloidal metallic elements. *J. Chem. Soc. Faraday Trans.* **1991**, *87*, 3881–3891.

[39] Zhang, M.; Zhang, B.; Li, X.; Yin, Z.; Guo, X. Synthesis and surface properties of submicron barium sulfate particles. *Appl. Surf. Sci.* **2011**, *258*, 24–29.

[40] Merk, V.; Rehbock, C.; Becker, F.; Hagemann, U.; Nienhaus, H.; Barcikowski, S.In situ non-DLVO stabilization of surfactant-free, plasmonic gold nanoparticles: Effect of Hofmeister's anions. *Langmuir* **2014**, *30*, 4213–4222.

[41] Muto, H.; Yamada, K.; Miyajima, K.; Mafune, F. Estimation of surface oxide on surfactant-free gold nanoparticles laser-ablated in water. *J. Phys. Chem. C* **2007**, *111*, 17221–17226.

[42] Petersen, S.; Barcikowski, S. Conjugation efficiency of laser-based bioconjugation of gold nanoparticles with nucleic acids. *J. Phys. Chem. C* **2009**, *113*, 19830–19835.

[43] Lee, H. Y.; Lee, S. H.; Xu, C.; Xie, J.; Lee, J. H.; Wu, B.; Koh, A. L.; Wang, X.; Sinclair, R.; Wang, S. X.; Nishimura, D. G.; Biswal, S.; Sun, S.; Cho, S. H.; Chen, X. Synthesis and characterization of PVP coated large core iron oxide nanoparticles as an MRI contrast agent *Nanotechnology* **2008**, *19*, 165101.

[44] Mahl, D.; Greulich, C.; Meyer-Zaika, W.; Köller, M.; Epple, M. Gold nanoparticles: dispersibility in biological media and cell-biological effect. *J. Mater. Chem.* **2011**, *20*, 6176–6181.

[45] Mdluli, P. S.; Sosibo, N. M.; Mashazi, P. N.; Nyokong, T.; Tshikhudo, R. T.; Skepu, A.; van der Lingen, E. Selective adsorption of PVP on the surface of silver nanoparticles: A molecular dynamics study. *J. Mol. Struct.* **2011**, *1004*, 131–137.

[46] Sperling, R. A.; Parak, W. J. Surface modification, functionalization and bioconjugation of colloidal inorganic nanoparticles. *Philos. Trans. A Math. Phys. Eng. Sci.* **2010**, *368*, 1333–1383.

[47] Love, J. C.; Estroff, L. A.; Kriebel, J. K.; Nuzzo, R. G.; Whitesides, G. M. Self-assembled monolayers of thiolates on metals as a form of nanotechnology. *Chem. Rev.* **2005**, *105*, 1103–1169.

[48] Meister, A. *Advances in Enzymology and Related Areas of Molecular Biology;* John Wiley & Sons (New York), 2009.

[49] Lide, D. R. *CRC Handbook of Chemistry and Physics (Internet Version);* CRC Press, 2005.

[50] Park, J. W. *Interfacial properties of asymmetrically functionalizes citrate-stabilized gold and silver nanoparticles related to molecular adsorption* PhD thesis, University of Utah,

2013.

[51] Park, J. W.; Shumaker-Parry, J. S. Structural study of citrate layers on gold nanoparticles: Role of intermolecular interactions in stabilizing nanoparticles. *J. Am. Chem. Soc.* **2014**, *136*, 1907–1921.

[52] Nichols, R. J.; Burgess, I.; Young, K. L.; Zamlynny, V.; Lipkowski, J. A quantitative evaluation of the adsorption of citrate on Au(111) using SNIFTIRS. *J. Electroanal. Chem.* **2004**, *563*, 33–39.

[53] Grasso, D.; Subramaniam, K.; Butkus, M.; Strevett, K.; Bergendahl, J. A review of non-DLVO interactions in environmental colloidal systems. *Rev. Environ. Sci. Biotechnol.* **2001**, *1*, 17–38.

1.1. Perpectives: Chemical and thermal stability of $PtCu_3$ nanoparticles adsorbed on titanium dioxide and carbon

Galina Marzun, Swen Zerebecki, Stephan Barcikowski

Abstract

The stability of nanoparticles deposited on a support material is crucial for application in catalysis. The chemical and thermal stability of laser-generated $PtCu_3$ nanoparticles adsorbed on TiO_2 and Carbon Black (CB) is investigated. In the previous chapter, the particle deposition in aqueous solvents was intensively studied. To minimize the formation of oxidic structures, the use of liquids such as acetone or ethanol is advised for the particle synthesis of non-noble metal alloys by pulsed laser ablation in liquids. Hence, in this present work, particle adsorption in organic solvents was studied. A homogeneous particle adsorption of the alloy nanoparticles in acetone has been achieved. While the prepared catalysts were stable against acid treatment (pH 1, H_2SO_4), particle detachment was observed after heating (80 °C) the catalyst in an acidic environment. Thus, further intensive studies on particle adsorption are recommended to appropriately link nanoparticles and supports as well as to substitute CB with corrosion-stable, conductive materials.

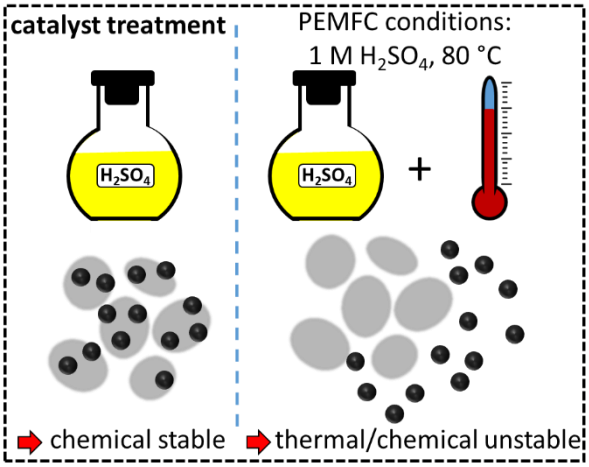

Introduction

Polymer electrolyte membrane fuel cells (PEMFCs), also known as proton exchange membrane fuel cells, have a high potential to reduce the use of fossil fuels and thus are considered to be green power sources for our future [1],[2]. PEMFCs convert chemical energy into electrical energy by using hydrogen as a fuel and air as an oxidant. At the anode, a hydrogen oxidation reaction (HOR) takes place. Hydrogen atoms bind to the catalyst, lose an electron and are

released from the metal surface as protons that are captured by the membrane and are carried towards the cathode, while the remaining electrons build up the anodic potential, causing a current through an external circuit [3]. On the other hand, the oxygen that is adsorbed at the cathode protonates and reduces due to incoming electrons, and the process finally forms water, which is forced to exit the fuel cell by the hydrophobic nature of the surrounding nature [3]. Figure 1 illustrates the well-known operating principle of the fuel cell reactions in a PEMFC. Even though PEMFCs are the most promising commercially available fuel cells, further developments – particularly relating to their production costs, activity and stability – are required [4]. In the past, it has already been shown that more than half of the voltage losses can be traced back to the oxygen reduction reaction (ORR), which is thus a major bottleneck for fuel cell reactions [5]. The main challenges to overcome these obstacles include the following [3], [6]:

- high stability of the catalyst even under extreme corrosive conditions
- sufficient oxygen activity without too high binding energies to enable a desorption of the product (the Sabatier principle)
- prevent undesirable H_2O_2 formation, which causes radical oxidative degradation of the membrane

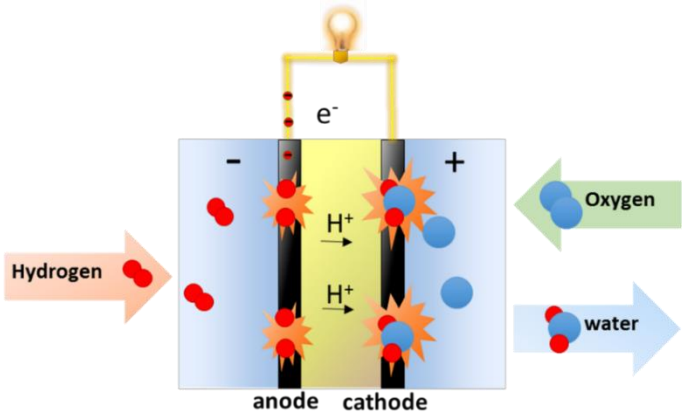

Net reaction: $2H_2 + O_2 \rightarrow 2H_2O$

Anode: hydrogen oxydation reaction (HOR)	Cathode: oxygen reduction reaction (ORR)
$\frac{1}{2}H_2 + {}^{*} \rightarrow H^{*}$ $H^{*} \rightarrow H^{+} + {}^{*} + e^{-}$ * = catalyst surface site	$\frac{1}{2}O_2 + {}^{*} \rightarrow O^{*}$ $O^{*} + H^{+} + e^{-} \rightarrow OH^{*}$ $OH^{*} + H^{+} + e^{-} \rightarrow H_2O + *$ $O_2 + {}^{*} \rightarrow O_2{}^{*}$ $O_2{}^{*} + H^{+} + e^{-} \rightarrow HO_2{}^{*}$ $HO_2{}^{*} + H^{+} + e^{-} \rightarrow H_2O_2{}^{*}$ $H_2O_2{}^{*} \rightarrow H_2O_2 + {}^{*}$
$2H_2 \rightarrow 4H^{+} + 4e^{-}$	$O_2 + 4H^{+} + 4e^{-} \rightarrow H_2O$ Side reaction $O_2 + 2H^{+} + 2e^{-} \rightarrow H_2O_2$

Figure 1: Scheme of a proton-exchange-membrane fuel cell, including the reactions (reconstructed from [3],[7]).

In order to overcome the previous challenges, alloy nanoparticles are great candidates to enhance the performance of electrocatalytic reactions such as ORR. In particular, Pt_xCu_y is a promising type of low Pt-content electrocatalyst [8], [9], [10], [11]. As already briefly described in Chapter 4.2, alloyed $PtCu_3$ can be easily synthesized by PLAL in acetone. However, one of the most important properties of the catalyst is its stability. The catalyst therefore should be able to perform under long-term reaction conditions without losing much activity. Low temperature PEMFCs operate at 80 °C under alkaline (~0.1-1 M NaOH) or acidic (~0.1-1 M H_2SO_4) conditions [12], [13]. Carbon Black (CB) is a commercial support material used in fuel cells [14]. Though doped TiO_2 does not have as good electrical conductivity as CB, oxide supports are investigated in the literature as alternative stable supports because of their good mechanical resistance and stability in acidic and oxidative environments[15], [16]. In this case, investigation on modification of TiO_2 are carried out, where an increased catalytic activity was observed due to a better interaction between the oxide and support. [17], [15].

Investigations on particle deposition of laser-generated nanoparticles is intensively studied by our group[18], [19], [20]. But, the stability of these particles on the support has not yet been studied. Thus, in the following, the chemical and thermal stability of laser-generated nanoparticles on carbon and TiO_2 supports is investigated. After $PtCu_3$ NPs are adsorbed on the supports (TiO_2 and CB), their tendency to remain on the support is examined.

Experimental

For the target preparation, 10 µm Pt and 60 µm Cu powder were mixed in a shaker (IKA Vibrax VXR) for 30 minutes and finely crushed with a pestle. The powder mixture was pressed at 60 kN for 5 min in a 13-mm diameter steel die using a hydraulic laboratory press (PW 10 from P/O/weber company). $PtCu_3$ nanoparticles were synthesized by ablating the prepared target in acetone in a flow-through chamber (13.5 ml/min, 5 mm liquid layer) using an Nd:YAG nanosecond laser (Edgewave IS400-1-L INNOSLAB) at a fundamental wavelength with a repetition rate of 5 kHz and 5.5 mJ focused with an f-theta lens.

The prepared colloid was deposited on TiO_2 (Hombikat II, Huntsman) and Carbon Black (Vulcan XC72R, CABOT). For this, the support powder was dispersed in acetone using ultrasonication for 10 min. Colloidal nanoparticles were added to the suspension up to 2 wt% and were shaken for 24 h. Subsequently, the clear supernatant was removed by decantation, and

the slurry was dried at 60 °C. For stability tests, the $PtCu_3/TiO_2$ and $PtCu_3$/CB powder was treated with 1M H_2SO_4 (Sigma Aldrich) and then heated under reflux at 80 °C for up to 72 h.

The colloid and the supernatant after particle adsorption was measured by UV-Vis extinction spectroscopy (Thermo Scientific Evolution 201) in a quartz cuvette with a 10-mm path length. For XPS analysis, the laser-generated particles were dropped on a Si wafer. A hemispherical electron energy analyzer (Phoibos 100 by SPECS) in a fixed analyzer transmission mode with a pass energy of 20 eV was used. An Al Kα X-ray source (1486.6 eV) served as a nonmonochromatic X-ray source. The stability of the catalyst was examined using TEM analysis of the particle distribution on the support. The analyses were performed using a JEOL 2200FS transmission electron microscope (TEM) and a Hitachi HF2000 TEM with an acceleration voltage of 200 kV.

Electrochemical measurements of $PtCu_3$ in acetone were carried out in a three-electrode electrochemical cell at room temperature using a VersaSTAT F3 from Princeton Applied Research. An adequate volume of the colloid solutions, which corresponded to a nanoparticle loading of 40 $\mu g_{Pt}/cm_{electrode}^2$, was mixed with 5 wt% Nafion and deposited on a glassy carbon (GC) disc electrode (5 mm diameter). Then, the solvent was left alone to evaporate. Prior to the measurements, the working electrode was ultrasonicated in ethanol and in deionized water for 5 minutes. The bare electrode was electrochemically pre-treated by 10 CV cycles at the same conditions as the electrochemical measurements. Cyclic voltammograms were recorded at 1 V/s from -0.2 V to 1.2 V using an Ag/AgCl-reference electrode in a saturated KCl solution and a platinum wire as the counter electrode. The electrolyte was 1 M H_2SO_4 (pH=1); it had been purged with nitrogen for at least 30 min followed by a continuous gas flow over the solution throughout the electrochemical measurements. The electrolyte and the electrode were not stirred during the electrochemical studies so that diffusion limitation artefacts could be excluded.

Results and discussion

For the synthesis of alloy nanoparticles, a target consisting of two mixed micro-powders was used after its consolidation by pressing. It is important that both metals were homogeneously distributed in the scale of the spot area – at least on the scale of the area that is hit by each laser pulse. Microscope images of the pressed pellet presented in Figure 2 shows larger bright areas with small dark spots. Due to the optical contrast of Pt, which is higher than Cu and the

manufacturer's specification of the particle size of the powder (Pt 10 µm, 60 µm Cu), the data suggests that the black dots are Pt, and the bright areas consist of Cu particles. Since the used laser has an elliptical lateral laser spot shape (Fig. S1 and S2), the red circle in Figure 2 represents the circle equivalent laser spot diameter. As can be seen, an adequate homogeneous ablation of both metals is ensured.

Using XPS and TEM-EDX, the elemental compositions of the particles were measured. The ratio of Cu/Pt derived from XPS is 3.4, while the Cu/Pt ratio in EDX of single particles is ~4.9 on average (Fig. S3). The particles' composition is similar to the adjusted metal composition in the target; however, the analysed metal ratio varies between the two methods. The reason for the slightly divergent results can be assigned to the different methods. While XPS enables to examine the elements of an average over a large amount of the sample, EDX on a TEM grid selectively analyses individual particles. This difference alone can lead to different metal-ratio results if segregated particles are present, and thus it can lead to different detections from the different methods. On the basis of the mean free path of the photoelectrons of Pt (λ_m~1.6 nm at 1414 eV≈Al Kα-E_{Pt})[21] and Cu (λ_m ~1.1 nm at 554 eV≈Al Kα-E_{Cu})[21], XPS only reflects the surface concentration, while EDX uses high energy X-ray photons and therefore has a large interaction volume. This may lead to a metal-ratio discrepancy analysed by XPS and EDX if the metal atoms are not homogeneously distributed within the particles or among the different particle sizes. Considering that a homogeneous metal distribution is present in the whole sample, as was shown in chapter 4.2, another explanation for the different XPS and EDX composition is conceivable. As already discussed by Petrykin et al., who analysed nanocrystalline $Ru_{1-x}Ni_xO_y$ oxides, an adventitious carbon species present on the Ruthenium surface can screen the produced photoelectrons and thus lead to a lower intensity of the carbon-coated metal species, while the signal of the other metal (Ni) appears to be enriched. This explanation may also be conceivable in the current study[22]. As already hypothesized in Chapter 4.2, the formation of a graphitic shell is catalysed by Cu when ablating the metal in acetone. Thus, it can be assumed that the carbonaceous species are adventitiously localized on Cu sites and may lower the detected intensity of Cu photoelectrons, resulting in a lower Cu/Pt ratio analysed by XPS. However, to better understand the causes, further reproducible analyses are required—for example, where the carbon is removed by calcination or (much more easily) by etching the surface using ion sputtering during the XPS analysis.

The colloidal nanoparticles were measured by UV-Vis spectroscopy directly after synthesis and after 3 days to examine the colloidal stability during the deposition procedure. As the adsorption

of nanoparticles is verified by a clear supernatant, it was required to distinguish between particle adsorption and agglomeration, since both result in a clear supernatant. For this, the colloid without mixing with the support was measured simultaneously as a reference (Cu_3Pt after 3 days). The supernatant was clear after precipitation of the nanoparticles on the TiO_2, while the colloid was still coloured. The extinction spectra clearly show that colloidal nanoparticles are still stable, while nanoparticles mixed with the support are deposited (Figure 2). Here, even increases in extinction were measured, which is probably due to a better mixing immediately prior to the measurement. A ripening of the particles within the 3 days may be excluded, since the shape of the spectra would have changed, where the extinction would be increased predominantly in the IR region. In case of the carbon support, it was difficult to perform UV-Vis spectra analyses after particle adsorption, since the carbon greatly dispersed, and even after a short centrifugation, no clear supernatant could be attained. Thus, for further experiments, the solvent was evaporated.

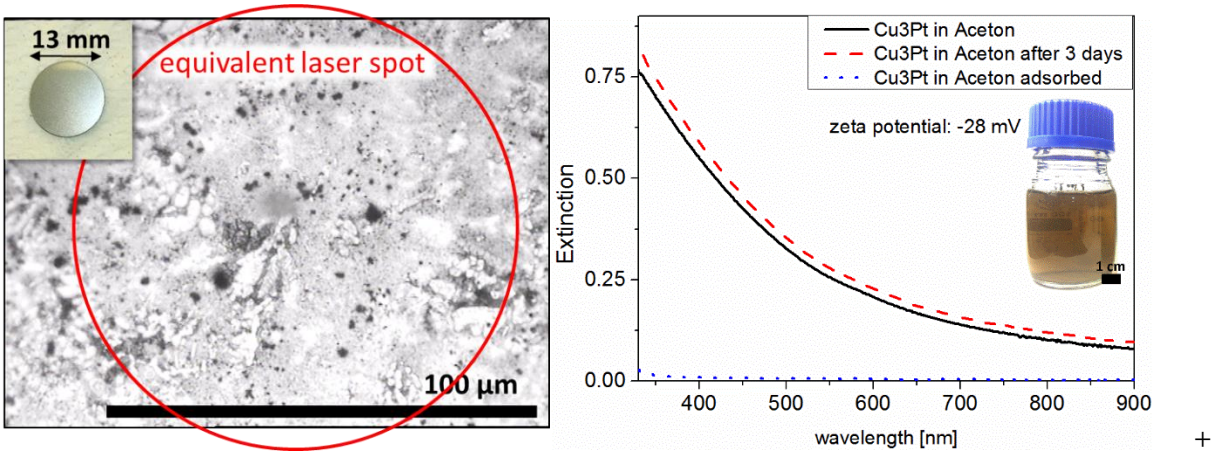

Figure 2: Microscope image of the pressed micro-powder mixture (Pt:Cu = 1:3) with a red circle that represents the equivalent laser spot diameter of 100 µm (left). Right: UV-Vis spectra of the $PtCu_3$ colloid after synthesis (black solid line), after 3 days (red dashed) and of the supernatant after particle adsorption on TiO_2 (blue dotted line).

Due to the different support surfaces, one would expect inequalities in the adsorption efficiency. Typically, laser-generated nanoparticles are partially charged on their surfaces, which makes them hydrophilic, whereas surfaces of carbon-coated particles are hydrophobic. Defect sites, such as on CB[23], where chemisorption of hetero atoms like oxygen or nitrogen can take place, enable dispersion in water. While particle adsorption on TiO_2 is favourable for hydrophilic, electrostatically charged species such as ligand-free particles, the deposition of hydrophobic surfaces on CB is preferred. In Chapter 3.2, the formation of a graphitic layer on nanoparticles synthesized in acetone was described in detail. As can be seen in Figure 3, this layer was also

observed after particle deposition on TiO_2. However, this layer seems not to completely cover the particle, as can be seen in the magnification in Figure 3 b). Note that the exposed part is in contact with the support. Therefore, particle attachment on TiO_2 may be due to the hydrophilic free sites on the particles, while the hydrophobic graphitic parts of the nanoparticles' surfaces may be compatible to bind to carbon supports. In addition, larger nanoparticles seemingly obtain a larger graphitic layer than smaller ones (Figure 3 a). However, more detailed and statistical analyses are necessary. In order to identify the binding sites and thus the driving force for particle adsorption, solvent extraction could be performed in further investigations. Due to this method, a targeted particle deposition could be performed. If small nanoparticles are lessened or not covered by a carbon shell, they would be enriched in the aqueous phase and vice versa.

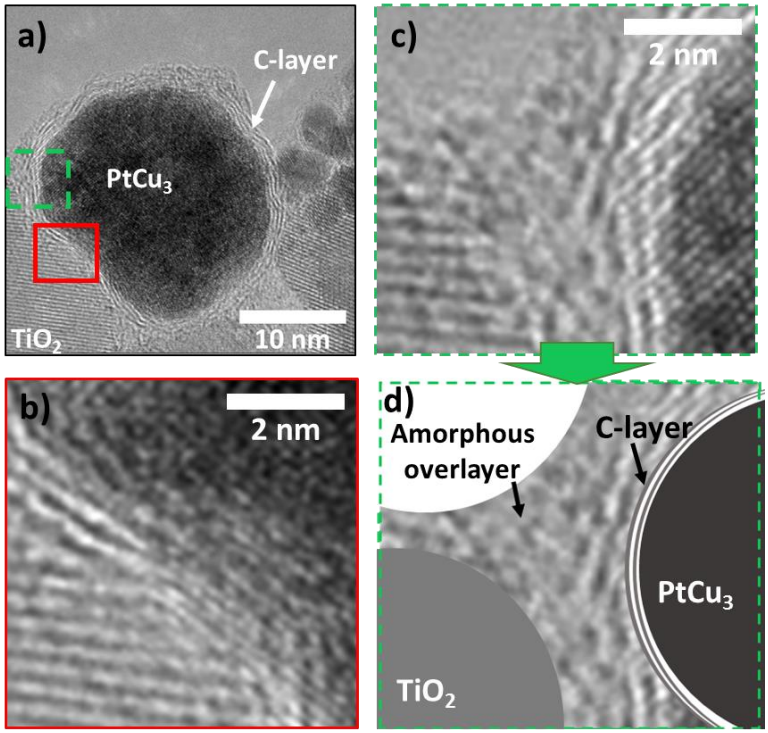

Figure 3: Interaction of the carbon-encapsulated $PtCu_3$ nanoparticle with TiO_2 (before treatment). The enlarged intermediated zones TiO_2/graphitic layer/$PtCu_3$, which are highlighted in red and green rectangles.

The non-sphericity of the metal nanoparticle in Figure 3 indicates a strong-metal-support-interaction (SMSI), which can facilitate the catalytic activity and selectivity [24], [25]. However, within the current study, a SMSI is not expected with TiO_2 for the as-prepared catalyst. Usually, nanoparticle deformation is observed after catalyst treatment at high temperatures (~300-500 °C) under reducing conditions, while an amorphous overlayer of the support is observed [25], [26]. According to Tauster [27], after the reduction of cations from the support, the loss of oxygen allow the metal atoms to be close enough to the reduced TiO_x and enables an electron

transfer from the d-orbitals of the cation. As a result, TiOx migrates over the metal surfaces and encapsulates the particles [24], [26]. Figure 3 shows an example of this amorphous layer around the particles in addition to the graphitic layer. However, since during particle deposition no reducing agents were used in this study and no spontaneous reduction of the support is favourable according the redox potentials of Pt/Pt^{2+} (+ 1.2 V), Cu/Cu^{2+} (+0.5 V) and Ti^{3+}/Ti^{4+} (+0.1 V), the amorphous layers are assumed to have been caused by the decomposition of the solvent acetone during laser irradiation (s. Section 4.2)[28], [29], [30], [31]. The graphitic layer could act as a barrier for a SMSI. Also, in pure water, X-ray absorption spectra of colloidal and supported Pt nanoparticles on TiO_2 (in Chapter 3.1) do not show a measureable impact on the geometric and electronic structure after particle adsorption[32]. Furthermore, reshaped nanoparticles could only seldomly be observed in this study, and thus a clear proof of the particle support interaction is still needed.

For the stability tests, the catalysts $PtCu_3$/CB and $PtCu_3/TiO_2$ were treated with sulfuric acid (pH = 0) and heated up to 80 °C in reflux for 27 h. TEM micrographs of these samples are summarized in Figure 4. As can be seen, the nanoparticles are homogeneously distributed on the supports before the post treatment (Figure 4 a and g). After mixing the catalyst with the acid, no significant changes in the particle distribution could be observed. In contrast to chemical treatment, heating-etching of the suspension (NP/support in H_2SO_4) obviously influences the catalysts' stability. It is evident from Figure 4 k) and l) that $PtCu_3$ nanoparticles are no longer localized on the carbon support. A micrograph of particles adsorbed on TiO_2 shows only sporadic, isolated particles, which indicates a significantly higher stability of the heterogeneous catalyst compared to particles on carbon due to corrosion of the support. A possible explanation for why the particles are partly detached from TiO_2 is that the graphitic layer, which is probably the interface between the particles and support, degrades. The resistance of graphite can vary depending on its nature. Consulting a resistance table from Schunk Ingenieurkeramik GmbH (S4), where the stability of several graphite materials are listed, a destabilization of certain graphite species is possible due to thermal treatment at 80 °C in an acidic environment. Due to the fact that the graphitic layer around the metal nanoparticles is small (~ 1 nm), it may have an even lower chemical and thermal resistance. A catalyst can degrade by several mechanisms, such as metal dissolution, Ostwald ripening, agglomeration, particle detachment or carbon corrosion. The latter can lead to particle detachment due to weaker interactions [14]. By measuring the particle size of $PtCu_3$ before and after thermal treatment, no significant changes could be observed (S5), which excludes metal dissolution and Ostwald ripening.

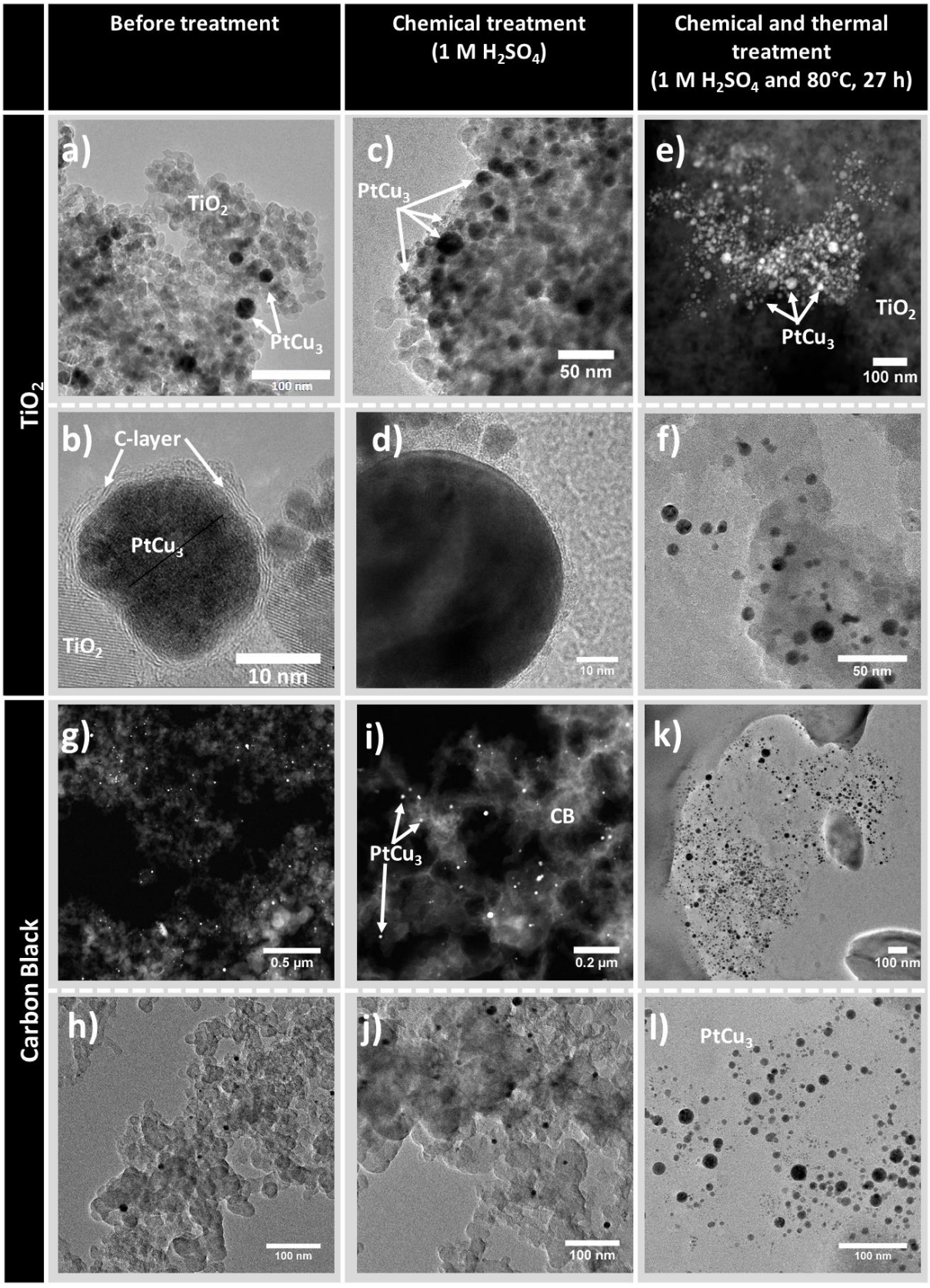

Figure 4: TEM micrographs of $PtCu_3$ deposited on TiO_2 (a-f) and carbon black (g-l) before and after chemical and thermal treatment. The pictures show particle detachment on carbon black after thermal treatment, while the catalyst is stable on TiO_2.

However, a clarification of the catalysts' instability is not possible within this study. Intensive studies to clarify the reason for the instability should be performed to potentially increase this stability. Furthermore, it should be noted that TEM analyses were performed only with a small amount of the sample, and the images always show a small part of the dropped sample. Also, no quantitative analyses were performed. Thus, further extensive investigations (e.g., ICP-MS of the supernatant after catalyst filtration) on catalyst stability are needed to represent a larger amount of the sample. It should be positively stressed that nanoparticles adsorbed on TiO_2 are largely stable under heavy acid, oxidative and thermal conditions. Further investigations such as the study of dealloying nanoparticles without impacting support corrosion should be pursued. Furthermore, due to the high catalyst stability, ongoing research on TiO_2 or other hard-based supports such as carbides is suggested. Another advantage for using hard material is that higher density and thinner catalyst layers (at the same metal loading) compared to carbon-based catalysts can be applied. This difference may be directly reflected in increased current density due to improved mass transfer kinetics. However, the conductivity of these hard-based supports still needs to be further improved. There are various approaches to solving this issue – for example, doping the support in addition to the metal particles with non-metal dopants, i.e., nitrogen, boron or carbon[33].

First, electrochemical performances of the colloidal $PtCu_3$ nanoparticles before deposition show that a dissolution of the non-noble metal copper is possible by applying a voltage of -0.2-1.2 V (Figure 5). Cyclic voltammograms show a typical dealloying behaviour as has been reported before for Pt_xCu_y alloys [34], [35].

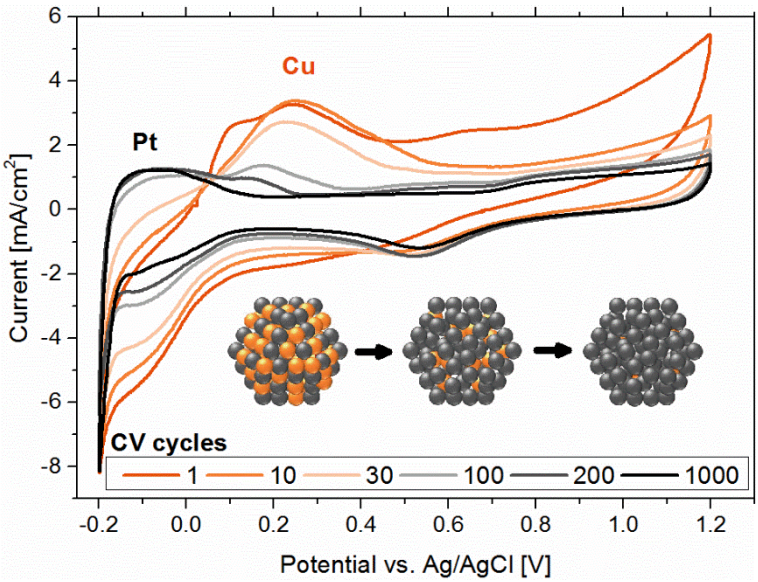

Figure 5: CV profiles of laser-generated colloidal $PtCu_3$ nanoparticles show dealloying of Cu with increasing cycles.

The first one-hundred cycles exhibit a dissolution of Cu in a cathodic current peak at ~ 0.25 V vs. Ag/AgCl. After 200 cycles, the Cu peak completely disappears and a typical Pt peak can be observed due to an electrochemical leaching of Cu. The resulting Pt-enriched nanoparticle surface with increased surface roughness then leads to higher catalytic activity and stability[34]. As previously described, the nanoparticles are surrounded by a carbon layer. Obviously, this layer does not significantly influence the electrochemistry, which is advantageous for further catalyst investigations using nanoparticles that are laser-synthesized in acetone. Although graphite is more stable than CB, the carbon may corrode in acid; this significantly occurs between 0.6 V-1.5 V vs. RHE (corresponds to ~0.4-1.3 V vs. Ag/AgCl)[36], [37], [38]. Since in the current study only a few layers are observed on the particle surface, the carbon is even less stable so that corrosion is more likely. Following on from this study, a comparison of the electrochemical mass-specific activity of laser-generated pure Pt nanoparticles in acetone with alloys should be done in future studies. Also, a comparison of nanoparticles without a graphitic shell on their surfaces as well as with commercial Pt/CB catalysts is of interest.

Conclusion

Pulsed laser ablation of a pressed micro-powder mixture of Pt:Cu (1:3) in acetone was conducted in order to obtain colloidal stable alloy nanoparticles. The colloidal particles were adsorbed quantitatively on Carbon Black and titanium dioxide by colloidal deposition in an analogous manner, although both supports have different solvation properties. TEM images indicate a particle binding on TiO_2 by exposed sites of the metal nanoparticles, while $PtCu_3$ surrounded by a hydrophobic graphitic shell may adsorb on Carbon Black. Both catalysts are chemically stable under aggressive conditions at pH 0 in H_2SO_4. Thermal treatment at 80 °C in the acid leads to particle detachment from the Carbon Black support, while $PtCu_3$ particles are stable on TiO_2. The particle detachment is possibly due to a degradation of the carbon under these conditions. The particle deposition on hydrophobic supports should be further investigated to gain knowledge about the driving force for the adsorption and then to understand how to increase the stability of catalysts. Another promising approach is the use of stable hard-based supports (TiO_2, TiC, TiB_2); further investigations should pursue how to increase their conductivity, for example, by particle size reduction of the support.

Acknowledgements

The study was supported by the German Federal Ministry of Education and Research (BMBF) within the young investigator competition NanoMatFutur (project INNOKAT, FKZ 03X5523). For TEM analysis we thank Bernd Spliethoff from Max-Planck-Institute for Coal research and Markus Heidelmann from the team of Interdisciplinary Center for Analytics on the Nanoscale (ICAN) at the University Duisburg-Essen. The authors also thank Ulrich Hagemann from ICAN for XPS analysis.

Literature

[1] X. Cheng, Z. Shi, N. Glass, L. Zhang, J. Zhang, D. Song, Z.-S. Liu, H. Wang, and J. Shen, "A review of PEM hydrogen fuel cell contamination: Impacts, mechanisms, and mitigation," *Journal of Power Sources*, vol. 165, no. 2, pp. 739–756, **2007**.

[2] J. M. Plc, "Fuel cell electric vehicles: The road ahead," *Fuel Cell Today*, pp. 1–24, **2013**.

[3] O. T. Holton and J. W. Stevenson, "The role of platinum in proton exchange membrane fuel cells," *Platinum Metals Review*, vol. 57, no. 4, pp. 259–271, **2013**.

[4] O. Z. Sharaf and M. F. Orhan, "An overview of fuel cell technology: Fundamentals and applications," *Renewable and Sustainable Energy Reviews*, vol. 32, pp. 810–853, **2014**.

[5] W. Sheng, H. A. Gasteiger, and Y. Shao-Horn, "Hydrogen oxidation and evolution reaction kinetics on platinum: acid vs alkaline electrolytes," *Journal of The Electrochemical Society*, vol. 157, no. 11, pp. B1529–B1536, **2010**.

[6] R. Borup, J. Meyers, B. Pivovar, Y. S. Kim, R. Mukundan, N. Garland, D. Myers, M. Wilson, F. Garzon, D. Wood, *et al.*, "Scientific aspects of polymer electrolyte fuel cell durability and degradation," *Chemical reviews*, vol. 107, no. 10, pp. 3904–3951, **2007**.

[7] C. Song and J. Zhang, "Electrocatalytic oxygen reduction reaction," in *PEM fuel cell electrocatalysts and catalyst layers*, pp. 89–134, Springer, **2008**.

[8] M. Oezaslan, M. Heggen, and P. Strasser, "Size-dependent morphology of dealloyed bimetallic catalysts: linking the nano to the macro scale," *Journal of the American Chemical Society*, vol. 134, no. 1, pp. 514–524, **2011**.

[9] D. Wang, Y. Yu, H. L. Xin, R. Hovden, P. Ercius, J. A. Mundy, H. Chen, J. H. Richard, D. A. Muller, F. J. DiSalvo, *et al.*, "Tuning oxygen reduction reaction activity via controllable dealloying: a model study of ordered Cu3Pt/C intermetallic nanocatalysts," *Nano letters*, vol. 12, no. 10, pp. 5230–5238, **2012**.

[10] D. Wang, Y. Yu, J. Zhu, S. Liu, D. A. Muller, and H. D. Abruna, "Morphology and activity tuning of Cu3Pt/C ordered intermetallic nanoparticles by selective electrochemical dealloying," *Nano letters*, vol. 15, no. 2, pp. 1343–1348, **2015**.

[11] N. Hodnik, C. Jeyabharathi, J. C. Meier, A. Kostka, K. L. Phani, A. Recnik, M. Bele, S. Hocevar, M. Gaberšček, and K. J. Mayrhofer, "Effect of ordering of PtCu3 nanoparticle structure on the activity and stability for the oxygen reduction reaction," *Physical Chemistry Chemical Physics*, vol. 16, no. 27, pp. 13610–13615, **2014**.

[12] R. A. Antunes, M. C. L. Oliveira, G. Ett, and V. Ett, "Corrosion of metal bipolar plates for pem fuel cells: a review," *International Journal of Hydrogen Energy*, vol. 35, no. 8, pp. 3632–3647, **2010**.

[13] H. A. Gasteiger and J. Garche, *Fuel Cells*. Wiley-VCH Verlag GmbH & Co. KGaA, **2008**.

[14] J. C. Meier, C. Galeano, I. Katsounaros, J. Witte, H. J. Bongard, A. A. Topalov, C. Baldizzone, S. Mezzavilla, F. Schüth, and K. J. Mayrhofer, "Design criteria for stable Pt/C fuel cell catalysts," *Beilstein journal of nanotechnology*, vol. 5, no. 1, pp. 44–67, **2014**.

[15] S.-Y. Huang, P. Ganesan, S. Park, and B. N. Popov, "Development of a titanium dioxide-supported platinum catalyst with ultrahigh stability for polymer electrolyte membrane fuel cell applications," *Journal of the American Chemical Society*, vol. 131, no. 39, pp. 13898–13899, **2009**.

[16] Y. Shao, R. Kou, J. Wang, V. V. Viswanathan, J. H. Kwak, J. Liu, Y. Wang, and Y. Lin, "The influence of the electrochemical stressing (potential step and potential-static holding) on the degradation of polymer electrolyte membrane fuel cell electrocatalysts," *J. Power Sources*, vol. 185, pp. 280–286, **2008**.

[17] K.-W. Park and K.-S. Seol, "Nb-TiO2 supported Pt cathode catalyst for polymer electrolyte membrane fuel cells," *Electrochemistry Communications*, vol. 9, no. 9, pp. 2256–2260, **2007**.

[18] P. Wagener, A. Schwenke, and S. Barcikowski, "How citrate ligands affect nanoparticle adsorption to microparticle supports," *Langmuir*, vol. 28, p. 6132–6140, **2012**.

[19] G. Marzun, C. Streich, S. Jendrzej, S. Barcikowski, and P. Wagener, "Adsorption of colloidal platinum nanoparticles to supports: Charge transfer and effects of electrostatic and steric interactions," *Langmuir*, **2014**.

[20] G. Marzun, J. Nakamura, X. Zhang, S. Barcikowski, and P. Wagener, "Size control and supporting of palladium nanoparticles made by laser ablation in saline solution as a facile route to heterogeneous catalysts," *Applied Surface Science*, vol. 348, pp. 75–84, **2015**.

[21] S. Tanuma, C. Powell, and D. Penn, "Calculations of electron inelastic mean free paths. ix. data for 41 elemental solids over the 50 eV to 30 keV range," *Surface and Interface Analysis*, vol. 43, no. 3, pp. 689–713, **2011**.

[22] V. Petrykin, Z. Bastl, J. Franc, K. Macounova, M. Makarova, S. Mukerjee, N. Ramaswamy, I. Spirovova, and P. Krtil, "Local structure of nanocrystalline Ru1-xNixO2-δ dioxide and its implications for electrocatalytic behaviorsan XPS and XAS study," *J. Phys. Chem*, vol. 100, no. 113, pp. 21657–21666, **2009**.

[23] H. Schmidt, *129-NMR-spektroskopische Untersuchungen an Carbon Black und Graphit*. PhD thesis, Universität Duisburg-Essen, faculty of Chemistry, Germany, **2003**.

[24] J. C. Matsubu, S. Zhang, L. DeRita, N. S. Marinkovic, J. G. Chen, G. W. Graham, X. Pan, and P. Christopher, "Adsorbate-mediated strong metal–support interactions in oxide-supported Rh catalysts," *Nature Chemistry*, **2016**.

[25] H. Tang, J. Wei, F. Liu, B. Qiao, X. Pan, L. Li, J. Liu, J. Wang, and T. Zhang, "Strong metal–support interactions between gold nanoparticles and nonoxides," *Journal of the American Chemical Society*, vol. 138, no. 1, pp. 56–59, **2015**.

[26] E. W. Zhao, H. Zheng, K. Ludden, Y. Xin, H. E. Hagelin-Weaver, and C. R. Bowers, "Strong metal–support interactions enhance the pairwise selectivity of parahydrogen addition over Ir/Tio2," *ACS Catalysis*, vol. 6, no. 2, pp. 974–978, **2016**.

[27] S. Tauster, S. Fung, and R. Garten, "Strong metal-support interactions. group 8 noble metals supported on titanium dioxide," *Journal of the American Chemical Society*, vol. 100, no. 1, pp. 170–175, **1978**.

[28] H. Zhang, C. Liang, J. Liu, Z. Tian, and G. Shao, "The formation of onion-like carbon-encapsulated cobalt carbide core/shell nanoparticles by the laser ablation of metallic cobalt in acetone," *Carbon*, vol. 55, pp. 108–115, **2013**.

[29] V. Amendola, G. A. Rizzi, S. Polizzi, and M. Meneghetti, "Synthesis of gold nanoparticles by laser ablation in toluene: Quenching and recovery of the surface plasmon absorption," *J. Phys. Chem. B*, vol. 109, pp. 23125–23128, **2005**.

[30] M. Kalbac, O. Frank, and L. Kavan, "The control of graphene double-layer formation in copper-catalyzed chemical vapor deposition," *Carbon*, vol. 50, no. 10, pp. 3682–3687, **2012**.

[31] X. Li, W. Cai, J. An, S. Kim, J. Nah, D. Yang, R. Piner, A. Velamakanni, I. Jung, E. Tutuc, *et al.*, "Large-area synthesis of high-quality and uniform graphene films on copper foils," *Science*, vol. 324, no. 5932, pp. 1312–1314, **2009**.

[32] M. Fischer, J. Hormes, G. Marzun, P. Wagener, U. Hagemann, and S. Barcikowski, "In situ investigations of laser-generated ligand-free platinum nanoparticles by x-ray absorption spectroscopy: How does the immediate environment influence the particle surface?," *Langmuir*, vol. 32, no. 35, pp. 8793–8802, **2016**.

[33] A. Zaleska, "Doped-TiO2: a review," *Recent Patents on Engineering*, vol. 2, no. 3, pp. 157–164, **2008**.

[34] M. Oezaslan, F. Hasché, and P. Strasser, "PtCu3, PtCu and Pt3Cu alloy nanoparticle electrocatalysts for oxygen reduction reaction in alkaline and acidic media," *Journal of The Electrochemical Society*, vol. 159, no. 4, pp. B444–B454, **2012**.

[35] I. Dutta, M. K. Carpenter, M. P. Balogh, J. M. Ziegelbauer, T. E. Moylan, M. H. Atwan, and N. P. Irish, "Electrochemical and structural study of a chemically dealloyed PtCu oxygen reduction catalyst," *The Journal of Physical Chemistry C*, vol. 114, no. 39, pp. 16309–16320, **2010**.

[36] K. Artyushkova, S. Pylypenko, M. Dowlapalli, and P. Atanassov, "Structure-to-property relationships in fuel cell catalyst supports: Correlation of surface chemistry and morphology with oxidation resistance of carbon blacks," *Journal of Power Sources*, vol. 214, pp. 303–313, **2012**.

[37] E. Pizzutilo, S. Geiger, J.-P. Grote, A. Mingers, K. J. J. Mayrhofer, M. Arenz, and S. Cherevko, "On the need of improved accelerated degradation protocols (adps): Examination

of platinum dissolution and carbon corrosion in half-cell tests," *Journal of The Electrochemical Society*, vol. 163, no. 14, pp. F1510–F1514, **2016**.

[38] L. Du, Y. Shao, J. Sun, G. Yin, J. Liu, and Y. Wang, "Advanced catalyst supports for PEM fuel cell cathodes," *Nano Energy*, vol. 29, pp. 314–322, **2016**.

2. Conclusion and Outlook

Pulsed laser ablation in liquids (PLAL) is a useful and valuable method for the synthesis of nanoparticles with desired surfaces and compositions. In the first section, the aim was to verify the charged surface of laser-generated nanoparticles in a colloidal state and to identify the influence of the immediate environment on the surfaces of the particles.

Using *in-situ* X-ray absorption spectroscopy (XAS), the features of laser-generated nanoparticle surfaces were elaborated in this thesis. The surface oxidation of laser-generated nanoparticles in liquids was confirmed by this technique for the first time. This work provides the first realistic insights into the atomic structures of particles, such as their atomic bond lengths and surface composition. Furthermore, it was shown that a direct exertion of influence on the surface electron density is possible by adding ions to the colloid, resulting in a partial reduction due to ion interaction with the fixed Stern layer, which directly affects the surfaces of particles. A further aspect of interest was the evaluation of the difference between laser-generated nanoparticles and the one synthesized by conventional preparation methods. The results show that while wet-chemically synthesized Pt nanoparticles obtain less charged surfaces, platinum nanoparticles produced by PLAL in pure water exhibit a more pronounced surface charge. In order to neglect the effect of ligands, an additional comparison of ligand functionalized laser-generated nanoparticles with wet-chemically synthesized ones revealed a similar strong oxidation in total but different types of PtO bonds.

Comparing colloidal and supported nanoparticles, no pronounced changes in XAS analysis were found. Yet, investigations on the metal-to-support interaction still need to be conducted. Further analysis could be carried out with materials where strong metal-support interactions have already been observed in the literature (e.g., smaller metal NPs < 5nm for more distinctive signals). Due to the absence of ligands on laser-generated particles, one would expect a stronger interaction with the support compared to ligand-functionalized particles. In this study, it was shown that a graphitic shell was formed on the surface of Cu and $PtCu_3$ nanoparticles synthesized in acetone. Thus, the influence of the graphitic shell on the particle adsorption could be analysed in future work by XAS in order to understand the interaction with the NPs and the support. In addition to particles synthesized in acetone, the experimental set-up could be assembled with a colloid produced in acetone, where a graphic shell formation was already observed. The particles then could be phase-transferred in water to clearly distinguish the effect of the graphitic shell and the surrounding solvent. It is not recommended to first produce the particles in water and transfer them to acetone, since Cu NPs in water show stronger oxidation

than in acetone, resulting in non-comparable surfaces. Switching to noble metals may not lead to a graphitic shell, since its formation was discussed to be favoured by copper or copper alloy surfaces. The difficulty during the particle transfer from acetone to water could be caused by the hydrophobic nature of the particles due to their surrounding graphitic shell, but, as hypothesized in chapter 6.2, the surface of the particles is not fully covered by the carbon shell, and thus the free sites could enable the dispersion of the particles in water. Since acetone is soluble in water, a clear phase boundary will not be apparent. In this case, acetone can easily be separated by evaporation due to the lower vapour pressure compared to water.

Furthermore, the influence of the particle size on the thickness of graphitic shell as well as the influence of the graphitic shell itself on the catalytic activity should be systematically investigated. For example, the layer thickness might be controlled by the composition of a solvent mixture (e.g., acetone with ethanol or methanol), for example, varying the C:H:O ratio within the laser-induced cavitation bubble. In this case, the ability to electrochemically dealloy and the activity for the oxygen reduction reaction should be examined. In relation to alloy nanoparticles, future works with XAS analysis could be used to gather information on the local geometric and electronic structure of laser-generated particles. Interesting features might be to determine the lattice transformation or to investigate the links between the catalytic activities by finding structure activity correlations. Also, a comparison of the catalytic performance between laser-generated nanoparticles with wet-chemically synthesized particles that have the same sizes is of great interest.

Apart from the influence of ions and ligands in the solvent, the role of dissolved oxygen is an important research subject to explore. Due to the increasing interest of transition alloy metals such as PtCu, it is crucial to learn which oxygen species determine the oxidation of particles when synthesizing the particles by pulsed laser ablation in liquids. The investigations on laser ablation of Cu in different solvents revealed that the oxygen bound in water molecules, rather than the dissolved molecular oxygen, mainly causes particle oxidation due to the decomposition of water and formation of reactive species. This outcome has proven that solvent degassing alone will not avoid particle oxidation of oxidation-sensitive metals. Nevertheless, the analysis of weaker oxidation in oxygen-free water show the possibility to influence the composition of particles in water without the addition of additives.

Further investigations showed that the particle oxidation inhibits the formation of alloyed $PtCu_3$ nanoparticles in pure water, while the alloy formation is achieved in acetone due to a stabilization of the metals against oxidation. In future work, alternative as well as more cost-

effective and environmental friendly solvents, where alloy formation of less noble metals is favoured, should be investigated to facilitate their use in a technical scale.

Synthesizing alloy nanoparticles by wet-chemical routes enables a fine control of the metal composition, but the main difficulties lie in the transferability of the synthesis parameter, which usually must be adapted. In the current study, the transferability of PLAL to a variety of materials and liquids was shown to enable a high-throughput screening of a molar fraction series of catalysts by simply irradiating a previously compressed target consisting of a mixture of prescribed micro powders. The aim of the studies in the chapter V (alloy nanoparticles) was to synthesize nanoalloys as a substitute to the expensive platinum group metals. Here, the focus was on the investigation of particle properties regarding catalytic activity. In this context, despite the formation of segregated and oxidized bimetallic nanoparticles in pure water, it was demonstrated that electrocatalytic analysis of nickel-molybdenum particles reveal a significantly higher activity compared to mixed mono-metals. The cause was attributed to synergetic effects, which were indicated by XRD analysis.

In further electrochemical investigations, a comparison of the catalytic activity of more homogeneous alloy nanoparticles synthesized in acetone with the ones prepared in water could help to estimate the economic benefits of different solvents. The difficulty here will be to obtain the same particle size distribution for a meaningful comparison. To that end, continuously operating downstream approaches such as (tube-) centrifugation or laser fragmentation may be used. In addition, the exchange current could be normalized on the electrochemical active surface area (ECSA), which is often difficult to investigate for exotic materials. However, for applications, the use of the catalysts will be determined by the catalytic turnover rate divided by the production costs, while the latter are mainly defined by the metal amount, solvent and required energy.

From the point of view of resource utilisation, the aim is to have comparably high activities with commercial catalysts to be able to replace or reduce the amount of cost-effective metals such as platinum. In addition to the solvent and particle size, the decisive influencing factor for the catalytic activity is the metal composition, and, in particular, the core-shell structures are the main focus. While the shell consists of noble active metals, cheaper non-noble materials can be used in the core. Laser ablation in liquid could help to facilitate the synthesis of core-shell nanoparticles. For this purpose, laser ablation of a noble metal in an already-prepared colloid of less noble nanoparticles could be synthesized. Alternatively, galvanic replacement in colloidal nanoparticles containing non-noble metals could be performed in a salt-precursor

solution of catalytically active noble metals; this would enable the formation of a thin layer of noble active materials on the surface. Through this, a formation of core-shell nanoparticles could be achieved, where only a minimum amount of the expensive material is used, and no ligands are necessary. In addition to the combination of different amounts of both metals in alloy or core-shell particles, a third element will undoubtedly influence the activity and – much more importantly – the stability of the particles.

In order to produce stable and active heterogeneous catalysts, a link between the particles and the support must be established. For this, individual parameters that influence the particle properties and thus their adsorption to carrier structures must be understood. In this work, the method of colloidal particle deposition on TiO_2 and on a CB support has been studied in detail. Experimental results show that nanoparticle adsorption can be generally achieved when nanoparticles and the support are oppositely charged, which causes attractive forces. This was found by the observation that the adsorption efficiency is a function of the pH and ionic strength, which controls the particles surface charge. By adjusting the pH between the isoelectric points of laser-generated nanoparticles and the oxide support, a strong electrostatic interaction enables efficient particle adsorption. Following this approach, a particle loading of up to 65 wt% of PtNP on TiO_2 was achieved in a quantitative yield. However, since an increasing nanoparticle loading leads to an increased IEP shift due to a net-charge transfer, the maximum particle loading on the support is limited by the IEPs. Thus, investigations to further improve particle adsorption should be considered. Recent results in our research group show that, in contrast to TiO_2 species Hombikat II (Anatas), laser-generated gold nanoparticles adsorb on P25 (Anatas/Rutil) even inside the electrostatic repulsion regime, which is probably due to a diffusion control. A conceivable hypothesis is that particle adsorption may also occur under different mechanisms based on the interaction between the nanoparticles and oxygen defect sites of the support.

After preparing the heterogeneous catalyst according to the previously established method, the catalyst stability was investigated under relevant application conditions. Preliminary results of PtCu nanoparticles on TiO_2 and carbon supports showed that the binding between nanoparticles and the support is strong enough to withstand a harsh acid treatment even without calcination. However, in case of CB, particle detachment was found when heating the catalysts under conditions typical of low-temperature PEM fuel cells. Thus, the binding strength in laser-based catalysts must be improved to enable future application. This may be achieved by a better link and a more homogeneous distribution of the particles on the supports. For example, by using

controlled functionalized particles or support materials (i.e., acid and base treated MWCNT), the connection can be enhanced as well as the particle distribution on the support; this, in turn, enables a consistent high inter-particle distance. Note that the additives used should not poison the catalyst. Conversely, targeted functionalization may even facilitate the activity of the particles. Compared to conventional methods, particle functionalization of ligand-free particles enables independent investigations of influencing factors without the side effects of other additives and sub-monolayer ligand loads.

In this thesis, the particle adsorption on oxide supports was intensively investigated. However, further investigations on influential parameters related to carbon-based support materials are necessary to facilitate a controlled catalyst synthesis within materials that upon which fuel cells rely.

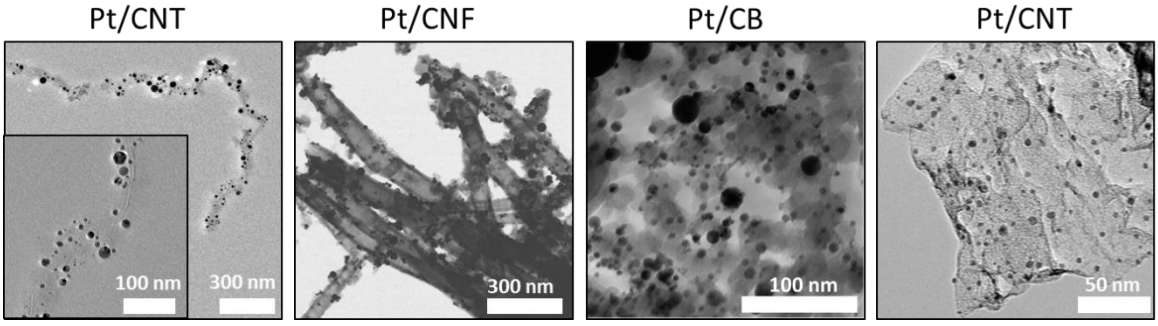

Fig. 1: Laser-generated platinum nanoparticles adsorbed on several carbon-based materials: carbon nanotubes (CNT), nano fiber (CNF), Carbon Black (CB) and graphene nanosheets (GNS).

Initial experiments show that laser-generated nanoparticles can be adsorbed on various carbon-based materials, such as carbon nanotubes/fiber (CNT/CNF), Carbon Black (CB) and graphene nanosheets (GNS) (Fig. 1). However, the parameters that influence efficient particle adsorption with high metal loading are not fully understood; therefore, further investigations are needed to synthesise active and stable catalysts.

The rapidly growing field of laser ablation in liquids will continue to be important in the future. The continuous ablation process with quantitative yields as well as the possibility to develop continuous downstream processing (i.e., centrifugation or fragmentation) and adsorption steps lend themselves to scaling, and thus they serve as easy entries into real-world applications. The pure surfaces of laser-generated particles significantly impact the properties of materials, which are of great importance in particular in both catalysis and bio-medical studies. The synthesis of systematic molar fractions of alloy materials in a desired solvent enables a high-throughput

screening of defined diverse samples and allows a transferability to various supports. Ultimately, there still remains much to be explored in the young field of pulsed laser ablation in liquids, and this is both exciting and inspiring.

What would be science without secrets?

3. Appendix

In situ investigations of laser-generated ligand-free platinum nanoparticles by x-ray absorption spectroscopy: How does the immediate environment influence the particle surface?

Figure S1 compares normalized Pt LIII edge XANES spectra, taken before and after centrifugation, of (a) Pt in H_2O and (b) Pt in citrate. The insets show just the whiteline regions:

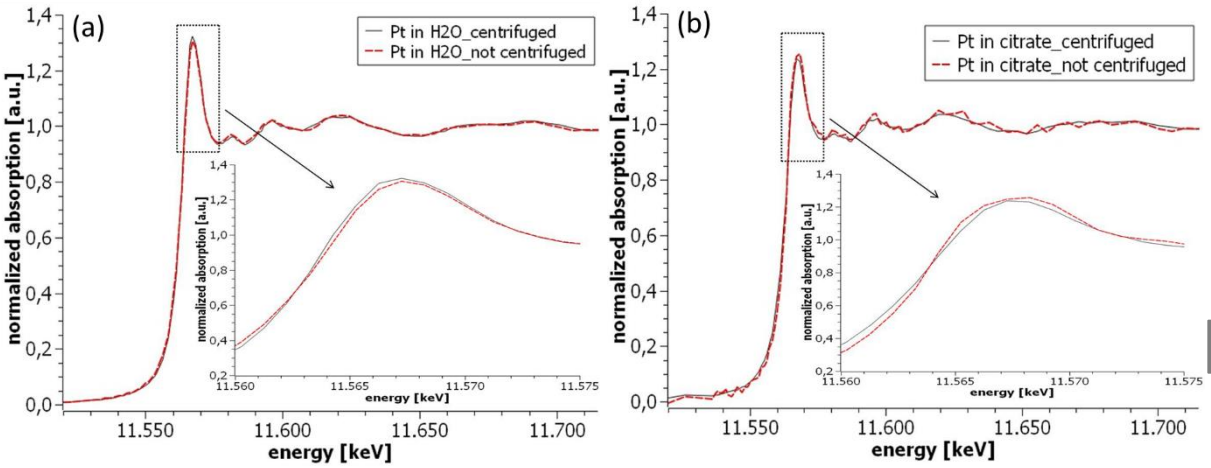

Fig. S1: normalized Pt LIII edge XANES spectra, taken before and after centrifugation, of (a) Pt in H_2O and (b) Pt in citrate. Insets: whiteline regions

VIII.i

As can be seen, centrifuging only improves the data quality while maintaining the particle-solvent interaction.

Why did we remove nanoparticles >10nm in this study?

Centrifugation of the colloidal nanoparticles leads to a dilution of the supernatant and enrichment of nanoparticles in the pellet. Particles >10nm were removed and smaller particles from the supernatant were used for XAFS measurements. We calculated the total number of nanoparticles based on the size distribution in the histograms of TEM images before and after centrifugation. The percentage of the small nanoparticle fraction, which was considered in the present study, was about 40%.

In principle, XAFS results can be extrapolated to bigger particles up to 10nm. However, from scan to scan whiteline intensities are subjected to minor fluctuations, for experimental reasons. Differences in whiteline intensity between spectra are thus considered significant only if they

exceed a certain (empirical) value. A smaller particle size means a higher relative number of surface atoms with a higher number of bonds (e.g. due to adsorption as is the case here) and thus more pronounced whiteline intensity differences. A bigger particle size results in less pronounced whiteline intensity differences and could therefore be misinterpreted as a statistical fluctuation. Thus we used smaller particle sized where 10nm as a threshold for Pt nanoparticles is again an empirical value. For bigger particles the results could be comparable to smaller ones. However, XAS is not suitable to verify this point and due to the higher sensitivity of smaller particles compared to bigger ones (assuming the same volume differently) the extrapolation to bigger particles is difficult. Most importantly, the centrifuged particle fraction analysed here represents the fraction most relevant for applications i.e. in catalysis.

Furthermore, wet-chemically synthesized particles already have a quite narrow particle size distribution (see Fig. 1b) whereas centrifugation of laser-generated samples was necessary to remove larger particles. Since the relative number of surface atoms is similar for particles synthesized wet-chemically and via PLAL (~20%), comparing XAS results of both groups of samples is feasible (Fig. S2).

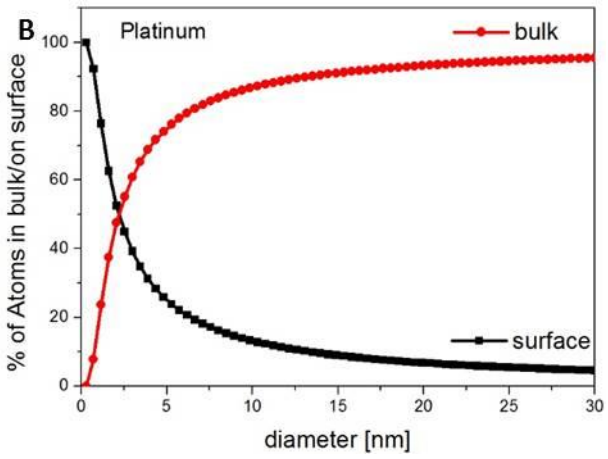

Fig. S2: Relative number of surface atoms and bulk atoms in Pt nanoparticles

Why didn't we perform a linear combination analysis of XAS data?

The spectra of a "PtO_2 monolayer is very different from that of bulk oxides consisting of Pt^{4+} (or Pt2+) and O^{-2}" due to the different binding partners of absorbing Pt atoms. [R1]. Thus, a linear combination analysis is not meaningful in the current study. In Fig. S3 it can be seen that the spectrum of (laser-generated) Pt in H_2O clearly differs from the one of the PtO_2 reference while it is in good accordance with the Pt foil spectrum. This result shows that, for nanoparticles in the Pt in H_2O sample, neutral core atoms have the strongest contribution to the spectrum. Whiteline intensity differences can be attributed to different oxidation states on the particle

surfaces. For the evaluation of the oxidation behaviour we thus focussed on whiteline intensity differences together with EXAFS Fourier transform magnitudes. This combination clearly shows differences between the surfaces of particles synthesized wet-chemically and via PLAL. Due to the similarity between the spectra of the three unsupported PLAL samples (Fig. 4) the same argumentation can reasonably be applied to the other two samples Pt in phosphate and Pt in citrate.

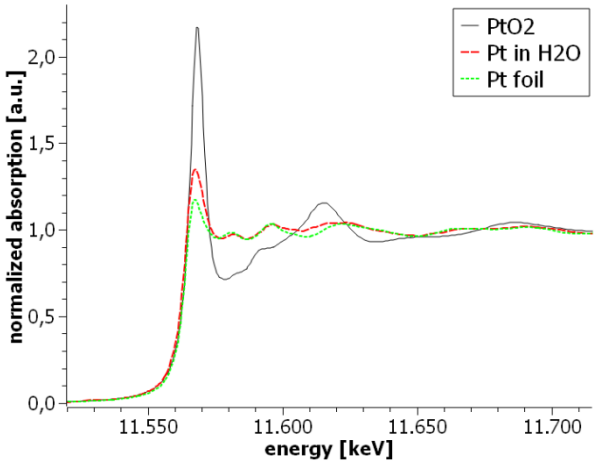

Fig. S3: XANES results show a good agreement between the spectra of laser-generated Pt nanoparticles and the Pt foil and little agreement to the one of PtO_2. This result can interpreted as Pt atoms in the nanoparticles having the same geometric structure as in the Pt foil, being overall electronically neutral while being slightly oxidized on the surface. Since there are no references available with similar characteristics a linear combination analysis is not possible.

Fig. S4 shows the zeta potentials measured for laser-generated Pt NPs in H_2O, a sodium phosphate buffer and sodium citrate solution. The last two have a concentration of 0.1mM each:

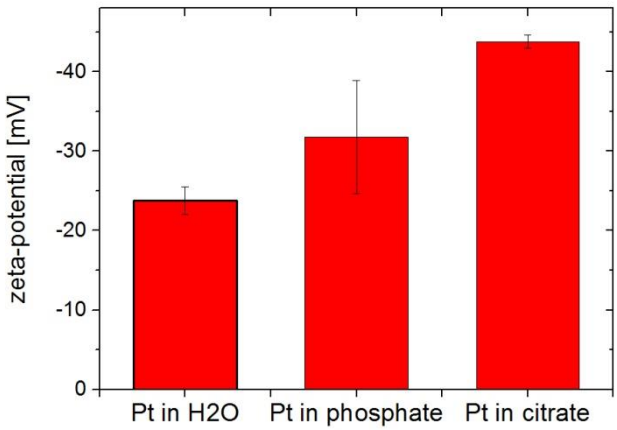

Fig. S4: Zeta potentials of laser-generated platinum nanoparticles in H_2O, a sodium phosphate buffer (pH 7, 0.1mM) and a sodium citrate (0.1mM) aqueous solution

[R1] Imai, H.; Izumi, K.; Matsumoto, M.; Kubo, Y.; Kato, K.; Imai, Y. In situ and real-time monitoring of oxide growth in a few monolayers at surfaces of platinum nanoparticles in aqueous media. *Journal of the American Chemical Society* 2009, 131(17), 6293-6300.

Role of dissolved and molecular oxygen on Cu and PtCu alloy particle structure during laser ablation synthesis in liquids

Oxygen-free water

For the preparation of oxygen-free water, 0.5 l deionized water was placed in a distillation apparatus and the water was evacuated by room temperature under stirring for 2-3 minutes. The liquid boiled quickly and a slight cooling down could be observed. The complete apparatus was flooded with argon and the water was distilled under atmospheric pressure with a light argon stream. The receiver flask was removed under argon and the water was stored under argon.

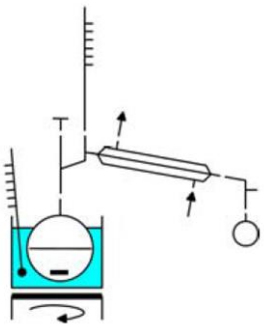

Figure S1 : Experimental set-up for the preparation of oxygen-free water.

Laser-generated copper:

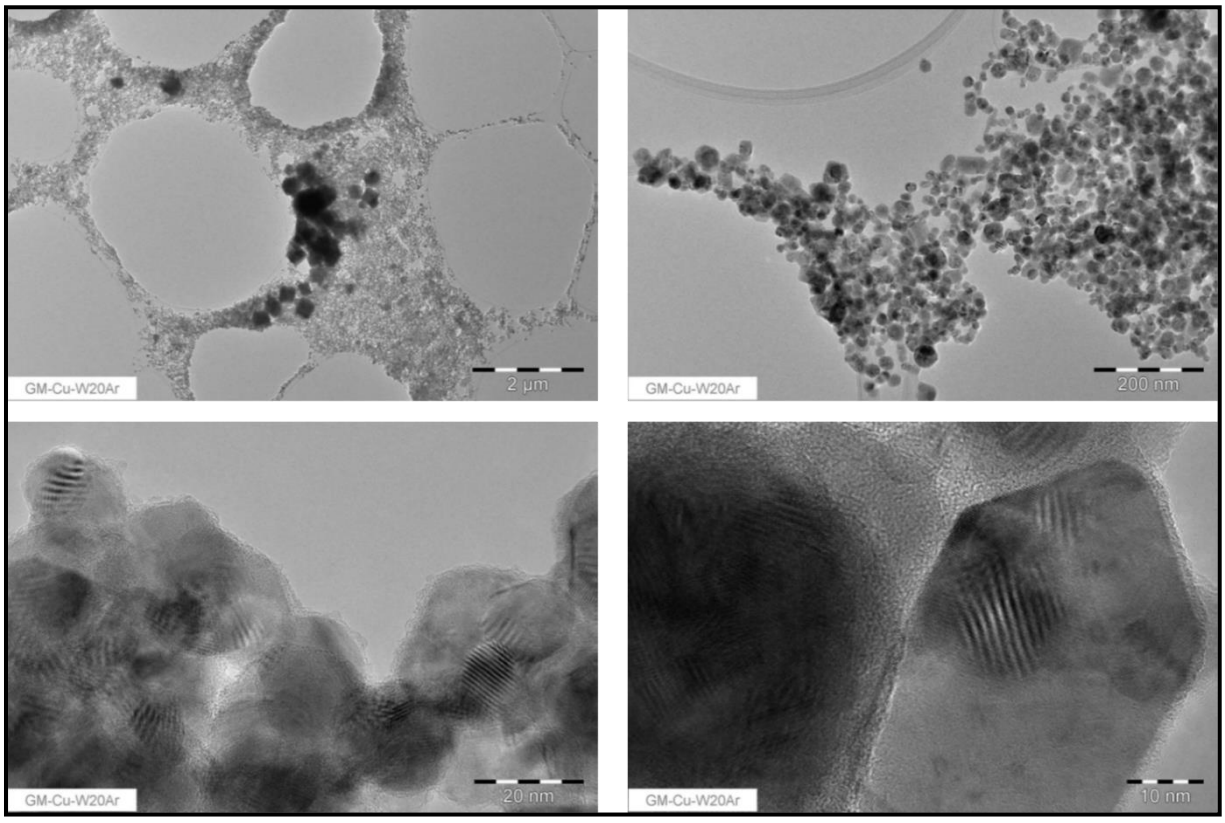

Figure S2: Nanoparticles synthesized by PLAL of Cu in freshly prepared oxygen-free water (H_2O_{Ar}).

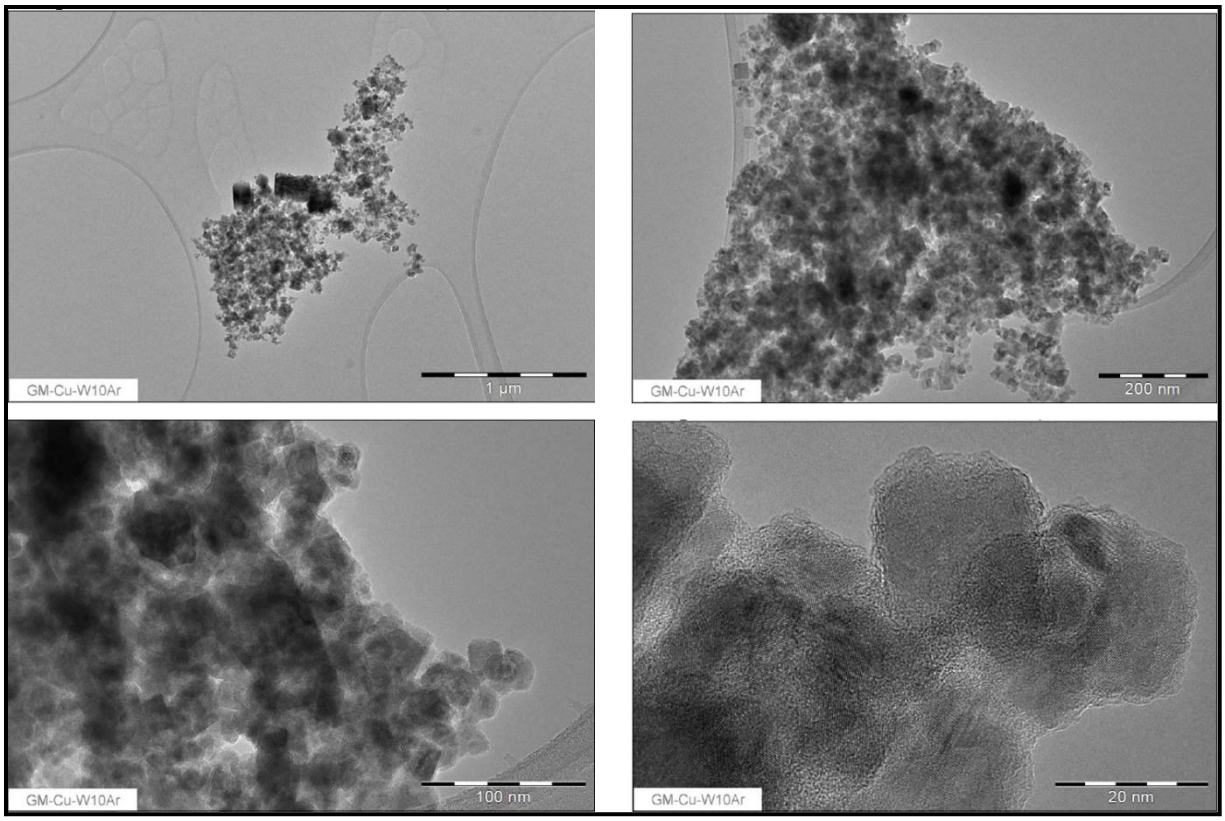

Figure S3: Nanoparticles synthesized by PLAL of Cu in oxygen-free water (H2OAr) – aged (~1 month) **VIII.i**

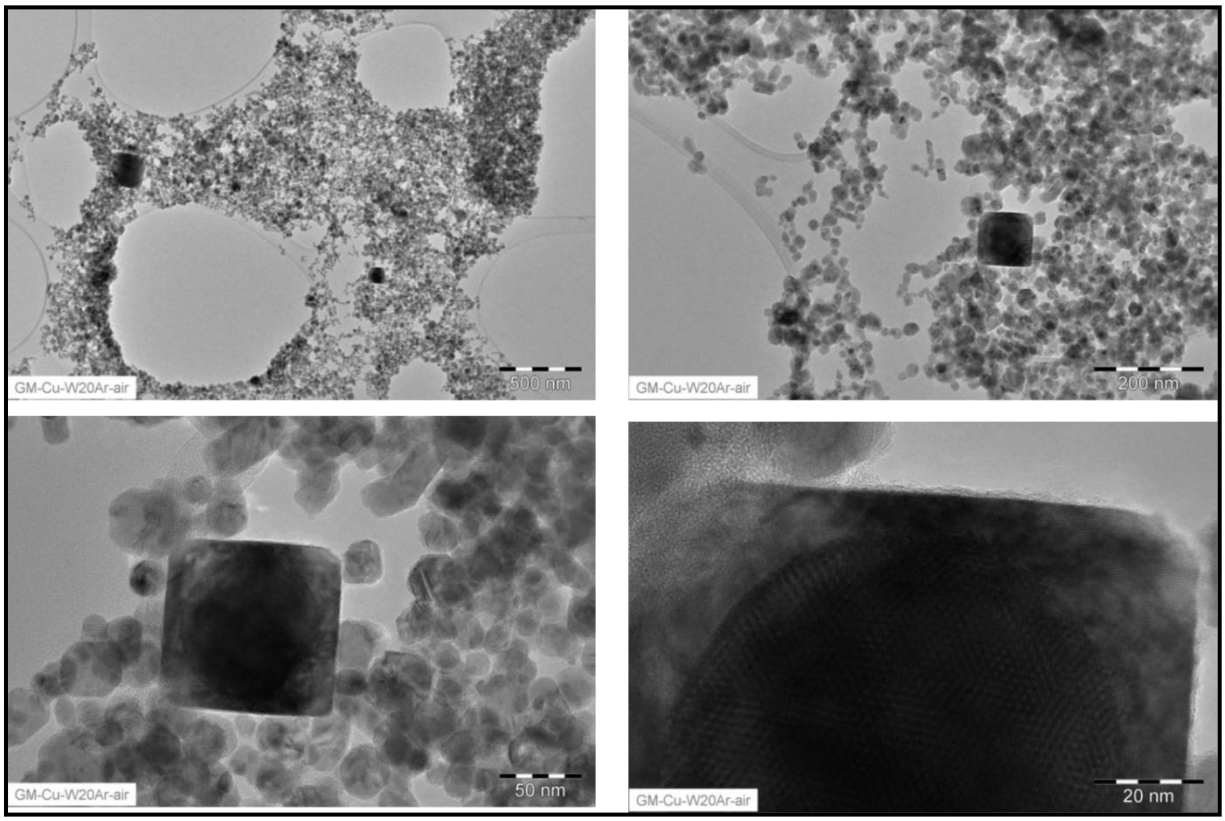

Figure S4: Nanoparticles synthesized by PLAL of Cu in oxygen-free water (H_2O_{Ar}) – after treated in air (1 day).

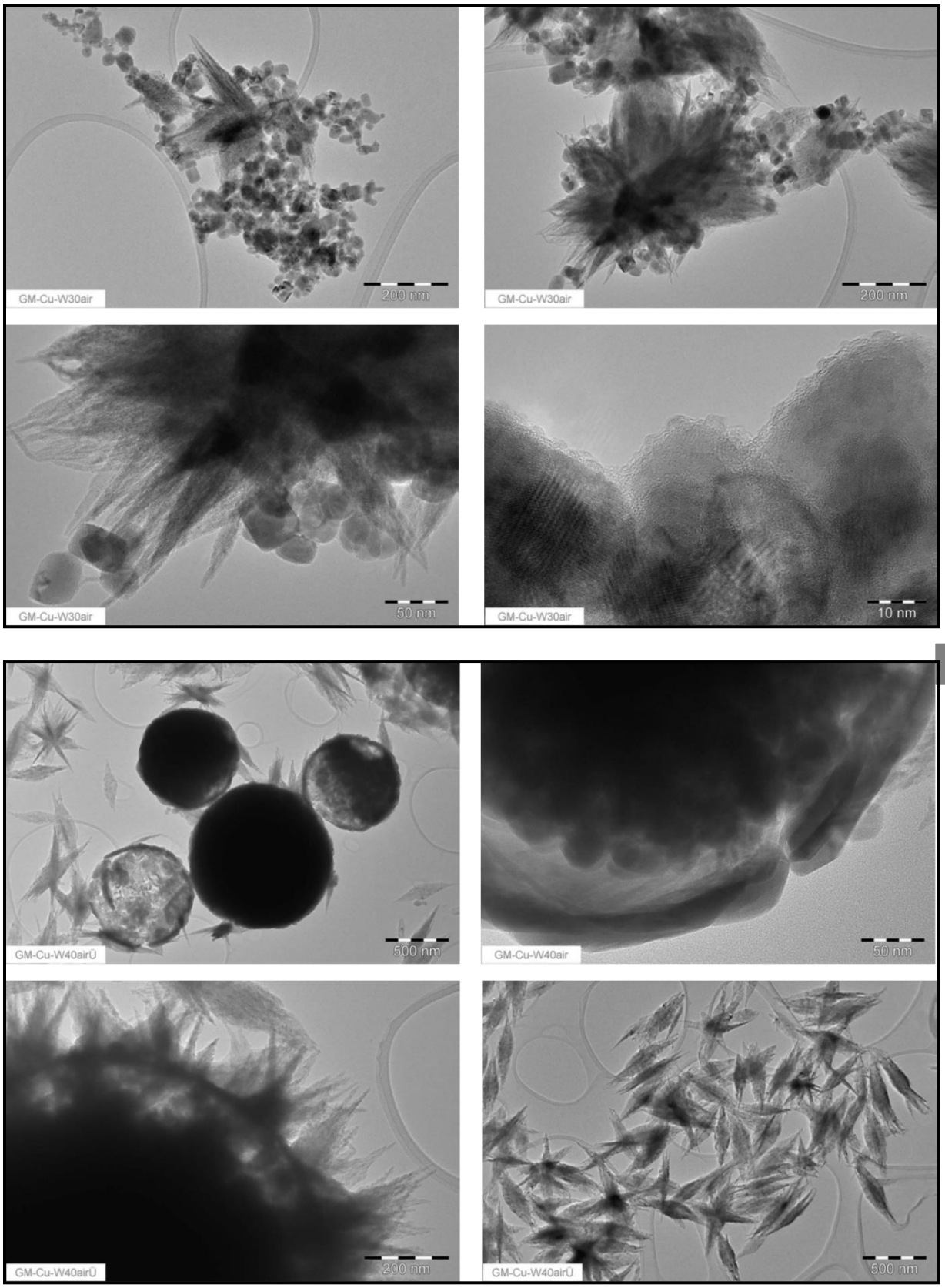

Figure S5: Nanoparticles synthesized by PLAL of Cu in freshly prepared water with oxygen (H_2O_{air}).

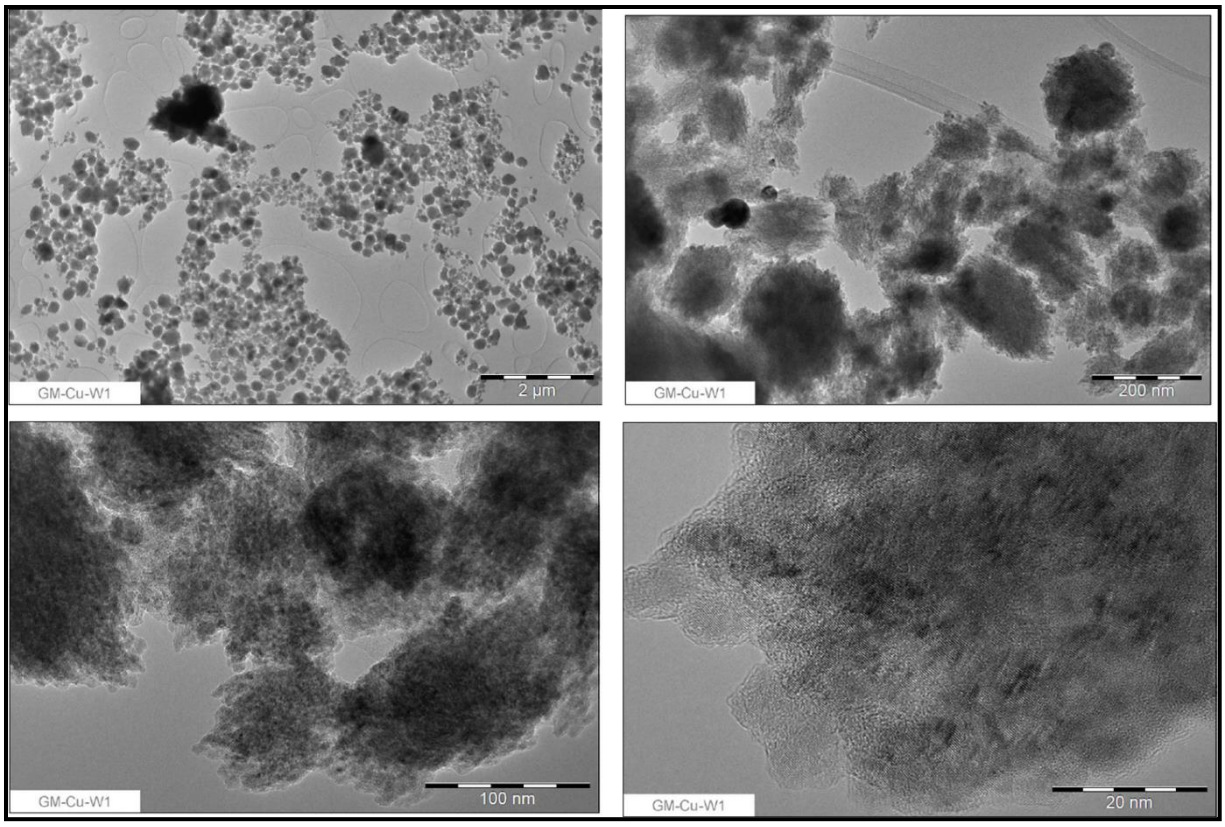

Figure S6: Nanoparticles synthesized by PLAL of Cu in water with oxygen (H_2O_{air}). –aged (~1 month).

VIII.i

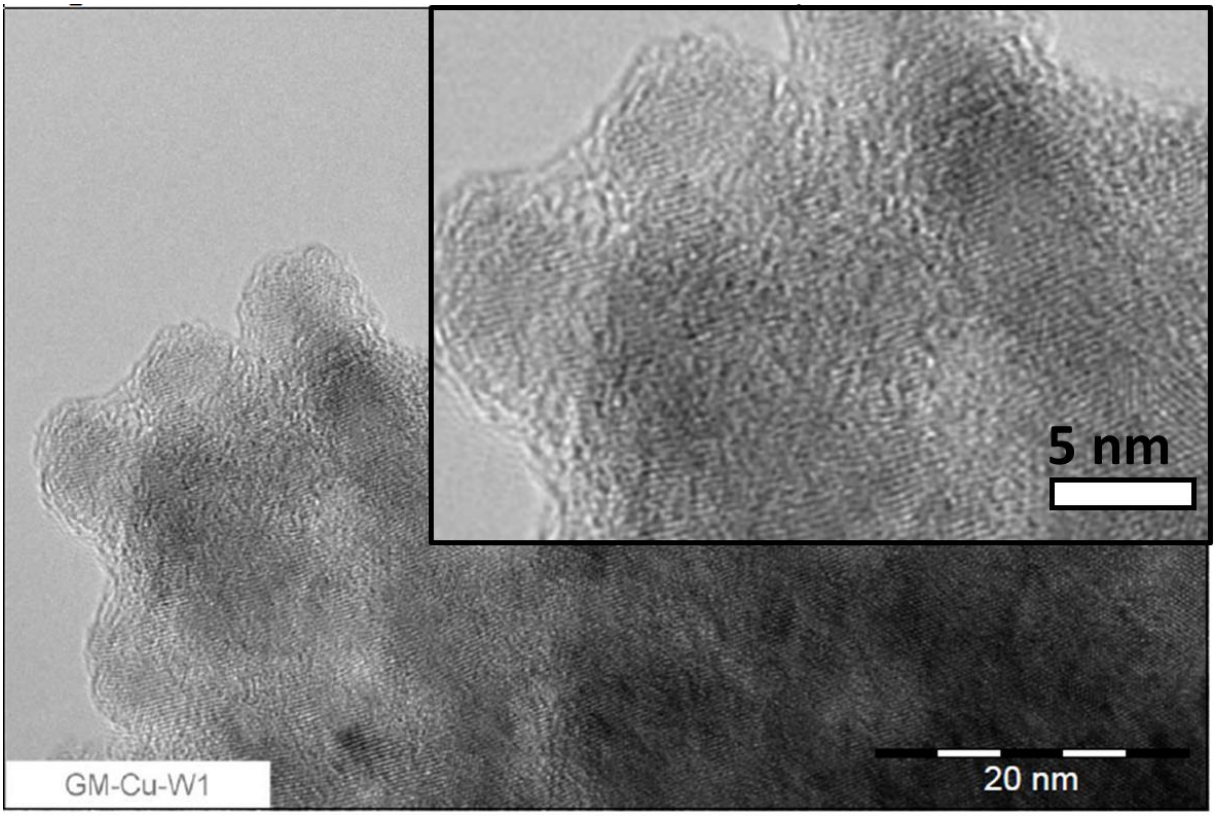

Figure S7: Enlarged view on small crystallites of nanoparticles synthesized by PLAL of Cu in water with oxygen –aged (~1 month)

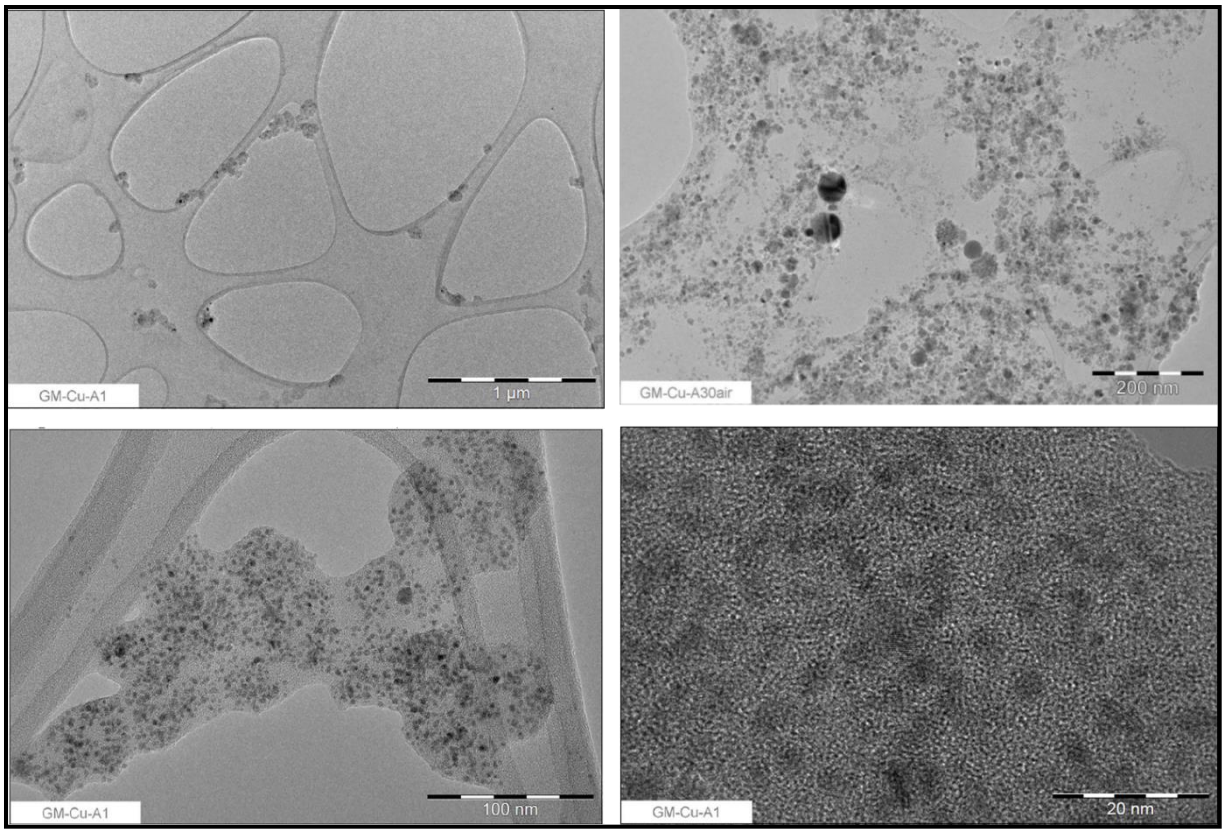

VIII.i

Figure S8: Nanoparticles synthesized by PLAL of Cu in air-saturated acetone.

XRD analysis of the particles in H_2O_{Air} reveal a broad peak at $\theta < 15°$. This part can be attributed to amorphous fractions. Comparing both size fractions in H_2O_{Air} it is obvious that the large crystallites have a higher proportion of CuO and elemental Cu (Figure S9 and Figure 3 in manuscript). However a comparison should be treated with caution since the particle structure changes due to ageing.

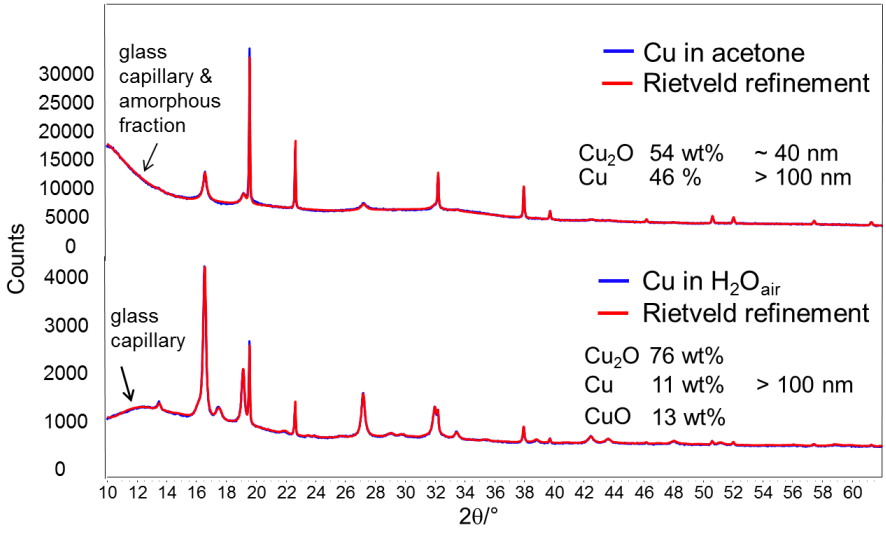

Figure S9: Rietveld refinement plots of centrifuged (> 20 nm) samples in in air-saturated water and acetone. Blue curve: measured data, red curve: refined data.

Table S1: TEM-EDX evaluation of nanoparticles laser-generated in acetone (a), H2OAr (b) and H2Oair (c), as well as aged nanoparticles in H2Oair (d) in summary. The circles represent the analysed area by EDX.

Cu in acetone with oxygen

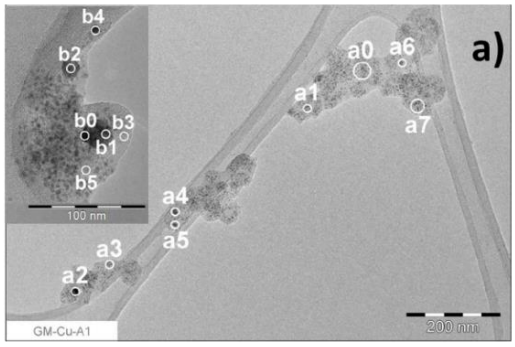

Area	Ratio Cu/O
a2, a4, a5,a6, b2, b2	1 : 0
b0	1 : 0.1
a0, a1, b4	1 : 0.4
b5	1 : 0.6
a3	1 : 0.7
a0, a5	1 : 0.9

Cu in H_2O oxygen-free (H_2O_{Ar})

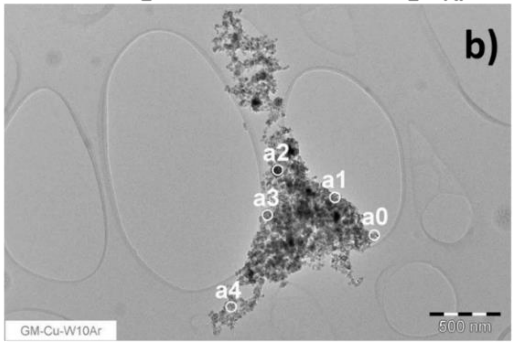

Area	Ratio Cu/O
a2	1 : 0.2
a1	1 : 0.6
a4	1 : 0.8
a0	1 : 0.9
a5	1 : 0.9
a3	1 : 2.3

VIII.i

Cu in H_2O with oxygen (H_2O_{air})

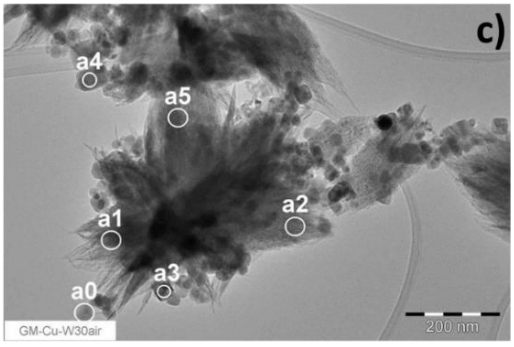

Area	Ratio Cu/O
a0	1 : 0.6
a3	1 : 0.7
a4	1 : 0.5
a1	1 : 1.1
a2	1 : 1.2
a5	1 : 1.1

Cu in H_2O with oxygen (aged)

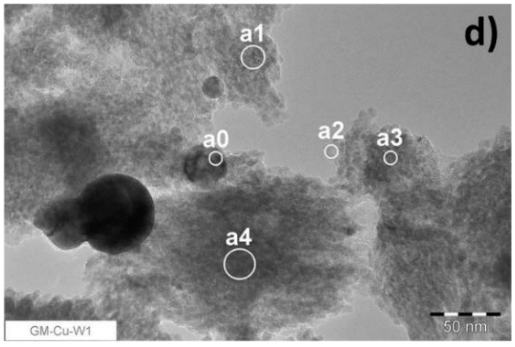

Area	Ratio Cu/O
a1	1 : 0.9
a3	1 : 1.0
a4	1 : 0.8
a0	1 : 2.0
a2	1 : 1.6

Graphitic shell

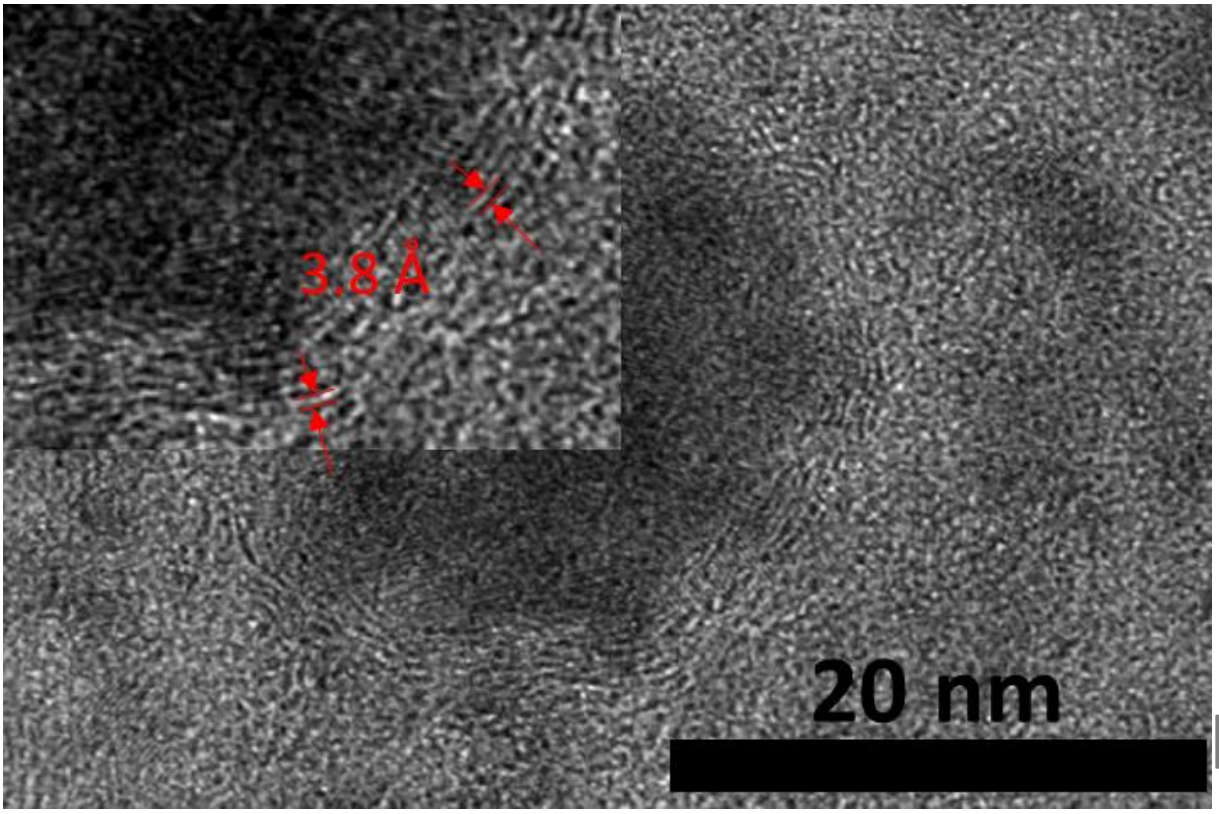

VIII.i

Figure S10: Nanoparticles synthesized by PLAL of Cu in air-saturated acetone. A nanoparticle surrounded by a graphitic layer.

Raman spectra of laser-generated nanoparticle in acetone clearly show peaks, that can be attributed to a graphitic species. Two peaks were identified. The G-Peak (G=graphite) is located at 1564 cm^{-1} while the D-Peak (D=disorder) can be measured at 1360 cm^{-1}. The G-peak position and the ratio of the intensities between the two peaks I(D)/I(G) may be used to evaluate the amorphization trajectory.[<ferrari07>] According to the Scheme of Ferrari et al. graphitic species are present in the acetone sample.

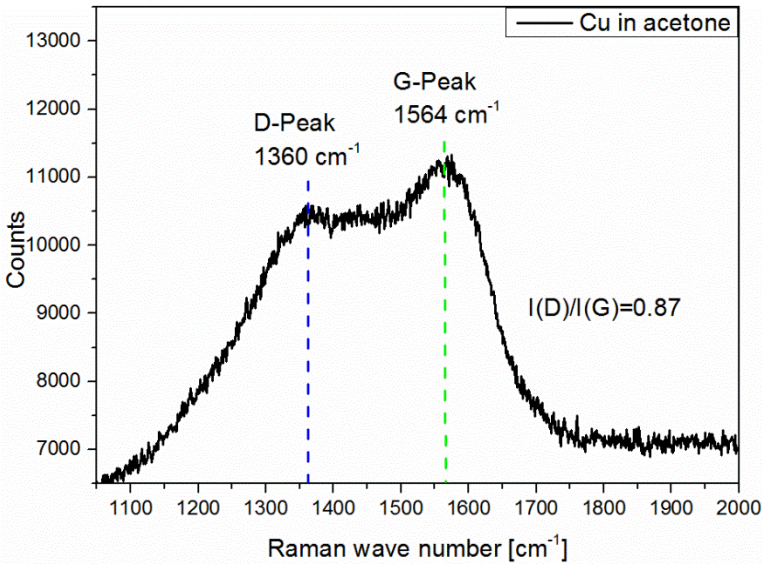

Figure S11: Raman spectra of laser-generated nanoparticles synthesized by laser ablation of Cu in acetone.

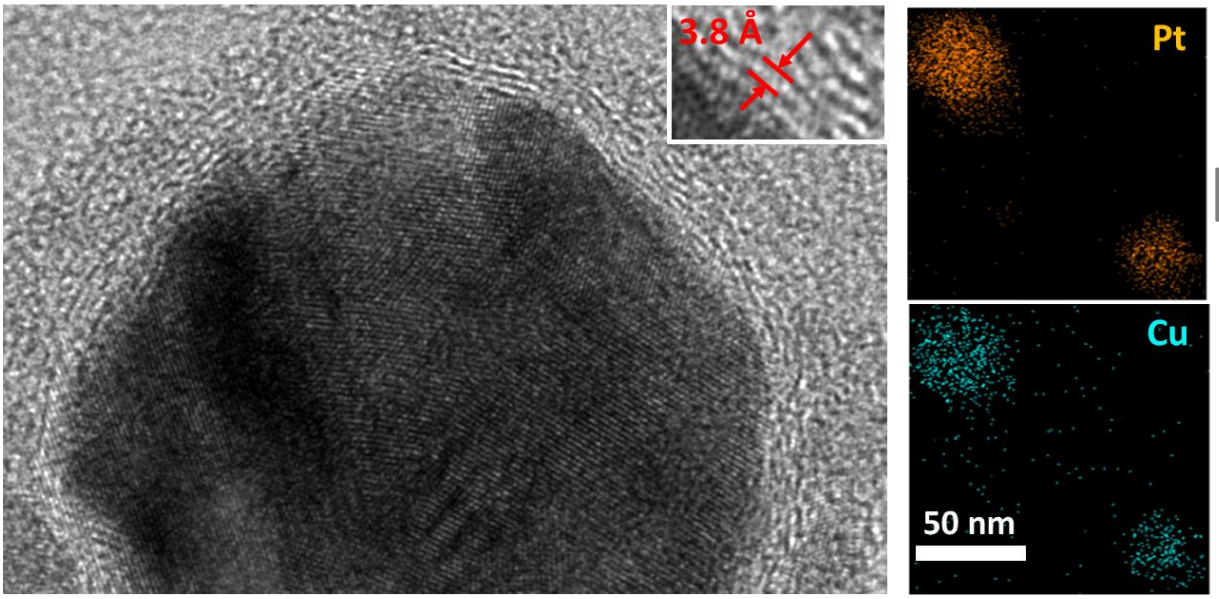

Figure S12: TEM image of encapsulated PtCu3 nanoparticles by a graphitic layer in acetone (a) and EDX mapping shows a homogeneous alloy formation.

VIII.i

Electron energy:

Electron energy in the plasma phase was calculated by taking plasma warming by inverse bremsstrahlung into consideration. The average kinetic electron energy is given by the statistic distribution of the electron velocities. When the local thermodynamic equilibrium is reached, the electron temperature T_e gives the average kinetic electron energy $=3/2k_BTe$ ($k_B = 8.617*10^{-5}$ eV/K). This leads to 0.65 eV at a plasma temperature of 5000K.

Reference:

[1] Andrea C Ferrari. Raman spectroscopy of graphene and graphite: disorder, electron–phonon coupling, doping and nonadiabatic effects. *Solid state communications*, 143(1):47–57, 2007.

Laser synthesis, structure and chemical properties of colloidal nickel-molybdenum nanoparticles for the substitution of noble metals in heterogeneous catalysis

1. Target preparation

Colloidal nanoparticles were produced by pulsed laser ablation of a pellet, which is made by pressing a powder of nickel and molybdenum micro particles in several compositions. The pressed pellets were characterized by scanning electron microscopy (SEM), energy-disperse X-ray spectroscopy (EDX) spectrometer and X-ray diffraction. In Fig. S1 SEM-EDX analysis of the pressed pellets show that both metals Ni and Mo are evenly distributed over the pellet that could be obtained simply by mixing the microparticles.

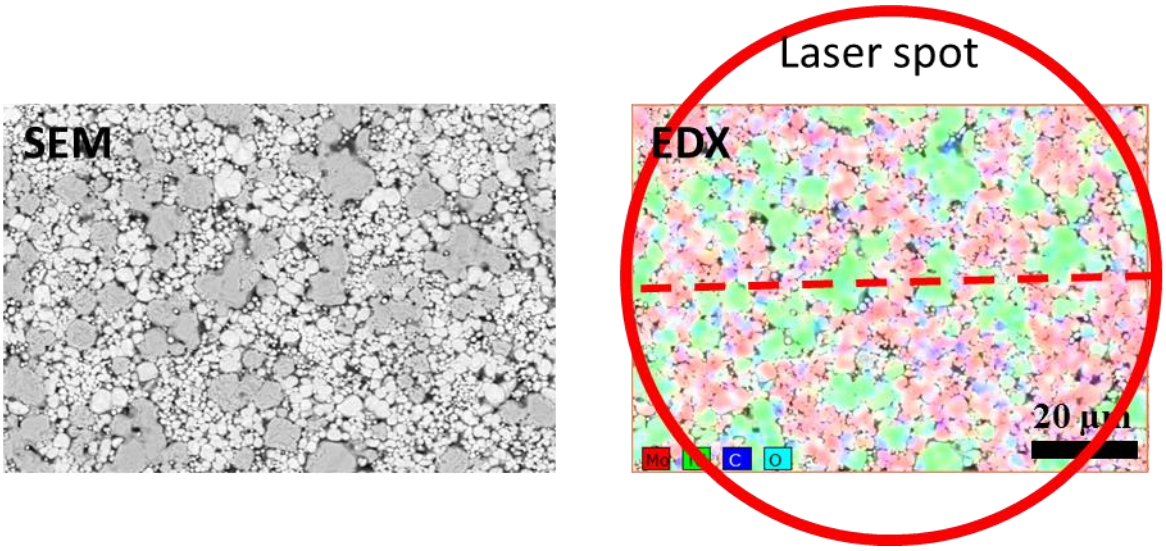

VIII.ii

Figure S1: SEM-EDX image of a pressed Ni50Mo50 powder mixture and indicated ablation spot size.

The laser spot has a diameter of about 100 µm (estimated by measuring a surface profile of the ablation groove with a profilometer – see Fig. S2) and the microparticles have a mean diameter of about 8.5 µm (Ni) and 4.5 µm (Mo) assembling to islands about 10-20 nm, that are distributed evenly over the target. This distribution enables laser ablation of areas within both elemental being present in the mixture set by the powder ratio before pressing the target.

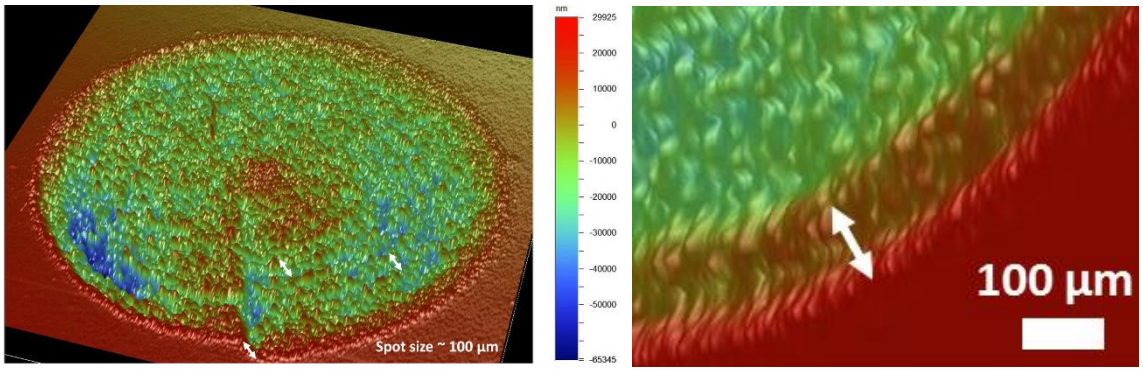

Fig. S2: Topography of the ablation crater on the pellet for the spot size determination.

We performed SEM-EDX analysis of the target also after pulsed laser ablation in water. In Fig S3 it can be clearly seen, that the microparticles are present separately and each grain can be clearly distinguished. After laser ablation the micro particle form a uniform structure. The elemental composition after irradiating the target indicate alloy formation of the target.

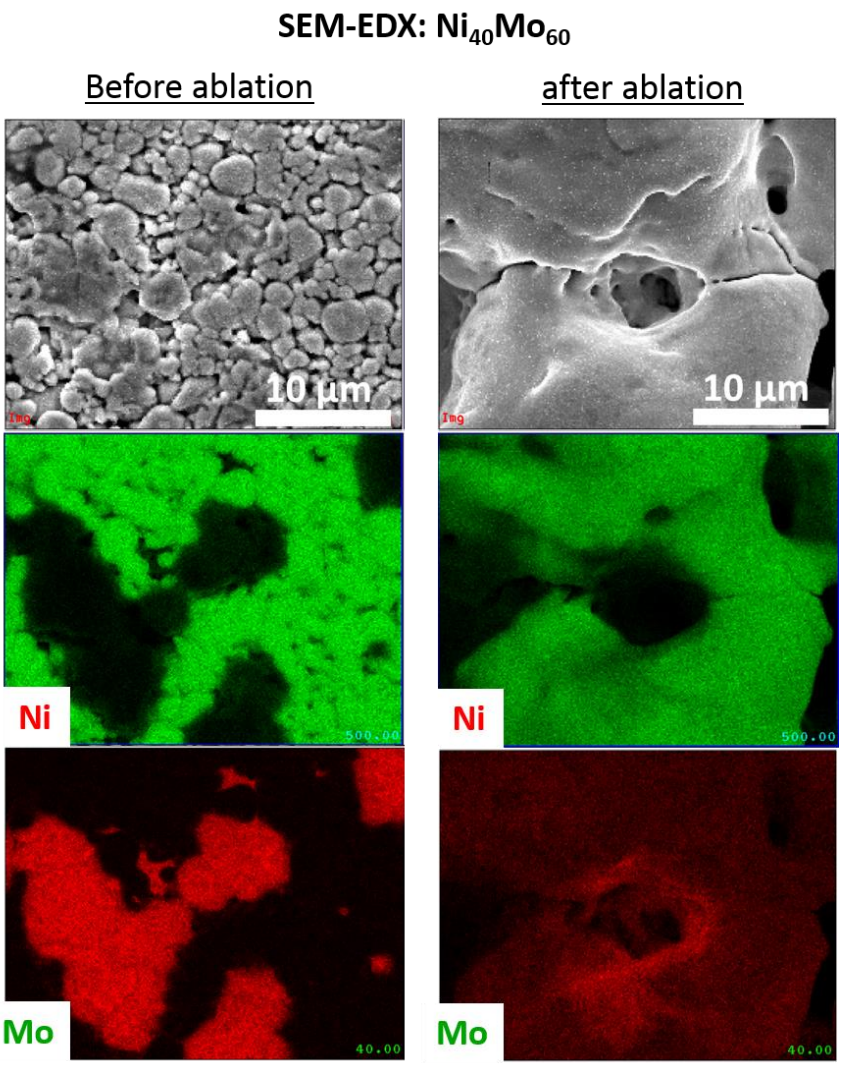

Figure S3: SEM-EDX image of a pressed $Ni_{40}Mo_{60}$ powder mixture before (left) and after (right) ns-laser ablation.

2. Molybdenum nanoparticles

Formation of oxides is not attributed to oxygen inclusion into the pressed pellets. UV-VIS spectrum of molybdenum nanoparticles synthesized by ablation of a cast Mo metal target show the same absorption band (Fig. S4).

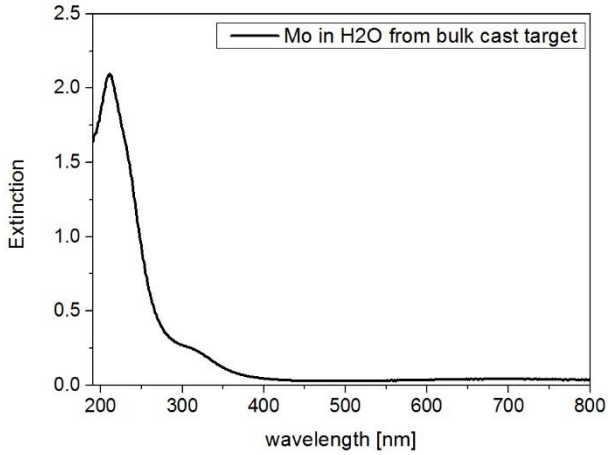

Fig. S4: UV-VIS extinction spectra of molybdenum nanoparticles synthesized using a bulk metal cast molybdenum target.

3. Particle oxidation: content of oxygen in water

To study the effect of oxygen on particle formation during laser ablation molybdenum and nickel nanoparticles were synthesized in air-saturated water (8 mg/l O_2) and in water, which was purged with nitrogen for at least 30 minutes (1.5 mg/l O_2). UV-VIS spectra of Mo in nitrogen saturated water show similar absorption in the UV-region as for the particles in air saturated water, which indicate MoO_3 and dissolved species such as MoO_4^{2-} and $HMoO_4$ (Fig. S5). Long-term stability of both colloidal solutions were measured at several days. Comparing the both colloids the shape of the spectra has not changed. As shown in the manuscript in Fig.1, molybdenum nanoparticles oxidize during their storage time. As in air-saturated water molybdenum particles are oxidized in nitrogen purged water, which is more obvious in their behaviour in UV-VIS spectra after several days. Absorbance in IR-region increases, which signify an oxidation of molybdenum. This indicate that either there is still enough dissolved oxygen in water to oxidize the particles or water molecules are converted into reactive oxygen species during laser ablation in liquid, which then can react with the metals.

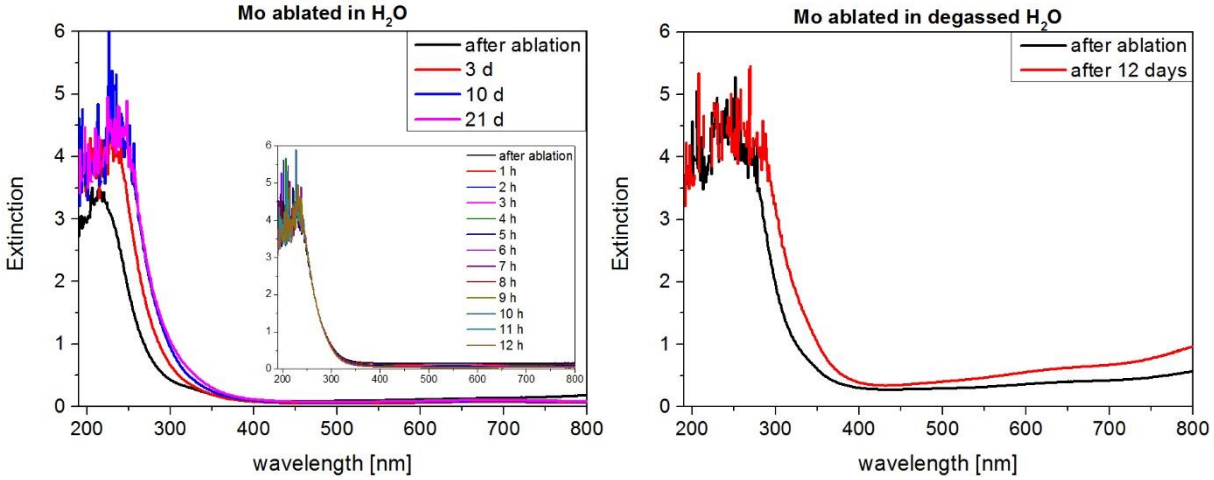

Fig. S5: Evolution UV-VIS spectra during 21 days of storage after laser ablation of molybdenum in air-saturated H_2O (left) and purged H_2O with N_2 (right).

UV-VIS spectra of the nickel colloid do not differ considerable from the air saturated water if laser ablation is done in the degassed solvent (Fig. S6). But it is remarkable that the colloid is not stable and agglomerates shortly after ablation. The stabilization of the particles can be attributed to a partially oxidation of the particles surface, where ions can adsorb and form an electrochemical double layer. Thus the agglomeration in a low oxygen containing solvent indicates, that the amount of oxygen is too less to stabilize the surface of nickel nanoparticles, due to a less amount of oxidized sites.

VIII.ii

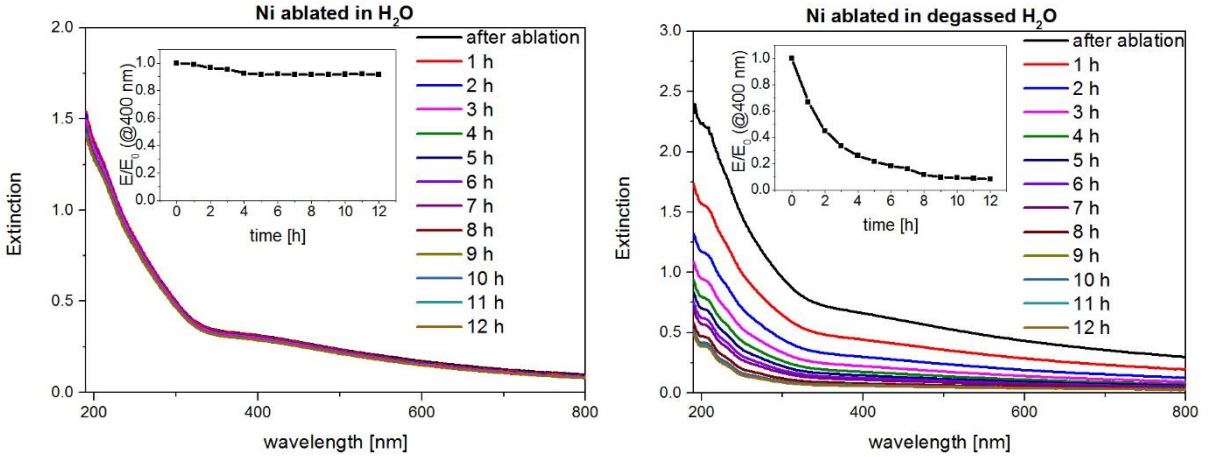

Fig. S6: Evolution UV-VIS spectra during 12 hours of storage after laser ablation of nickel in air-saturated H_2O (left) and purged H_2O with N_2 (right).

We measured the amount of oxygen and then calculated the molar ratio of O_2 to Mo and Ni, to find out whether the amount of oxygen in the nitrogen purged water is still enough to oxidize the particles. By assuming, that Mo will be oxidized to MoO_3 a molar ratio of 3:1 and for NiO O_2/Ni 1:1is necessary. We found, that the molar ratio $O_2/NP_{surface}$ is already low in air saturated water (for Ni and Mo with about 0.01 and 0.03 respectively, cf. table S1), assuming, that the

particles are not fully but partially oxidized on their surface (XPS measurements shown below in Fig. S9 and S10). Due to a stronger oxidation of the particles that was measured compared to the calculated one, this calculations support the assumption that reactive oxygen species from H_2O molecule decomposition take part in the Ni and Mo oxidation.

Table S1: Calculations on surface oxidation of Mo and Ni in air saturated and degassed water

calculations on surface oxidation		
	Mo	**Ni**
total number of nanoparticles in 1ml	7.53E+16	7.22E+15
radius nanoparticle [nm]	1.4	3.5
latice constant [nm]	3.23	9.76
metal surface atoms [mol]	2.21E-05	9.81E-06
	amount of O2 mg/L	**molar amount of O2 in 1 ml [mol]**
O2 content in air saturated water	8.0	2.50E-07
O2 content in degassed water	1.5	4.69E-08
	molar ratio O2/Mo atoms	**molar ratio O2/Ni atoms**
O2 content in air saturated water	1.13E-02	2.55E-02
O2 content in degased water	2.12E-03	4.78E-03

Particle synthesis in in acetone, where no oxidation was observed (Fig. S7), suggest that the dissolved oxygen in the solvent plays a minor role regarding the particle oxidation. Rather decomposition of water molecules is the most influencing factor. Fig S7 show, that the extinction spectra of particles in acetone is consistent over at least 21 days after laser ablation, showing that the particles stay stable and do not tend to agglomeration.

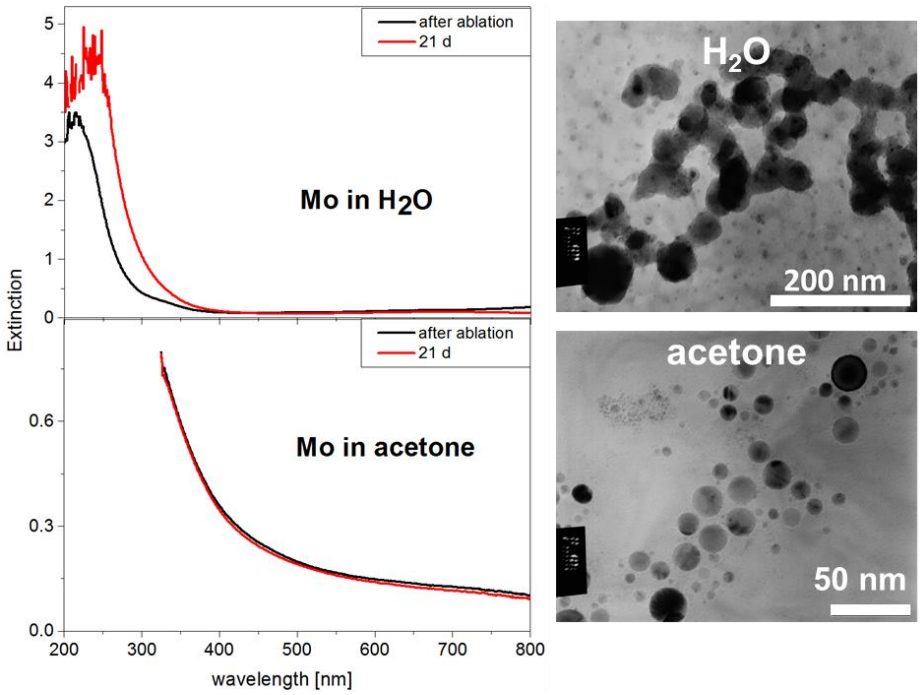

Fig. S7: UV-VIS spectra of Mo nanoparticles ablated in water and acetone (left) and the corresponding TEM images (right).

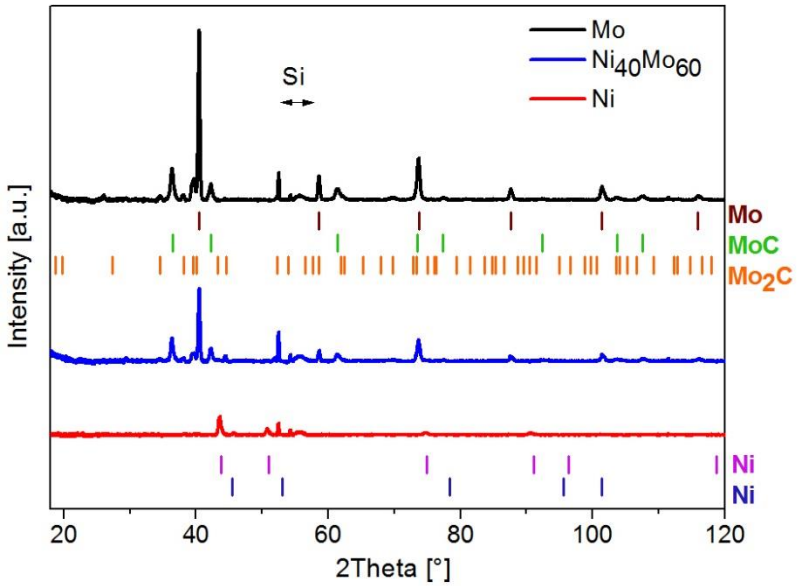

Fig. S8: X-Ray diffractograms of Ni, Mo and $Ni_{40}Mo_{60}$ nanoparticles laser-generated in acetone.

For XPS analysis of the nanoparticles synthesized in water we separated the particle sizes by centrifugation using Svedberg equation to calculate the cut off size.

$$\Delta t = \frac{9 \cdot \Delta h \cdot \eta_0}{2 \cdot r_P{}^2 \cdot (\rho_P - \rho_0) \cdot RCF \cdot g} \qquad \text{Eq. S1}$$

Δh	=	Filling high of the centrifugation tube with colloid
η_0	=	dynamic viscosity of the solvent
r_p	=	particle diameter
ρ_P	=	density of the material to be centrifuged
ρ_0	=	density of the solvent
g	=	acceleration due to gravity, 9,81 m/s²
RCF	=	relative centrifugal force:

$$RCF = \frac{4 \cdot \pi^2}{g} \cdot r \cdot n^2$$

n	=	rounds per minute
r	=	centrifuge radius

VIII.ii

XPS analysis (Fig. S9) of nickel nanoparticles show peaks, which indicate the formation of $Ni(OH)_2$ [1[,[2] . By comparing the X-ray photoelectron spectra of small (<10 nm) and large (> 10 nm) nickel nanoparticles, no differences can be observed. This shows that all nickel particles have the same oxidation state on their surfaces regardless of their size.

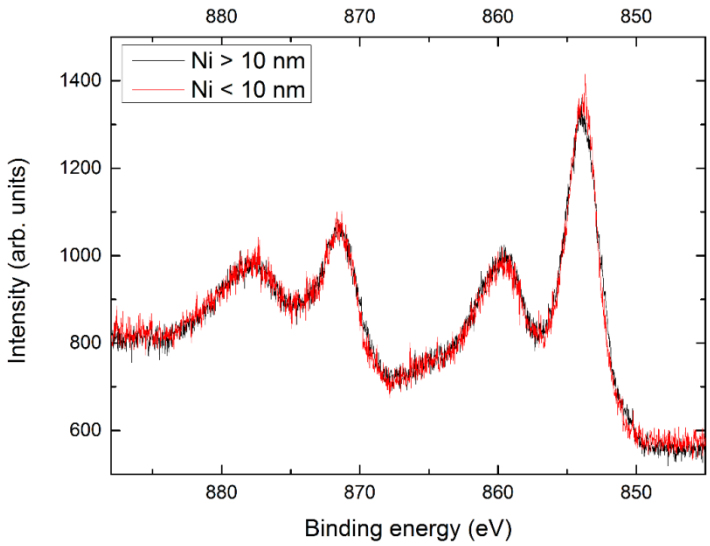

Fig. S9: X-ray photoelectron spectroscopy of nickel nanoparticles for the two different size fractions

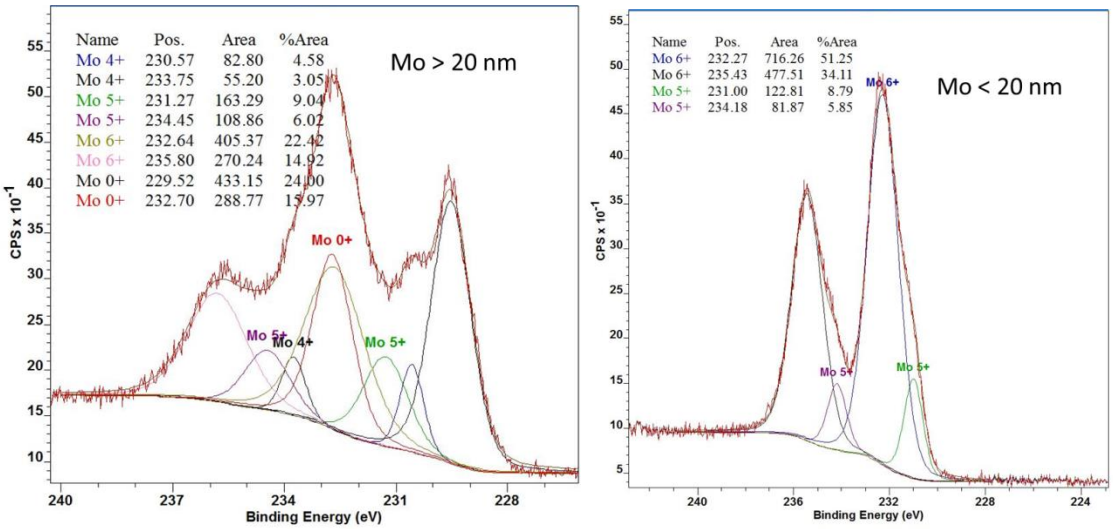

Fig. S10: X-ray photoelectron spectroscopy of molybdenum nanoparticles for different size fractions

In contrast to this molybdenum nanoparticles show different properties (Fig. S10). The large particle fraction (>20 nm) contains several oxidation species such as Mo^{4+}, Mo^{5+}, Mo^{6+} but also Mo^{0}. This results correlate with the observations from UV-VIS spectra (Fig.1 manuscript) where MoO_3 and from XRD investigations (Fig. 5 manuscript) other species such as Mo and MoO_2 could be found. Considering all elemental analysis we suppose, that the particles (>20 nm) consist of a metallic core and are surrounded by a few layers of oxidized species. XRD analysis, which is volume sensitive, show pronounced peaks of metallic Mo. Due to the fact that also MoO_2 species can be detected by this method, shows that the oxidic shell do not only consist of one layer, which is usually difficult to detect by XRD, but a pronounced coating of the oxidized MoO_2 species. The surface sensitive analysis method by XPS point the existence of further oxidized species (Fig. S11).

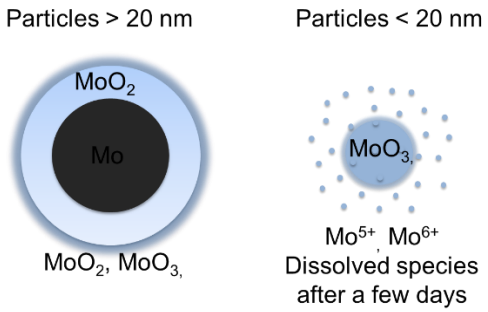

Fig. S11: Scheme of the composition of molybdenum nanoparticles in water

Analysing particles <20 nm, we could observe that no metallic molybdenum could be detected, showing that smaller particles tend to faster oxidation than larger ones. Since the particles tend to further oxidation during their storage dissolved species are conceivable. Considering TEM images of pure Mo (Fig. 2 in manuscript), shows that the largest fraction consist of particles <

20 nm. The fraction >20 nm is a minority which because of their lower specific surface barely influences the particles' electrochemical properties. Due to the alteration of the molybdenum colloid (Fig. 1 in manuscript) we repeated TEM measurements right away after ablation, which show that a higher fraction of particles > 20 nm exist in the freshly prepared colloid, which obviously dissolve or decay to smaller particles due to their oxidation (Fig. S12).

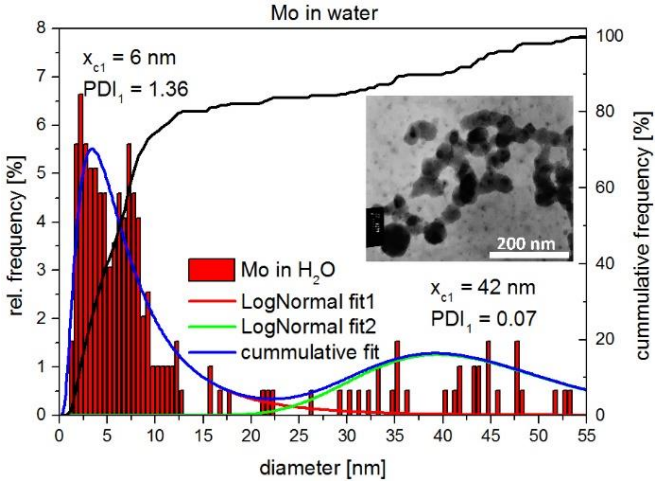

Fig. S12: Transmission electron microscopy of molybdenum nanoparticles in H_2O just after synthesis showing the existence of particles > 20 nm, with fresh prepared particles ~6 nm (x_{c1}). **VIII.ii**

4. Electrochemical investigations

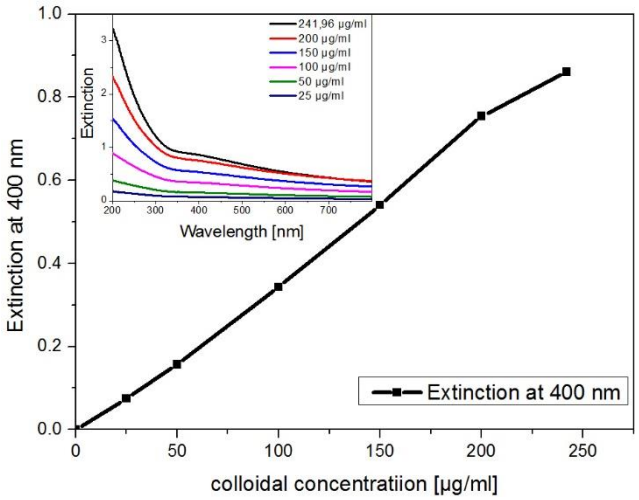

Fig. S13: Extinction at 400 nm of $Ni_{40}Mo_{60}$ as a function of the colloidal concentration. The inset shows the UV-Vis spectra for colloids at different concentrations.

In Fig. 3, it can be seen that $Ni_{40}Mo_{60}$ particles are quite polydisperse. Since particle size influence the electrocatalytic activity, we carried out cyclic voltammetry on size-fractionated particles. For this purpose, we centrifuged the colloids to a cut-off of 100 nm and separated the

particles. The particle concentration was estimated by UV-Vis spectroscopy, since the particle concentration correlates linearly (for low concentrations) with the extinction at 400 nm (Fig. S13).

After centrifugation, the size-separated $Ni_{40}Mo_{60}$ colloids can be compared with the non-centrifuged particles. The particle mass deposited on the disc electrode correspond to the same NiMo amount as in the non-centrifuged colloid, so that the samples are comparable. Cyclic voltammetry of the size separated $Ni_{40}Mo_{60}$ nanoparticles < 100 nm show, that the current density is similar to the non-centrifuged sample, while lower current densities were measured for particles >100 nm (Fig. S14). These results indicate, that the catalytic activity measured in Fig. 7 (manuscript) is mostly influenced by small particles due to the larger active surface area related to their volume. Since the activity for the non-centrifuged colloid is nearly the same for particles <100 nm, we assume, that the polydispersity of the colloids plays a minor role in regards to their HER/OER activity. The smaller nanoparticle fraction (~1-15 nm; Fig. 3) are the representative species in the colloidal solutions in this study regarding their catalytic activity.

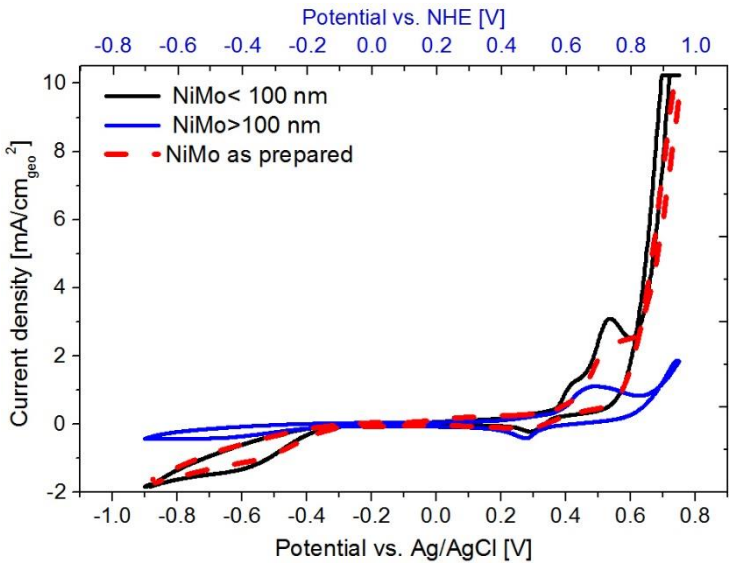

Fig. S14: Cyclic voltammograms of size fractionated $Ni_{40}Mo_{60}$ nanoparticles with a cut-off of 100 nm and as prepared colloid in comparison.

The nanoparticle loading on the electrode was controlled by knowing the particle concentration (determined by weighting target before and after laser ablation) and dropping a certain volume of the colloid (calibrated pipette) on the electrode surface.

Since we used colloidal stable nanoparticles to deposit them on the electrode surface, the particle distribution on the electrode was mostly homogeneous. In some cases, due to drying

process of the colloid an uneven distribution of the particles on the electrode surface was observed, where some areas were not completely covered (F b). However, a homogeneous distribution on the electrode was confirmed before electrochemical measurements by using a microscope (Fig. S15 c).

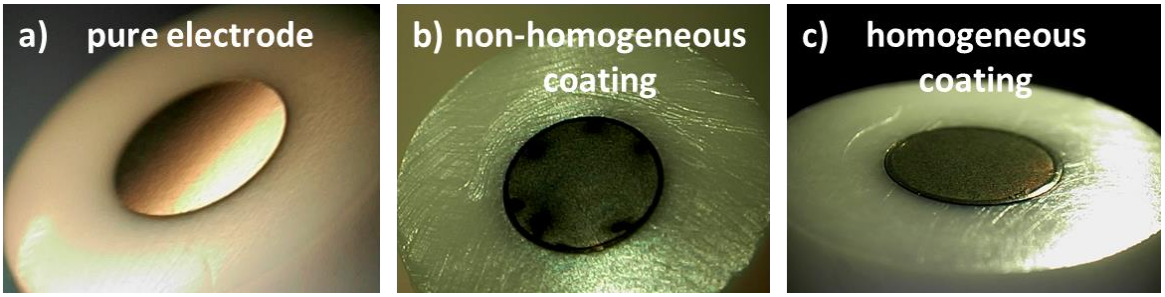

Fig. S15: Glassy carbon electrode before (a) and (b +c) after particle deposition.

Before each electrochemical measurement the working electrode was purified by using ultrasonication in ethanol and in deionized water for at least 5 minutes. The purity was verified by CV scans of the unloaded electrode (Fig. S16).

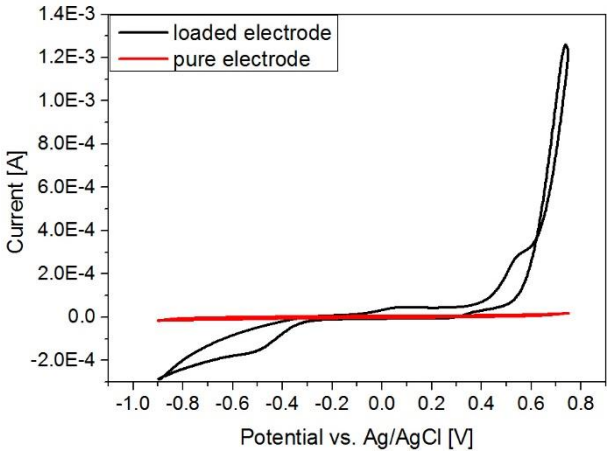

Fig. S16: Cyclic voltammogram of uncoated pure glassy carbon electrode and with Ni nanoparticles coated electrode.

During the measurements, the particle loading on the electrode surface was always kept the same, as well as the measure protocol. At least three repeated measurements were performed to ensure the reproducibility of our data. We evaluated the OER activity of the voltammograms of Mo, Ni, $Ni_{40}Mo_{60}$ and the colloidal mixture, respectively and calculated the error bars. shows the mean current density at 0.75 V vs Ag/AgCl with the corresponding error bars.

In general, potential cycling were performed for determining the durability of the catalyst material. This is important from practical point of view, especially for electrolyser used for storage of intermittent energy where cyclic operation is needed. The potential cycling induces changes in the (surface) structure of the electrocatalyst and this can result in degradation of the material. Therefore, we have selected potential cycling as the method for studying stability of the synthetized materials. For further electrochemical investigations chronoamperometry and chronopotentiometry measurements are valuable methods to determine the stability of the catalysts.

References

[1] M. C. Biesinger, B. P. Payne, L. W. Lau, A. Gerson, and R. S. C. Smart, "X-ray photoelectron spectroscopic chemical state quantification of mixed nickel metal, oxide and hydroxide systems," *Surf. Interface Anal*, vol. 41, no. 4, pp. 324–332, 2009.

[2] A. P. Grosvenor, M. C. Biesinger, R. S. C. Smart, and N. S. McIntyre, "New interpretations of xps spectra of nickel metal and oxides," *Surface Science*, vol. 600, no. 9, pp. 1771–1779, 2006.

Adsorption of Colloidal Platinum Nanoparticles to Supports: Charge Transfer and Effects of Electrostatic and Steric Interactions

1. Platinum concentration

To calculate the adsorption efficiency the nanoparticle concentration has to be measured. This was done using the interband extinction of platinum at 300 nm. For calibration, the extinction of a colloid at 300 nm is plotted as a function of the colloidal concentration while the inset shows the corresponding UV-Vis spectra at different colloidal concentrations. It can be seen, that the platinum concentration correlates linearly with the interband extinction and can be used as measure for nanoparticle concentration.

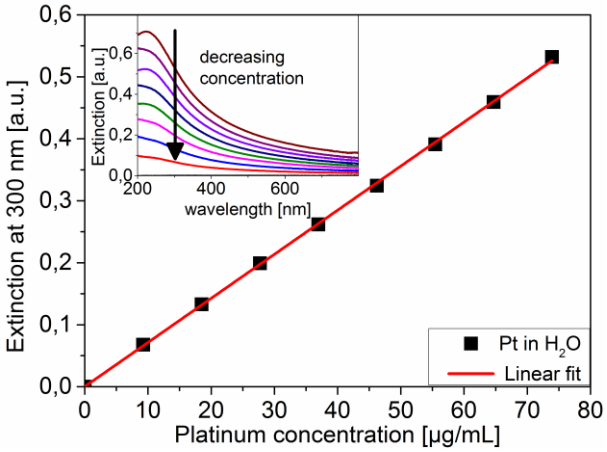

Figure S1: Interband extinction at 300 nm of platinum as a function of the colloidal concentration. The inset shows the UV-Vis spectra for colloids at different concentrations.

2. Used Laser systems

For the fabrication of ligand-free platinum nanoparticles we used two different laser systems which are listed in Table S1 including all technical parameter

Table S1: Specifications of used laser systems

Laser system	**λ [nm]**	**Pulse energy [mJ]**	***f* [kHz]**	**Focal distance [mm]**	**Pulse duration [ns]**	**Peak Power [MW]**
Rofin-Sinar RS-Marker 100D	1064	6.4	5	63	40	0.16
Rofin Powerline E	1064	0.385	10	130	8	0.05

The use of two different laser systems turned out to be necessary since nanoparticle productivity of the low-powered laser was not sufficient to perform a wide experimental matrix. Since both laser systems are quite equivalent in their parameters (fundamental wavelength at 1064 nm, pulse duration in nanosecond regime, similar peak power (0.16 MW and 0.05 MW)) the differences in nanoparticle properties should be minor. In literature, there is a number of studies on laser-generated platinum nanoparticles using nanosecond-pulsed Nd:YAG-laser[1-3]. Although pulse duration, wavelength and pulse energy is varying, they all show platinum nanoparticles with a number-weighted particle size distribution in the range from 5-10 nm particle size which is in very good agreement with the results produced by both of our laser systems.

2. Ligand surface coverage of nanoparticles

Nanoparticles were conjugated with an excess amount of ligand molecules in order to determine the number of unbound ligands in the supernatant and subsequently the number of surface bound ligands. The number of ligands attached on the nanoparticle surface (c_{bound}) was obtained as difference of the initially applied ligand dose (c_0) and the experimentally determined ligand

concentration in the supernatant after ligand adsorption on the nanoparticle ($c_{unbound}$) and removal of nanoparticles via ultracentrifugation.

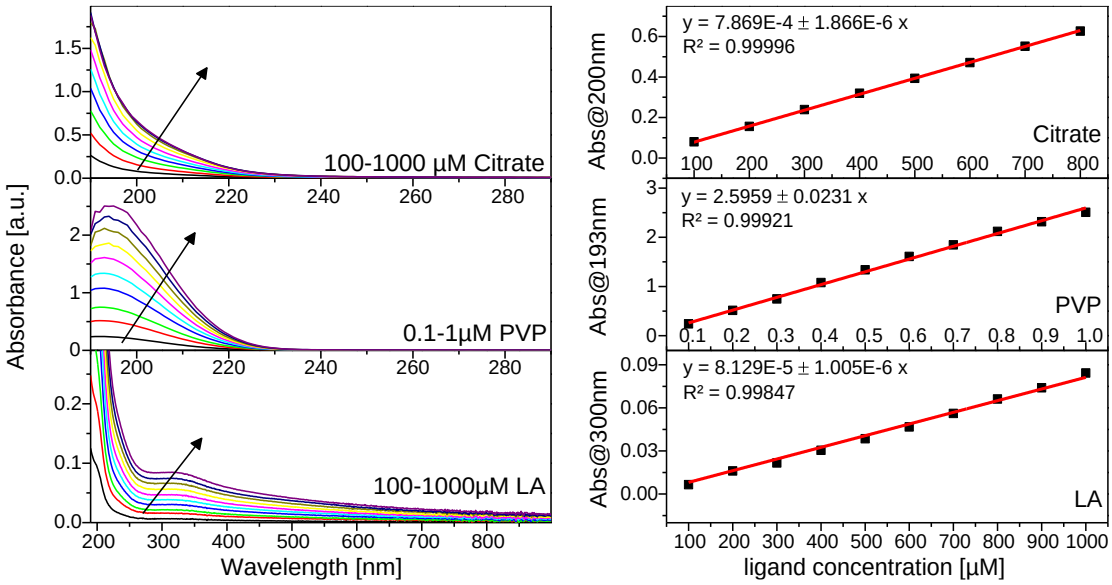

Figure S2: UV/Vis spectra of ligands dissolved in ultrapure water (left). Arrows indicate increasing ligand concentration. Citrate and LA concentrations increase in 100µM increments from 100µM to 1000µM, whereas PVP concentrations increase in 0.1µM increments from 0.1µM to 1µM. Resulting calibration curves show a linear correlation between absorbance and ligand concentration (right).

VIII.iii

Ultracentrifugation (30.000 g, 60 min; Beckman Coulter, Optima MAX-XP) was employed to obtain a nanoparticle-free supernatant with residual ligands, which was then analyzed by UV/Vis spectroscopy. Because the ligands citrate, PVP and LA do not show a characteristic peak in the spectrum, calibration curves could be obtained by relating the ligand concentration to the absorbance at a certain wavelength (see Figure S2). By assuming that all particles have a constant average size and a spherical shape, the total surface of the colloid ($A_{NP,tot}$) and the number of nanoparticles per mL ($N_{NP,tot}$) was calculated by the following equations:

$$N_{NP,tot} = \frac{\beta_{NP}}{m_{NP}} = \frac{3\beta_{NP}}{4\rho\,\pi\,r_{NP}{}^3} \quad \text{with} \quad m_{NP} = \rho V_{NP} = \rho\frac{4}{3}\pi\,r_{NP}{}^3 \qquad (1)$$

$$A_{NP,tot} = N_{NP,tot}\,A_{NP} = \frac{3\beta_{NP}}{\rho\,r_{NP}} \quad \text{with} \quad A = 4\,\pi\,r_{NP}{}^2 \qquad (2)$$

ρ [µg/cm³] = density
r [cm] = nanoparticle radius

m_{NP} [µg] = nanoparticle mass
A_{NP} [cm²/mL] = nanoparticle surface area
V_{NP} [cm³] = nanoparticle volume
β_{NP} [µg/mL] = mass concentration

Moreover, when determining the amount of ligands present at the nanoparticle surface, the footprint of the ligands and the absolute number of ligands per nanoparticle was calculated as follows:

$$N_{ligands} = \frac{c_{ligands} N_{Av.}}{N_{NP,tot}} \quad \text{and} \quad F = \frac{A_{NP,tot}}{c_{ligands} N_{Av.}} \qquad (3)$$

$N_{Av.}$ [1/mol] Avogadro constant
$c_{ligands}$ [mol/L] Ligand concentration
$N_{ligands}$ [#/nanoparticle] Number of ligands per nanoparticle
F [cm² ≙ 10^{14} nm²] Ligand footprint

Conjugation experiments with ligands were done with platinum nanoparticles with a diameter of 12.3 nm (mass-weighted) shown in Figure S3. All information on footprints and ligand surface coverage (citrate, PVP, LA) are collected in Table S2 and S3.

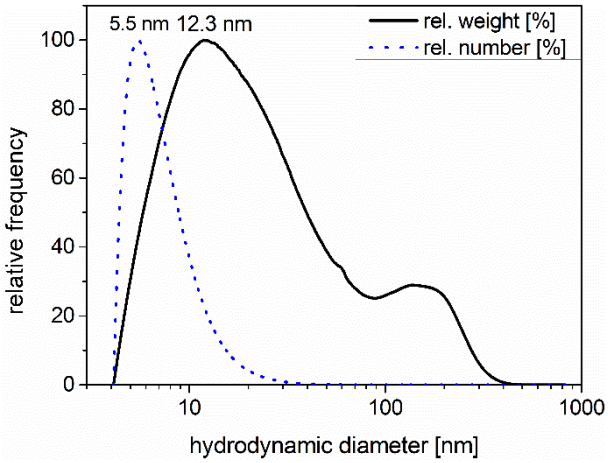

Figure S3: Particle size of platinum nanoparticles measured by analytical disc centrifugation (ADC) in mass-weighted (black line) and number-weighted (dotted blue line) representation

Table S2: Calculations of the footprint for the ligands LA, citrate and PVP based on a 12.3 nm platinum nanoparticle.

		LA	Citrate	PVP
characteristic wavelength for each ligand calibration	nm	300	200	193
measured absorbance of the supernatant of nanoparticles and ligands after centrifugation (unbound ligands)	a.u.	0.0083	0.0966	2.4710
measured absorbance of the supernatant of pure nanoparticles (blank correction)	a.u.	0.0044	0.0341	0.0595
corrected absorbance of the supernatant after centrifugation (unbound ligands)	a.u.	0.0039	0.0626	2.4115
factor to calculate ligand concentration (1/slope of calibration curve); see Figure S1		12302	1271	0.385
calc. concentration of unbound ligands	µM	48.5	79.5	0.929
absolute number of unbound ligands	#/10mL	2.91E+17	4.77E+17	5.57E+15
initially applied ligand conc.	µM	100.00	100.00	1.00
absolute number of initially applied ligands	#/10mL	6.00E+17	6.00E+17	6.00E+15
absolute number of attached ligands	#/10mL	3.09E+17	1.23E+17	4.26E+14
calc. total nanoparticle surface (V=10mL PtNP; c=50µg/mL; d=12.3nm); see Formula 2	nm^2/10mL	1.13E+16	1.13E+16	1.13E+16
calc. ligand footprint; see Formula 3	nm^2	0.04	0.09	26.7

Table S3: Calculations of the ligand surface coverage for the different footprints

Platin d= 12.3 nm 50µg/mL							
					surface coverage %		
surface	number	Ligands		Ligand/NP	F = 0.09 nm²	F = 0.04 nm²	F = 26.67 nm²
cm²/mL	#/mL	µM	Ligands/mL		citrate	LA	PVP
11.37	2.39E+12	0.001	6.02E+11	0	4.8E-05	2.1E-05	1.4E-02
11.37	2.39E+12	0.002	1.20E+12	1	9.5E-05	4.2E-05	2.8E-02
11.37	2.39E+12	0.004	2.41E+12	1	1.9E-04	8.5E-05	5.7E-02
11.37	2.39E+12	0.008	4.82E+12	2	3.8E-04	1.7E-04	1.1E-01
11.37	2.39E+12	0.01	6.02E+12	3	4.8E-04	2.1E-04	1.4E-01
11.37	2.39E+12	0.015	9.03E+12	4	7.2E-04	3.2E-04	2.1E-01
11.37	2.39E+12	0.02	1.20E+13	5	9.5E-04	4.2E-04	2.8E-01
11.37	2.39E+12	0.025	1.51E+13	6	1.2E-03	5.3E-04	3.5E-01
11.37	2.39E+12	0.028	1.69E+13	7	1.3E-03	5.9E-04	4.0E-01
11.37	2.39E+12	0.03	1.81E+13	8	1.4E-03	6.4E-04	4.2E-01
11.37	2.39E+12	0.04	2.41E+13	10	1.9E-03	8.5E-04	5.7E-01
11.37	2.39E+12	0.05	3.01E+13	13	2.4E-03	1.1E-03	7.1E-01
11.37	2.39E+12	0.075	4.52E+13	19	3.6E-03	1.6E-03	1.1E+00
11.37	2.39E+12	0.1	6.02E+13	25	4.8E-03	2.1E-03	1.4E+00
11.37	2.39E+12	0.25	1.51E+14	63	1.2E-02	5.3E-03	3.5E+00
11.37	2.39E+12	0.5	3.01E+14	126	2.4E-02	1.1E-02	7.1E+00
11.37	2.39E+12	0.75	4.52E+14	189	3.6E-02	1.6E-02	1.1E+01
11.37	2.39E+12	1	6.02E+14	252	4.8E-02	2.1E-02	1.4E+01
11.37	2.39E+12	1.2	7.23E+14	302	5.7E-02	2.5E-02	1.7E+01
11.37	2.39E+12	1.5	9.03E+14	378	7.2E-02	3.2E-02	2.1E+01

11.37	2.39E+12	1.7	1.02E+15	428	8.1E-02	3.6E-02	2.4E+01
11.37	2.39E+12	1.8	1.08E+15	453	8.6E-02	3.8E-02	2.5E+01
11.37	2.39E+12	2	1.20E+15	504	9.5E-02	4.2E-02	2.8E+01
11.37	2.39E+12	2.5	1.51E+15	629	1.2E-01	5.3E-02	3.5E+01
11.37	2.39E+12	5	3.01E+15	1259	2.4E-01	1.1E-01	7.1E+01
11.37	2.39E+12	7.5	4.52E+15	1888	3.6E-01	1.6E-01	1.1E+02
11.37	2.39E+12	10	6.02E+15	2518	4.8E-01	2.1E-01	1.4E+02
11.37	2.39E+12	15	9.03E+15	3776	7.2E-01	3.2E-01	2.1E+02
11.37	2.39E+12	20	1.20E+16	5035	9.5E-01	4.2E-01	2.8E+02
11.37	2.39E+12	25	1.51E+16	6294	1.2E+00	5.3E-01	3.5E+02
11.37	2.39E+12	50	3.01E+16	12588	2.4E+00	1.1E+00	7.1E+02
11.37	2.39E+12	100	6.02E+16	25176	4.8E+00	2.1E+00	1.4E+03
11.37	2.39E+12	500	3.01E+17	125879	2.4E+01	1.1E+01	7.1E+03
11.37	2.39E+12	1000	6.02E+17	251758	4.8E+01	2.1E+01	1.4E+04

3. Incomplete nanoparticle adsorption

Under certain experimental conditions (high salinity or pH), TiO_2 nanoparticles are dispersed during the supporting process and contribute to the UV/VIS absorption after centrifugation. Figure S4 shows the UV/VIS spectra of dispersed TiO_2 particles, platinum nanoparticles and their mixture. The spectrum of the mixture may qualitatively represented by a superposition of its individual components (TiO_2 and platinum NPs) which indicates that both species are present in a dispersed state. However, in case of a mixture, calculation of the adsorption efficiency using equation 1 leads to negative values although obviously no adsorption process takes places.

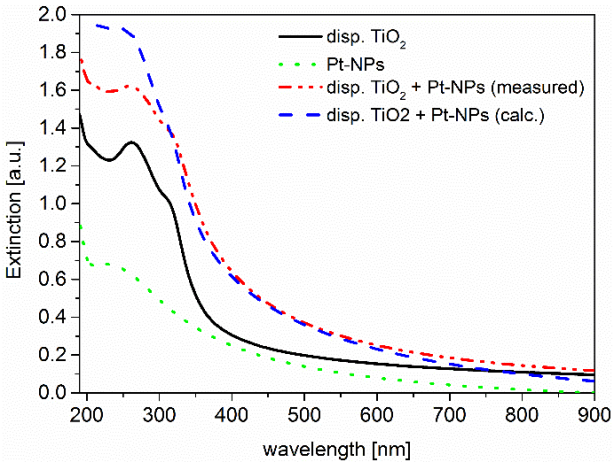

Figure S4: UV/VIS spectra of dispersed TiO_2 particles (black line), platinum nanoparticles (red line), mixture of disp. TiO_2 and platinum nanoparticles (blue line) and calc. spectra from disp. TiO_2 and platinum nanoparticles (dashed blue line)

To verify whether the platinum nanoparticles are still in colloidal state and do not adsorb to the TiO_2 particles, we centrifuged the mixture until complete precipitation and analysed the precipitates. Figure S6 (right) shows an image of the centrifuged sample. It consists of white TiO_2 and black platinum nanoparticles precipitate separated from each other obviously forming no adsorption product. Without centrifugation the mixture precipitates within days but shows a similar behaviour as it also consists of white TiO_2 powder and black platinum nanoparticle precipitant (Figure S5, right). In case of successful platinum nanoparticle adsorption (Figure S5, middle), the resulting Pt/TiO_2 appears as a homogeneous grey powder. Electron microscopy clearly reveals the presence of platinum nanoparticles adsorbed to TiO_2 as can be seen in Figure S5 (left).

Particle size analysis by analytical disc centrifugation (ADC) shows similar results (Figure S6 left): In case of uncompleted adsorption, platinum nanoparticles with a hydrodynamical diameter of 20 nm are present in the supernatant (black line) with a minor peak < 5 nm (TiO_2) indicating that no adsorbates are formed. In case of complete adsorption, ADC analysis of supernatant only reveals dispersed TiO_2 (dotted lines, red: pure TiO_2, blue: TiO_2 with adsorbed TiO_2) and no more present platinum nanoparticles.

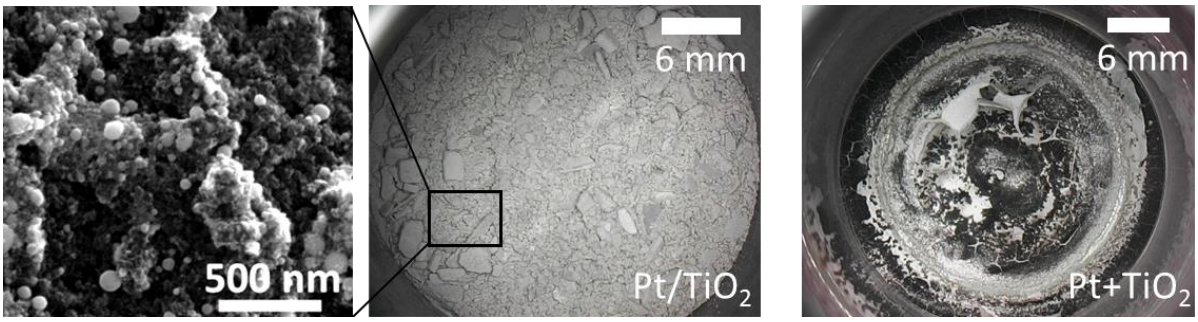

Figure S5: Supported platinum nanoparticles on TiO_2 (left) and agglomerated, not adsorbed platinum nanoparticles with TiO_2 support (right)

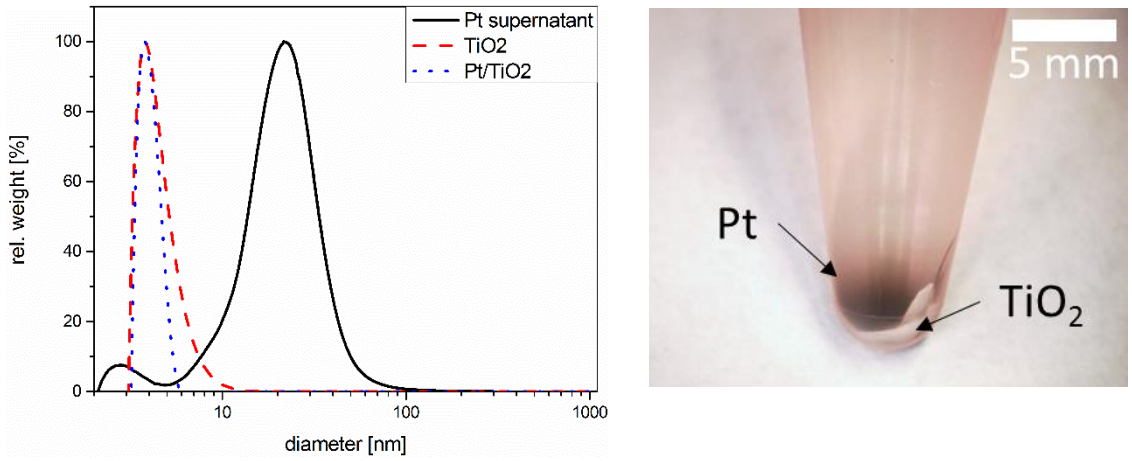

Figure S6: Size of supported platinum nanoparticles on TiO_2, unsupported separated platinum nanoparticles and TiO_2 measured by analytical disc centrifugation (ADC) (left). Platinum- and TiO_2 nanoparticles separated by centrifugation (15000 RPM, 2 min) in case adsorption took place (right)

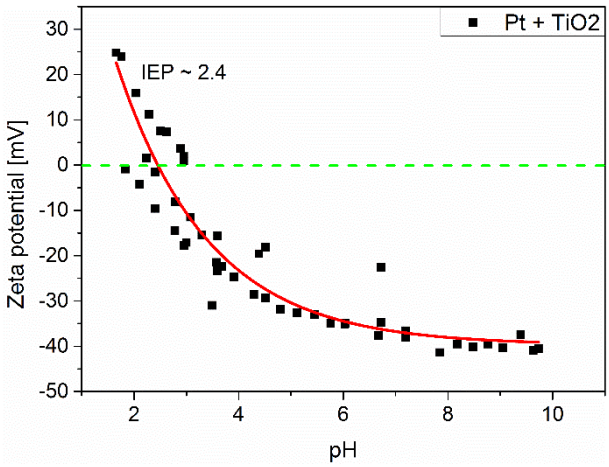

Figure S7: Zeta potential and isoelectric points of unsupported platinum nanoparticles in mixture with TiO_2

Incomplete adsorption has been also shown by measurement of the isoelectric point (IEP). In case of adsorption, the IEP of TiO_2 shifts towards a lower pH value of 5 (see Figure 4 of the manuscript). When no adsorption takes place, the IEP of the measured supernatant is about 2.4 which is close to the IEP of colloidal platinum nanoparticles (see Figure S7).

Consequently, calculated negative values of the adsorption efficiency in the manuscript´s diagrams correspond to dispersed TiO_2 and have to be considered as “no adsorption”.

4. Isoelectric point as a function of nanoparticle load

Isoelectric points were measured for a number of Pt/TiO_2 composites with different nanoparticle loadings between 0 wt% Pt and pure Pt. The results can be found in Figure S8 (left). The IEP as a function of nanoparticle load is shown in the manuscript in Fig. 3 (bottom). Figure S8 (right) shows the photometric mass loading of Pt/TiO_2 as a function of the Pt/TiO_2 ratio in the suspension before adsorption. It can be seen by the deviation from the black reference line that adsorption efficiency is lower than one at nanoparticle loads > 10 wt% (between 60-80%).

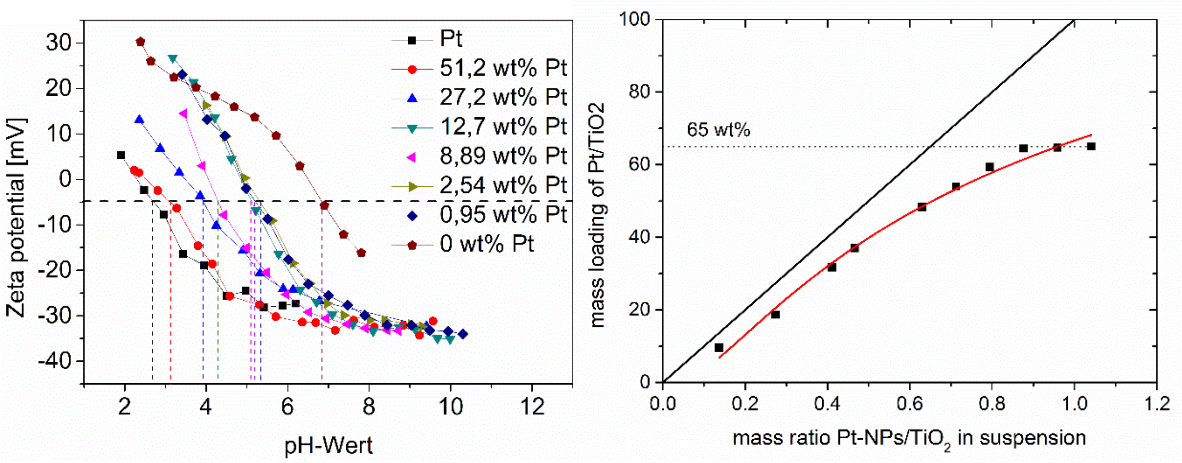

Figure S8: Left: Zeta potential and isoelectric points of Pt/TiO_2 composites for a set of different nanoparticle loadings and pure TiO_2 and platinum nanoparticles. Right: Mass of Pt/TiO_2 composites as a function of mass ratio Pt-NPs/TiO_2 in suspension. Black line represents a line with unity slope that is equal to complete nanoparticle adsorption.

5. Adsorption models

VIII.iii

Adsorption studies for the adaptability of different adsorption models (Langmuir, Henry, Freundlich, Temkin) were carried out by adsorption of platinum nanoparticles to TiO_2 with different nanoparticle loadings between 13 wt% and 95 wt% Pt. The adsorptive (Pt-NPs) concentration c [cm^2 Pt/mL solution] is plotted against the coverage of the support surface θ.

The TiO_2 coverage θ by platinum nanoparticles is defined as the ratio of the projected nanoparticle area to the surface of TiO_2 (eq. 4) and is given in cm^2 Pt/cm^2 TiO_2.

The surface area of TiO_2 is assumed to be A = 100 cm^2/g TiO_2 (BET surface taken from material data sheet), while the adsorbed platinum surface area was calculated by circular area-projection-surface equivalent A (Pt) ($A = \pi r^2$) with r (Pt) = 2.3 nm) and the particle number N (Pt) (see Fig. S9). The TiO_2-amount was kept constant while the Pt amount was gradually increased. Spectroscopic measurements of the supernatant of the hybrid-solution provide data about the adsorption efficiency corresponding to the coverage degree θ of TiO_2.

Please note, that the surface coverage θ is not the same as the mass loading in wt%. In our experiments, we showed that a maximal mass load of 65 wt% platinum nanoparticles could be adsorbed to the titania support (see Figure S8). This mass loading is equivalent to a surface coverage θ of 9,5 % of TiO_2. Further additions of Pt nanoparticles to TiO_2 support do not increase this value (see Figure S8).

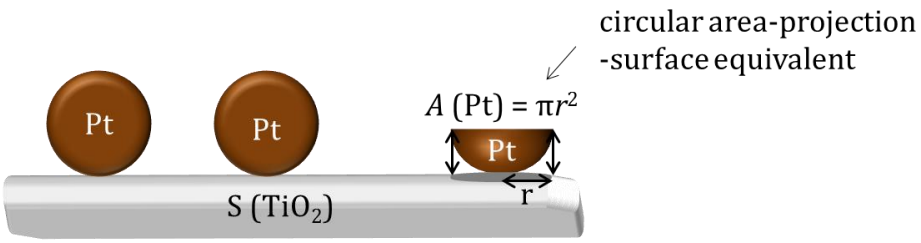

$$\theta\ (TiO2) = \frac{A(Pt)\cdot N(Pt)}{S(TiO2)} \qquad 4$$

Figure S9: Schematics of TiO_2 coverage with platinum nanoparticles.

Linear regression analysis of Henry, Langmuir, Freundlich, and Temkin equations were applied (see Table S4) of the data points for the determination of optimum adsorption isotherm. The adsorption process can be best described if experimental data points agree with linear curve corresponding to a high coefficient of determination R^2 (see Figure S10 and Table S5).

VIII.iii

Table S4: Equations and linear forms of adsorption isotherms (Henry, Langmuir, Freundlich, Temkin)

	Equation	**Linear regression**
Henry isotherm	$\theta = Kc$	$\theta = Kc$
Langmuir isotherm	$\theta = \frac{K\theta_{max}c}{1+Kc}$	$\frac{c}{\theta} = \frac{1}{\theta_{max}}c + \frac{1}{K\theta_{max}}$
Freundlich isotherm	$\theta = Kc^{1/a}$	$\log\theta = \frac{1}{a}\log(c) + \log(K)$
Temkin isotherm	$\theta = K\ln(bc)$	$\theta = K\ln(c) + K\ln(b)$

The specific adsorption coefficient is described by ratio of rate constants of adsorption and desorption.

$$K = \frac{k_{ads}}{k_{des}} \qquad 5$$

θ = coverage of adsorbent (TiO_2)

c = concentration of adsorptive (circular area-projection-surface equivalent (A) per colloid volumen, $A(Pt)/V_{colloid}$ [cm^2/ml])

K = specific adsorption coefficient

k_{ads} = rate constant of adsorption

k_{des} = rate constant of desorption

a = Freundlich coefficient

b = Temkin coefficient

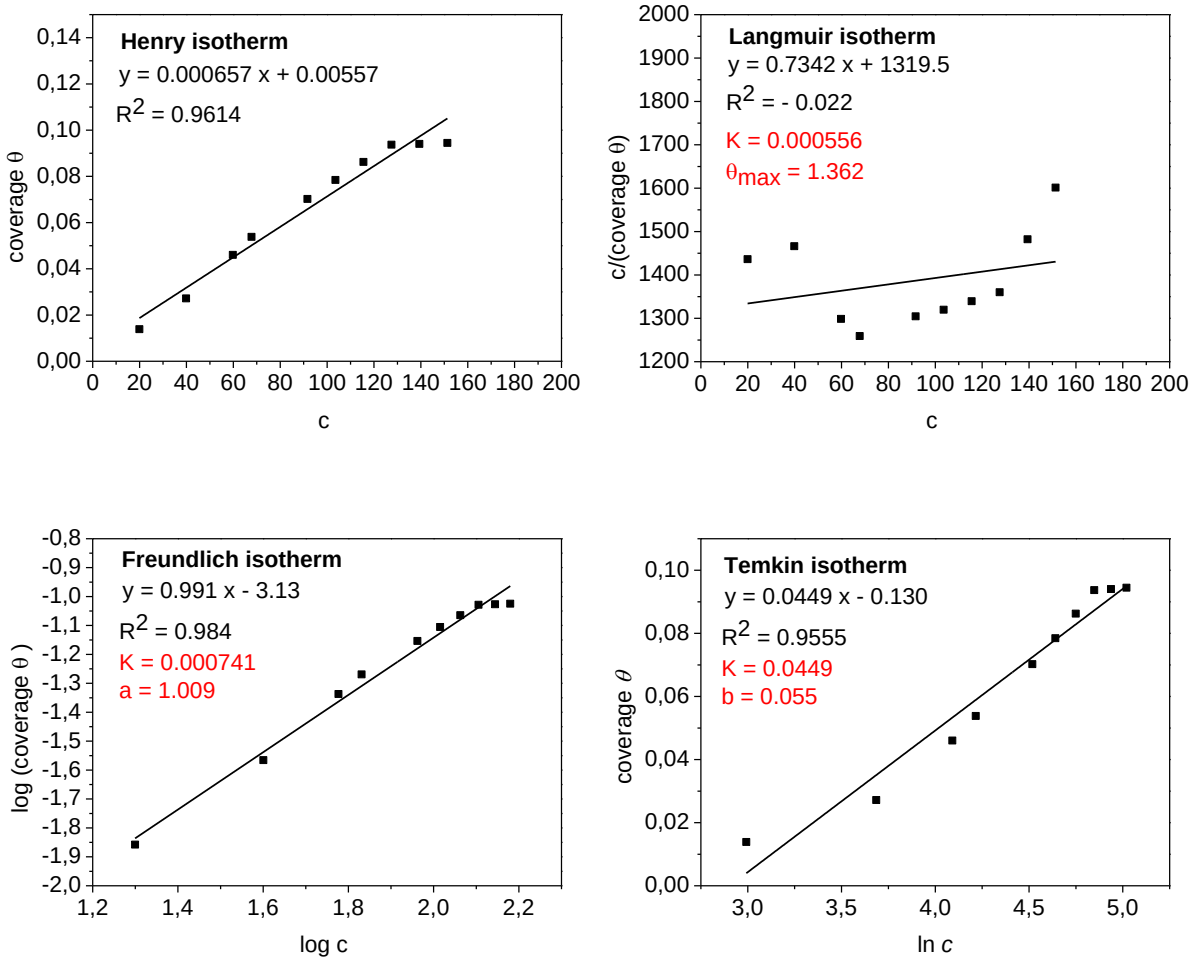

Figure S10: Fitted adsorption isothermes (Henry, Langmuir, Freundlich, Temkin) of different nanoparticle loads Pt/TiO_2

Table S5: R^2 of fitted adsorption isothermes (Henry, Langmuir, Freundlich, Temkin)

	Henry	Langmuir	Freundlich	Temkin
R^2	0.961	-0.022	0.984	0.955

6. Reproducibility of the adsorption experiments

To test reproducibility, we repeated the adsorption experiments for platinum in phosphate buffer in triplicate. In Figure S11 the adsorption efficiency is plotted as a function of ionic strength for three experimental series. For experiment 3 (dark green triangles), error bars (light green) were calculated for the adsorption efficiency by measuring the UV-Vis spectra several times as well as for the ionic strength by making the use of error propagation. It can be seen that the error for each measurement is very low, which shows a high reproducibility if several colloids (ionic strength and pH) are analysed at different conditions.

At a pH below the IEP of TiO_2, where the nanoparticle adsorption is almost complete (>98%), the data for several experiments are in very good agreement and show small errors (see Figure S11). If the pH is close to the IEP of the support, the extinction at 300 nm remains the same or is increased by not completely sedimented TiO_2, resulting in negative adsorption efficiencies. In this case, the values for the single experiments differ from each other because the amount of sedimented TiO_2 varies in each reproduced experiment and is hard to capture by error bars.

Our focus in this study is to verify the limitation of nanoparticle adsorption and to identify the adsorption mechanism. In each experiment is it obvious, that the adsorption efficiency is strongly influenced by the pH, which affects nanoparticle surface charge and finally the electrostatic interaction between the adsorptive and adsorbent. Figure S11 shows an almost identical ionic strength and corresponding pH value that results in decrease of adsorption efficiency: As soon as the pH is near the IEP of TiO_2 the adsorption is prevented due to electrostatic repulsion forces.

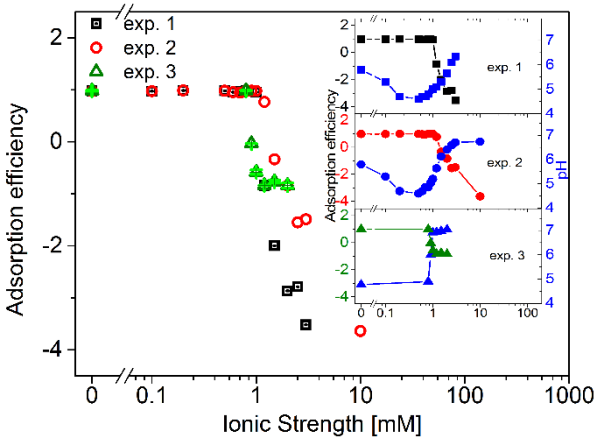

Figure S11: Adsorption efficiency as a function of ionic strength in phosphate buffer reproduced with three seperate experiments.

References

[1] M. Cueto, M. Sanz, M. Oujja, F. Gamez, B. Martinez-Haya, and M. Castillejo. Platinum nanoparticles prepared by laser ablation in aqueous solutions: Fabrication and application to laser desorption ionization. *J. Phys. Chem. C*, 115:22217–22224, 2011.

[2] F. Mafune, J. Y. Kohno, Y. Takeda, and T. Kondow. Formation of stable platinum nanoparticles by laser ablation in water. *J. Phys. Chem. B*, 107:4218–4223, 2003.

[3] W. T. Nichols, T. Sasaki, and N. Koshizaki. Laser ablation of a platinum target in water. ii. ablation rate and nanoparticle size distributions. *J. Appl. Phys.*, 100:114912, 2006.

Perpectives: Chemical and thermal stability of adsorbed $PtCu_3$ nanoparticles on titanium dioxide and carbon

The laser intensity distribution was measured by a beam profiler from Coherent. An elliptical shape of the profile could be detected (Figure S 1). It is Remarkable is that the laser intensity distributes with a horizontal decreasing gradient. The uneven laser energy intensity may contribute to a formation of bimodal size distributions, which is observed for the laser-synthesized $PtCu_3$ nanoparticles (Figure S 5).

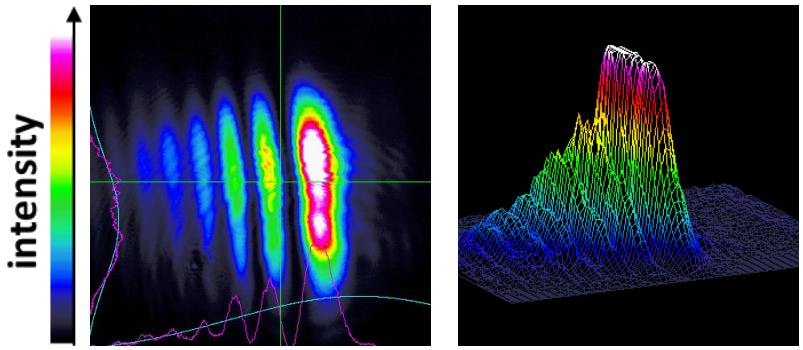

VIII.iii

Figure S 1: Beam intensity profile of the used nanosecond laser (edgewave) at 1064 nm.

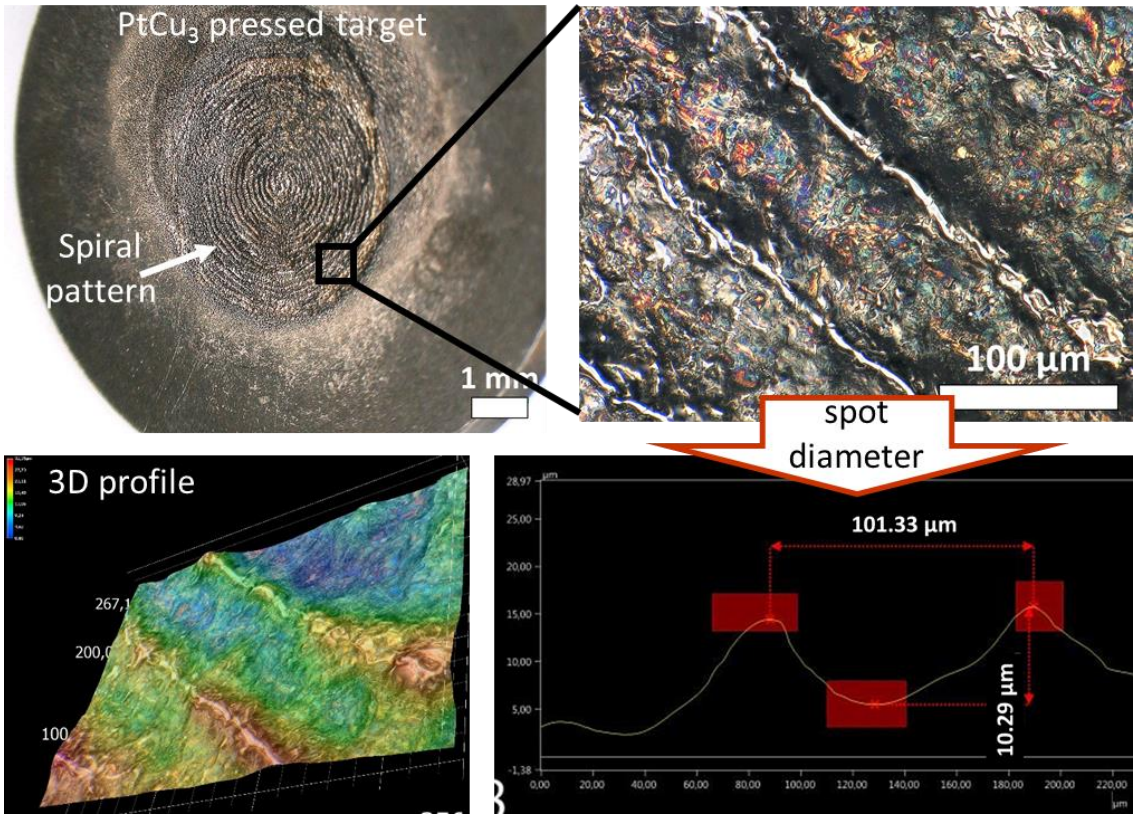

Figure S 2: Optical microscopy of the pressed $PtCu_3$ target with an enlargement of the spiral pattern. The distance between the crater is measured to be about 100 µm.

The diameter of the laser spot was estimated by measuring the ablating crater at the target using the optical microscope VHX-500 from Keyence (Figure S 2).

X-ray photoelectron spectroscopy show the partial oxidation of the particles surface. As already described in Chapter 6.2, Cu nanoparticles are stabilized in acetone against oxidation. 60 % of elementary copper can be analysed also on $PtCu_3$ nanoparticles (Figure S 3).

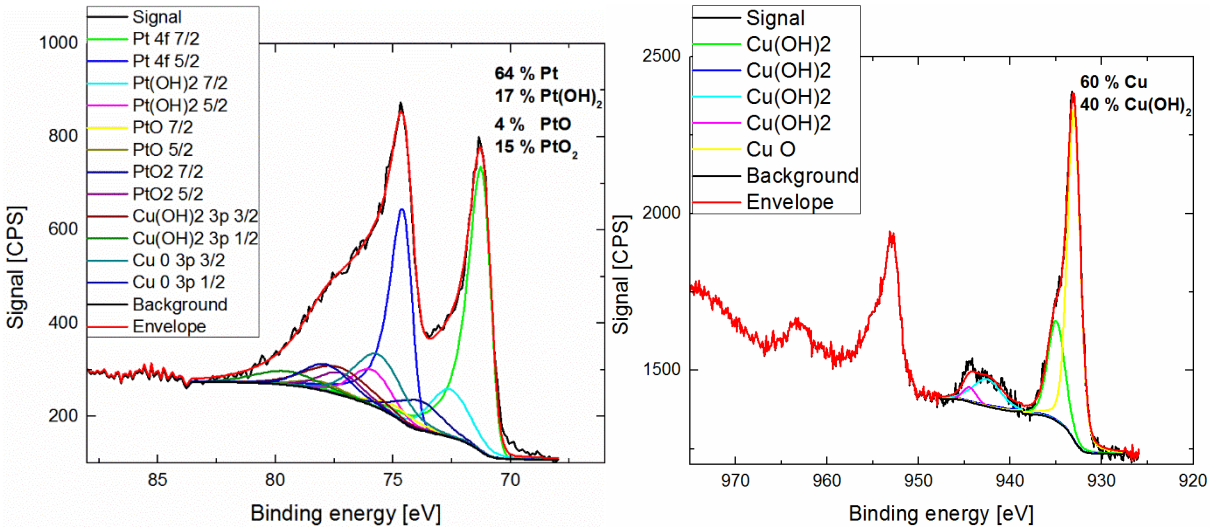

VIII.iii

Figure S 3: XPS-spectra of laser-generated $PtCu_3$ alloy nanoparticles.

The resistance table of graphene is derived from Schunk GmbH (Figure S 4): http://www.schunk-sik.com/de/sik/ChemicalResistanceCarbonGraphite/schunk01.c.39802.en (28.12.2016)

Inorganic compounds

Test medium 1. Acids	Chemical formula	Concentration %	temperature °C	pressure (bar)	carbon graphite, not inpregnated	graphite, not inpregnated	carbon graphite, resin impregnated	graphite, resin impregnated	resin bonded carbon	carbon graphite and graphite, antimony impregnated	carbon graphite and graphite, lead impregnated	carbon graphite and graphite, copper impregnated
Boric acid, aqueous	H_3BO_3	15	80	-	+	+	+	+	+	+	o	o
Chromic acid, aqueous	CrO_3+ H_2O	20	20	-	+	+	+	+	+	+	+	-
Chromic acid, aqueous	CrO_3 + H_2O	20	80	-	-	-	-	-	-	-	-	-
Chromic acid, aqueous	CrO_3 + H_2O	40	20	-	+	+	+	+	+	+	+	-
Chromic acid, aqueous	CrO_3 + H_2O	50	20	-	-	+	+	+	+	+	+	-
Chromic acid, aqueous	CrO_3 + H_2O	50	40	-	-	+	-	+	-	-	+	-
Chromic acid, aqueous	CrO_3 + H_2O	50	60	-	-	-	-	-	-	-	o	-
Chromic acid, aqueous	CrO_3 + H_2O	60	20	-	-	o	o	o	-	-	o	-
Hydrofluoric acid, diluted	HF	20	20	-	+	+	+	+	+	-	-	o
Hydrofluoric acid, concentrated	HF	40	20	-	+	+	+	+	o	-	-	o
Aqua regia	HCl/HNO_3 3:1	100	20	-	+	+	+	+	+	-	-	-
Mixed acid	HNO_3/H_2SO_4 2:3	100	20	-	-	-	-	-	-	-	-	-
Perchloric acid, aqueous	$HClO_4$	ca. 70	20	-	+	+	+	+	+	+	o	o
Phosphoric acid, ortho, concentrated	H_3PO_4	85	130	-	+	+	+	+	+	+	-	-
Nitric acid, diluted	HNO_3	38	20	-	+	+	+	+	-	-	-	-
Nitric acid, concentrated	HNO_3	65	20	-	+	+	+	+	-	-	-	-
Nitric acid, concentrated	HNO_3	65	80	-	-	+	-	-	-	-	-	-
Nitric acid, red fumins	HNO_3 + N-Oxide	100	20	-	-	-	-	-	-	-	-	-
Nitric acid, vapors	NO_2	100	20	-	-	-	-	-	-	-	-	-
Hydrochloric acid, diluted	HCl	20	20	-	+	+	+	+	+	+	-	o
Hydrochloric acid, diluted	HCl	20	50	-	+	+	+	+	+	-	-	o
Hydrochloric acid, diluted	HCl	20	80	-	+	+	+	+	+	-	-	-
Hydrochloric acid, concentrated	HCl	32	20	-	+	+	+	+	+	+	-	o
Hydrochloric acid, concentrated	HCl	32	50	-	+	+	+	+	+	-	-	-
Hydrochloric acid, concentrated	HCl	32	80	-	+	+	+	+	+	-	-	-
Hydrochloric acid, gas	HCl	100	20	-	+	+	+	+	-	+	-	+
Hadrochl. Acid, concentr.+chlorine	HCl + Cl_2	40g Cl_2/l	20	-	+	+	+	+	+	o	-	o
Sulphur dioxide, concentr., liquid	SO_2	99,7	10	ca. 3,35	+	+	+	+	+	+	+	+
Sulphuric acid, aqueous	H_2SO_3	50g SO_2/l	20	-	+	+	+	+	+	+	+	+
Sulphuric acid, diluted	H_2SO_4	25	20	-	+	+	+	+	+	+	+	+
Sulphuric acid, diluted	H_2SO_4	25	80	-	+	+	+	+	+	o	+	-
Sulphuric acid, diluted	H_2SO_4	50	20	-	+	+	+	+	+	+	+	+
Sulphuric acid, diluted	H_2SO_4	50	80	-	+	+	+	+	+	o	o	-
Sulphuric acid, diluted	H_2SO_4	62	20	-	+	+	+	+	+	+	+	+
Sulphuric acid, concentrated	H_2SO_4	96	20	-	+	+	+	+	+	+	+	+
Sulphuric acid, concentrated	H_2SO_4	96	50	-	+	+	+	+	+	+	+	+
Sulphuric acid, concentrated	H_2SO_4	96	80	-	+	+	+	+	-	-	o	-
Sulphuric acid, concentrated	H_2SO_4	96	120	-	+	+	+	+	-	-	-	-
Sulphuric acid, concentrated	H_2SO_4	96	160	-	+	+	-	-	-	-	-	-
Sulphuric acid, concentrated	H_2SO_4	96	200	-	o	o	-	-	-	-	-	-
Sulphuric acid, fumins (oleum)	H_2SO_4 + SO_3	H_2SO_4 (100) + 60% SO_3	20	-	-	-	-	-	-	-	-	-
Hydrogen sulfide water, cold, saturated	H_2S + H_2O	-	20	-	+	+	+	+	+	+	+	o

+ resistant o partially resistant - not resistant

Figure S 4: Resistance table of graphite from Schunk GmbH. The line that matches to the used conditions in the current study is marked in yellow.

The size of laser-generated $PtCu_3$ nanoparticles were measured by counting the particles of the colloidal and the supported nanoparticles on TiO_2 and Carbon black. Figure S 5 b-c) shows the corresponding histograms with a bimodal fit of the particle size, a cumulative volume distribution and the concluded parameter x_c (mean particle size), d_{50} (particle size at 50% of the volume distribution) and PDI (poly dispersity index). .In Figure S 5 a) the three size distribution from b-c) are summarized for a better comparison.

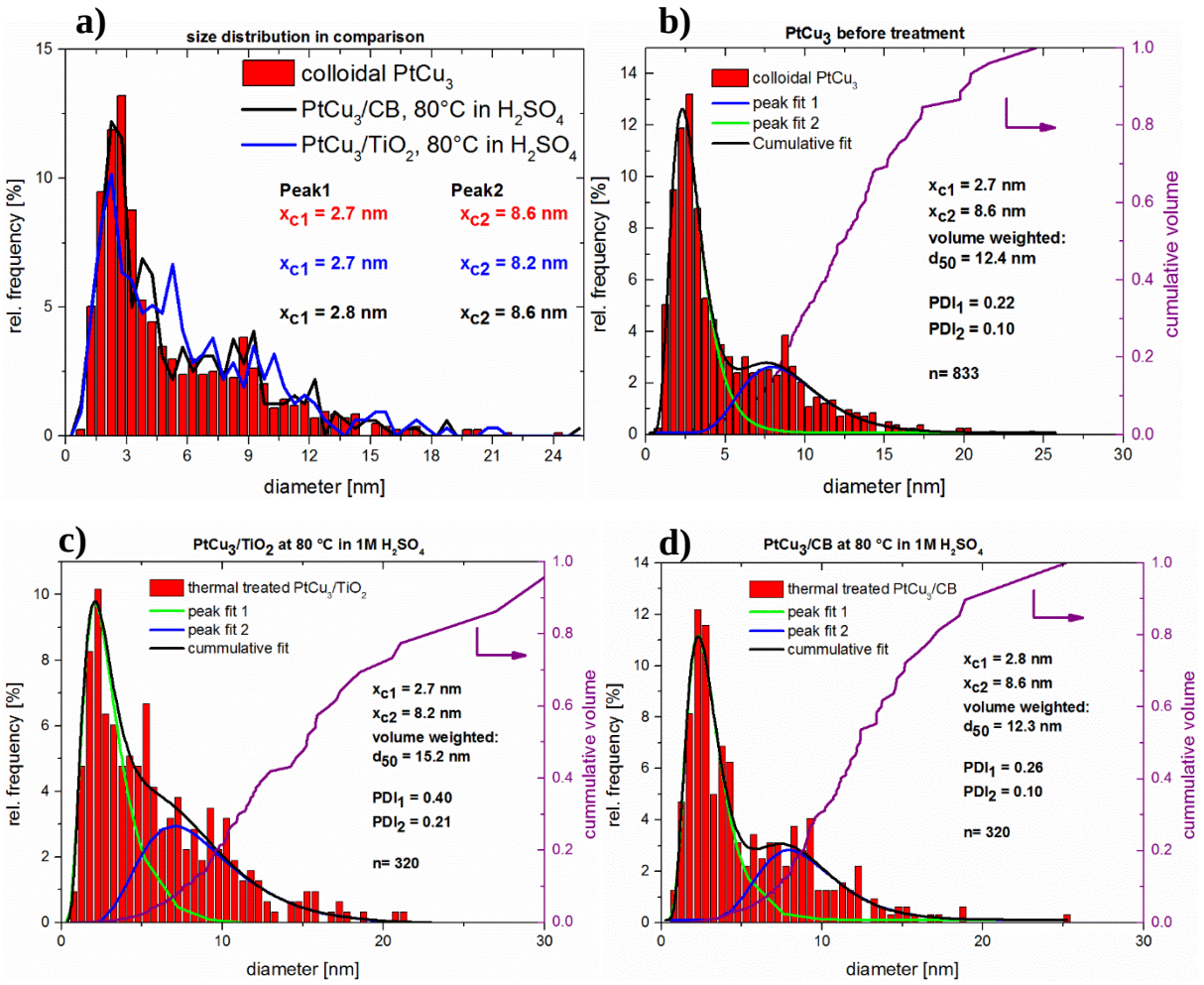

Figure S 5: Size histograms derived from TEM micrographs of laser-generated $PtCu_3$ nanoparticles before and after thermal treatment of $PtCu_3/TiO_2$ and $PtCu_3/CB$.

4. Declaration

4.1. Eidesstatt

Hiermit versichere ich, dass ich die vorliegende Arbeit mit dem Titel

„Laser synthesis and functionality of heterogeneous catalysts"

selbst verfasst und keine außer den angegebenen Hilfsmitteln und Quellen benutzt habe, und dass die Arbeit in dieser oder ähnlicher Form noch bei keiner anderen Universität eingereicht wurde.

Essen, 25 April 2017

4.2. Declaration of the contributions included within the thesis

This thesis includes scientific work that has been published with co-authors. My own contribution is declared as follows:

Chapter 1

> Sven Reichenberger, Stephan Barcikowski, Galina Marzun
> *Laser-generated nanoparticles as perspective materials for heterogeneous catalysis*, unpublished manuscript

Declaration of own contribution: This chapter is an excerpt from a planned scientific review on the subject area of PLAL in catalysis and was initiated by SB. GM defined the structure with a short draft of introduction and conclusions, while SR primarily created the draft under supervision of GM who also revised the manuscript. In this thesis, the text was slightly modified and rephrased by omitting the results, which were developed within this work.

Chapter 4.1

> Mathias Fischer, Josef Hormes, Galina Marzun, Philipp Wagener, Ulrich Hagemann, Stephan Barcikowski
> *In situ investigations of laser-generated ligand-free platinum nanoparticles by x-ray absorption spectroscopy: How does the immediate environment influence the particle surface?* Langmuir, 32, 8793-8802, **2016**

Declaration of own contribution: The authors MF and GM contributed equally. MF has performed and analysed X-ray absorption measurements. He has created a first draft of the manuscript. Experiments on colloid synthesis and data analysis including figures were performed by GM. Experimental design was done by PW. UH performed and evaluated XPS analysis. All authors have extensively discussed the interpretation of the data. Several parts of the manuscript were rewritten by GM and MF. This work was conducted under supervision of JF and SB who also revised the manuscript.

Chapter 4.2

> Galina Marzun, Helmut Bönnemann, Christian Lehmann, Bernd Spliethoff, Claudia Weidenthaler, Stephan Barcikowski
> *Role of dissolved and molecular oxygen on Cu and PtCu alloy particle structure during laser ablation synthesis in liquids*, ChemPhysChem, 18, **2017,** DOI: 10.1002/cphc.201601315

Declaration of own contribution: Experimental design, initial synthesis experiments, analysis of results (axcept XRD and TEM) and draft of the manuscript were done by GM. HB initiated this work and established the contact between UDE and MPI. BS performed TEM analysis and

evaluated the micrographs. CW conducted XRD analysis and the evaluation. CL, CW and SB revised the manuscript. All authors contributed with many discussions to the research.

Chapter 5.1

> Galina Marzun, Alexander Levish, Viktor Mackert, Tanja Kallio, Stephan Barcikowski, Philipp Wagener
> *Laser synthesis, structure and chemical properties of colloidal nickel-molybdenum nanoparticles for the substitution of noble metals in heterogeneous catalysis*, Journal of Colloid and Interface Science, 489, 57-67, **2016**

Declaration of own contribution: Experimental design, electrochemical analysis and construction of the manuscript was realized by GM. AL and VM conducted large part of the experiments (colloidal synthes, UV-VIS, XRD and its interpretation) under the supervision of GM. TK revised in particular the electrochemical part. SB brought useful ideas to the experimental design, interpretation and draft. The work was supervised by PW and SB. All authors revised the manuscript.

Chapter 6.1

> Galina Marzun, Carmen Streich, Sandra Jendrzej, Stephan Barcikowski and Philipp Wagener,
> *Adsorption of colloidal platinum nanoparticles to supports: Charge transfer and effects of electrostatic and steric interactions*, Langmuir, 30 (40),11928-11936, **2014**.

Declaration of own contribution: GM made experiments on particle adsorption performing pH and ionic strength studies as well as data evaluation and interpretation. CS and SJ conducted adorption experiments and analysis on the impact of ligands. SB have critically revised the manuscript and valuable input on data interpretation. PW supervised this work and designed the first draft. All authors contributed meaningfully by revision of the manuscript.

Chapter 6.2

> Galina Marzun, Swen Zerebecki, Stephan Barcikowski
> *Perspectives: Chemical and thermal stability of adsorbed $PtCu_3$ nanoparticles on titanium dioxide and carbon*, unpublished results

The experimental design was given by SB and GM. Preliminary experiments were conducted by GM and pursued by SZ under supervision of GM. TEM analysis were conducted partially an the UDE (Markus Heidelmann) and MPI-Kofo (Bernd Spliethoff/Christian Lehmann). The first draft was revised under supervision of SB.

Furthermore, language polishing was performed by the "American Manuscript editors" of the following sections:

- Abstract (ii-iii)
- Aims and objectives (pp.47-48)
- Laser-induced properties on precious and non-precious metal nanoparticles (pp. 51-53)
- Synthesis and functionality of laser-generated alloy nanoparticles for electrochemical catalysts (pp. 96-97)
- Synthesis of heterogeneous catalysts – method, mechanism and challenges of colloidal nanoparticle deposition (pp. 125-126)
- Perspectives: Chemical and thermal stability of adsorbed $PtCu_3$ nanoparticles on titanium dioxide and carbon (pp. 148-159)

5. Danksagung

Eine wissenschaftliche Arbeit wie diese braucht die Unterstützung Vieler. Daher möchte ich an dieser Stelle meinen aufrichtigen Dank an alle, die mich während meiner Promotion unterstützt haben, aussprechen.

Mein außerordentlicher Dank gilt meinem Doktorvater Prof. Dr. Ing. Stephan Barcikowski, der mir nicht nur stets mit Rat und Tat bei der wissenschaftlichen Betreuung mit vielen kreativen Ideen zur Seite stand, sondern auch darüber hinaus in schwierigen Situationen immer ein offenes Ohr für mich hatte. Danke für die Möglichkeit und das Vertrauen in mich eine eigene Forschungsgruppe leiten und mich entfalten zu dürfen.

Bei Prof. Dr. Jennifer Strunk möchte ich mich für die bisherige Zusammenarbeit und die konstruktiven sowie motivierenden Diskussionen danken. Herzlichen Dank für das kurzfristige und spotane Einspringen als Zweitgutachterin.

Desweiteren möchte ich Dr. Philipp Wagener für die Möglichkeit der Mitarbeit in seiner Nachwuchsgruppe in den ersten zwei Jahren meiner Promotion bedanken. Insbesondere danke für die sehr angenehme Betreuung mit vielen Freiheiten und zielführenden Diskussionen, welche mich in neue fruchtbare thematische Bahnen gelenkt haben.

Bei meiner Freundin Ina Haxhiaj bedanke ich mich für die aufregende Zeit wärend des gesamten Studiums, das unter anderem aufgrund schlafloser und dennoch amüsanter Nächte, unvergesslich bleibt.

Für die gute Zusammenarbeit und das außergewöhnlich tolle Arbeitsklima in der NETZ-Gruppe möchte ich mich bei meinen Kollegen Sven Reichenberger, Sebastian Kohsakowski, Marc Labusch, Christoph Mechler und Erwan Bertin bedanken. Für die stete Hilfsbereitschaft jedemenge Spaß auch außerhalb der Arbeitszeit danke ich ebenfalls allen Mitarbeitern der TCI: Claudine Florian, Lisa Gamrad, Bilal Gökce, Alexander Heinemann, Dieter Jacobi, Jurij Jakobi, Sandra Jendrzej, Mark Kalus, Sven Koenen, Marcus Lau, Alexander Letzel, Frank Marx, Nina Million, Elisabeth Mühlhausen, Christoph Rehbock, Tim Schmitz, Carmen Streich, Rene Streubel, Anna Tymoczko, Friedrich Waag, Dongshi Zhang, Anna Ziefuß.

Auch meinen fleißigen Studenten Matin Funck, Oliver Knipping, Thomas Lange, Alexander Levish, Daniel Neuland, Viktor Mackert, Andreas Schielke, Sebastian Tigges, Thomas Winter und Swen Zerebecki gilt mein Dank.

Meiner Familie möchte ich mich für ihre liebevolle Unterstützung und die entgegengebrachte Nachsicht, wenn ich mal keine Zeit hatte, danken. Ganz besonders danke ich meinem Freund Dominik Melcher, der mich stets motivierte und mich während meines gesamten Studiums und Promotion unterstützt und an mich geglaubt hat.

Für die finanzielle Unterstützung meiner Promotion, auch nach dem Weggang von Philipp Wagener, möchte ich mich besonders beim Bundesministerium für Bildung und Forschung (BMBF) bedanken. Die fruchtbaren Diskussionen bei den jährlichen INNOKAT-Projekttreffen haben wesentlich zu meiner Arbeit beigetragen. Daher möchte ich mich für die hilfreiche wissenschaftliche Unterstützung auch bei dem Beirat bedanken.

Ganz besonders möchte ich Herrn Prof. Dr. Helmut Bönnemann (†2017) danken, der sich mit Freude bereit erklärt hatte meine Arbeit mit zu begutachten. Seine mannigfachen und wegweisenden Ideen bei den Projekttreffen und die Kontakherstellung zu wichtigen Kooperationspartnern und mittlerweile Mitautoren, haben meine Arbeit stark bereichert. Daher möchte ich ihm diese Arbeit widmen. Auch wenn Prof. Bönnemann nicht mehr unter uns weilt, bleibt er in meinen Gedanken.